

RD-A182 341

THE ENTRAINMENT AND HOMOGENIZATION OF TRACERS WITHIN  
THE CYCLONIC GULF ST (U) WOODS HOLE OCEANOGRAPHIC  
INSTITUTION NA R S PICKART MAY 87 WHOI-87-9

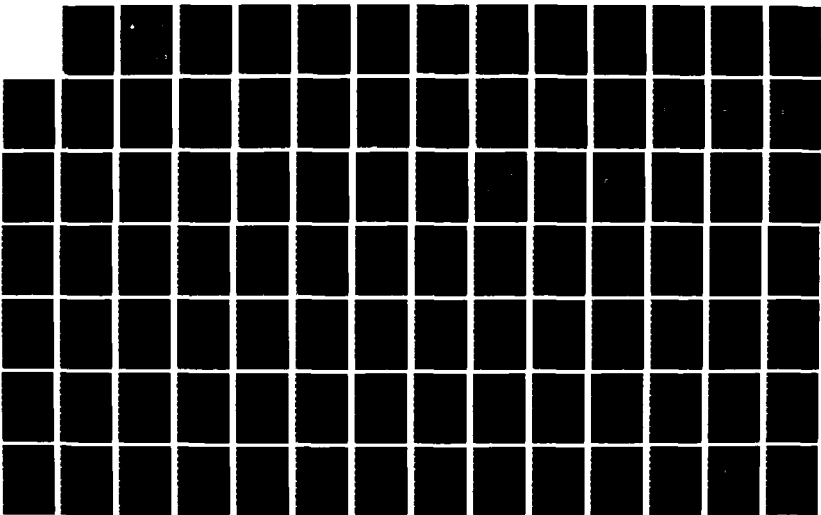
1/3

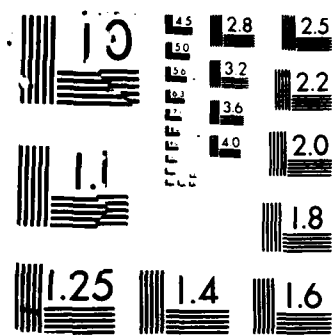
UNCLASSIFIED

N00014-76-C-8197

F/G 8/3

NL





2

WHOI-87-9

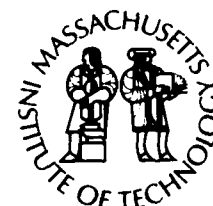
DTIC FILE COPY

**Woods Hole Oceanographic Institution  
Massachusetts Institute of Technology**

AD-A182 341



**Joint Program  
in Oceanography  
and  
Oceanographic Engineering**



**DOCTORAL DISSERTATION**

**The Entrainment and Homogenization of Tracers  
within the Cyclonic Gulf Stream Recirculation Gyre**

by

**Robert S. Pickart**

May 1987

DTIC  
ELECTE  
JUL 09 1987  
S D  
E

This document has been approved  
for public release and sale; its  
distribution is unlimited.

87 2 9

**The Entrainment and Homogenization of Tracers  
within the Cyclonic Gulf Stream Recirculation Gyre**

by

Robert S. Pickart

Woods Hole Oceanographic Institution  
Woods Hole, Massachusetts 02543

and

The Massachusetts Institute of Technology  
Cambridge, Massachusetts 02139

May 1987

**Doctoral Dissertation**

<b>Accession For</b>	
NTIS GRA&I	<input checked="" type="checkbox"/>
DTIC TAB	<input checked="" type="checkbox"/>
Unannounced	<input type="checkbox"/>
Justification	
By _____	
Distribution/	
Availability Codes	
Dist	Avail and/or Special
A-1	

Funding provided by the Office of Naval Research under contract Numbers N00014-76-C-0197, N00014-84-C-0134, NR 083-004; N00014-82-C-0019, N00014-85-C-0001, NR 083-400; and by the National Science Foundation under grant Number OCE 82-14925.



Reproduction in whole or in part is permitted for any purpose of the United States Government. This thesis should be cited as: Robert S. Pickart, 1987. The Entrainment and Homogenization of Tracers within the Cyclonic Gulf Stream Recirculation Gyre. Ph.D. Thesis. MIT/WHOI, WHOI-87-9.

Approved for publication; distribution unlimited.

**Approved for Distribution:**

*Robert C. Beardsley*

**Robert C. Beardsley, Chairman**  
Department of Physical Oceanography

*Charles D. Hollister*

**Charles D. Hollister**  
Dean of Graduate Studies



THE ENTRAINMENT AND HOMOGENIZATION OF TRACERS  
WITHIN THE CYCLONIC GULF STREAM RECIRCULATION GYRE

by

Robert S. Pickart

B.A. Susquehanna University, Selinsgrove, Pennsylvania  
(1981)

SUBMITTED IN PARTIAL FULFILLMENT OF THE REQUIREMENTS FOR  
THE DEGREE OF DOCTOR OF PHILOSOPHY

at the

Massachusetts Institute of Technology

and the

Woods Hole Oceanographic Institution

January 1987

Signature of the Author

Robert S. Pickart

Joint Program In Oceanography, Massachusetts  
Institute of Technology - Woods Hole Oceanographic  
Institution

Certified by

William Hogg

Thesis Supervisor

Accepted by:

Joseph Pedley

Chairman, Joint Committee for Physical Oceanography,  
Massachusetts Institute of Technology - Woods Hole  
Oceanographic Institution

The Entrainment and Homogenization of Tracers  
within the Cyclonic Gulf Stream Recirculation Gyre

Robert S. Pickart

The various distributions of tracer associated with the Northern Recirculation Gyre of the Gulf Stream (NRG) are studied to try to obtain information about the flow. An advective-diffusive numerical model is implemented to aid in the investigation. The model is composed of a gyre adjacent to a boundary current in which a source of tracer is specified at the upstream edge of the current. This set up attempts to simulate the lateral transfer of properties from the Deep Western Boundary Current (DWBC) to the NRG in the region where the two flows are in close contact west of the Grand Banks.

The results of the model are analyzed in some detail. Tracer is entrained into the gyre as a plume which extends from the boundary current and spirals across streamlines toward the gyre center. The maintenance of the spiral during spin-up and its relationship to the occurrence of homogenization at steady state is examined. An asymmetry in the spiral exists due to the ellipticity of the gyre, which also effects homogenization.

The anomalous properties that are fluxed into the NRG include salt, oxygen, and freon. These particular tracers are independent from each other, the former two because they are characterized by different vertical profiles in the deep layer. This results in a decay of oxygen but not salt, due to the presence of vertical mixing as discussed by Hogg et al. (1986, Deep-Sea Research, 33, 1139-1165). Their analysis is expanded upon here. The effect of vertical mixing on the gyre/boundary current system is examined within the context of the numerical model. Results are applied to recently collected water sample data from the region which leads to an estimate of the lateral and vertical eddy diffusion coefficients and an estimate of the amount of oxygen in the NRG that has diffused from the DWBC.

The accumulation of freon within the NRG is considered in addition to salt and oxygen. Appreciable levels of freon have been present in the ocean only since 1950, and the atmospheric source functions have been increasing steadily since then. A simple overflow model is presented of the manner in

which freon may be stirred in the Norwegian-Greenland basin prior to overflowing and entering the DWBC. Once in the boundary current the concentrations are diluted by way of mixing with surrounding water. Two different schemes are considered in which the immediate surrounding water accumulates a substantial amount of freon as time progresses. These models suggest that the freon-11:freon-12 ratio may not be a conserved quantity for the water in the core of the DWBC. It is found that the level of freon in the NRG is barely above the existing background level.

## TABLE OF CONTENTS

	Page
Introduction	1
CHAPTER ONE: Gyre Processes	7
Preliminaries	7
Initial Penetration	10
Homogenization	42
CHAPTER TWO: The Northern Recirculation Gyre	60
Preliminaries	60
Model Study	61
Data Comparison	105
CHAPTER THREE: Time-Dependent Input	130
Preliminaries	130
Overflow Basin Model	132
Boundary Current Models	141
Time-Dependent Transfer Model	179
Conclusions	187
Summary	190
Acknowledgements	191
References	192
Appendix	195

## Introduction

Over the past several years a clearer picture has emerged of the mean abyssal circulation of the western North Atlantic. In particular the existence of a deep cyclonic gyre situated between the New England seamounts and Grand Banks, whose eastward flowing portion contributes to the deep Gulf Stream, has been addressed by Hogg in a series of works. This is in contrast to the deep anticyclonic subtropical gyre described by Worthington (1976).

Worthington postulated using a historical data set that roughly 60 Sverdrups of water colder than  $4^{\circ}\text{C}$  recirculate to the south of the Gulf Stream. In order to produce a consistent flow pattern, the constraint of geostrophy was relaxed in certain regions of the gyre where instead the continuity of water properties was used as a guide for flow lines. Several years later Wunsch and Grant (1982), with the same data set, produced a very different deep flow pattern using inverse methods. They postulated a cyclonic gyre transporting roughly 25 Sverdrups (which did satisfy geostrophy everywhere). In addition to this evidence based on hydrographic data, there is also direct evidence for cyclonic recirculation.

In 1983 Hogg compiled all the available deep, long-term current meter measurements in this region of the North Atlantic. From this data he inferred a consistent streamline pattern which includes a cyclonic gyre that he estimates to be carrying ~20 Sverdrups. It is somewhat different from the Wunsch and Grant gyre however; it is smaller in extent both zonally and meridionally. Also in contrast to the Wunsch and Grant pattern is the presence of a small anticyclonic gyre just to the south of the cyclonic recirculation. Hogg estimates this flow to be 10 Sverdrups.

Recently additional current meter data has become available in this region of the Gulf Stream. Hogg et al. (1986) incorporated these measurements into the existing historical data set, and refined the earlier picture presented by Hogg (1983). In particular, the north-south length scale of the cyclonic recirculation appears to be even smaller yet. A schematic streamline of the gyre, which Hogg et al. have termed the Northern Recirculation Gyre (NRG), is shown in Figure 1.1. One of the experiments that yielded the new current meter data was the Abyssal Circulation Experiment (ABCE). In

1983-84 ABCE was carried out to learn more about the NRG. It consisted in part of a moored array of current meters centered near  $67^{\circ}\text{W}$ ,  $40^{\circ}\text{N}$ . In addition to the evidence for tighter recirculation it was found that the westward return flow of the gyre is nearly depth independent.

At this point it seems evident that there is a substantial cyclonic recirculation of the deep Gulf Stream. It is not evident, however, what drives this gyre. There has been a considerable amount of modelling work that has addressed in one form or another the presence of deep flow in this region. A feature of eddy resolving Gulf Stream numerical simulations is the existence of one or more regions of closed circulation in the deep layer. Some models exhibit only anticyclonic deep flow while others contain both anticyclonic and cyclonic deep gyres (Holland and Lin, 1975). Harrison (1982) proposes that the cyclonic recirculation in these models may be inherently related to quasigeostrophic, adiabatic considerations.

One such numerical experiment which contains deep cyclonic flow is that of Holland (1978). The model is a two layer quasigeostrophic flow driven by symmetric wind stress. Holland and Rhines (1980) analyzed this model in some detail, and showed that the deep gyres (both anticyclonic and cyclonic) are driven by eddy thickness fluxes (or equivalently, heat fluxes) in the surface layer. Hogg (personal communication) has applied this idea to the NRG using a limited heat flux data set. This first attempt has suggested that this may not be the driving mechanism in the ocean.

The mean, lower layer potential vorticity field ( $\bar{Q}$ ) in the Holland (1978) simulation shows an area of uniform  $\bar{Q}$  in the region of the two most intense counter-rotating gyres. Rhines and Young (1982a) have shown that in the presence of weak eddies, homogenization of  $\bar{Q}$  will tend to occur within closed streamlines. Hogg and Stommel (1985) used as a premise the condition of uniform potential vorticity and derived deep cyclonic recirculation to the north of the Gulf Stream in an analytical framework. Their model relies on the presence of variable bottom topography and the thermocline topography associated with the Gulf Stream (both of which were modelled realistically). In the model they show that the southward extent of the gyre flow is determined by the position of the surface Gulf Stream, which lends support to the idea of tight recirculation suggested by the newer data.

One of the inconsistencies between the numerical models and the data is that in the ocean, directly beneath the surface Gulf Stream, is the westward return flow of the NRG. In the models the separated Gulf Stream extends from top to bottom. Richardson (1985) constructed from a combination of current meter, surface drifter, and SOFAR float data an average velocity section at  $55^{\circ}\text{W}$  which seems to resolve this inconsistency. He shows a Gulf Stream that is top to bottom but in the vertical is sloped to the south. On either side of the Stream is westward flow, consistent with the double gyre scheme of Hogg (1983). The other inconsistency between the model ocean and real ocean, that regarding the driving mechanism, remains to be sorted out. Hogg and Stommel (1985) have revealed some elements that seem important in regard to cyclonic recirculation, but this has no direct bearing on what forces the flow.

The homogenization that accompanies flow within closed streamlines reveals itself in another context as well, that of passive tracers. The uniformity of  $\bar{Q}$  is crucially tied to the structure and dynamics of the circulation field, which also makes it difficult to address. In terms of a passive tracer however homogenization is more easily studied, which suggests that the case of a passive tracer be carefully examined. It is the hope that the ideas and insights developed in these simpler surroundings can then be applied to the more complicated case of a dynamically active quantity.

Musgrave (1985) did a numerical study of the homogenization of passive tracers in the thermocline of a subtropical gyre. The process he modelled was that of tracer being subducted into the gyre from outcropping lines in the northern regions. The abyssal gyres are not subject to this type of ventilation. However, as depicted in Figure 1.1, a portion of the Northern Recirculation Gyre passes very closely to the North Atlantic Deep Western Boundary Current (DWBC) which flows along the continental slope. The water in the boundary current, having recently come from high latitudes, has very distinctive characteristics, and so the DWBC represents a source of tracer into the deep layer.

The other component of ABCE was a hydrographic cruise covering a sizable portion of the NRG, in which water sample data was also collected. Hogg et al. (1986), using data from several previous cruises as well, mapped out

the corresponding lateral distributions of various tracers. The conspicuous feature in all of the distributions was a region of very weak gradients, believed to be in response to the stirring action of the cyclonic recirculation. Hogg et al. presented a simple model of the manner in which tracer diffuses from the boundary current and subsequently becomes homogenized within the gyre. In this work we examine this process in some detail. We analyze more thoroughly various aspects of the model used by Hogg et al., and apply the results to the ABCE data set.

The DWBC is characterized by a distinct signal in salt, oxygen, silica, freon, and various other tracers. As described in Hogg et al. (1986) it is believed that the eastward flow of the NRG pulls a plume of these tracers away from the boundary. This type of process was mentioned by McCartney et al. (1980) in describing a meridional section of silica at  $55^{\circ}\text{W}$ . Here we consider only the distributions of salt, oxygen, and freon. By studying the interaction between diffusion from the current and advection from the nearby recirculation we can obtain information about the entrainment and homogenization that occurs in a gyre, and about specific characteristics of the NRG.

To aid in this study a simple two-dimensional advective-diffusive model was implemented which was designed to represent the DWBC/NRG system. The velocity field in the model is specified, and a source of tracer is introduced. In chapter one we discuss some of the results of the numerical model. We split the analysis into two parts, the first part focussing on the process by which tracer penetrates the streamlines of the gyre during spin-up. A single numerical experiment is analyzed to understand the details of how this occurs. The entrainment is characterized by a plume of tracer which extends from the boundary current and wraps into the gyre, spiralling across streamlines towards the gyre center. We first examine what factors cause the plume to cross streamlines in the simpler context of a rectilinear shear flow. Results obtained for this idealized flow pattern are then applied to the full-blown case of the gyre in the numerical model.

The second part of the numerical model analysis focusses on the occurrence of homogenization within the gyre at steady state. We discuss how the velocity structure of the gyre and the character of the spiralling plume are tied into this process. Results from several different numerical runs are



compared as well to illustrate the effect that varying the diffusivity has on homogenization.

Chapter one deals with the model gyre circulation alone, and results obtained apply to any closed circulation of this form, not just the NRG. In chapter two we take a broader perspective and include the fact that the tracer filling the interior diffused from the boundary current. We use the numerical model to help analyze tracer distributions from ABCE in order to learn more about the NRG. To make the comparison between model and data more revealing a simplified box model representation of the numerical model is solved analytically. We first apply the box model to the numerical model in order to help interpret some of the results. The information obtained by this comparison is then used to interpret the data. Among other things we learn about the size of the NRG, how much tracer it entrains, and what values of diffusivity (lateral and vertical) are associated with the flow. We also learn what factors dictate how quickly the gyre is filled and relate this to the analytical results of Rhines and Young (1983).

In their work regarding the tracer distributions associated with the NRG, Hogg et al. (1986) discussed a subtle difference between those distributions of salt and oxygen. They explained the difference as a result of vertical mixing. In chapter two this distinction is considered in greater detail. We are able to distinguish between a salt-type tracer and oxygen-type tracer in the numerical model and box model. (Chapter one deals exclusively with a salt-type tracer, so the results apply directly to the ABCE salinity data.) In chapter two we compare the results of two numerical runs that include vertical mixing with two of the runs of chapter one (without vertical mixing), and show that some of the information about the NRG can only come from an oxygen-type tracer. A further run without vertical mixing is presented to illustrate the effect of western intensification of the gyre.

Freon is also an oxygen-type tracer, but it is unique in that the amount of freon in the world oceans is increasing very rapidly. While it is believed that the oxygen and salt distributions in the region of the NRG are close to steady state, the distribution of freon is constantly changing. In order to understand the evolution it is necessary to know how the DWBC source strength changes in time. It is evident then that to study freon, a regional

model is not sufficient; we must consider the evolution of freon in high latitude source waters, and throughout the DWBC.

Chapter three addresses this previous history of the freon and how it affects the distribution found in the NRG. The treatment is in three parts: the overflow process in the Norwegian-Greenland Sea which leads to the formation of the DWBC, the advection and mixing that occurs in the boundary current, and finally the diffusion into the NRG (within the regional domain of the previous chapters). The treatment in chapter three is analytical. Simple models are used to determine freon concentrations in the overflow water and DWBC, and this information is used to drive the box model of the NRG region. (It is not feasible to use the numerical model of the previous chapters.) Freon has been in the ocean since roughly 1950. Its atmospheric source function is well defined and in recent years measurement techniques have improved, both of which make freon an appealing tracer to study. Correspondingly freon studies have become more common, and experiments have now been carried out in various regions including the Arctic, Antarctic, and Mediterranean. Studies in the Atlantic include TTO (Transient Tracers in the Ocean) and ABCE.

Using the atmospheric freon concentrations and seawater solubilities, estimates have been made of the rate in which water is being transported from northern latitudes along the western boundary of the Atlantic (Smethie and Trumbore, 1984; Weiss et al., 1985). When this type of calculation is applied to the DWBC, it predicts a core speed of  $\sim 1$  cm/sec. These estimates do not take into account water formation processes and also rely on the assumption that the dilution which occurs is with freon-free water. In chapter three we address both of these points. We find that the overflow process has significant bearing on the calculation, and using two separate boundary current models arrive at larger core speeds for the DWBC. Estimates of the diffusivities that come out of these models are similar to the independent estimate from the NRG calculation of chapter two. We find also that freon is only now beginning to accumulate within the Northern Recirculation Gyre.

## CHAPTER ONE: GYRE PROCESSES

Preliminaries

The northern recirculation gyre (NRG) is believed to be a weakly depth dependent flow transporting roughly 20 Sverdrups, driven by eddies from the surface Gulf Stream (Hogg et al., 1986). During a portion of its circuit the water passes closely to the DWBC (Figure 1.1) at which point it is ventilated by lateral diffusive transfer of various water properties from the current (ventilated in the sense that the gyre is replenished by younger boundary current water). A simple two-dimensional numerical model was constructed to represent this process. The streamlines of the model are shown in Figure 1.2 and consist of a boundary current situated alongside a gyre. Flow speeds are representative of the current meter data in Hogg (1983), and the size of the gyre is roughly that suggested by Hogg. At the northern edge of the model boundary current a steady Gaussian source of tracer is specified, and at the southern edge tracer is allowed to advect out of the domain. Everywhere else along the boundary there is no flow (velocities there were set identically equal to zero) and open boundary conditions enable tracer to diffuse out of the region.

The evolution of tracer in the interior is governed by a finite-difference approximation of the two-dimensional advective-diffusive equation,

$$\frac{\partial \theta}{\partial t} + \vec{u} \cdot \vec{\nabla} \theta = \vec{\nabla} \cdot \kappa \vec{\nabla} \theta \quad (1.1)$$

where  $\theta(x,y)$  = tracer concentration,  
 $\kappa$  = eddy diffusivity (constant),  
 $\vec{u}(x,y)$  = velocity vector,

and  $\vec{\nabla} = \vec{i} \frac{\partial}{\partial x} + \vec{j} \frac{\partial}{\partial y}$ .

The circulation is steady, and initially the domain is tracer free. We set the diffusivity  $\kappa = 10^6 \text{ cm}^2/\text{sec}$ . Details of the set up and numerics of the

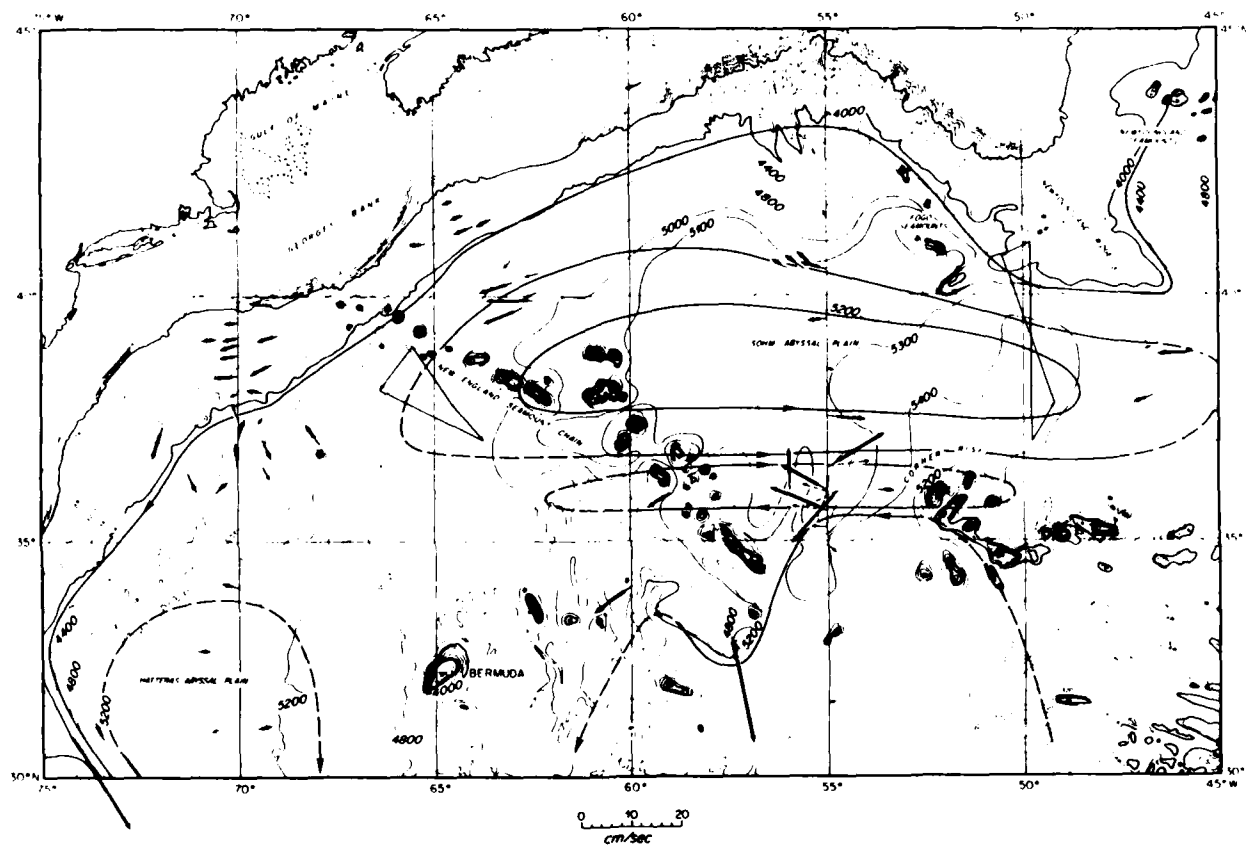


Figure 1.1: Schematic flow pattern of the Northern Recirculation Gyre and Deep Western Boundary Current as deduced from long term current meter data (from Hogg, 1983). A smaller scale anticyclonic recirculation is outlined as well.

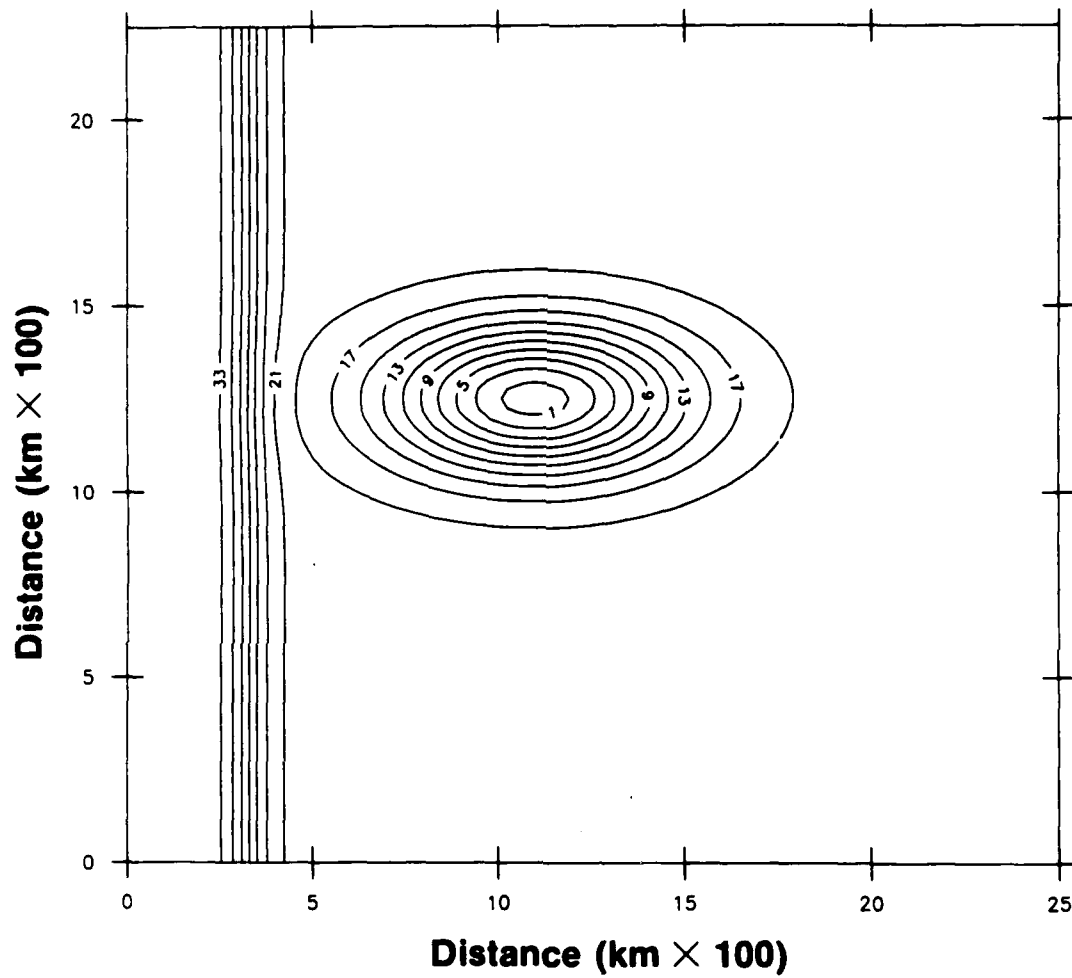


Figure 1.2: Streamlines of the numerical model. Values are in Sverdrups (assuming a depth of 1000 m).

model are discussed in Appendix A. The scheme that was used is based on that of Smolarkiewicz (1983), with the addition of a centered-differenced diffusion term, and so includes a corrective step to minimize implicit diffusion. As the simulation is allowed to progress, tracer advects downstream and spreads laterally. Some of it, having diffused into the edge of the gyre, is pulled eastward forming a plume which wraps around the gyre (Figure 1.3). Tracer slowly fills the gyre in this manner until at steady state a homogeneous pool forms within the gyre.

The focus of this chapter is an analysis of the processes involved in the subsequent entrainment, i.e. once tracer has entered the edge of the gyre. The ideas that are discussed apply then not only to the NRG but to any closed circulation of this form near an external source. The discussion first centers on the initial penetration of tracer into the gyre. This process is isolated in the context of a simpler flow field. Then the occurrence of homogenization at steady state is discussed.

### Initial Penetration

Closer inspection of Figure 1.3 shows that the plume of tracer, as it winds around the gyre, migrates across streamlines toward the gyre center. The reason for this spiral is that the portion of the plume which spreads inward enters a region of stronger velocity and advects around more quickly. Note also that the spiral is asymmetric in that where the flow is zonal the spiral is not as pronounced as in the meridional flow. The spiral characterizes the entrainment of tracer into the gyre and it is of interest to consider it in some detail. To understand why the asymmetry exists it must be understood what factors govern the spiral. To do this, a problem involving diffusion in a simple shear flow is considered.

The effect that velocity shear has on the spreading of a passive tracer has been studied considerably, in particular the process of shear dispersion whereby cross-stream shear enhances the spreading of tracer along streamlines (Rhines, 1983). Here a different aspect in which cross-stream shear influences the diffusion of tracer is addressed.

For a given distribution of tracer consider the parameter which is the ratio of the alongstream gradient to the cross-stream gradient:

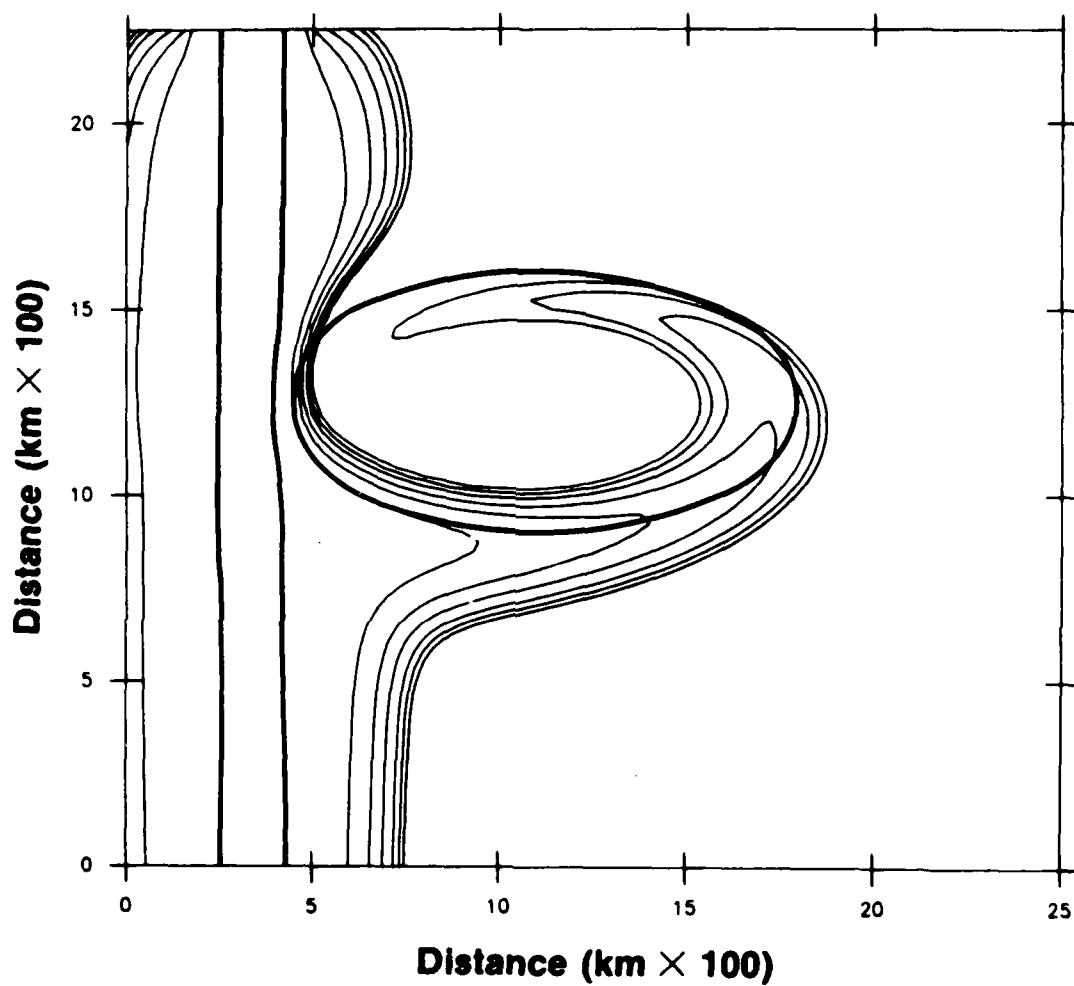


Figure 1.3: Plume of tracer spiralling into gyre (instantaneous distribution during spin-up). The dark lines are the bounding streamlines of the gyre and boundary current.

$$\frac{\theta_x}{\theta_y} \equiv \delta_L$$

The value of  $\delta_L$  is one measure of the extent to which shear dispersion occurs. For the same shear and diffusivity, a large  $\delta_L$  means prevalent shear dispersion whereas a small  $\delta_L$  means this effect is negligible. Shear dispersion acts on a distribution of tracer to reduce its  $\delta_L$  (Rhines, 1983).

Here we are interested in the effect that cross-stream shear has in the spreading of tracer across streamlines, when the distribution of tracer is characterized by a small  $\delta_L$ . The analysis applies to situations in which there is a localized source of tracer. Such a distribution in a linear shear flow is analogous to the plume of tracer penetrating the edge of the gyre.

#### A) Linear Shear Flow

The equation governing the horizontal evolution of tracer is the two-dimensional advective-diffusive equation,

$$\theta_t + u\theta_x + v\theta_y = \kappa\theta_{xx} + \kappa\theta_{yy}, \quad (1.2)$$

where  $x$  = zonal distance,  
 $y$  = meridional distance,  
 $\theta$  = concentration of tracer,  
 $u$  = zonal velocity,  
 $v$  = meridional velocity,  
 and  $\kappa$  = diffusivity.

Solutions were obtained numerically using the finite grid approximation discussed in Appendix A. In the region of inflow a Gaussian concentration of tracer is assigned, and where there is outflow tracer advects out of the domain. Where the cross boundary flow is insignificant the diffusive open boundary conditions are applied.

The set up of the problem is depicted in Figure 1.4. At  $t = 0$  a step function source is turned on, and tracer progresses downstream while spreading laterally. The center of mass of the tongue proceeds to migrate



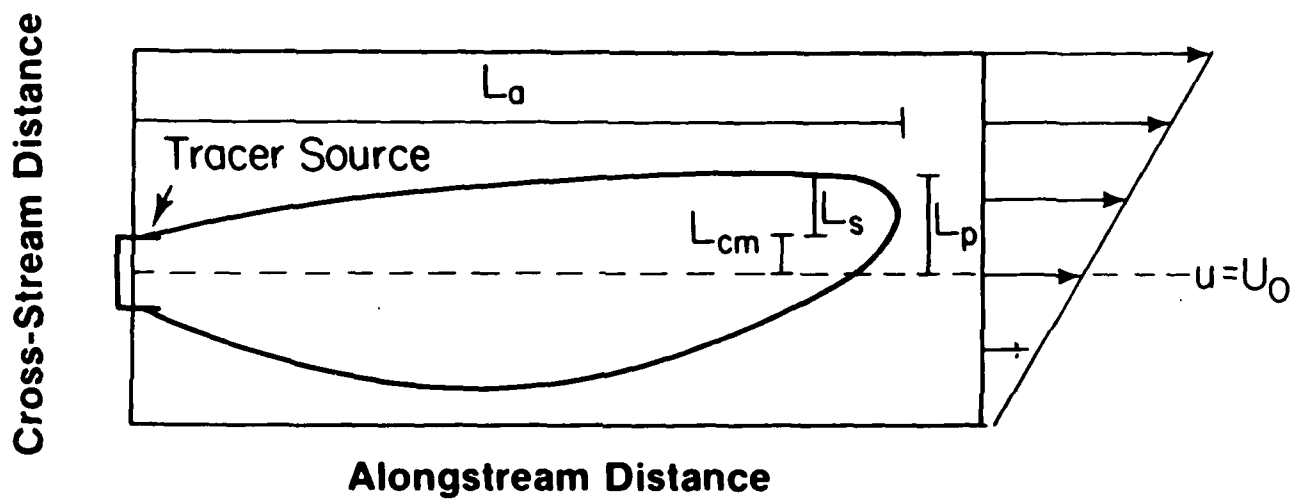


Figure 1.4: Graphic depicting a plume of tracer in a linear show flow. Length scales of the plume are as shown; tracer is introduced at  $u = U_0$ .

across streamlines as with the gyre flow. It is relevant to define four length scales for this problem:

- $L_p$  = The cross-stream penetration of tracer, defined as the maximum meridional extent of a chosen concentration of tracer.
- $L_a$  = The alongstream length of the tongue, defined as the zonal distance to where the meridional penetration is greatest.
- $L_{cm}$  = The displacement of the center of mass of the tongue across streamlines at the point where the meridional penetration is greatest. This measures migration of the tongue. (Note that migration requires cross-stream shear.)
- $L_s = L_p - L_{cm}$ . This measures spreading of the tongue.

The quantities  $L_a$  and  $L_p$  are the respective  $x$  and  $y$  length scales of the tracer distribution,  $L_{cm}$  and  $L_s$  are the first and second  $y$ -moments (Figure 1.4).

For a northward diffusing particle of tracer, consider the balance between advection and diffusion where  $u = U_0 + \alpha y$  ( $v = 0$ ),

$$(U_0 + \alpha y)\theta_x = \kappa \theta_{xx} + \kappa \theta_{yy}, \quad (1.3)$$

where  $U_0$  = (constant) reference velocity,  
and  $\alpha$  = cross-stream shear.

We estimate the order of magnitude of each term in (1.3) using the  $x$  and  $y$  length scales, and define the following non-dimensional parameters:

$$\delta \equiv \frac{L_p}{L_a} \quad \text{is the aspect ratio,}$$

$$P_a \equiv \frac{(U_0 + \alpha L_p)L_a}{\kappa} \quad \text{is the alongstream Peclet number} = \frac{\text{alongstream diffusive time scale}}{\text{advective time scale}},$$

$$P_c \equiv P_a \delta^2 \quad \text{is the cross-stream Peclet number} = \frac{\text{cross-stream diffusive time scale}}{\text{advective time scale}}.$$

In terms of these parameters (1.3) becomes

$$P_a \delta^2 \sim \delta^2 + 1. \quad (1.4)$$

(i) Large alongstream Peclet number: relationships between length scales.

Consider first the limit of small diffusivity where  $P_a \gg 1$  but  $P_c$  remains  $O(1)$ . In this limit the aspect ratio will necessarily be small,  $\delta \ll 1$ , and the dominant balance in (1.4) is

$$P_a \delta^2 \sim 1. \quad (1.5)$$

Note that the alongstream Peclet number is composed of two parts which can be thought of as two separate alongstream Peclet numbers, one for the shear part of the flow and one for the uniform part. We define the parameter  $S$  as the ratio of these two Peclet numbers, which is a measure of the shear which the tracer experiences,

$$S \equiv \frac{\alpha L_p}{U_0}.$$

Using this, (1.5) can be rewritten,

$$1 + S \sim \frac{\kappa}{L_a U_0 \delta^2}.$$

Limits:  $S \ll 1$

This condition causes the shear to be negligible, and  $L_p$  obeys the rule,

$$L_p \sim \left( \frac{\kappa L_a}{U_0} \right)^{1/2}. \quad (1.6)$$

$S \gg 1$

In this case the shear is so strong that the reference velocity is negligible. Here  $L_p$  obeys the rule,

$$L_p \sim \left(\frac{\kappa L_a}{\alpha}\right)^{1/3} \quad (1.7)$$

$$\underline{S \sim 1}$$

Both the shear and the reference velocity are important,

$$\frac{\alpha L_p}{U_0} \sim 1,$$

$$L_p \sim \frac{U_0}{\alpha}.$$

Three different examples of distributions in which  $P_a \gg 1$ ,  $P_c \sim 1$  appear in Figure 1.5. Each one represents a snapshot as the tongue evolves. In the first, corresponding to  $S \ll 1$ ,

$$S = .1, \text{ and } L_p \sim L_s \gg L_{cm}.$$

In the second, corresponding to  $S \gg 1$ ,

$$S = 2.3, \text{ and } L_p \sim L_{cm} \gg L_s.$$

In the third,

$$S = .6, \text{ and } L_p > L_{cm} \sim L_s.$$

(A complete listing of parameters appears in Table 1.1.)

As seen in Figure 1.5, as the plume in the first example progresses downstream  $L_p$  is consistent with the  $S \ll 1$  law, and in the second example it is consistent with the  $S \gg 1$  law. (In the former, where the shear is negligible, an analytic solution is obtainable which agrees with the numerical result that  $L_p$  traces out a parabola.) In the third example,  $L_p$  corresponds to neither of these laws. Initially the slope is close to  $1/2$  as the shear is not yet felt, but approaches that of  $1/3$  as penetration increases.

TABLE 1.1: Parameters associated with the different examples in the linear shear flow problem.

S	P <sub>a</sub>	$\alpha$ ( $\frac{\text{cm/sec}}{\text{km} \times 100}$ )	U <sub>0</sub> (cm/sec)	L <sub>p</sub> (km x 100)
.1	7.7	.5	5	1.4
2.3	7.6	4	2	1.2
.6	7.5	1.5	3.5	1.4
1.1	10.4	2	3	1.6
1.2	.2	.3	.5	2.0

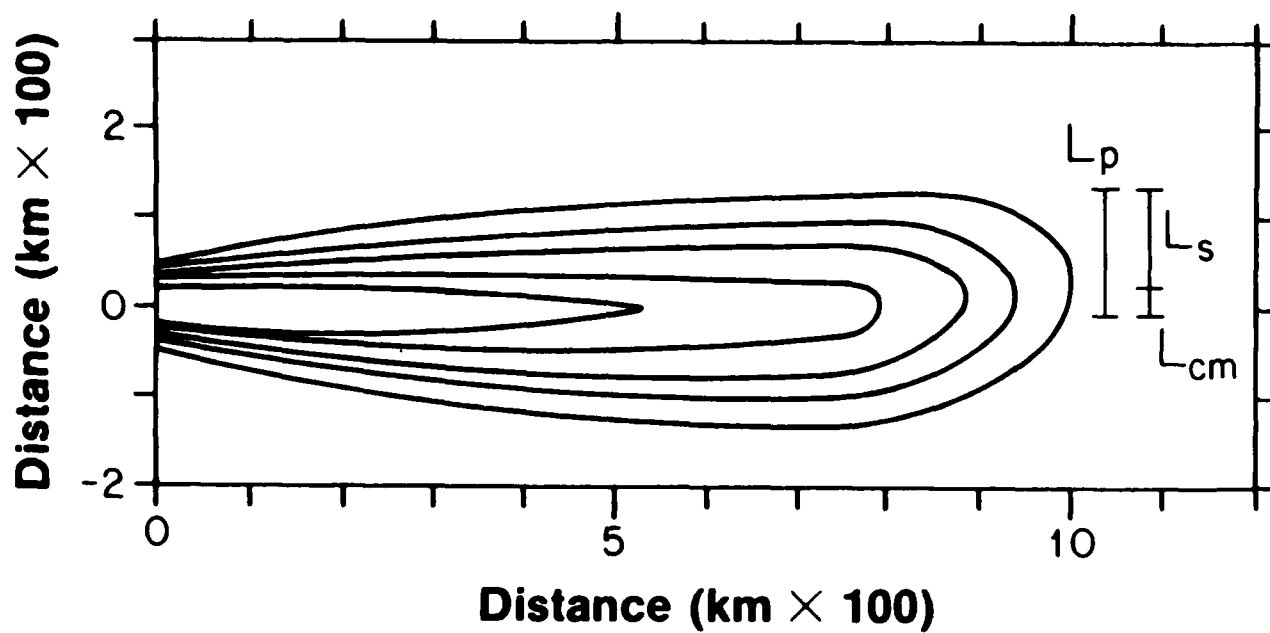
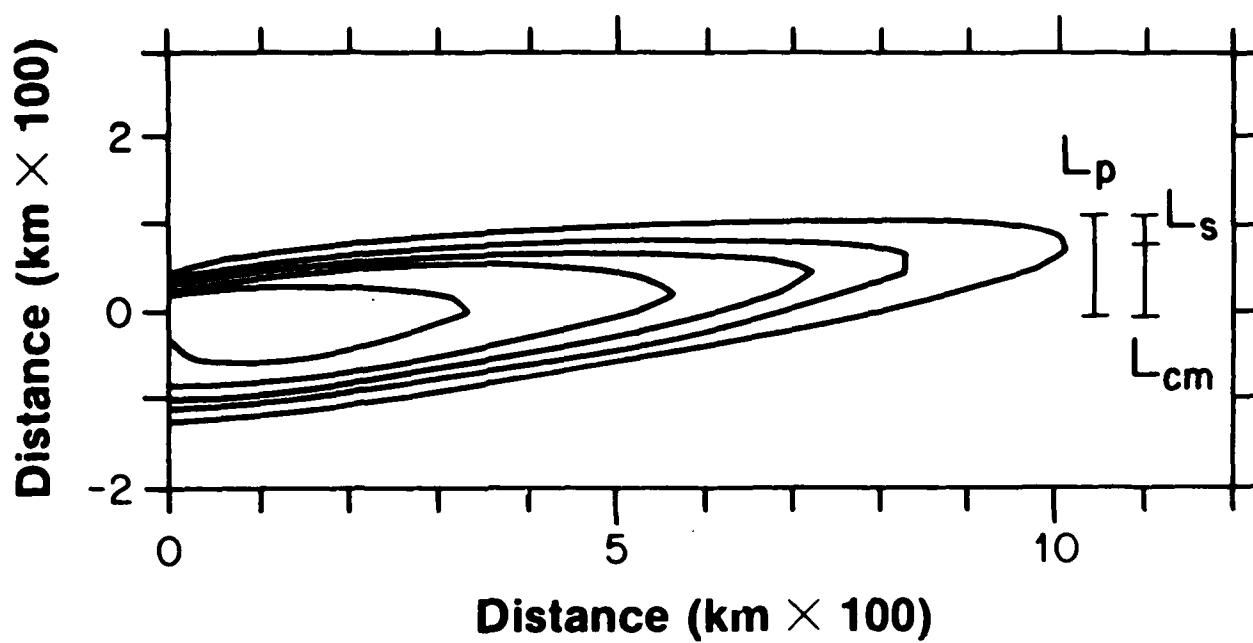
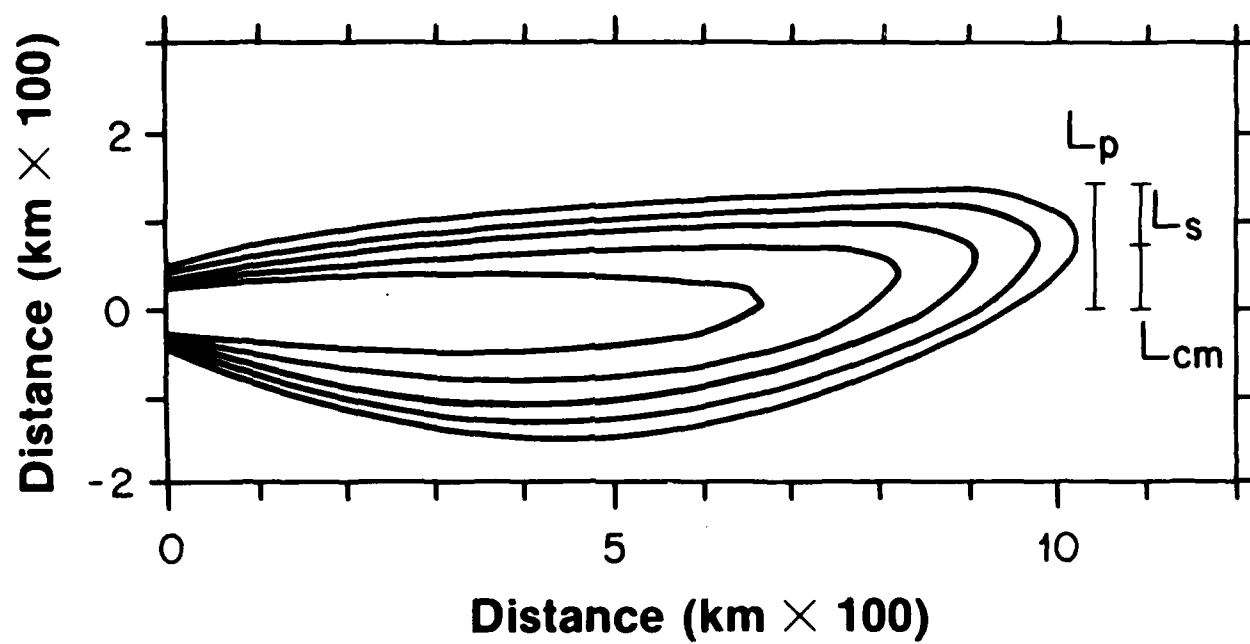


Figure 1.5: Instantaneous distribution of tracer in which  $P_a \gg 1$ ,  $P_c \sim 1$ .  
 (a)  $S = .1$ , which corresponds to spreading.



(b)  $S = 2.3$ , which corresponds to migration.



(c)  $S = .6$ , which is in between the limits of spreading and migration.



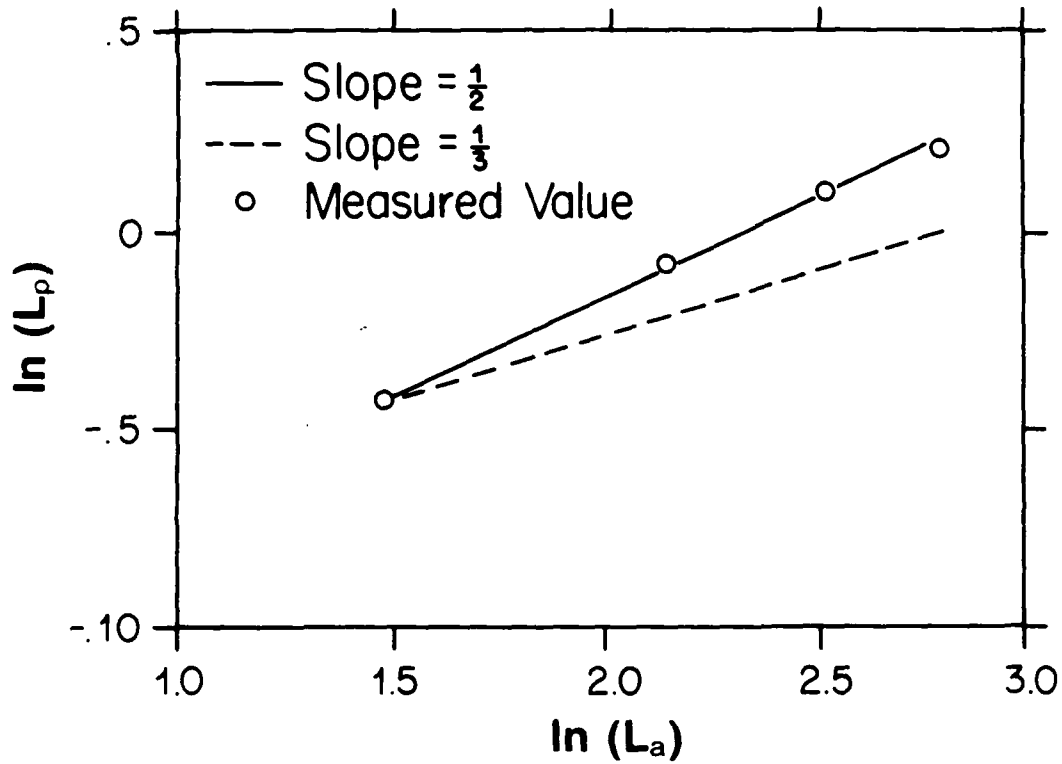
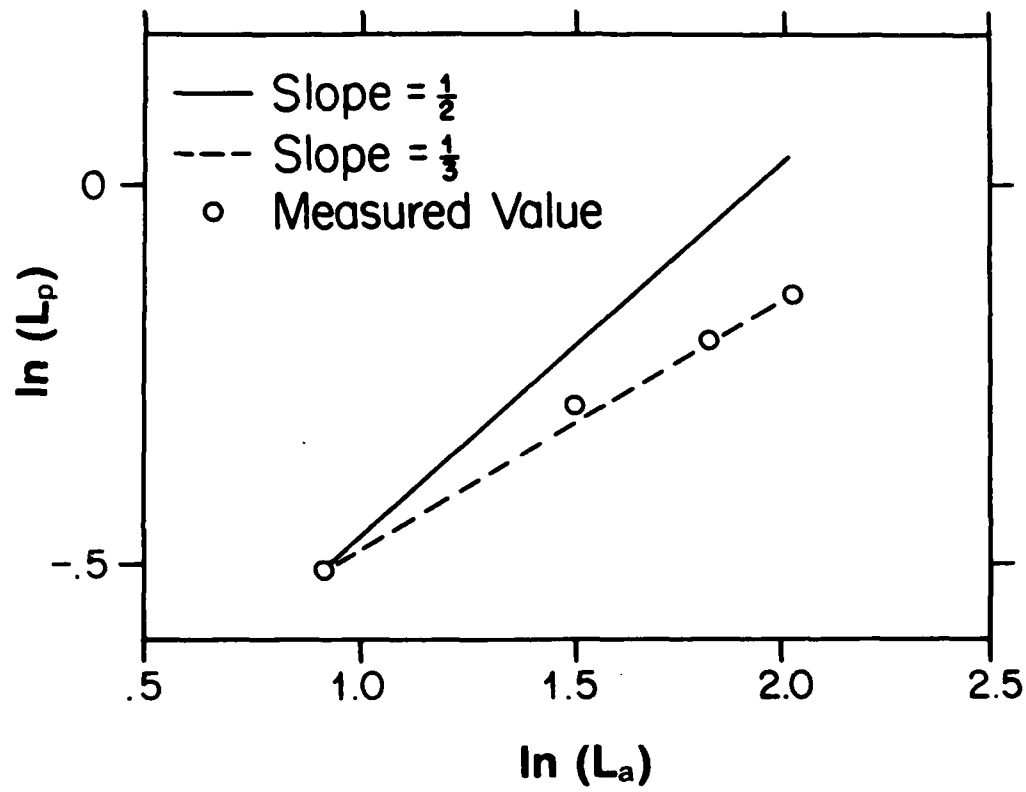
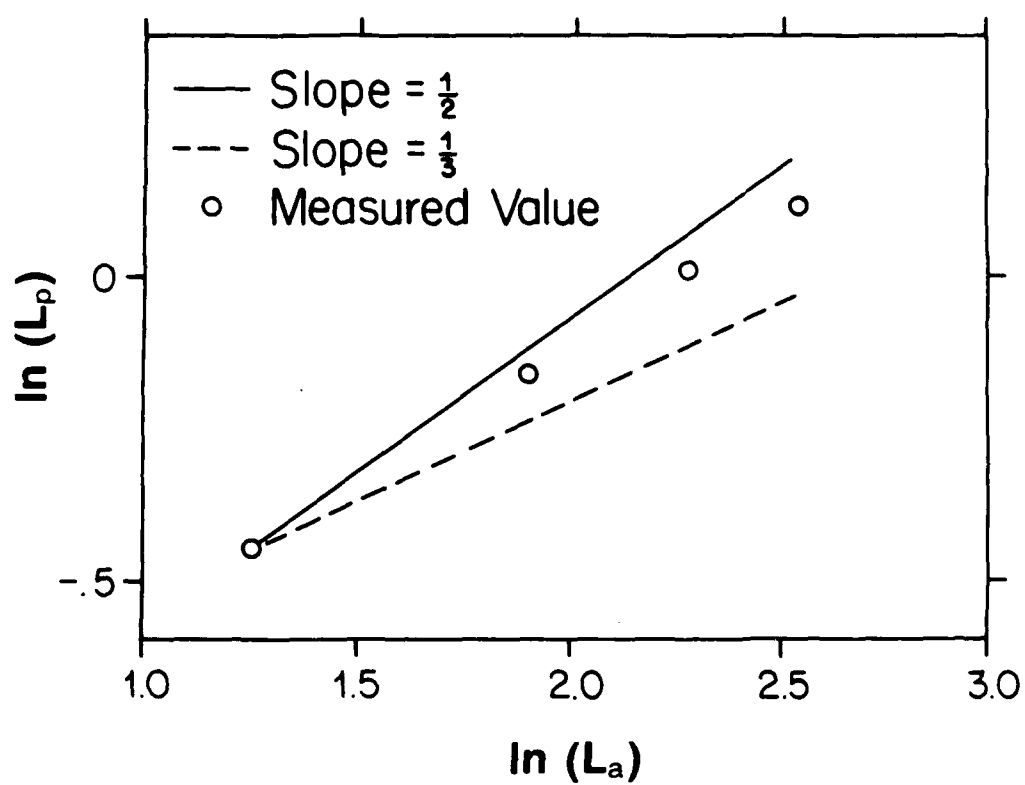


Figure 1.6: The relationship between the x and y length scales of the plumes in Figure 1.5 at four successive times. A slope equal to one-half is consistent with (1.6); a slope equal to one-third is consistent with (1.7).

(a) For the plume of Figure 1.5a.



(b) For the plume of Figure 1.5b.



(c) For the plume of Figure 1.5c.

When the shear is negligible, spreading of the tongue accounts for most of the penetration of tracer across streamlines. On the other hand, in a strongly sheared flow the penetration is mostly due to migration of the tongue. In the third example, which is between these extremes, spreading and migration are both substantial, but with increasing penetration the situation approaches that of the shear extreme, and correspondingly  $L_{cm}$  becomes more closely correlated with  $L_p$ . Note that this example does not correspond exactly to the  $S \sim 1$  case discussed above. This means that when  $u$  and  $\Delta u$  are of equal magnitude, spreading and migration do not contribute equally to the penetration but rather migration is somewhat more prevalent.

These results can also be obtained analytically through an analysis of a slightly different problem, that of a point discharge of dye in a linear shear flow. Smith (1982) solved this case, and while the discharge is not a continuous source but rather an initial spot that evolves, the same information regarding penetration can be derived. In terms of the present notation the flow field considered by Smith is

$$u = U_0(t) + \alpha(t)y ,$$

and the level of discharge is  $y = 0$ . In our case both the reference velocity and cross-stream shear are constants,  $U_0(t) = U_0$  and  $\alpha(t) = \alpha$ .

The solution is a Gaussian in the cross-stream direction of the form

$$\theta(x,y,t) = c(x,t) \exp \left\{ \frac{-(y-y_0(x,t))^2}{v(t)} \right\}$$

where  $v(t)$  = variance,

$y_0(x,t)$  = position of the origin,

and  $c(x,t)$  = amplitude.

In each section across-stream the Gaussian is centered progressively further to the north looking downstream, with a different amplitude. The variance is independent of alongstream direction but varies in time. A snapshot of a spot of tracer progressing downstream appears in Figure 1.7.

The analogy to the continuous source case is that the leading edge of the dye spot evolves the same as the leading edge of the plume discussed

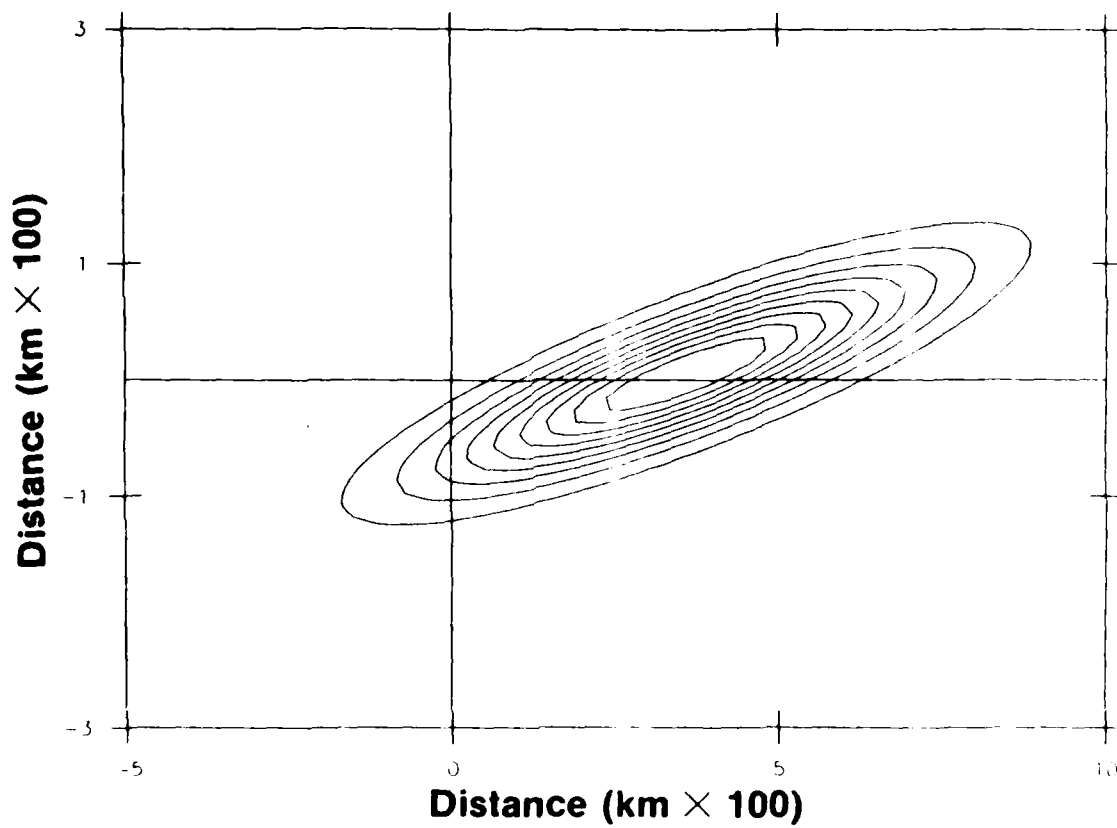


Figure 1.7: Instantaneous distribution of tracer in the linear shear flow of Figure 1.5b. Initially the distribution was a delta function at the origin.

previously. The penetration here is defined exactly as before: the maximum cross-stream extent of a given concentration isoline. Note that for the example shown this does not occur at the extreme downstream edge of the dye spot, but rather just upstream of this (Figure 1.8). As before we define the alongstream position that corresponds to the maximum cross-stream penetration as  $x = L_a$ . In the limit of small shear  $L_a$  corresponds to the center of the dye spot, whereas in the opposite limit  $L_a$  corresponds to its downstream edge.

The penetration is equal to the sum of the distance to the origin of the Gaussian and the square root of its variance,  $L_p = y_0 + \sqrt{v}$  ( $y_0$  and  $\sqrt{v}$  are analogous to  $L_{cm}$  and  $L_s$  respectively, Figure 1.8). The shear parameter  $S$  is defined as before,  $S = \frac{aL_p}{U_0}$ . In Figure 1.9 the relationship between  $L_p$  and  $L_a$  is plotted as time progresses for a strongly sheared flow. Also shown is  $S$  versus  $L_a$ . Consistent with what was found earlier, when the penetration is so small that the shear is negligible with respect to the reference velocity ( $S \ll 1$ )  $L_p$  obeys a square root law. At longer times when the dye spot has diffused far enough across stream that the opposite is true ( $S \gg 1$ ),  $L_p$  obeys a cube root law. It is evident that in the weak shear limit  $L_p \sim \sqrt{v}$ , whereas in the strong shear limit  $L_p \sim y_0$ .

(ii) Small alongstream Peclet number: enhancement of spreading.

In the first set of examples it is seen that for  $S \gg 1$  migration of the plume (i.e. movement of its center of mass) is more prevalent than spreading, and for  $S \ll 1$  the opposite is true. In each of these cases  $P_a \gg 1$ . With a smaller  $P_a$  the system becomes less sensitive to the velocity and, more importantly, changes in the velocity. Thus we might expect that a reduced  $P_a$  will diminish the importance of migration versus spreading in contributing to the penetration, as is the case with a reduced  $S$ . The distinction between  $S \ll 1$  versus  $P_a \ll 1$  should remain clear however: in the first instance the cross-stream change in velocity is not important because it is small, in the second instance it is not important because the system does not recognize it.

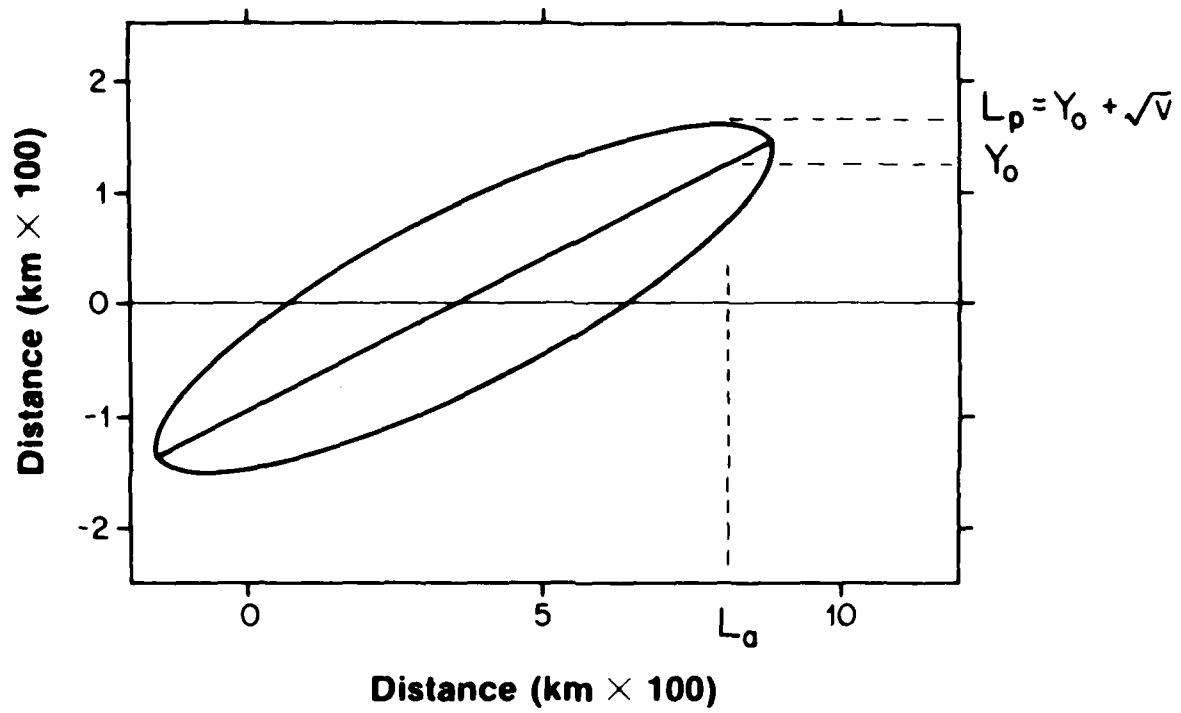


Figure 1.8: The scales associated with the distribution of tracer in the point discharge problem.

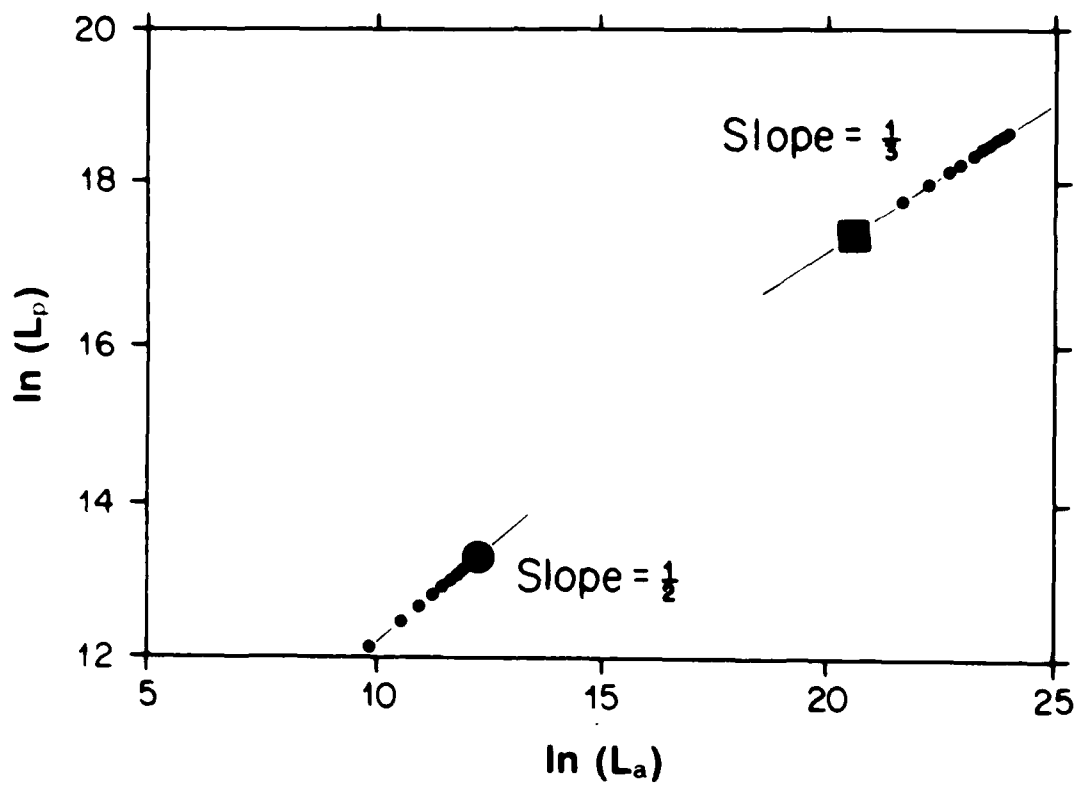
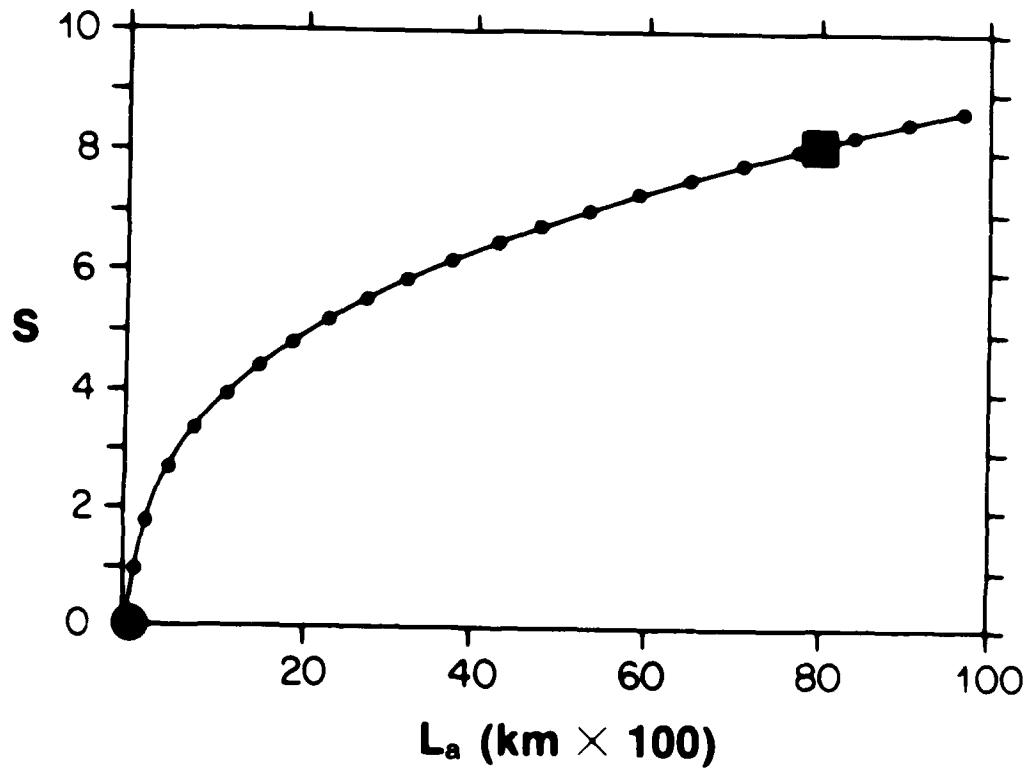


Figure 1.9: (a) The relationship between  $L_a$  and  $L_p$  for the distribution in the point discharge problem. The early stage of evolution is characterized by a slope of one-half and later stages by a slope of one-third.





(b) The value of the shear parameter as the distribution progresses downstream. The enlarged circle and square represent the same stage of evolution in both (a) and (b).

A second set of examples appears in Figure 1.10. In 1.10a  $P_a \sim 10$  whereas in 1.10b  $P_a \sim .1$  ( $S$  is comparable in each, see Table 1.1). Indeed with a large alongstream Peclet number  $L_{cm} > L_s$ , and with a small alongstream Peclet number  $L_s > L_{cm}$ . Note in 1.10b that  $L_p \sim L_a$ , so that for this example the balance of terms in (1.5) is no longer applicable, i.e. the aspect ratio is now  $O(1)$  and the alongstream diffusive flux term must be retained. Here both the alongstream and cross-stream Peclet numbers are small, whereas previously  $P_a \gg 1$  and  $P_c \sim 1$ . The dominant balance in (1.4) for this example is thus

$$-S^2 \sim 1.$$

(iii) Discussion

It is seen that variation in the alongstream Peclet number  $P_a$  alters the importance of the alongstream diffusive term versus the advective term in balancing the cross-stream diffusion. Variation in the shear parameter  $S$  on the other hand, serves to enhance or diminish advection by a constant velocity field versus a sheared velocity field. This means that two criteria must be satisfied in order to obtain migration of the plume. First,  $P_a$  must be large enough so that the system is sensitive to the velocity field. This condition is necessary but not sufficient. In addition,  $S$  must be large enough so that the cross-stream shear is significant.

The parameter  $S$  depends on the meridional length scale  $L_p$  which is only known after the tongue has evolved. As with all problems in scaling, a discussion of relevant balances requires some knowledge of the solution. It would be desirable however if, given the values of  $\alpha$ ,  $U_0$  and  $\kappa$ , we could say whether or not the tongue will migrate (provided the diffusivity is small enough that the advective flux is important). What we can do is cast the answer in terms of  $L_a$ .

The idea is to substitute for  $L_p$  in the expression for  $S$ . When  $S \ll 1$  we use (1.6) with the definition of  $S$  to obtain

$$S \sim 2\alpha \left( \frac{\kappa L_a}{U_0} \right)^{1/2}. \quad (1.8)$$

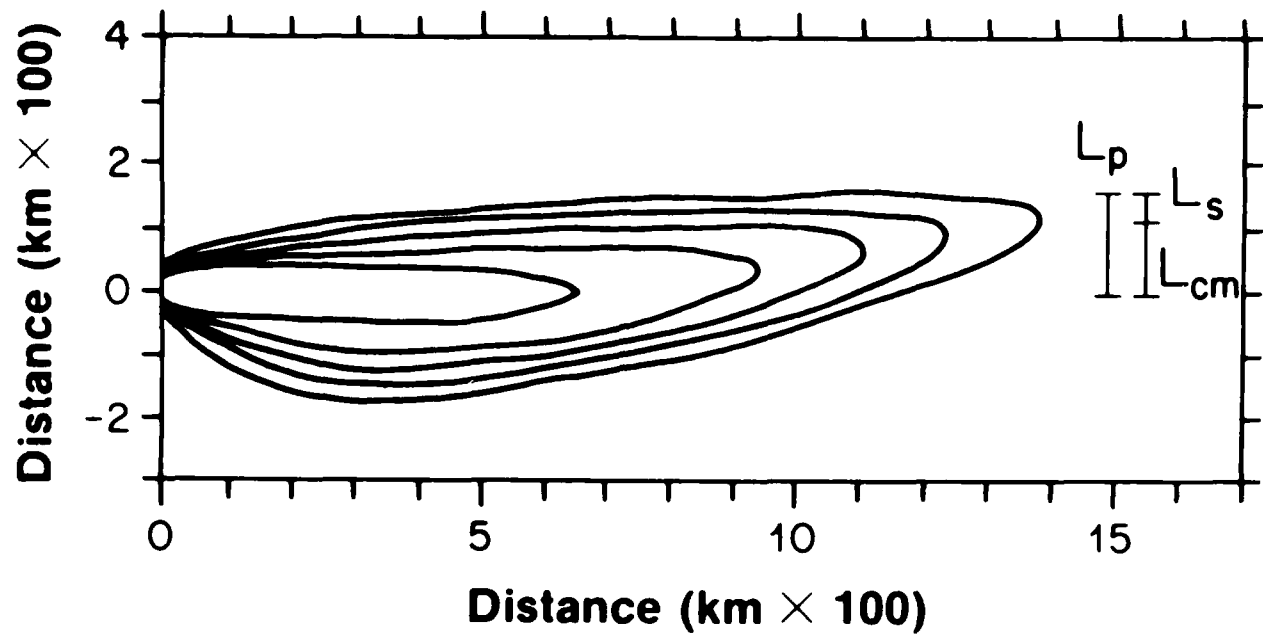
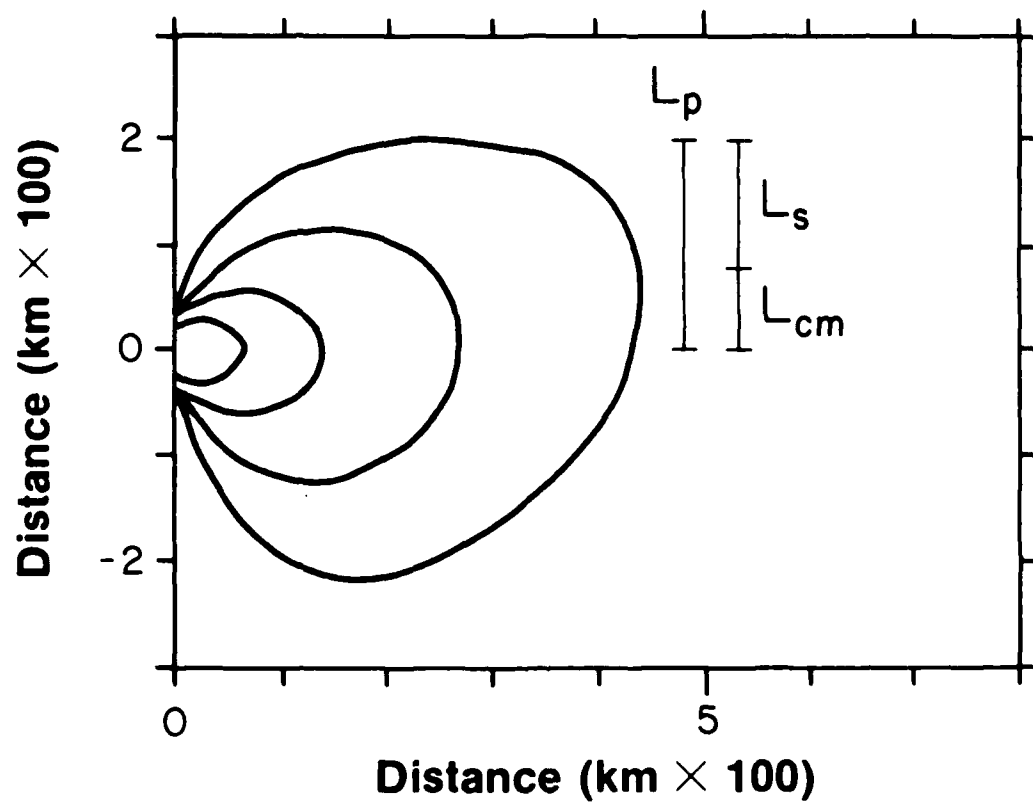


Figure 1.10: (a) Instantaneous distribution of tracer in which  $P_a \gg 1$ ,  $P_c \sim 1$ . The value of  $S$  is such that migration is more prevalent than spreading.



(b)  $P_a \ll 1$ ,  $P_c \ll 1$ . Spreading is more prevalent than migration for a similar value of  $S$ .

Provided  $U_0$  is not identically zero (it can be arbitrarily small) we have seen that for every problem the shear is at first negligible, but eventually dominant. We thus set  $S = 1$  in (1.8) and determine the value of  $L_a$ ,  $L_a = L_{aT}$ , when the transition occurs, i.e. when (1.8) breaks down. For those cases in which the tongue migrates, the transition occurs "instantly" (in the example of Figure 1.5b  $L_{aT} \sim 10^2$  km) and for those in which the tongue spreads, the transition "never" occurs (in the example of Figure 1.5a  $L_{aT} \sim 10^5$  km).

Besides discussing trends in  $L_p$  and its relationship with  $L_{cm}$  and  $L_s$ , it is important to say a few words about the extent of the penetration. As an alternative to  $L_p$  as a measure of cross-stream penetration, consider the integral of tracer in the region  $y \geq 0$ ,  $x \leq L_x$ , i.e. the total amount of tracer that has penetrated northward. Here lies a further distinction between the  $S \gg 1$  case and  $S \ll 1$  case. For two plumes -- one in a strongly sheared flow and one in a uniform flow -- in which  $L_a$  and  $L_p$  are the same, there is significantly less tracer north of  $y = 0$  in the shear flow. This is because the effect of northward shear on a distribution of tracer is to increase its northward gradient, and (Figure 1.11) this causes a southward flux of tracer across part of the  $y = 0$  line. So whereas tracer has penetrated just as far across stream in the shear flow, there is less of it.

Although the  $P_a \ll 1$  case resembles that for  $P_a \gg 1$ ,  $S \ll 1$  in that spreading of the plume dominates migration, these instances represent opposite extremes in penetration. For a given flow field ( $U_0$  and  $\alpha$ ) and a given  $L_a$ , the value of  $L_p$  depends on the value of  $\kappa$ . A sufficiently small  $\kappa$  means that  $L_p$  is not large enough for the plume to notice the shear -- large  $P_a$  spreading occurs. With increased  $\kappa$  (and  $L_p$ ) the large  $S$  regime is approached and migration becomes important. Small  $P_a$  spreading, on the other hand, occurs with large enough  $\kappa$ , and this represents the upper extreme of penetration.

#### B) Application to Gyre Flow

We return now to the gyre problem. The process in which the plume of tracer gets caught in the edge of the gyre and diffuses into a region of

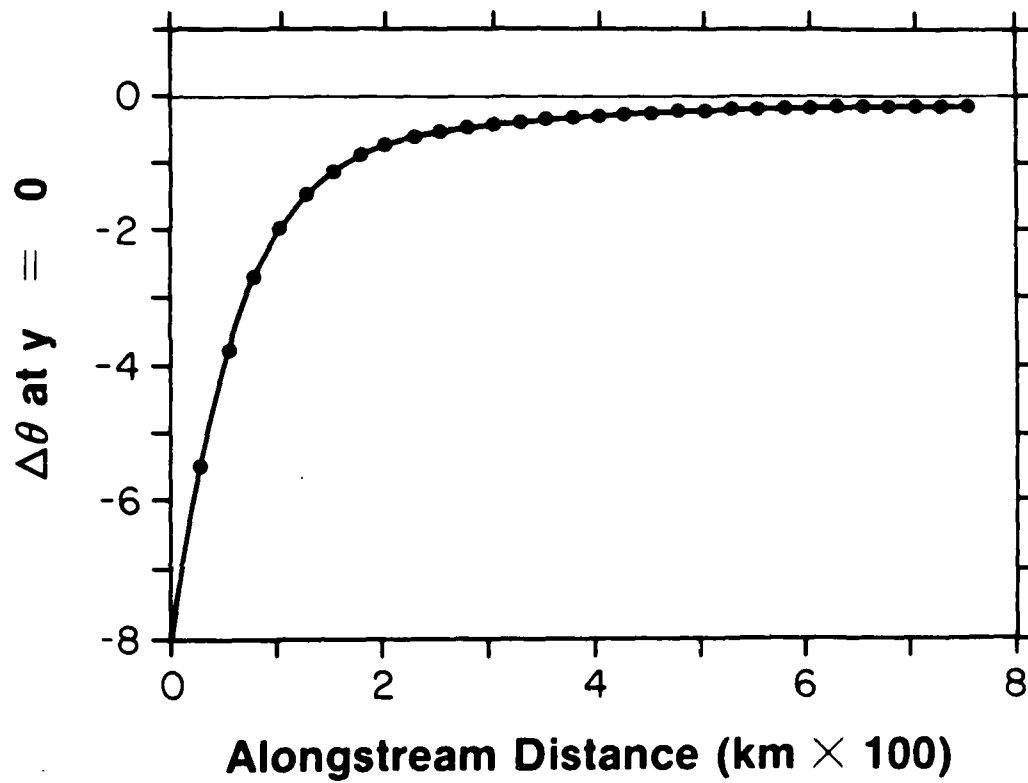
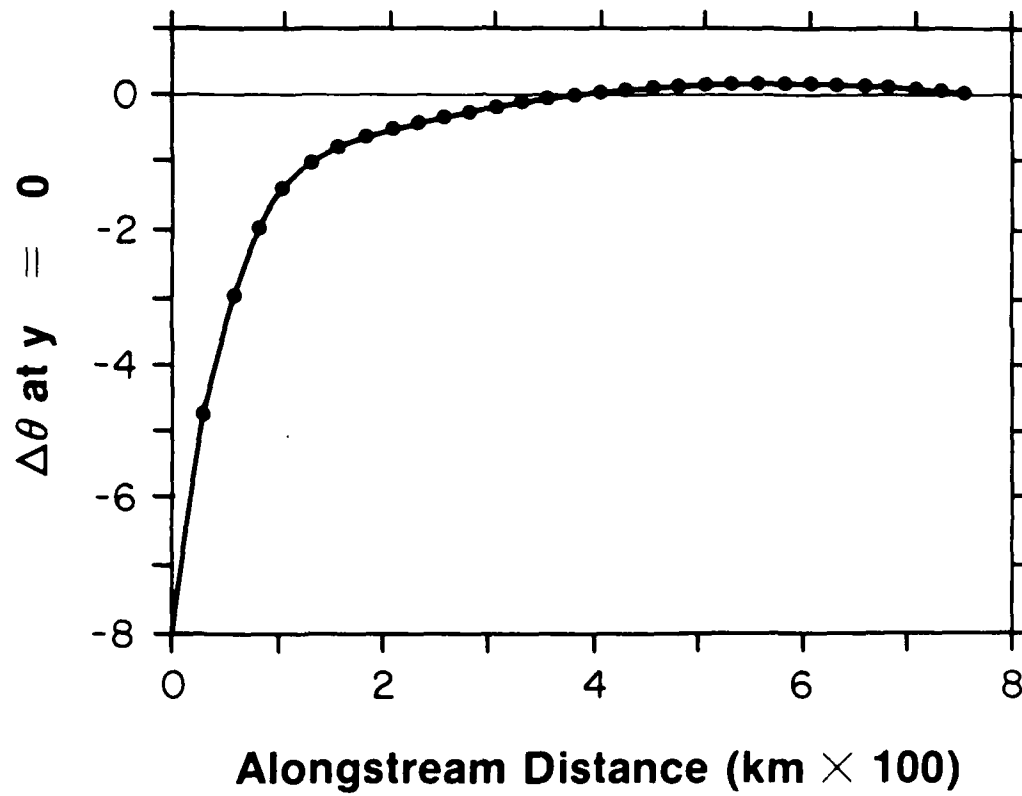


Figure 1.11: Value of  $\Delta\theta$  along the line  $y = 0$ .  
(a) Uniform flow. The meridional flux of tracer is everywhere northward.



(b) Strongly sheared flow. Downstream of  $x \sim 3.7$  tracer is being fluxed southward.

stronger flow resembles the shear flow example analyzed above, and some of the ideas that were developed are now applied to this problem. Keep in mind however that there are differences between the two examples. For instance here the cross-stream shear  $\alpha$  varies both alongstream and across stream, there is alongstream shear as well, the flow is curved rather than rectilinear, and the input of tracer into the gyre is not a step function in time.

Figure 1.12 shows a time history of tracer entering the gyre. The advancement of the plume in each one year segment can be thought of as different example of the shear flow problem examined above, with the following definitions:

- $L_a$  = the distance that the leading edge of the plume travels alongstream in a year.
- $L_{cm}$  = movement of the center of mass of the leading edge of the plume across-stream in a year.
- $\alpha$  = cross-stream shear at the midpoint of  $L_a$  (the alongstream shear is negligible).
- $U_0$  = velocity at  $L_a = 0$ ,  $L_{cm} = 0$ .

These quantities are analogous to those similarly named in the previous shear flow problem. The source at the northern edge of the DWBC is applied as a step function at  $t = 0$ , but by the time tracer reaches the gyre it is no longer characterized by a front, i.e. the "source" for each of the above examples grows in amplitude and width. This means we are unable to define the analog to  $L_p$ , which in turn means we are unable to measure directly the values of  $P_a$  and  $S$ . We can however estimate the size of  $P_a$  by noting that  $\delta$ , the aspect ratio, is much less than one for each single year segment, and this necessarily implies that  $P_a \gg 1$ . So the first condition for migration is satisfied everywhere around the gyre.

Because a spiral does occur it is natural to assume that the second condition for migration,  $S \gg 1$ , is satisfied as well. Recall that in the migration limit  $L_p \sim L_{cm}$ . Since we can measure  $L_{cm}$  we are able then to check this assertion. For each single year segment we can substitute the values of  $\alpha$ ,  $L_a$ , and  $\kappa$  into (1.7), where  $L_p$  is replaced by  $L_{cm}$  (the



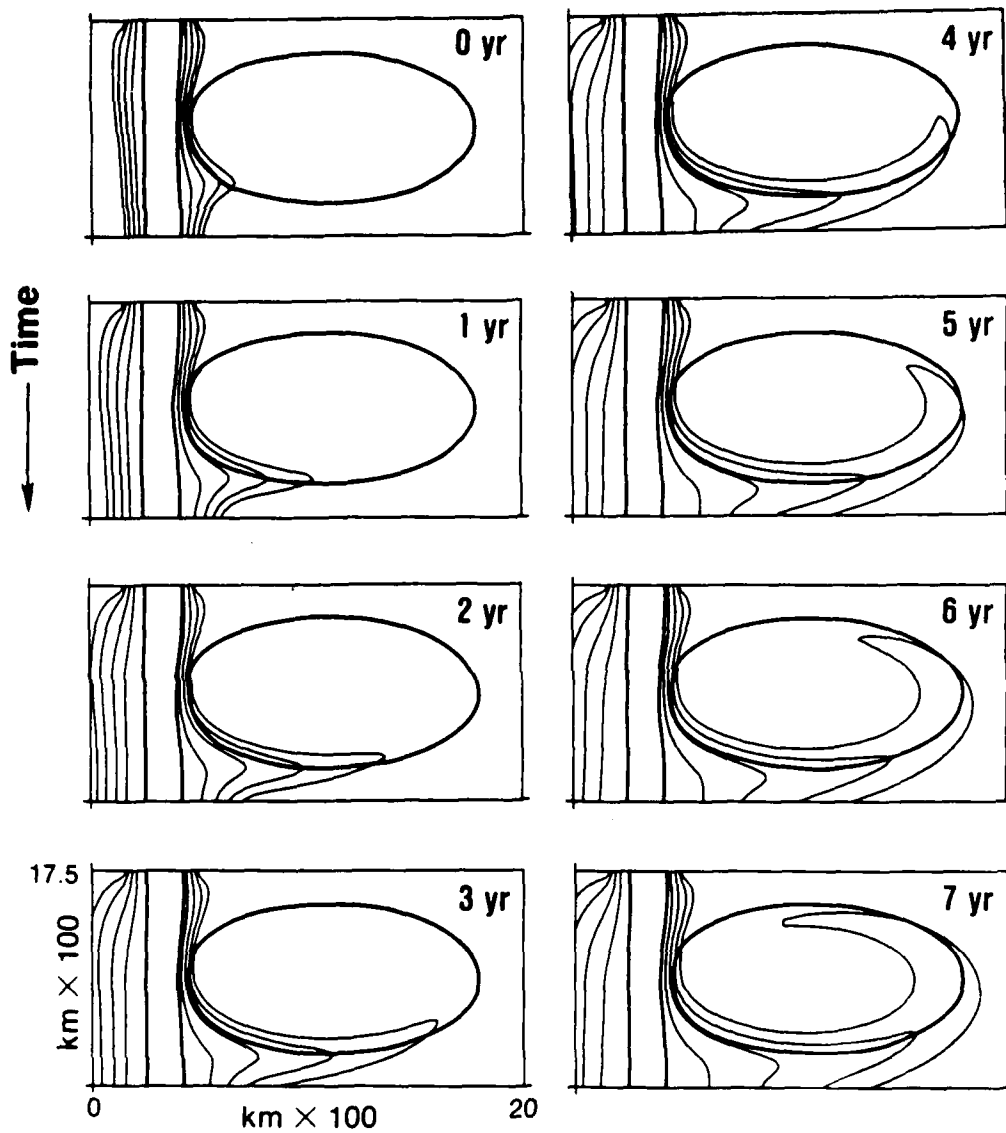


Figure 1.12: Time sequence of tracer diffusing from the boundary current and becoming entrained into the gyre. The dark lines are the bounding streamlines of the two components of flow.

proportionality constant for (1.7) was determined numerically). This predicted value of  $L_{cm}$  can in turn be compared to the measured value. The results of this comparison are displayed in Figure 1.13. It is seen that there is good agreement between the predicted and measured values where the flow is meridional. However, while the predicted curve does display less penetration in the zonal flow, the degree to which it is less is not nearly as pronounced as that which actually occurs, suggesting that something else is happening while the plume travels zonally.

Figure 1.14 graphs the values of  $U_0$  and  $\alpha$  that the plume experiences as it travels around the gyre. Also shown is the extent of the corresponding spiral. The fact that both  $\alpha$  and  $U_0$  are larger in the zonal flow, together with the small extent of migration there suggests that this corresponds to the advective limit. In particular, in these regions not only is  $P_a \gg 1$ , but  $P_c \gg 1$  as well so that isolines of tracer nearly coincide with streamlines. It is more accurate then to think of the plume as mirroring streamlines when it travels in the stronger zonal flow, while spiraling across streamlines in the manner of the shear flow example when it travels in the weaker meridional flow.

### C) Discussion

The preceding analysis focussed on the entrainment of tracer into a gyre which initially was tracer-free. This process is characterized by a plume of tracer spiralling asymmetrically inward across streamlines as a result of the cross-stream shear. In particular, in the zonal flow the spiral is minimal as the strong flow causes the plume to follow streamlines. In the meridional flow the spiral is of considerable extent conforming to the ideas developed in a simpler shear flow analysis.

Previous work has been done on the mixing of tracer within a subtropical gyre. Musgrave (1985) analyzed steady state solutions in which the northern boundary is maintained at a uniform positive concentration while the southern boundary is kept uniformly negative. He discusses the presence of a spiral that extends from the boundary to the stagnation point of the flow in the center of the gyre. The spiral arises because of the choice of boundary conditions (the cross-stream shear of the gyre is of the wrong sense to cause

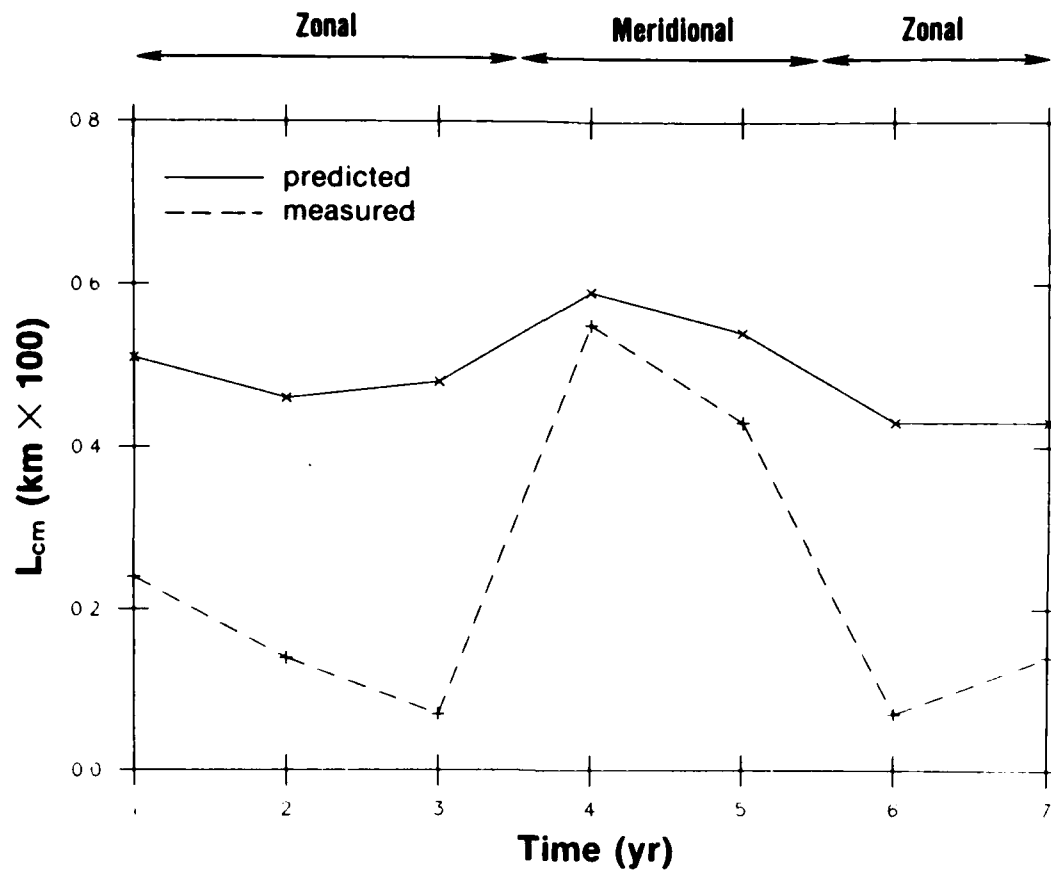


Figure 1.13: Comparison of  $L_{cm}$  as measured from successive distributions of Figure 1.12 versus the value predicted using (1.7). The plume's direction of travel is indicated above.

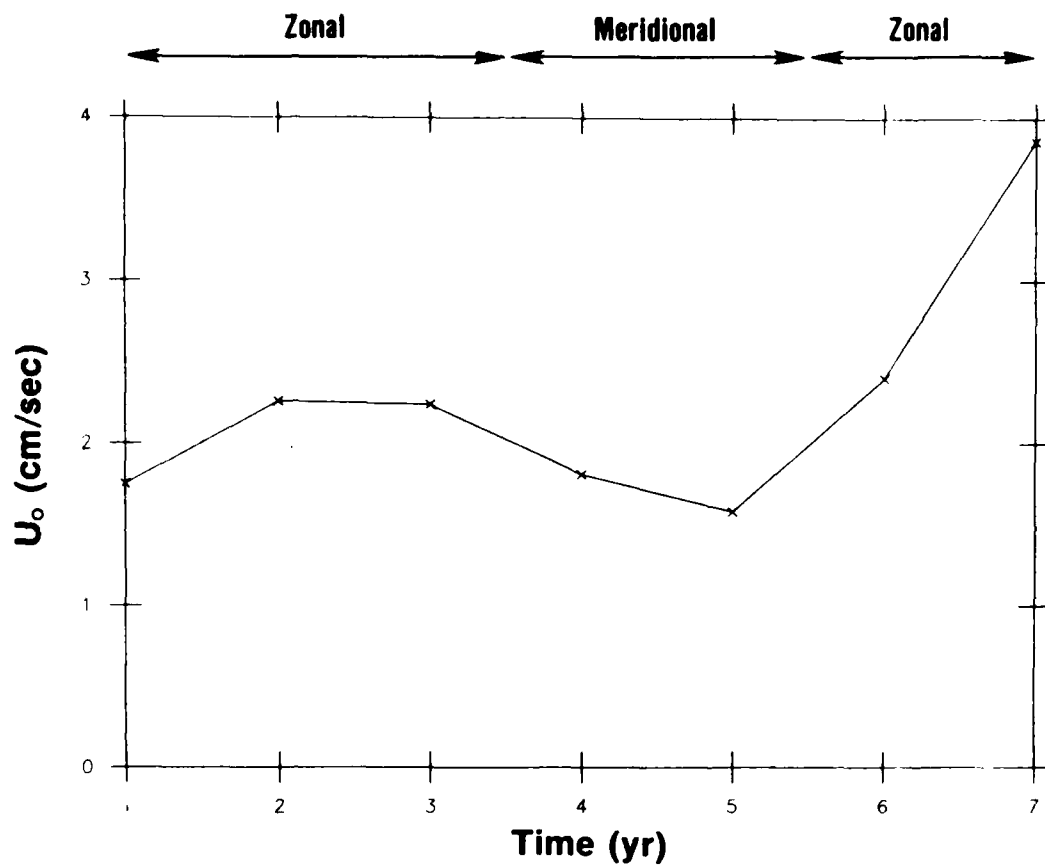
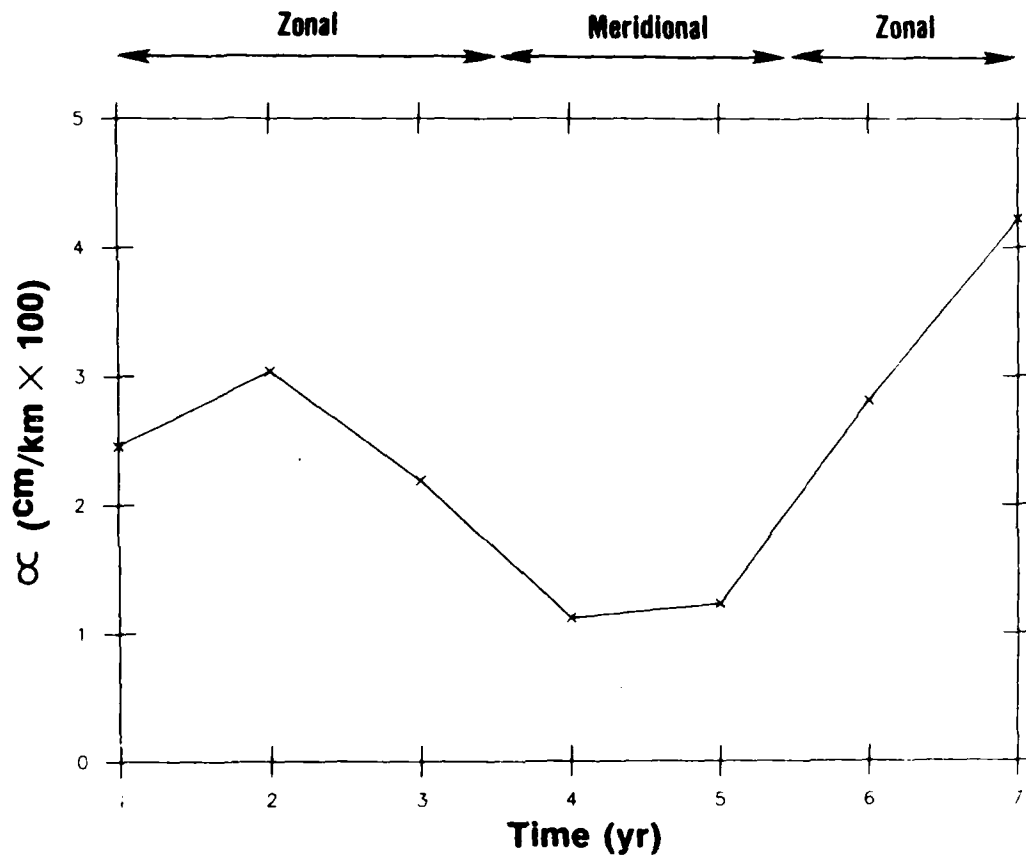
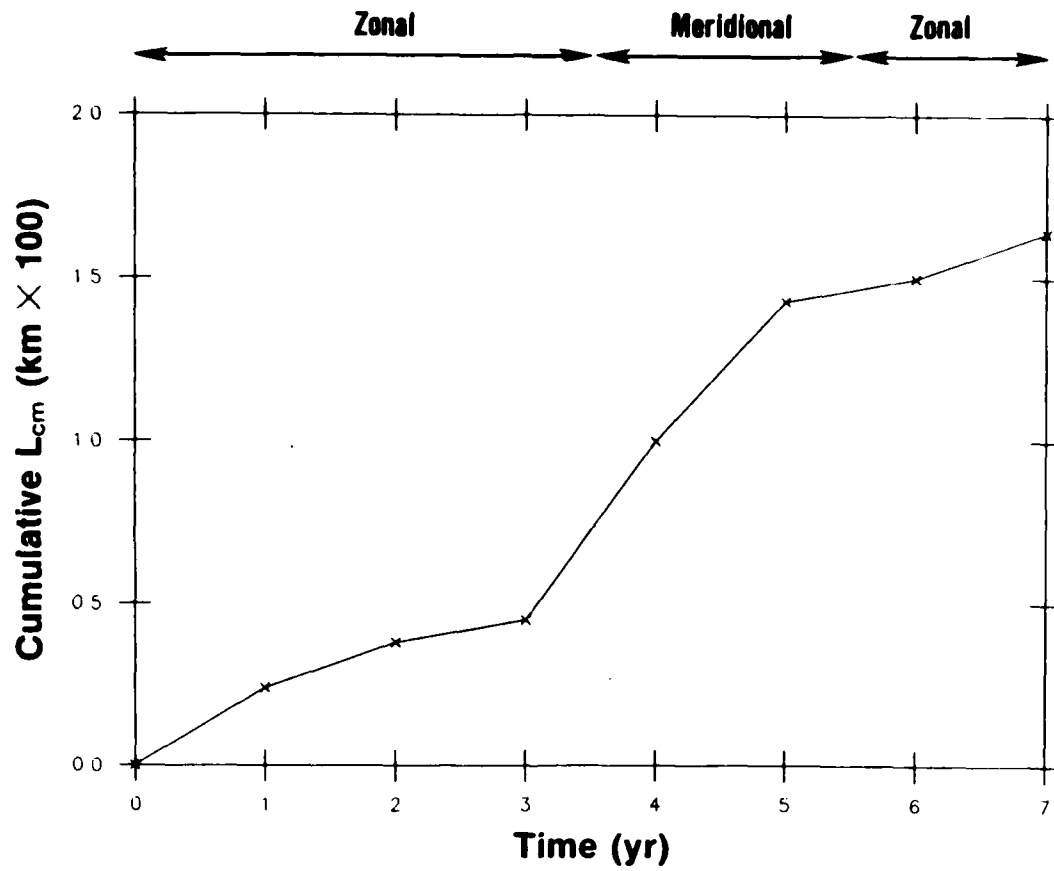


Figure 1.14: (a) The value of the reference velocity for the distributions of Figure 1.12.



(b) The value of the cross-stream shear.



(c) The cumulative migration of the plume.

the type of spiral discussed here, i.e.  $\alpha$  is everywhere  $< 0$ ). As tracer enters from the northern boundary it travels anticyclonically and spreads into the interior. Upon encountering the negative plume that extends from the south, the region of positive concentration shifts away from the boundary, hence the spiral.

For the type of gyre considered here the inward extent of the spiral depends on the flow parameters and diffusivity. Far enough into the gyre the velocity reaches a maximum before decreasing to zero at the gyre center. The maximum distance over which the spiral can extend is to the region where the cross-stream shear vanishes. As steady state is approached the tracer within the gyre becomes homogenized. This process is discussed in the next section.

### Homogenization

A feature of closed circulation is the tendency for properties to become homogenized in steady state in the interior of the flow. The homogenization of potential vorticity has been studied by Rhines and Young (1982a) and is an ingredient in their theory of wind-driven ocean circulation (Rhines and Young, 1982b). The occurrence of such homogenization is a regular feature of numerical flow simulations (e.g. Holland and Rhines, 1980), and evidence for this is found in data from the North Atlantic (McDowell et al., 1982). In the context of passive tracers, Musgrave (1985) conducted a numerical study of homogenization in a subtropical gyre. The situation he considered however is quite different than that presently being addressed. Rhines and Young (1983) examined the time history of the process by which gradients are expelled from a closed circulation, results of which are applicable here. In the ocean, Niiler (1982) discussed the homogeneity of the salinity field in a portion of the subtropical North Atlantic. The tracer data presented by Hogg et al. (1986) for the region of the northern recirculation gyre also exhibits homogenization, a result which this study addresses.

It is useful to consider homogenization in the context of a passive tracer, as results may provide insight into the more complicated case of a dynamically active quantity such as potential vorticity. Here the occurrence of homogenization is related to the penetration process that was analyzed

above. Before proceeding with the present problem though we first review the argument for homogenization following the presentation in Rhines and Young (1982a).

#### A) Review of Homogenization

Consider the steady state balance of advection and diffusion in a gyre, governed by the steady form of (1.1),

$$\vec{u} \cdot \vec{\nabla} \theta = \vec{\nabla} \cdot \kappa \vec{\nabla} \theta .$$

Integrating over the area bounded by a streamline and applying the divergence theorem,

$$\int_S \vec{u} \cdot \vec{n} \, ds = \int_S \kappa \vec{\nabla} \theta \cdot \vec{n} \, ds , \quad (1.9)$$

where  $S$  is the boundary streamline and  $\vec{n}$  is the unit normal to the streamline. Note that the lefthand side of (1.9) is identically equal to zero because  $\vec{u}$  and  $\vec{n}$  are perpendicular.

In the limit of strong advection the isolines of tracer nearly coincide with streamlines, i.e.  $\theta = \theta(\psi)$ . This gives

$$\vec{\nabla} \theta = \theta(\psi)_{\psi} \vec{\nabla} \psi ,$$

and since the integral is around a streamline,

$$\theta(\psi)_{\psi} \int_S \kappa \vec{\nabla} \psi \cdot \vec{n} \, ds = 0 .$$

The quantity inside the integral is positive definite, which further implies that

$$\theta(\psi)_{\psi} = 0 , \quad \text{i.e. } \theta = \text{constant} ,$$

Homogenization is thus obtained in a strongly advective system.



### B) Spatially Decaying Gyre

The flow field that Musgrave (1985) considered in his numerical study of homogenization consisted of a Stommel-type gyre in which the strongest flow occurs at the edge of the gyre. He defined a Peclet number,  $P = UL/\kappa$ , using the length scale of the basin and the characteristic velocity of the gyre, and discussed the extent of the homogeneous pool versus  $P$  as well as the meridional flux of tracer versus  $P$ . In terms of (1.1) the Peclet number determines to what extent advection balances diffusion, and  $L$  should be defined in terms of the tracer distribution. It is unclear how to discuss results in terms of a Peclet number so defined, especially in regards to homogenization when locally the length scale becomes infinite. What we do here is define  $P$  in terms of the plume of tracer which penetrates the gyre, as was done in the previous section.

The gyre presently being considered has its maximum velocity relatively close to the center, decaying from this point to the edge. (A velocity section through the gyre is shown in Figure 1.15.) For simplicity, for the time being we consider a symmetric (i.e. circular) gyre. Think of the gyre as being divided into two regions: the outskirts of the gyre where the flow is weak, and the inner part where the flow is more intense (close to the gyre center the flow once again becomes weak.)

As the plume of tracer enters the outer, weaker part of the flow it spirals across streamlines (provided the shear is strong enough) in the manner discussed in the previous section. This region is characterized by  $P_a \gg 1$ ,  $P_c \sim 1$ . Eventually the plume reaches strong enough flow (we clarify below what is meant by strong enough) that it is nearly pulled right around a streamline. At this point the spiral has "collapsed" to a streamline, and here  $P_a \gg 1$ ,  $P_c \gg 1$ . Recall that these latter conditions imply that we are in the advective limit, which is the necessary condition for homogenization. Specifically then, the outer region of the gyre is where the spiral occurs, and the inner region, delimited by the collapsed spiral, is where homogenization occurs.

For the asymmetric gyre, we saw earlier that where the plume first enters the gyre heading east the fast flow keeps it nearly tracked to a streamline. However, after the plume has turned the corner to the north,

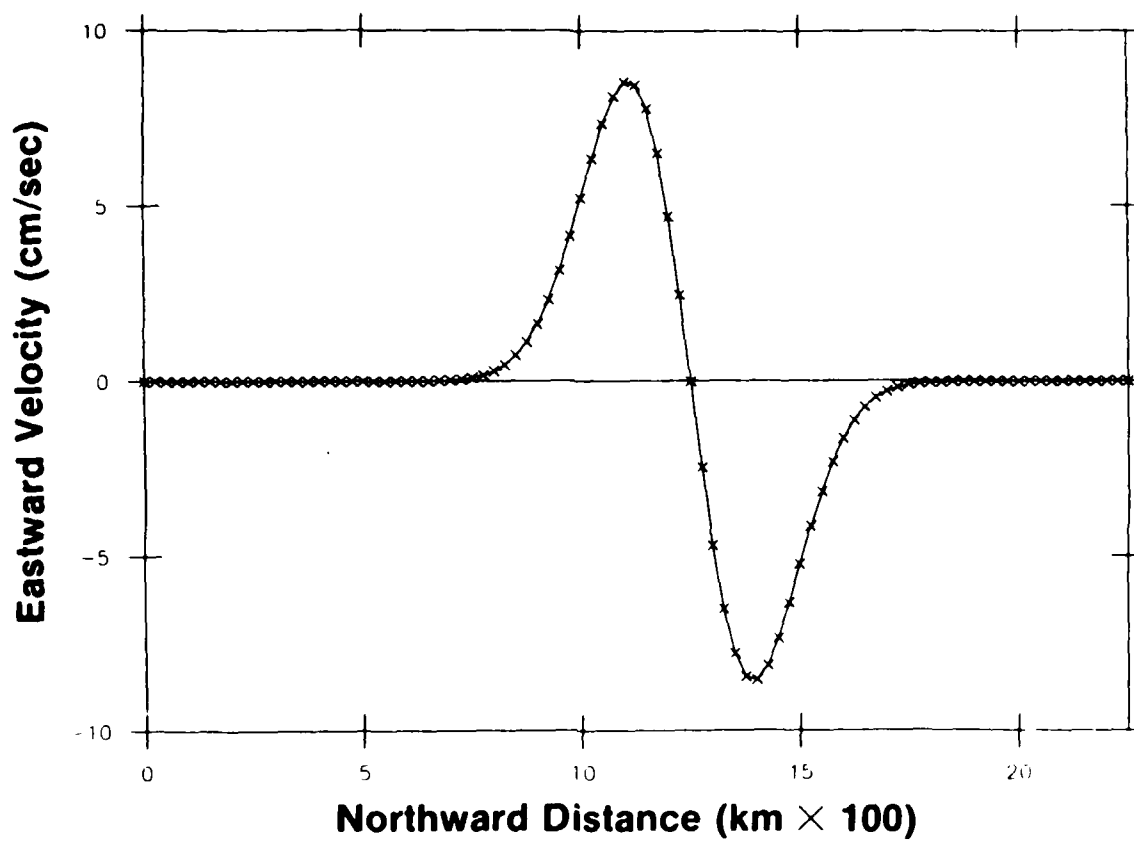


Figure 1.15: North-south velocity section through the center of the gyre of Figure 1.2.

the flow along that same streamline weakens and the plume proceeds to spiral significantly inward. In this case the division between the two regions of the gyre is not so clear cut. However, homogenization will not occur until the plume tracks a streamline around an entire circuit. So even though portions of the spiral may collapse, it is only where the cumulative spiral collapses that marks the transition between the two regions.

We now examine more clearly the condition that the flow be strong enough to keep the plume from diffusing appreciably across stream in the time it takes to recirculate. The advective limit corresponds to  $P_a \gg 1$  and  $P_c \gg 1$ . The more stringent of these is  $P_c \gg 1$ , or in terms of scales,

$$P_c = \left(\frac{U}{L_a}\right) \left(\frac{L_p^2}{\kappa}\right) \gg 1.$$

In considering a circuit around the gyre the relevant  $L_a$  is  $L_a = L_s \equiv$  perimeter of the streamline, and the relevant  $U$  is  $U = \bar{v}_s \equiv$  average velocity around the streamline. We define the homogenization function  $H$  as the ratio of these two quantities, which gives

$$P_c = H(\psi) \left(\frac{L_p^2}{\kappa}\right),$$

where  $H(\psi) = \frac{\bar{v}_s(\psi)}{L_s(\psi)}$ . The function  $H$ , which is the inverse of the circulation time, can be thought of as a measure of the tendency for homogenization to occur based only on flow characteristics. A larger  $H$  means a greater likelihood for homogenization.

Consider again the symmetric gyre, whose streamfunction is given by

$$\psi = \psi_0 \left(1 - e^{-\frac{r^2}{L^2}}\right), \quad (1.10)$$

where  $\psi_0 =$  amplitude,  $L =$  e-folding scale of the gyre. In this case  $\bar{v}_s = v_s$ . From (1.10),

$$v_s = \frac{\partial \psi}{\partial r} = \frac{2}{L^2} (\psi_0 - \psi) r .$$

The perimeter  $L_s = 2\pi r$ , which gives

$$H(\psi) = \frac{1}{\pi L^2} (\psi_0 - \psi) .$$

This says that the greatest tendency for homogenization occurs at the center of the gyre, decreasing linearly with increasing  $\psi$ . So the part of the gyre near the center, where the flow becomes weak again, is included in the advective region because the flow is strong enough in the sense that the circulation time is small (the perimeter of a streamline is small). Contrast this to a solid body rotation gyre,  $\psi = \psi_0 r^2$ , where the circulation time is constant for each streamline. Here  $v_s = 2 \psi_0 r$  and  $H(\psi) = \frac{\psi_0}{\pi}$ , and the tendency for homogenization is the same everywhere.

In the asymmetric gyre the velocity along a streamline varies around the gyre. The streamfunction is

$$\psi = \psi_0 \left( 1 - e^{-\frac{x^2}{L_x^2} - \frac{y^2}{L_y^2}} \right) , \quad (1.11)$$

where  $L_x$  and  $L_y$  are the  $x$  and  $y$  e-folding length scales. Note that

$$H = \frac{\bar{v}_s}{L_s} = \frac{\frac{1}{L_s} \int_S \tilde{u} \cdot d\tilde{s}}{L_s} = \frac{\Gamma}{L_s^2} ,$$

where  $\Gamma$  is the circulation around the streamline  $S$ . From (1.11),

$$\Gamma = 2\pi \psi_0 \left( \frac{L_x^2 + L_y^2}{L_x L_y} \right) \left( 1 - \frac{\psi}{\psi_0} \right) \ln \left( 1 - \frac{\psi}{\psi_0} \right)^{-1} ,$$

$$L_s^2 = 4\pi^2 L_x L_y \ln \left( 1 - \frac{\psi}{\psi_0} \right)^{-1} ,$$

which gives

$$H(\psi) = \frac{H_0}{2\pi}(\psi_0 - \psi), \quad (1.12)$$

where  $H_0 = \left( \frac{L_x^2 + L_y^2}{L_x^2 L_y^2} \right)$ . Figure 1.16 graphs  $H_0$  as a function of the

skewness of a gyre. It shows that for a given value of  $\psi$ , homogenization is more likely to occur in a more skewed gyre. Note that this is true even though the velocity at the two widest sections of the gyre approaches zero as the gyre's skewness increases. This is because the portion of the streamline in these sections gets vanishingly small as well.

### C) Limits of Diffusivity

We examined homogenization within the asymmetric gyre of Figure 1.2 for various values of the diffusivity  $\kappa$ . The smallest value considered was  $\kappa \sim 10^6 \text{ cm}^2/\text{sec}$ , and the homogeneous pool of tracer that formed in steady state is shown in Figure 1.17. This is the final state of the same example that was previously analyzed in terms of the asymmetric spiral. Figure 1.17b shows the path of the spiral and how it indeed closes in on the region that eventually becomes homogenized.

When the diffusivity is increased to  $\kappa \sim 5 \times 10^6 \text{ cm}^2/\text{sec}$  for the same gyre, this in effect causes the flow to appear weaker to the incoming plume of tracer. In particular, the zonal flow where the plume first enters the gyre is not fast enough anymore to be in the advective limit, so a pronounced spiral occurs there as well as in the meridional flow (the asymmetry no longer exists, Figure 1.17d). Consistent with (1.12), the plume now has to penetrate further into the gyre before it encounters flow strong enough to induce homogenization. Correspondingly, the steady state pool is reduced in extent (Figure 1.17c).

Upon increasing  $\kappa$  even more ( $\kappa \sim 10^7 \text{ cm}^2/\text{sec}$ ) an abrupt transition occurs in the manner in which tracer fills the gyre. What happens is that the meridional flow, which is weaker than the zonal flow, is essentially turned off. That is to say the diffusive flux there is now of the order of

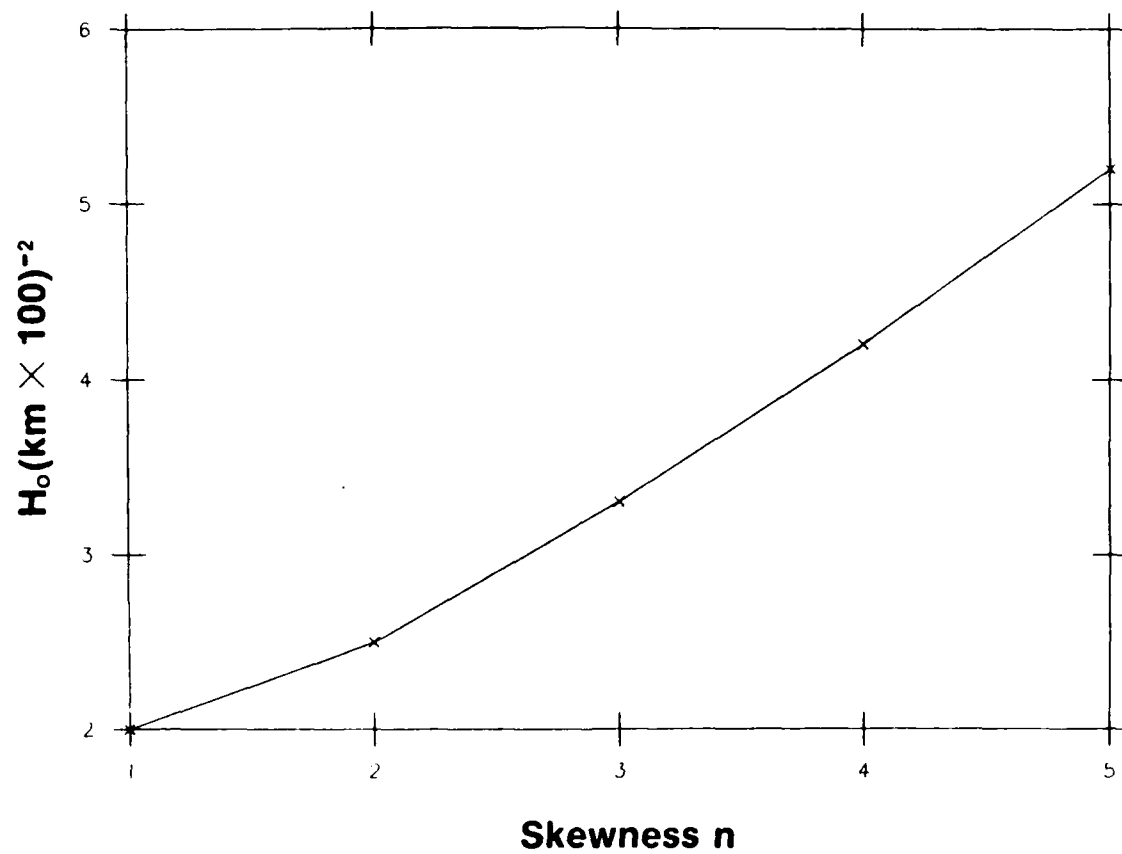


Figure 1.16: The value of the homogenization function versus the skewness of a gyre. The skewness  $n$  is defined as the ratio of the major axis of the ellipse to the minor axis. The area of the gyre is the same in each case and set equal to  $\pi$ .

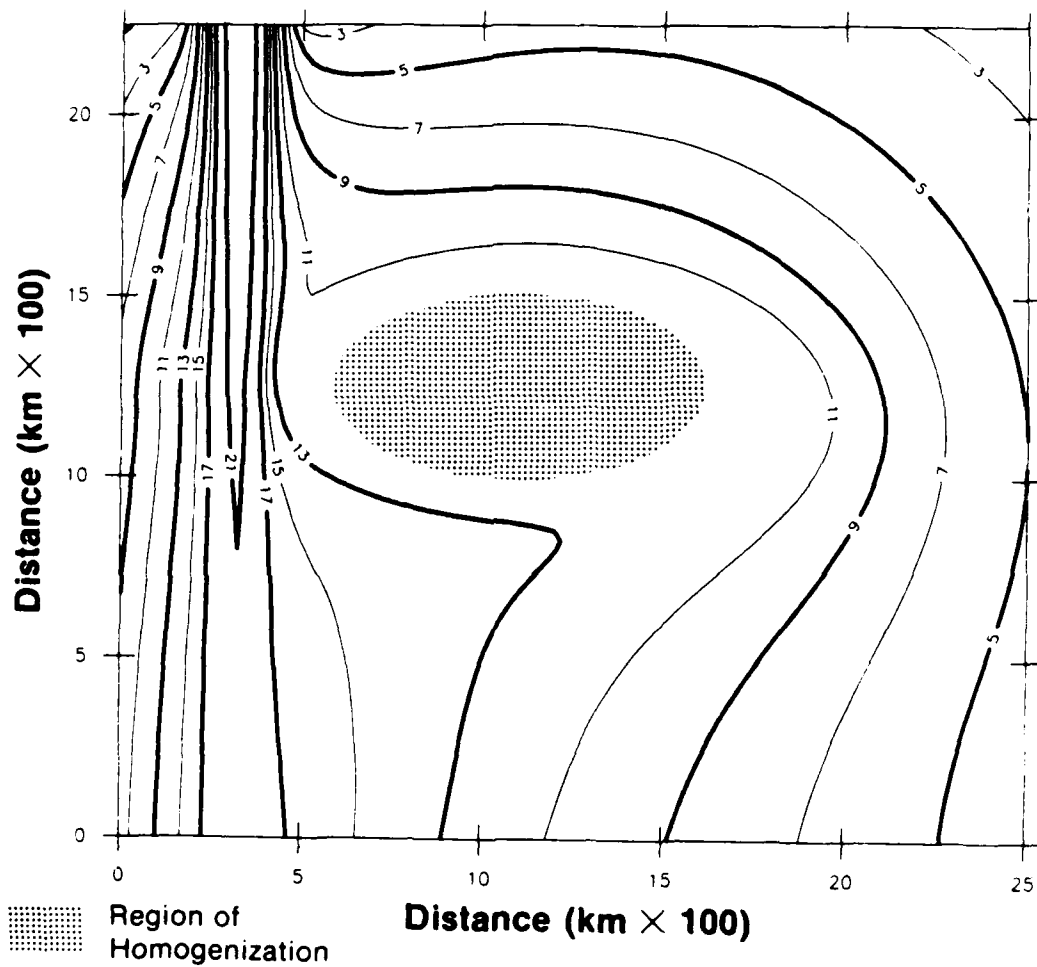
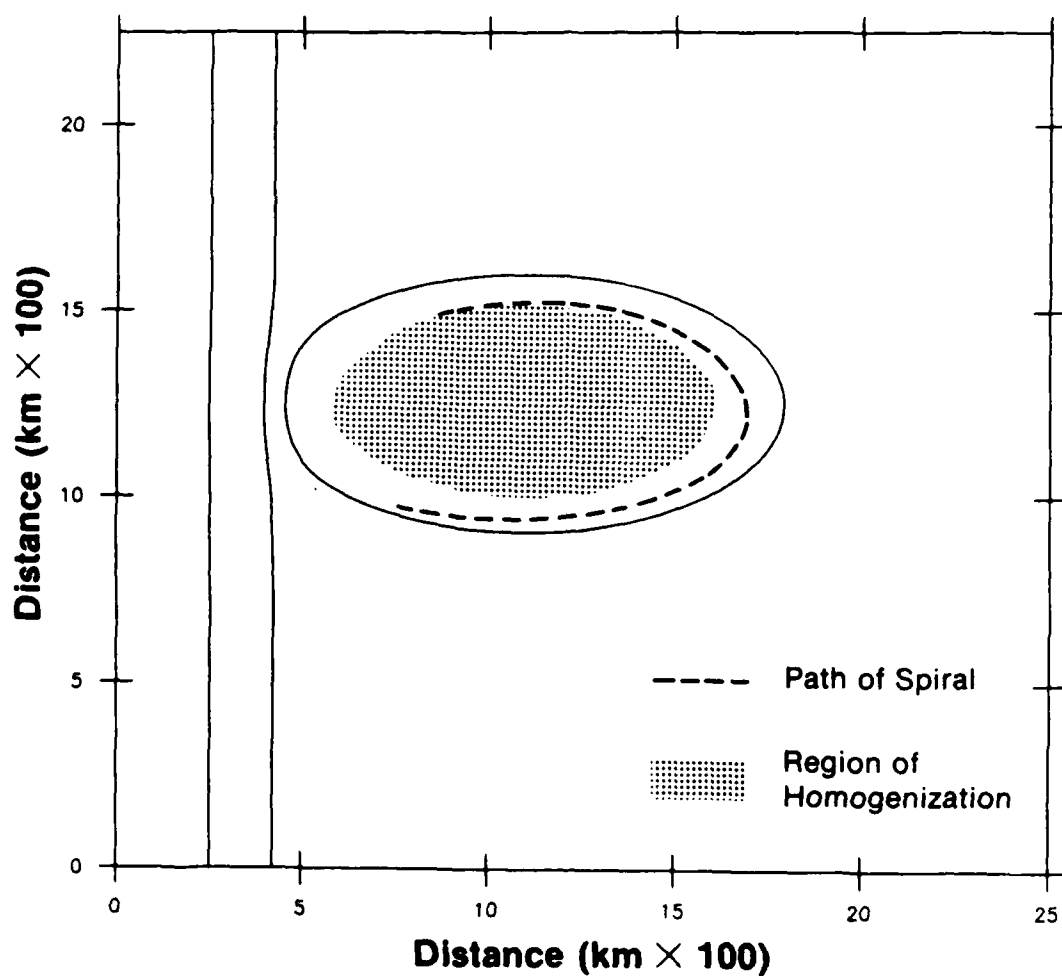
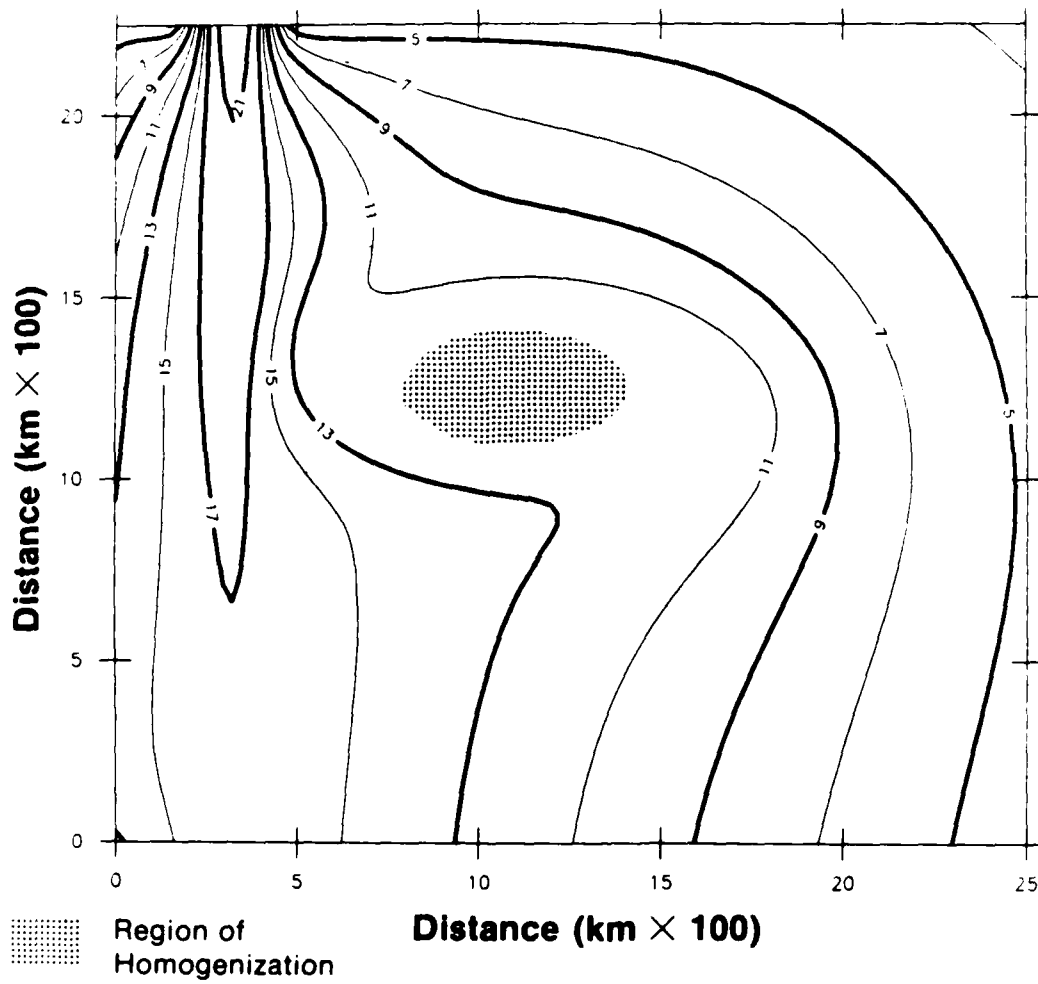


Figure 1.17: (a) Steady state distribution of tracer for  $\kappa \sim 10^6 \text{cm}^2/\text{sec}$ . The shaded region corresponds to that area of the gyre in which the gradient of tracer is  $\leq .1$  concentration units/km  $\times$  100. This is taken as the criterion for homogenization.

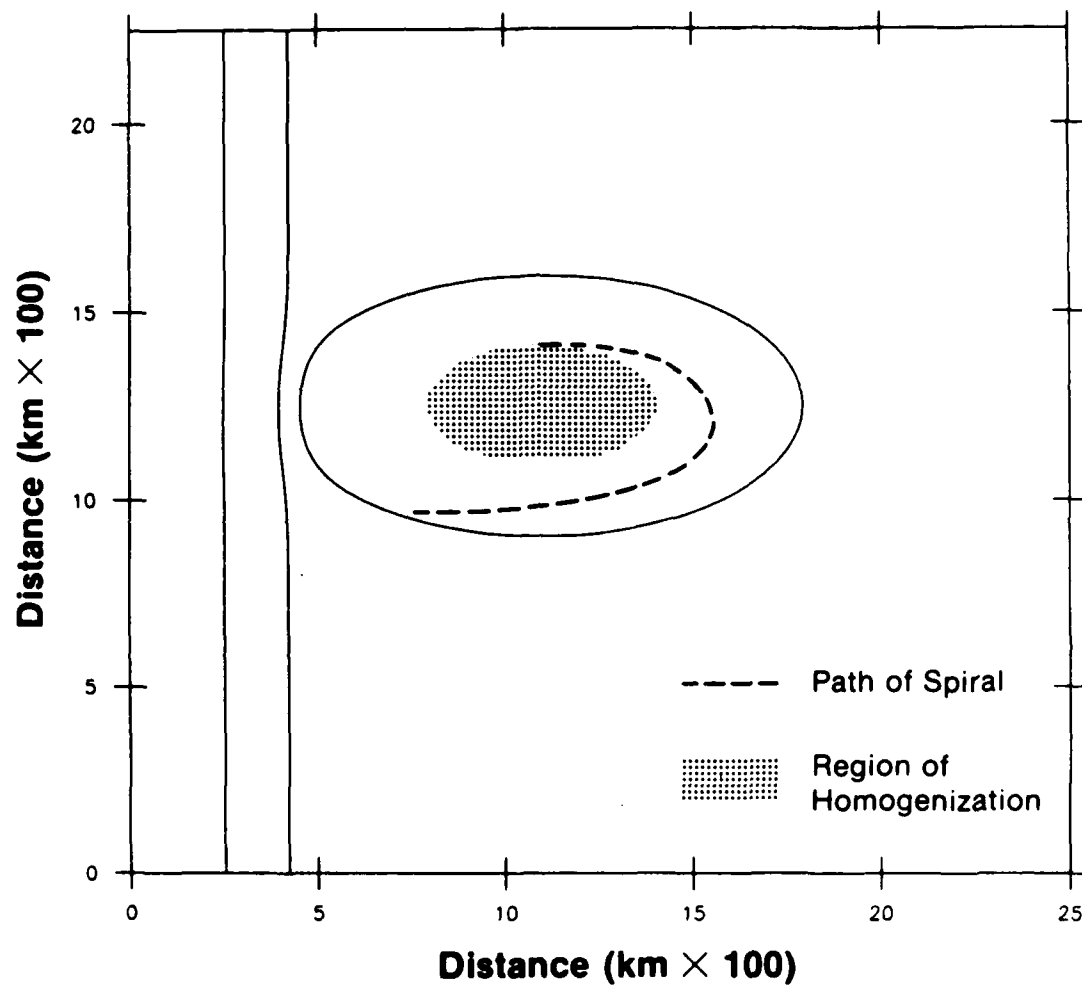


(b) The region of homogenization in (a) shown in relation to the inward spiral of the plume of tracer during spin-up. The solid lines are the bounding streamlines.





(c) Steady state distribution for  $\kappa \sim 5 \times 10^6 \text{ cm}^2/\text{sec}$ .



(d) Homogenized region and spiral for  $\kappa \sim 5 \times 10^6 \text{ cm}^2 \text{ sec.}$

the advective flux. Thus the plume enters the gyre, gets pulled eastward, turns the corner and stagnates. By the time tracer diffuses northward and gets caught in the zonal flow and subsequently advected westward, the westward diffusing tracer from the stagnation point has penetrated the center of the gyre. So whereas in the previous two cases tracer was advected completely around the gyre and filled the center in a bowl-like fashion, here it is advected to the east and proceeds to fill the gyre from east to west (Figure 1.19). A small amount of homogenization does occur at the center of the gyre (Figure 1.18).

The final case considered can be thought of as the diffusive limit ( $\kappa \sim 5 \times 10^7 \text{ cm}^2/\text{sec}$ ). Here the presence of the zonal flow is hardly felt as well and the manner in which the gyre is ventilated undergoes yet another change. As shown in Figure 1.19 tracer basically diffuses from west to east across the gyre, with an undulation corresponding to the eastward and westward flows.

#### D) Conclusions

Homogenization is the steady state manifestation of tracer penetrating a closed circulation, provided the system is strongly advective. For the spatially decaying gyre considered here, the occurrence of homogenization is closely tied to the characteristics of the spiral of the incoming plume of tracer that forms during spin up. In particular, where the spiral collapses to a streamline marks the outer extent of the homogeneous pool that eventually develops. As the diffusivity is increased the size of this pool shrinks. This is consistent with the idea that homogenization occurs more readily nearer the center of the gyre for this type of flow, based on the shorter circulation times there.

Rhines and Young (1983) have investigated how long it takes homogenization to occur in a closed circulation. They showed that the process occurs in two stages, the slower of which is the diffusive time of the gyre. The problem they solved is simpler than the one being analyzed here. Their initial state consisted of a given distribution of tracer in the gyre, which evolved within an insulating boundary. In the present problem in order to understand the time history of homogenization, the nature of the sources and sinks of tracer must be considered. This is done in chapter two.

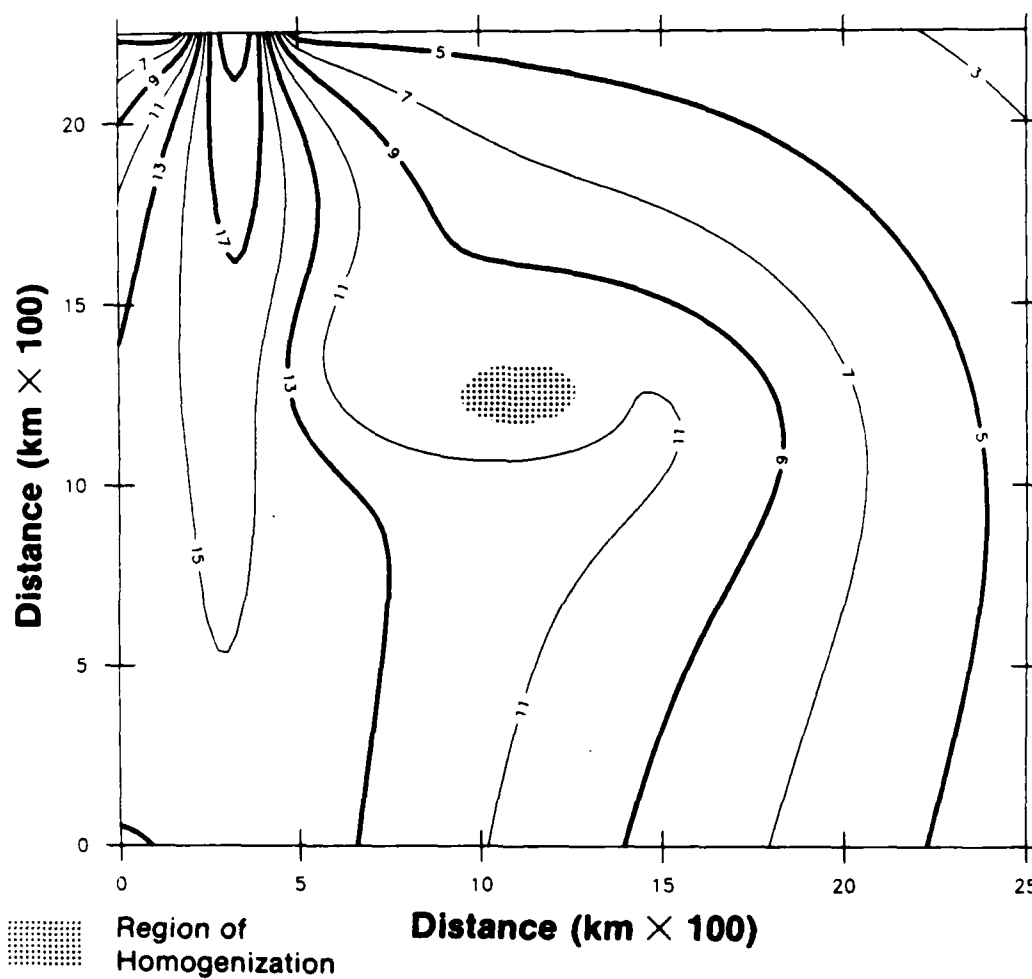


Figure 1.18: Steady state distribution for  $\kappa \sim 10^7 \text{ cm}^2/\text{sec}$ .

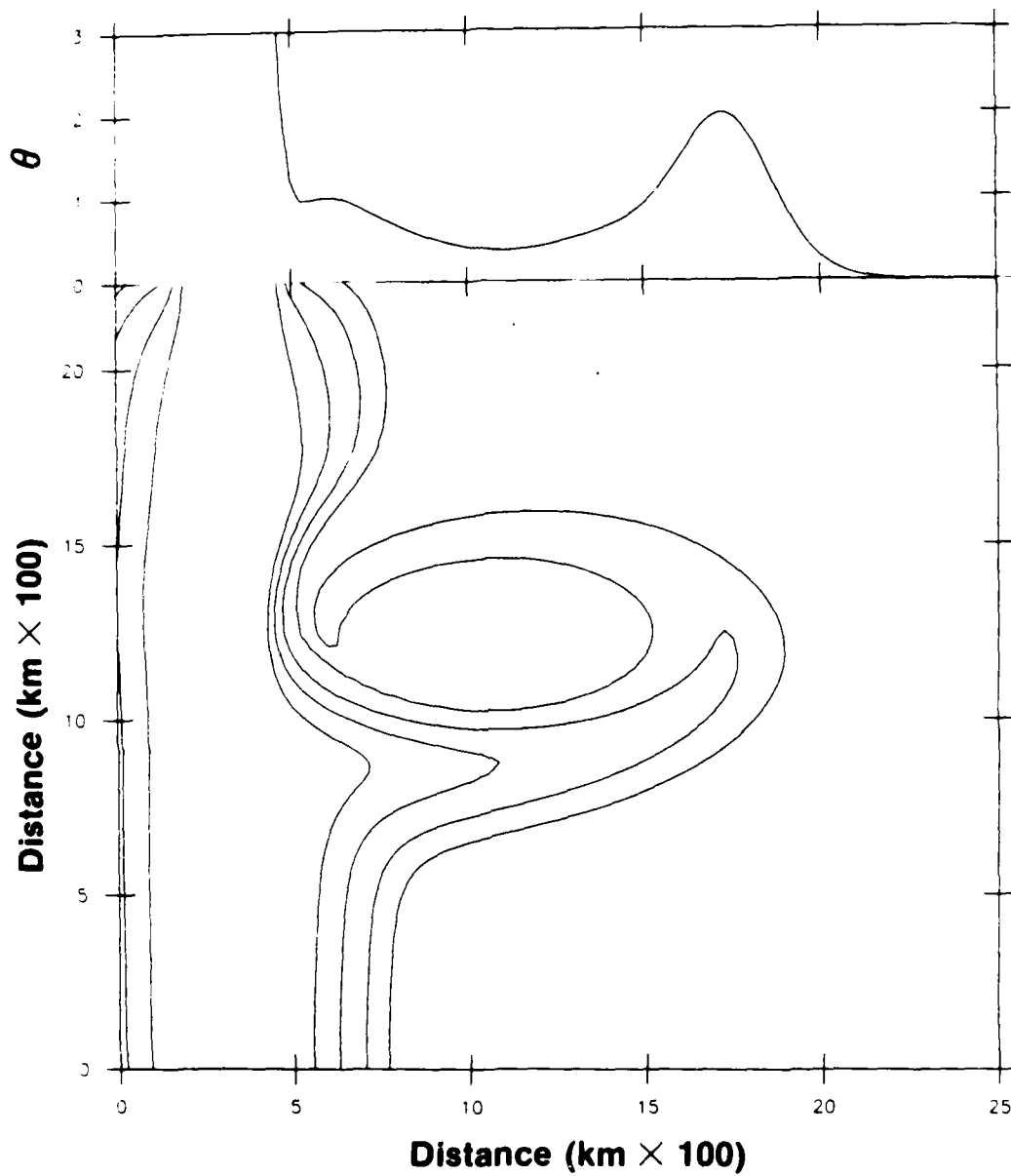
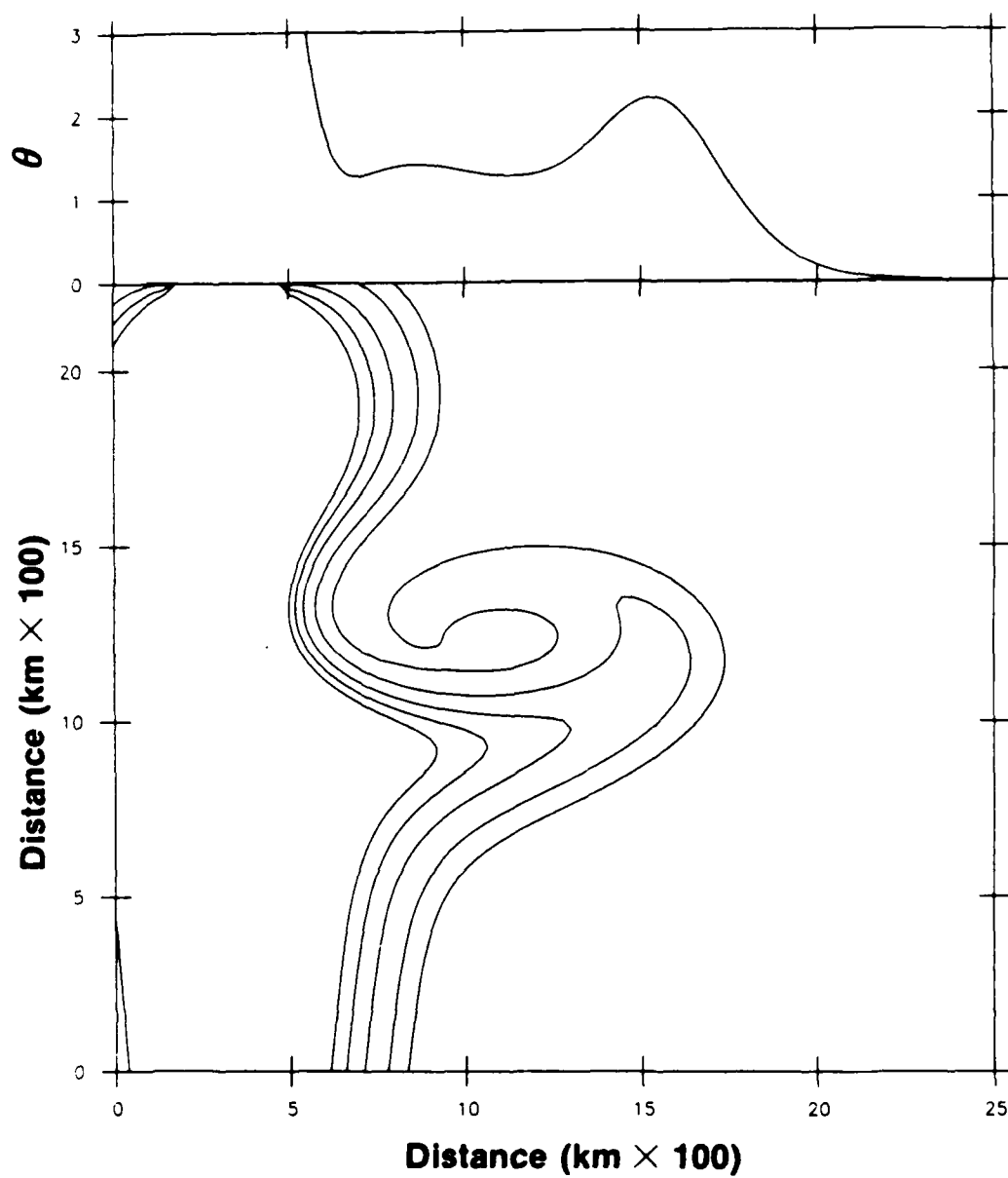
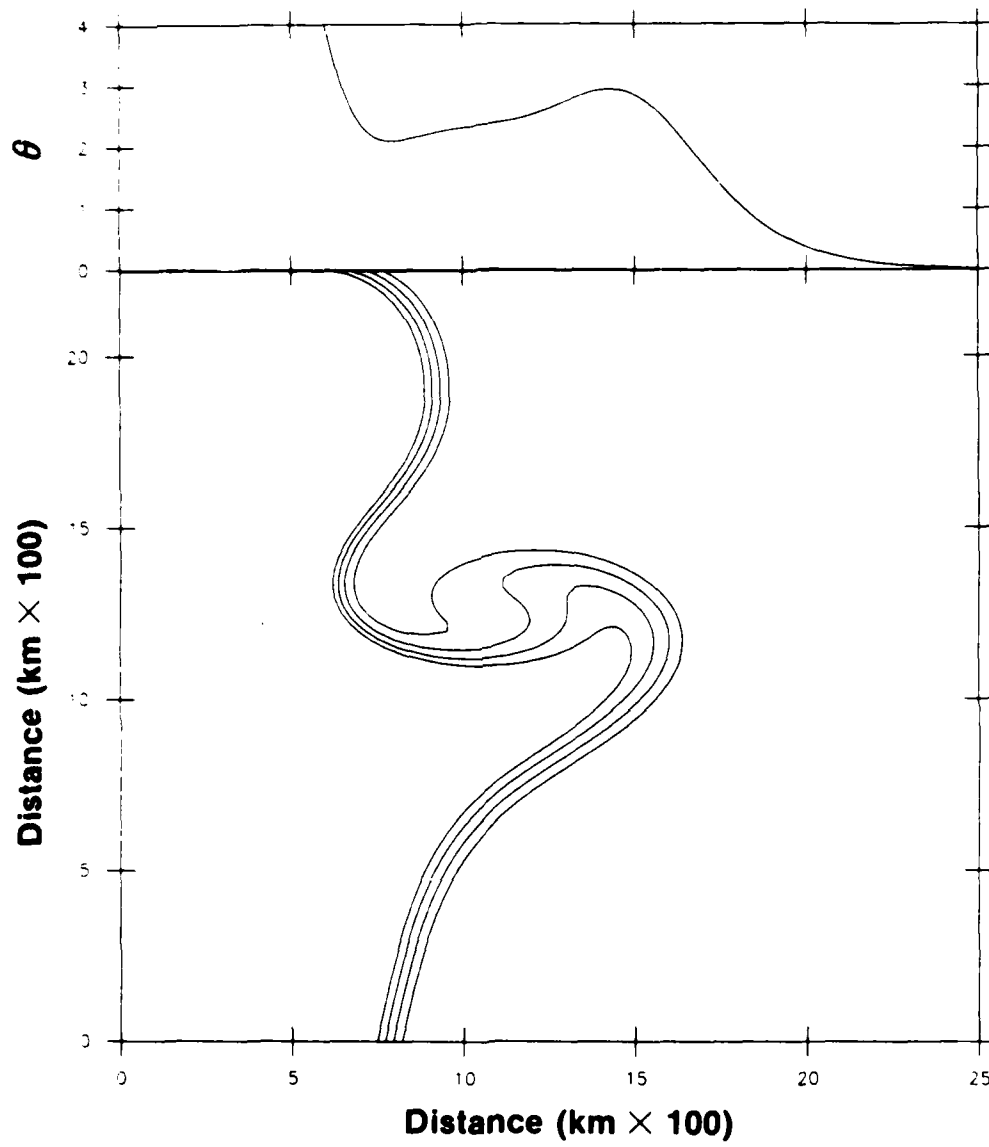


Figure 1.19: Instantaneous distribution of tracer during spin-up illustrating manner in which tracer fills the gyre. Shown above is a zonal section through the center of the gyre.

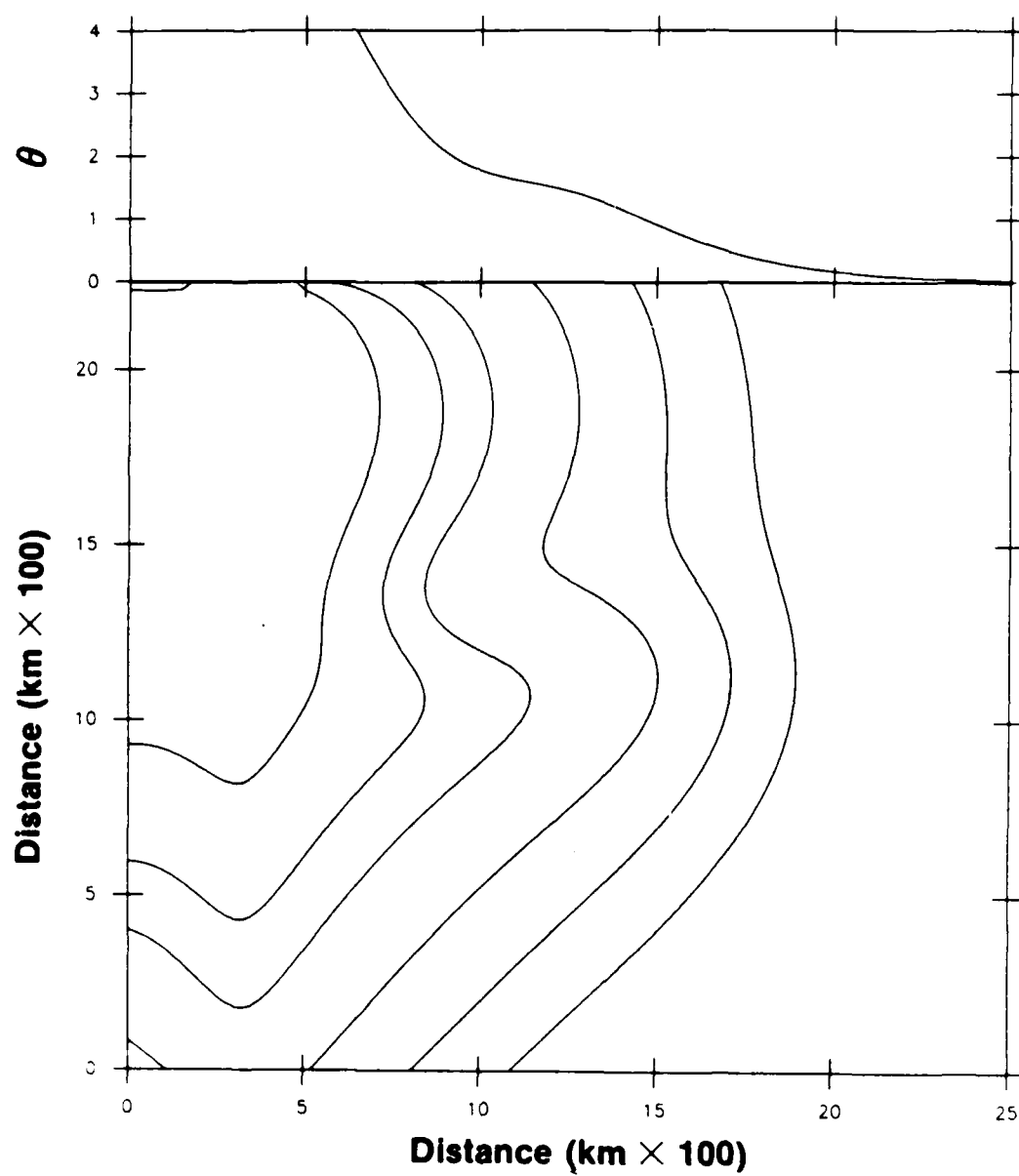
(a)  $\kappa \sim 10^6 \text{ cm}^2/\text{sec.}$



(b)  $\kappa \sim 5 \times 10^6 \text{ cm}^2/\text{sec}.$



(c)  $\kappa \sim 10^7 \text{ cm}^2/\text{sec.}$



(d)  $\kappa \sim 5 \times 10^7 \text{ cm}^2/\text{sec.}$



## CHAPTER TWO: THE NORTHERN RECIRCULATION GYRE

Preliminaries

Up until now we have focussed on the gyre circulation of the numerical model, isolating the processes involved in the penetration of tracer into the gyre. Having understood the entrainment and homogenization that occur we now consider the coupled gyre/boundary current system; i.e. we now examine how the DWBC supplies tracer to the NRG.

As mentioned earlier, the DWBC is a source of different tracers to the abyssal North Atlantic. Having been in recent contact with the atmosphere its waters are rich in oxygen, tritium, and freons. Its waters are also relatively cold and fresh and marked by a distinct signal in silica. Recently Hogg et al. (1986) presented results from the OCEANUS 134 hydrographic survey of the region where the NRG and DWBC are in close contact, highlighting several of these tracers. (Some data from previous cruises was also included.) They discussed the data in relation to this associated flow pattern, remarking on the area of nearly uniform tracer concentration in the region of the NRG. It was also shown that there is no point in considering each of the tracers individually as they do not all give independent information. In particular, the distribution of salinity was independent from those of the other tracers, the rest of which show nearly identical features. This difference, the presence of a slight minimum near the location of the NRG for all of the tracers except salinity, was explained in terms of vertical processes.

Here we consider three different tracers: salinity, oxygen, and freons. Using the numerical model in association with a simple analytical model, we explore what these tracer distributions can tell us about the NRG and its relationship to the DWBC and about various other properties of the system. We examine more closely the distinction between salt and oxygen suggested in Hogg et al. (1986). Freons are considered as well because they are in a transient state and the atmospheric forcing functions are known. An investigation of time dependent input is the focus of chapter three.

We start with an analysis of numerical model results only. In order to understand these results more clearly a simpler representation of the model is solved analytically. Some of the ideas that are derived from this analysis are then applied to the same data set discussed in Hogg et al. (1986).

### Model Study

It is assumed that a turbulent transfer of properties from the DWBC to the NRG occurs along density surfaces, the entire gyre being ventilated in this fashion. It is often the case that along-isopycnal mixing in the ocean is presumed to dominate cross-isopycnal mixing. However, it is the presence of cross-isopycnal mixing that Hogg et al. suggest may be the reason for the difference in the distributions of salinity and oxygen.

Consider the vertical profiles of Figure 2.1 for a station from the OCEANUS 134 data set. At the density level of the DWBC core (average depth  $\approx 3600$  m) the salinity distribution decreases monotonically with depth (dense water of Antarctic influence keeps near bottom levels fresh). However, the oxygen profile has a relative maximum at this level. Thus in light of the associated gradients, for oxygen there is a cross-isopycnal flux out of the deep layer into the water above and the water below, whereas for salt there is a flux into the layer from above and out of the layer into the bottom water. This suggests that the effect of cross-isopycnal mixing in the deep layer may be more pronounced for oxygen than for salinity.

Consider the three-dimensional form of the advective-diffusive governing equation (1.1),

$$\frac{\partial \theta}{\partial t} + \underline{u} \cdot \underline{\nabla}_h \theta + w \frac{\partial \theta}{\partial z} = \underline{\nabla}_h \cdot \kappa \underline{\nabla}_h \theta + \frac{\partial}{\partial z} \nu \frac{\partial \theta}{\partial z} , \quad (2.1)$$

where  $\theta(x,y,z)$  = tracer concentration,

$\underline{u}(x,y,z)$  = horizontal velocity vector,

$w(x,y,z)$  = vertical velocity,

$$\underline{\nabla}_h = \underline{i} \frac{\partial}{\partial x} + \underline{j} \frac{\partial}{\partial y} ,$$

$\kappa$  = lateral eddy diffusivity (constant),

and  $\nu$  = vertical eddy diffusivity (constant).

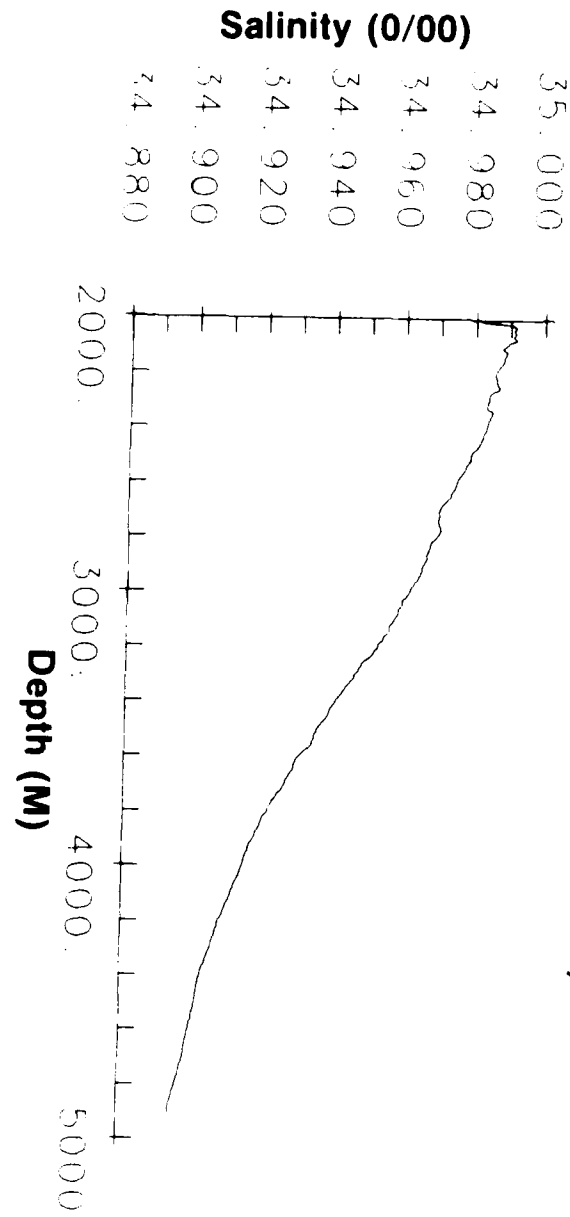
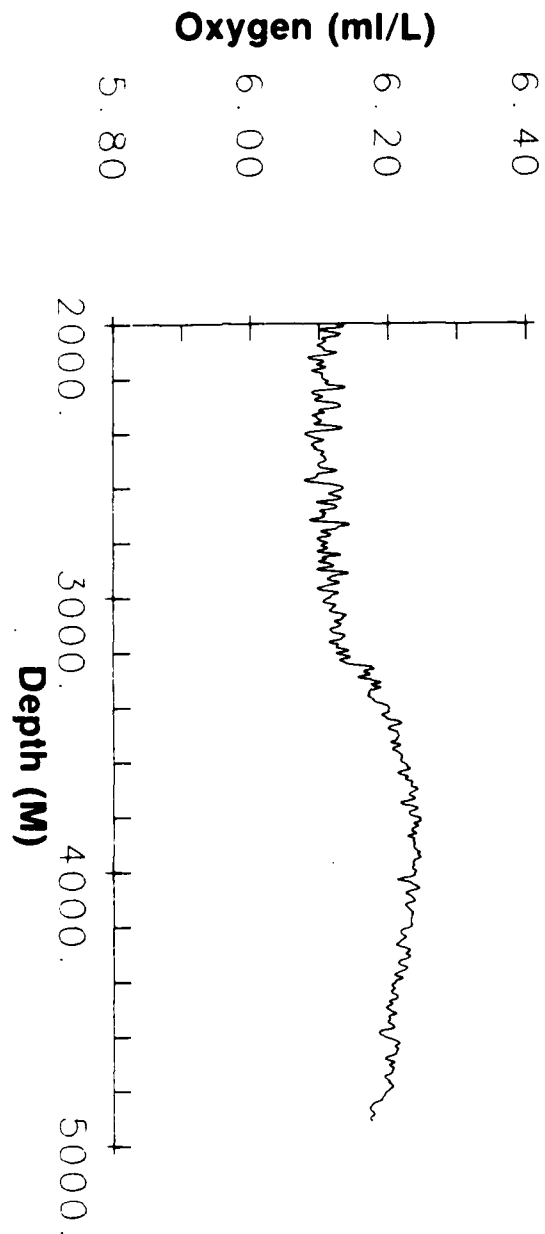


Figure 2.1: (a) CTD profile of salinity versus depth below 2000 m for OC134 station 40 (in the gyre).



(b) Oxygen profile.

We are interested in the evolution of tracer in the deep layer which we assume is bounded above and below by density surfaces which are nearly flat (thus along-isopycnal is synonymous with horizontal, cross-isopycnal is synonymous with vertical).

In a finite-difference sense we represent the vertical structure with three grid points, but only the center one is active, corresponding to the concentration in the center of the layer. The upper and lower points are fixed boundary conditions (representing reservoir values above and below the deep layer, Figure 2.2). Applying this approximation to (2.1) ( $w \equiv 0$ ),

$$\frac{\partial \theta_M}{\partial t} + u \frac{\partial \theta_M}{\partial x} + v \frac{\partial \theta_M}{\partial y} = \kappa \left( \frac{\partial^2 \theta_M}{\partial x^2} + \frac{\partial^2 \theta_M}{\partial y^2} \right) - \frac{8v}{H^2} \left( \theta_M - \frac{\theta_u + \theta_L}{2} \right),$$

where  $\theta_M(x,y)$  = value of tracer at the center of the layer,

$\theta_u$  = value of upper reservoir (constant),

$\theta_L$  = value of lower reservoir (constant),

$H$  = layer thickness (vertical grid spacing =  $\frac{H}{2}$ ),

or in terms of the anomaly  $\theta' \equiv \left( \theta_M - \frac{\theta_u + \theta_L}{2} \right)$ ,

$$\frac{\partial \theta'}{\partial t} + u \frac{\partial \theta'}{\partial x} + v \frac{\partial \theta'}{\partial y} = \kappa \left( \frac{\partial^2 \theta'}{\partial x^2} + \frac{\partial^2 \theta'}{\partial y^2} \right) - \frac{8v}{H^2} \theta'. \quad (2.2)$$

This equation is quasi-three-dimensional in that it contains a parameterization of a vertical process. Note that this vertical flux term has the form of a radioactive decay term (although for a property such as silica, which is characterized by a relative minimum in the deep layer, it is a growth term). As discussed in Hogg et al. (1986), for the scales involved, this type of decay in oxygen concentration in the abyssal ocean overwhelms any consumption that may be occurring.

Equation (2.2) is that which was analyzed by Hogg et al. in differentiating between salt and oxygen. That analysis is expanded upon here. For the salt case it is assumed that  $\frac{\theta_u + \theta_L}{2} \approx \theta_M$  ( $\theta' \approx 0$ ) so that the vertical

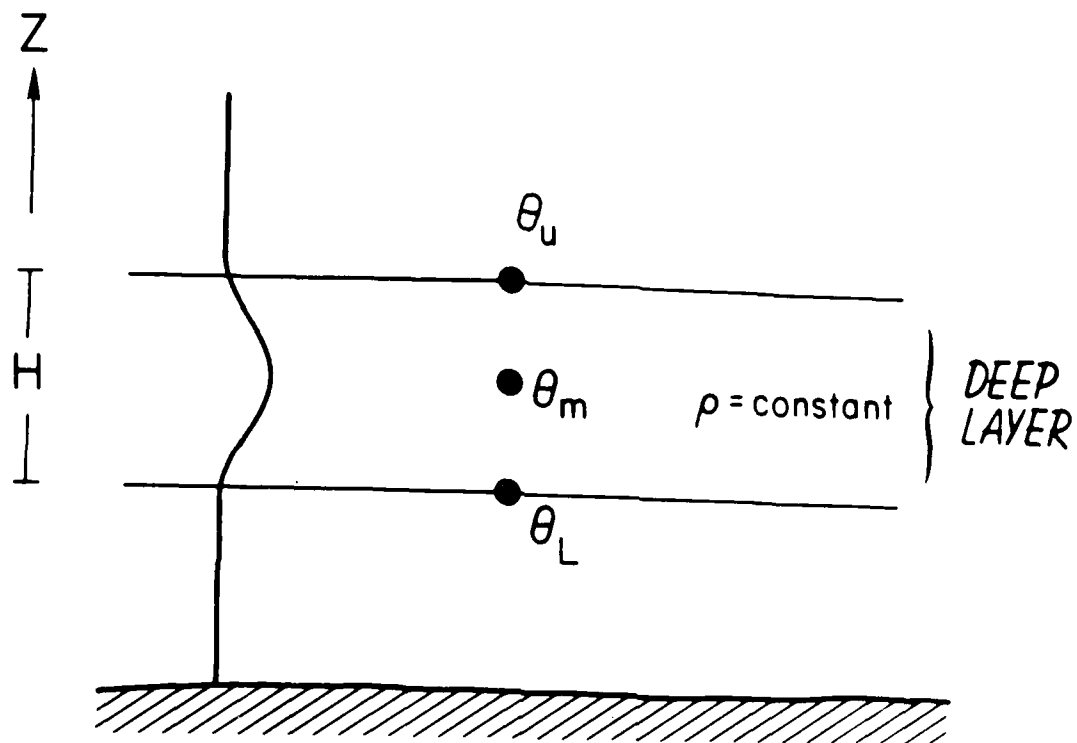


Figure 2.2: Schematic showing the vertical resolution of the deep layer in the numerical model. Three grid points are used to represent a continuous profile as such.

flux term is not large enough to affect the distribution. Setting it identically equal to zero reduces (2.2) to the equation which was studied in chapter one, (1.1). The previous results concerning entrainment and homogenization can be thought of then as applying to the salt case. We consider this case further. For oxygen it is assumed that  $\frac{\theta_u + \theta_L}{2} < \theta_M$  and the vertical flux term is retained. Using the same two-dimensional finite-difference scheme that was applied to (1.1), equation (2.2) is then analyzed numerically and compared to the salt case. (Hereafter the prime is dropped and  $\theta$  refers to the deep anomaly.)

#### A) Without Vertical Flux

We turn our attention once again to the same numerical simulation that was analyzed in the previous chapter (the small diffusivity limit only), but here we take a broader perspective and consider the fact that the tracer which collects in the gyre originally came from the boundary current. As tracer first advects downstream from the northern source and spreads laterally, the eastward flux of tracer into the interior is inhibited by the westward flow of the gyre and accentuated by the eastward flow further to the south. All along the region of contact tracer diffuses from the boundary current directly into the gyre. However, because of the strong gyre flow, tracer does not penetrate substantially into the gyre before the flow turns off shore. For this reason the plume of tracer which extends from the boundary does not coincide with the region of maximum eastward flow of the gyre, rather the plume is well south of this region (Figure 2.3). This is an example then of when a tongue of tracer does not coincide with the core of the current (rather it defines the current's edge).

Each successive plume originates from the boundary a bit further to the south, as it is made up of tracer that diffused further from within the current and so was subject to stronger southward advection. Throughout the simulation the level of tracer across the gyre is nearly flat. (There is a slight minimum in the center of the gyre, Figure 2.4.) The entire system eventually reaches a steady state as input at the northern edge of the current is balanced by advective output at its southern edge and diffusive output along the remaining (quiescent) part of the boundary. The gyre itself

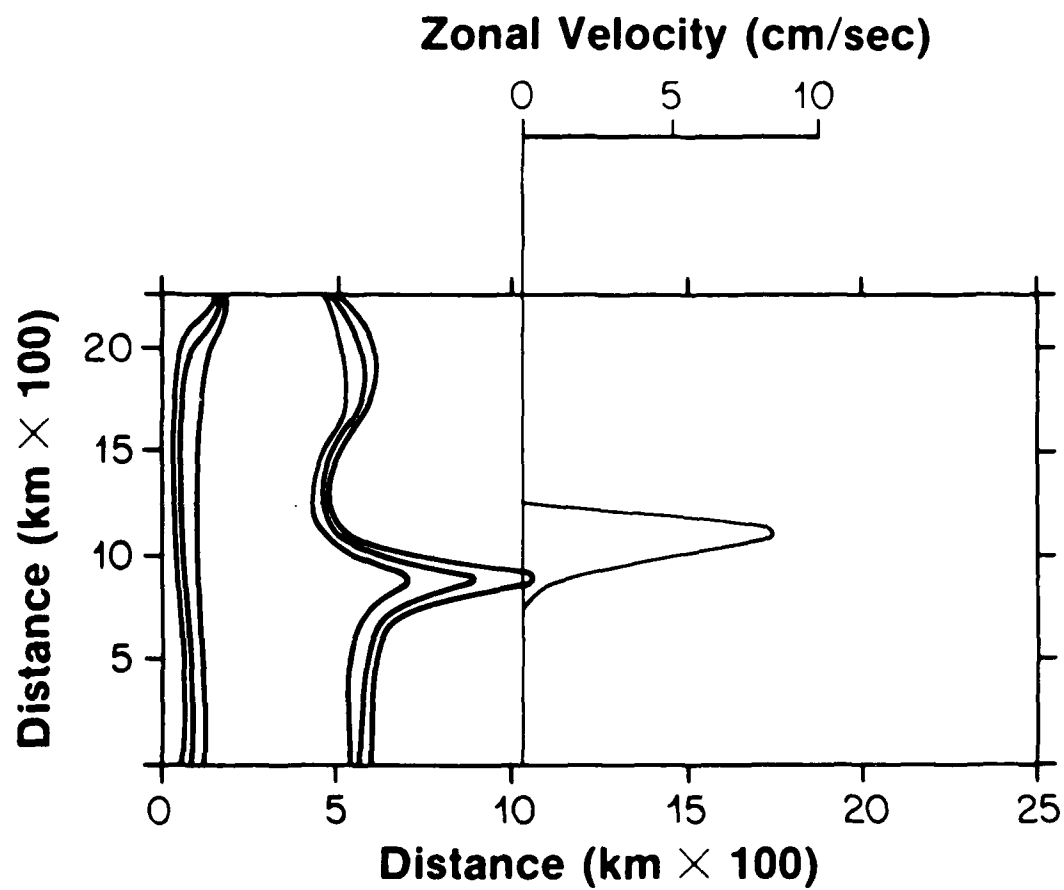


Figure 2.3: Plume of tracer being pulled from boundary in relation to the eastward jet of the gyre.



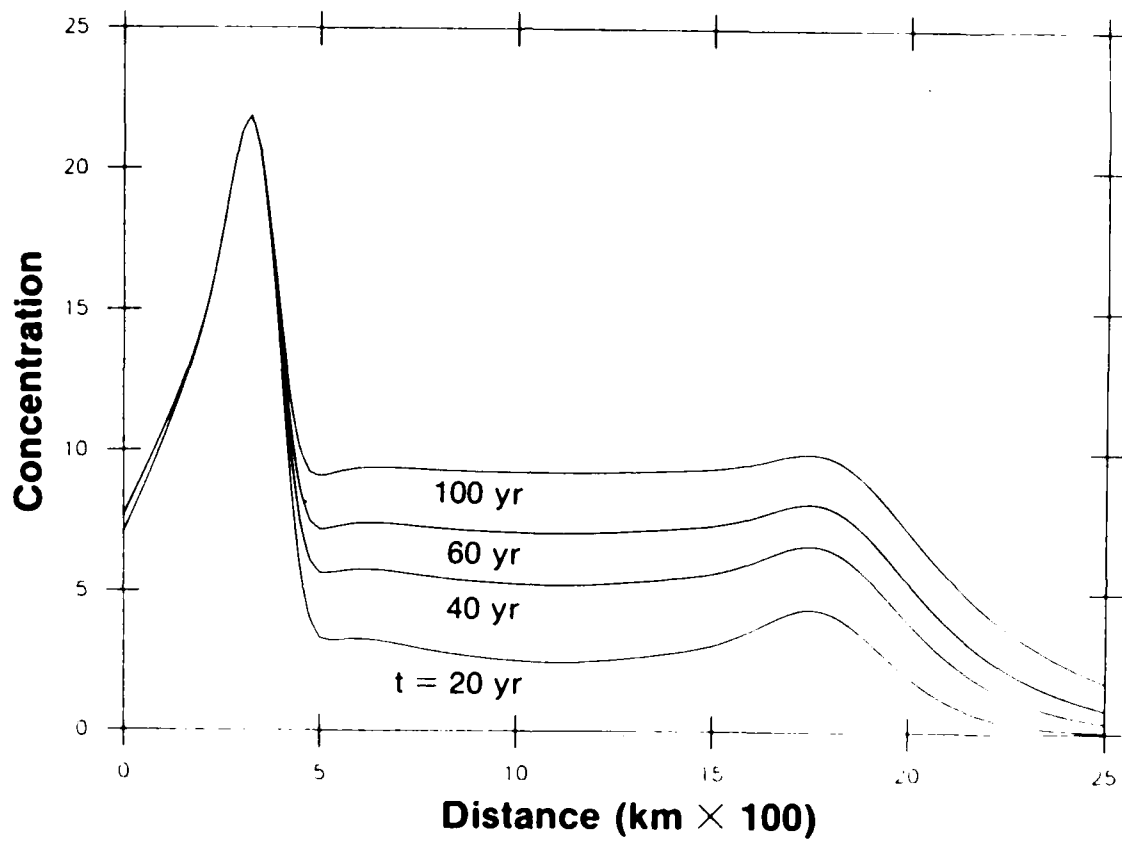


Figure 2.4: Zonal section of tracer through the boundary current and center of the gyre at four different times during spin-up.

at steady state is marked by perfect homogenization, there is no input anywhere around the gyre nor is there output.

Two different cases were considered in some detail  $\kappa \sim 10^6 \text{cm}^2/\text{sec}$  and  $\kappa \sim 5 \times 10^6 \text{cm}^2/\text{sec}$  (hereafter referred to as  $\kappa_1$  and  $\kappa_5$ ). Figure 2.5 shows the accumulation of tracer at the center of the gyre for the two cases. (The interior portion of the gyre is the last place in the domain to reach steady state.) There are two things to note. First, it took over three times longer for steady state to be reached in the smaller  $\kappa$  example (an e-folding time of  $\sim 80$  years versus  $\sim 25$  years). Second, the value of the homogenized pool at steady state is the same for both cases. (All simulations were halted when the yearly accumulation rate fell below 2 percent of its earlier maximum rate.) In  $\kappa_5$  tracer readily diffuses off the boundary and spin up occurs relatively quickly, whereas in  $\kappa_1$  tracer diffuses from the current slowly but spin up occurs much later and tracer accumulates in the gyre for a longer time. It is not obvious why these effects exactly balance each other to produce the same level.

In their work on homogenization of passive tracers in gyres Rhines and Young (1983) showed that the time scale for homogenization to occur is the diffusive time scale of the gyre. It is interesting then to compare estimates based on this to the e-folding times observed above. Since the e-folding times differ in the two examples by only a factor of 3, it is not sufficient to merely consider order of magnitude estimates. We therefore make use of results from the following example of tracer diffusing into a closed region.

Consider a circular domain of area  $A_0$  within which tracer is free to diffuse. The edge of the domain is maintained at a constant value  $\theta = \theta_0$  and initially there is no tracer in the interior. The steady state distribution will be  $\theta = \theta_0$  everywhere, and we are interested in how long it takes to reach this state. The governing equation is the radially symmetric diffusion equation,

$$\frac{\partial \theta}{\partial t} = \kappa \frac{\partial}{\partial A} \left( 4\pi A \frac{\partial \theta}{\partial A} \right), \quad (2.3)$$

where  $A$  = area corresponding to a given radial distance.

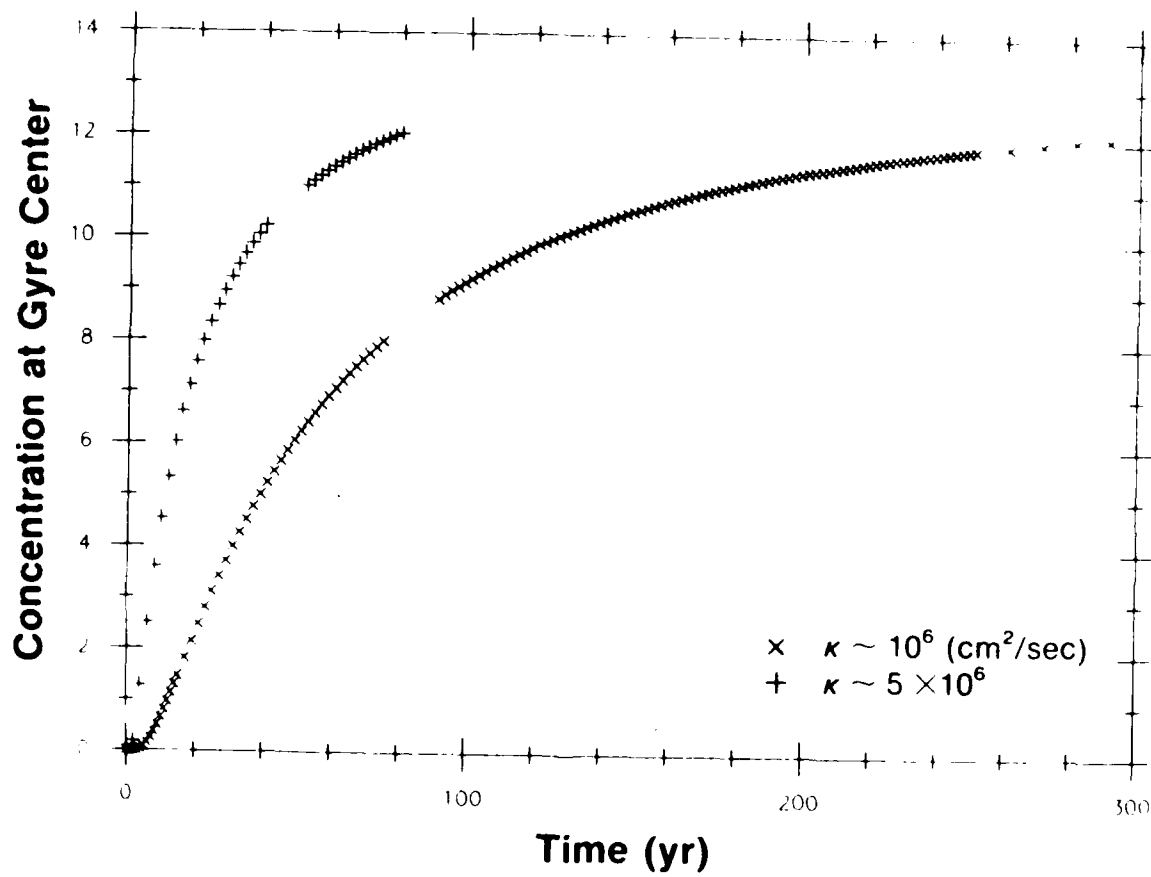


Figure 2.5: Time history of tracer accumulating at the center of the gyre for two different diffusivities.

(The equation here is written in its area form rather than in terms of radial distance.)

This problem was solved by Young (personal communication), the solution being

$$\theta(A, t) = \theta_0 + (e^{-\frac{t}{\tau_G}}) J_0 \left( 2 \sqrt{\frac{A}{\tau}} \frac{1}{4\pi\kappa} \right),$$

where  $\theta_0$  = homogenized value,

$\tau_G$  = spin up time,

and  $J_0$  = zeroth order Bessel function.

The expression for the e-folding time  $\tau_G$  is,

$$\tau_G = \frac{(.05)A_0}{\kappa}.$$

In our case the gyre is not circular but elliptical, so  $A_0 = \pi L_z L_M$ ,  $L_z$  and  $L_M$  being the zonal and meridional scales of the domain. Also, because the distance between streamlines varies around the gyre (which influences the cross-stream gradients),  $\kappa$  is replaced by an effective diffusivity  $\kappa_e$ . The details of why this is so are given in Rhines and Young (1983). In that work they show that the elliptical analog to (2.3) is

$$\theta_t = \kappa \frac{\partial}{\partial A} \left( D \frac{\partial \theta}{\partial A} \right), \quad (2.4)$$

where  $A$  = area within a streamline defined by  $\psi = \text{constant}$ ,

$$D = \Gamma \frac{dA}{d\psi},$$

$$\Gamma = \iint_A v^2 \psi dA = \text{circulation around a streamline.}$$

The example that they solve is an elliptical solid body flow defined by the streamfunction

$$\psi = \psi_0 \left( \frac{x^2}{L_x^2} + \frac{y^2}{L_y^2} \right),$$

$\psi_0$  being the amplitude of the flow,  $L_x$  and  $L_y$  the  $x$  and  $y$  length scales. For the gyre that we are considering, (1.11), it turns out that the expression for  $D$  is exactly the same as for the solid body case,

$$D = 2\pi \left( \frac{L_x^2 + L_y^2}{L_x L_y} \right) A .$$

With this, (2.4) becomes

$$\theta_t = \left[ \frac{L_x^2 + L_y^2}{L_x L_y} \kappa \right] \frac{\partial}{\partial A} (4\pi A \frac{\partial \theta}{\partial A}) . \quad (2.5)$$

Rhines and Young call the quantity in brackets the effective diffusivity  $\kappa_e$ , as (2.5) is just (2.3) with  $\kappa$  replaced by  $\kappa_e$ .

The expression then for the diffusive time of the elliptical gyre of the model is

$$\tau_G = \frac{L_z L_M}{\kappa} \left[ .42 \frac{L_x L_y}{L_x^2 + L_y^2} \right] . \quad (2.6)$$

(The term inside the brackets represents the deviation from the simple scale analysis estimate.)

The scales  $L_z$  and  $L_M$  define the size of the domain in question, so the pair of them take on different values for the two examples being considered, as the homogenized region is smaller for larger  $\kappa$ . In  $\kappa_1$ , homogenization occurs to roughly the  $\psi = 16$  streamline, while in  $\kappa_5$  only to the  $\psi = 9$  streamline (Figure 1.17). Substituting the appropriate values into (2.6) gives a diffusive time of 5 years for  $\kappa_1$  and .5 years for  $\kappa_5$ . Comparing these values to the actual times we see that in the first case spin up is 15 times longer than the diffusive time of the gyre, and in the second case it is 50 times longer.

In light of the character of the spin up process that occurs in the model, this result is not surprising. It is evident, since the level throughout the gyre rises uniformly, that the rate of spin up is being controlled by

the diffusion of tracer from the boundary current (i.e. it takes little time for tracer to diffuse throughout the gyre once it reaches the edge). In order to quantify this idea, as well as understand what factors dictate the level of the homogeneous pool, a simple analytical model is examined below.

### Diffusive Transfer Model

It is instructive to consider the domain of the numerical model as being composed of several subregions. The motivation behind this is to consider regions which can only communicate with one another diffusively, so as to create a simplified, coarsely resolved system with one less degree of freedom (i.e. no advection). The idea is that in the strongly advective limit of the numerical model it is the slow diffusive processes which regulate the spin up and dictate the net transfer of properties into the interior. In conjunction with the simplified domain we consider a simplified spin up process. We assume that the plume of tracer which penetrates the gyre immediately conforms to a streamline, i.e. that the advective limit applies everywhere in the gyre (which implies homogenization, as discussed in chapter one).

The four regions that are considered are depicted in Figure 2.6. The first region corresponds to the boundary current. Advection from the northern source fills this region quickly and continually acts to maintain the amount of tracer so contained within it. The second region is the outer strip of the gyre (subsequently referred to as the edge of the gyre). Tracer diffuses into this region from the boundary current, and quickly gets pulled around the circuit forming a ridge. From here the tracer proceeds to spread laterally, diffusing inward to the center portion of the gyre (the third region) and diffusing outward to the vast area surrounding the gyre (the fourth region).

We call this model the diffusive transfer model. Each of the subregions of the domain is represented by a single value of concentration, and the diffusive transfer between them is characterized by a set of time scales which represents the amount of time it takes tracer to diffuse from one region to another. The exchange occurs such that the strength of the flux is proportional to the difference in concentration. (Note that the regions

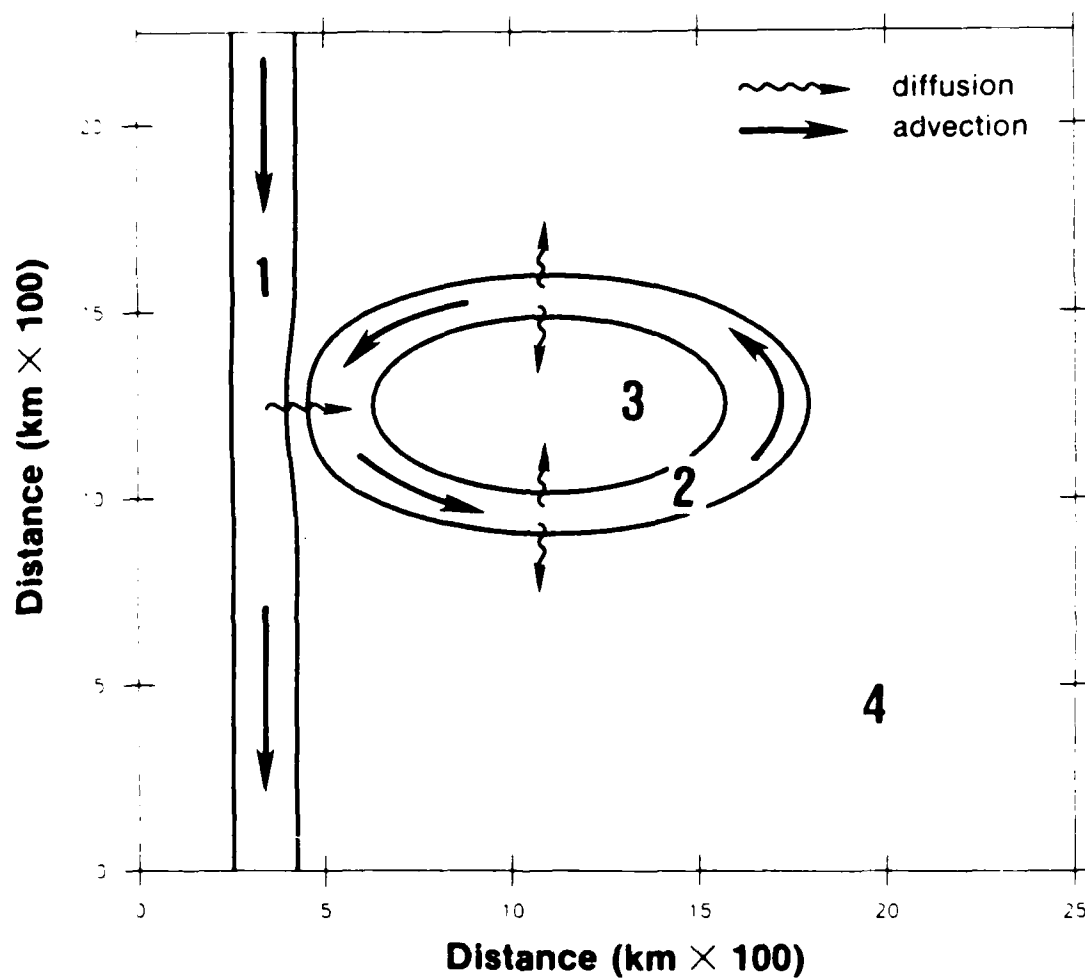


Figure 2.6: Domain of the diffusive transfer model consisting of four regions. Tracer passes into adjacent regions by way of diffusion only.

expressed as such do not have "sizes"; this information is contained within the time scales.) Because of the strong advective input into the boundary current region, its value is fixed throughout the spin up. Also, we take the fourth region to be an infinitely large background reservoir whose value cannot be altered and so is set equal to zero. As such then there are only two active regions in the model, those which comprise the gyre. The governing equations for the gyre edge and gyre center are

$$\frac{d\phi_e}{dt} = \frac{(\phi - \phi_e)}{\tau_B} + \frac{(\phi_c - \phi_e)}{\tau_G} + \frac{(0 - \phi_e)}{\tau_R} \quad (2.7)$$

$$\frac{d\phi_c}{dt} = \frac{(\phi_e - \phi_c)}{\tau_G}$$

where  $\phi_e$  = concentration of gyre edge,  
 $\phi_c$  = concentration of gyre center,  
 $\phi$  = concentration of boundary current region,  
 $\tau_B$  = boundary time scale (diffusion between boundary current and gyre edge),  
 $\tau_G$  = gyre time scale (diffusion between gyre edge and center),  
 $\tau_R$  = reservoir time scale (diffusion between gyre edge and background reservoir).

The initial conditions are that the entire gyre is free of tracer, i.e.  $\phi_c = \phi_e = 0$  at  $t = 0$ .

The system (2.7) is a pair of ordinary first order linear differential equations which is solved straightforwardly using the operator method (Zill, 1979). It is convenient to express the results in terms of the nondimensional parameters representing the relative sizes of the three diffusive time scales,

$$\Delta_{GB} = \frac{\tau_G}{\tau_B}, \quad \Delta_{GR} = \frac{\tau_G}{\tau_R}, \quad \Delta_{BR} = \frac{\Delta_{GR}}{\Delta_{GB}} = \frac{\tau_B}{\tau_R}.$$

It is not obvious a priori what the magnitudes of these parameters are. However, the results of the numerical model can be used to constrain them.



The solutions for  $\phi_e$  and  $\phi_c$  are of the form

$$\phi(t) = \phi_0 + \phi_1 e^{-\frac{t}{\tau_1}} + \phi_2 e^{-\frac{t}{\tau_2}} \quad (2.8)$$

where  $\phi_0$  is the steady state value and the other two terms are transients. Of the transients, the slower mode ( $\tau_2$ ) dictates the spin up of the system. We define the spin up time then as  $\tau \equiv \tau_2$ . In terms of the nondimensional parameters,

$$\tau = S(\Delta_{GB}, \Delta_{GR}) \tau_G, \quad (2.9)$$

$$S(\Delta_{GB}, \Delta_{GR}) = \frac{1}{1 + \frac{\Delta_{GB}}{2} + \frac{\Delta_{GR}}{2} - \frac{1}{2} \sqrt{\Delta_{GB}^2 + \Delta_{GR}^2 + 2\Delta_{GB}\Delta_{GR} + 4}}.$$

The function  $S$  measures how long the spin up is compared with the diffusive time of the gyre. Recall that the time scale over which homogenization occurs in the numerical model is many times greater than the diffusive time of the gyre ( $\tau \gg \tau_G$ ) due to the fact that spin up is controlled by the diffusion of tracer from the boundary. This (by the definition of  $\Delta_{GB}$ ) implies that  $\Delta_{GB} \ll 1$ . Consider now the effect that varying  $\Delta_{GR}$  has on the value of  $S$  (keeping  $\Delta_{GB} \ll 1$ ).

1.  $\Delta_{GR} \equiv 0$  ( $\tau_R \gg \infty$ ).

This condition corresponds to the case when there is no background reservoir (as if there were an insulating boundary around the gyre). When  $\Delta_{GB} > 0$  (2.9) implies that  $S \gg \infty$ . However, with no reservoir it is evident that in steady state the gyre will equilibrate to the value of the boundary current region, which is not the case (Figure 1.17).

2.  $\Delta_{GR} \sim 1$  ( $\tau_G \sim \tau_R$ ).

This says that as tracer progresses around the edge of the gyre it just as readily diffuses inward as outward. In this case as  $\Delta_{GB} > 0$  the

function  $S > 2.6$ , i.e. spin up can at most be roughly two and a half times longer than the diffusive time of the gyre. However, in  $\kappa_1 \tau \sim 15 \tau_G$  and in  $\kappa_5 \tau \sim 50 \tau_G$ , so this case is unacceptable as well.

The reason for the difference in the limiting value of  $S$  for the two cases can be understood as follows. When there is no background a large amount of tracer must accumulate in the gyre ( $\phi_C > \phi$ ) so it takes a long time. However, when the reservoir is characterized by  $\Delta_{GR} \sim 1$ , the corresponding condition that  $\Delta_{GB} > 0$  implies that  $\tau_R$  is small, i.e. there is strong diffusion into the reservoir. This together with the fact that the reservoir concentration is maintained at zero (by definition) means that this region acts as a strong sink. Thus only a small amount of tracer accumulates in the gyre ( $\phi_C \ll \phi$ ) and so spin up does not take as long. Note that in the extreme limit no tracer accumulates in the gyre, which also means this case is unacceptable.

3.  $\Delta_{GR} \gg 1$  ( $\tau_G \gg \tau_R$ ).

This condition leads to the same problems as in case 2, as diffusion into the reservoir is now even stronger.

We see then that the condition imposed by the spin up implies that both  $\Delta_{GB} \ll 1$  and  $\Delta_{GR} \ll 1$ . However it tells us nothing about the relative magnitudes of these two parameters. For this information we examine another result of the numerical model, that regarding the level of tracer in the gyre. In (2.8) the expression for  $\phi_0$  for the center of the gyre is

$$\phi_{0_C} = P(\Delta_{BR})\phi = \phi_C(t \rightarrow \infty) , \quad (2.10)$$

$$P(\Delta_{BR}) = \left( \frac{1}{1 + \Delta_{BR}} \right) .$$

The function  $P$  represents the fraction of the boundary input value that the gyre equilibrates to. Note that  $P$  depends only on  $\Delta_{BR}$ , which measures the relative importance of  $\Delta_{GB}$  and  $\Delta_{GR}$ . We saw earlier that the level of the homogeneous pool in the numerical model was independent of diffusivity. In terms of the diffusive transfer model this suggests that  $\phi_{0_C}$  not depend

on any of the diffusive time scales. For this to be so  $\Delta_{BR}$  must take on the same value in each example. To determine this value we can match (2.10) to the level of the homogenized pool.

In order to do this we have to relate the boundary value  $\phi$  to an appropriate quantity in the numerical model. Note that the set up of the transfer model is such that  $\phi$  is independent of diffusivity as well. Since the total amount of tracer in the boundary current region varies with the size of  $\kappa$  (Figure 1.17) we take the peak value of the input at the northern boundary as the value for  $\phi$ . (The transfer is based on the presumption that the system is strongly advective. In the extreme advective limit the entire boundary current would equilibrate to the input distribution, in which case it is evident that the peak value of the Gaussian would be the correct choice.)

The homogenized level of the gyre is approximately equal to one half the peak value of the input (Figure 1.17) which implies then that  $\Delta_{BR} \sim 1$ . This condition in turn says that, in each case, the time scale in which the edge of the gyre equilibrates to the boundary value is also the time scale in which the edge of the gyre decays into the background reservoir. It is not obvious why this is so, but the following simple argument suggests that this is the case.

Consider the circular domain in Figure 2.7, which is meant to represent the edge of the gyre. The outer perimeter is divided into two parts: the section in contact with the boundary and that in contact with the background reservoir. It is assumed that the advection serves only to stir up the tracer such that the concentration  $\theta$  varies only in the radial direction. The governing equation is the radially symmetric diffusion equation (2.3) (written in radial form)

$$\frac{\partial \theta}{\partial t} = \frac{\kappa}{r} \frac{\partial}{\partial r} \left( r \frac{\partial \theta}{\partial r} \right) . \quad (2.11)$$

Integrating over the area of the edge,  $A_e$ ,

$$\frac{\partial \bar{\theta}}{\partial t} = \frac{\kappa}{A_e} \int_{\lambda_1}^{\lambda_2} \int_{r_1}^{r_2} d\lambda dr \frac{\partial}{\partial r} \left( r \frac{\partial \theta}{\partial r} \right) + \frac{\kappa}{A_e} \int_{-(2\pi-\lambda_2)}^{\lambda_1} \int_{r_1}^{r_2} d\lambda dr \frac{\partial}{\partial r} \left( r \frac{\partial \theta}{\partial r} \right) \quad (2.12)$$

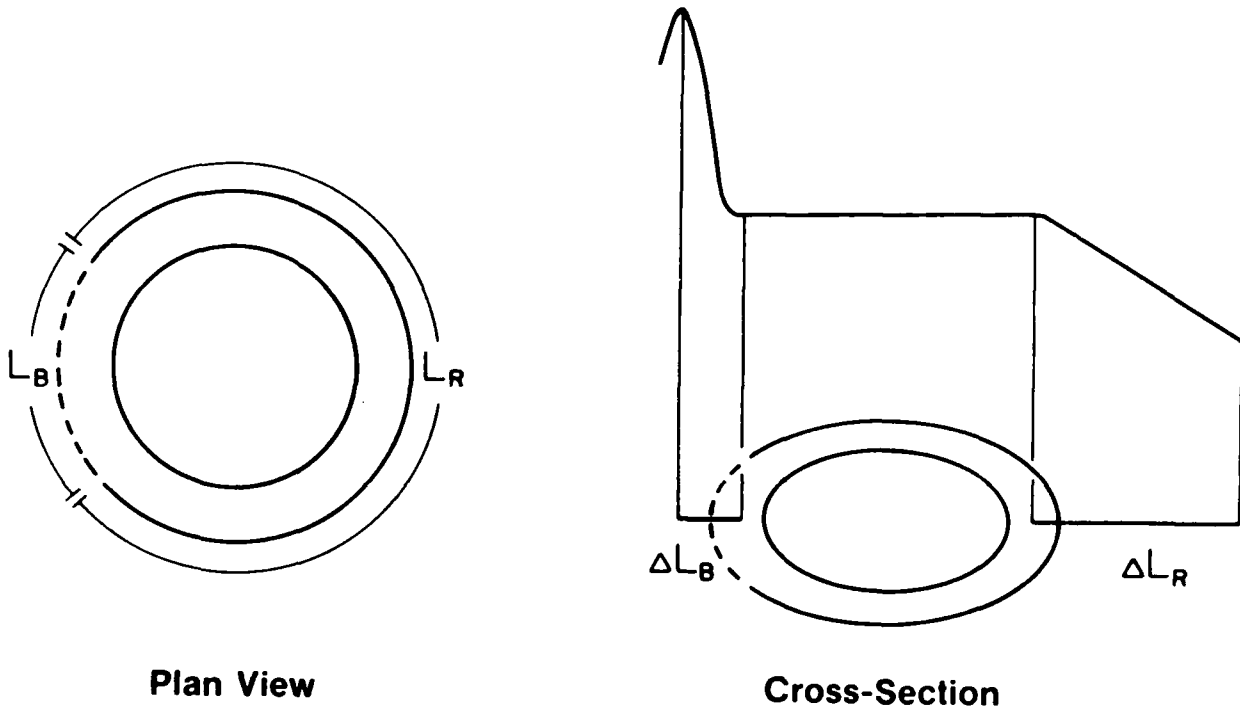


Figure 2.7: A simplified representation of diffusion into and out of the edge of the gyre. A strong flux of tracer into the edge occurs across the dashed border and a weak flux out of the edge across the solid border.

where the bar denotes the average over  $A_e$ . The first term on the right hand side is the contribution associated with the boundary and the second is that associated with the reservoir ( $\lambda$  is the azimuthal coordinate). From (2.12) it follows that

$$\frac{\partial \bar{\theta}}{\partial t} = \left[ \frac{\kappa L_B}{A_e} \frac{\partial \theta}{\partial r}(r_2) - \frac{\kappa(\lambda_2 - \lambda_1)r_1}{A_e} \frac{\partial \theta}{\partial r}(r_1) \right] + \left[ \frac{\kappa L_R}{A_e} \frac{\partial \theta}{\partial r}(r_2) - \frac{\kappa(2\pi - (\lambda_2 - \lambda_1))r_1}{A_e} \frac{\partial \theta}{\partial r}(r_1) \right] \quad (2.13)$$

where  $L_B$  and  $L_R$  are the arc lengths of the boundary and reservoir sections respectively.

The expressions inside the brackets represent the flux of tracer into and out of the edge of the gyre in the two regions. In line with the transfer model we approximate the gradients in a finite-difference sense. In particular, where the gyre is adjacent to the boundary

$$\frac{\partial \theta}{\partial r}(r_2) \sim \frac{\Delta \theta_B}{\Delta L_B},$$

and where it borders the reservoir

$$\frac{\partial \theta}{\partial r}(r_2) \sim \frac{\Delta \theta_R}{\Delta L_R},$$

where  $\Delta \theta_B, \Delta \theta_R$  = typical change in concentration from boundary to edge, edge to reservoir,

$\Delta L_B, \Delta L_R$  = boundary, reservoir length scales associated with  $\Delta \theta_B, \Delta \theta_R$  (Figure 2.7).

With the approximations, (2.13) becomes

$$\frac{\partial \bar{\theta}}{\partial t} = \left( \frac{\kappa L_B}{A_e \Delta L_B} \right) \Delta \theta_B + \left( \frac{\kappa L_R}{A_e \Delta L_R} \right) \Delta \theta_R - \frac{2\pi \kappa r_1}{A_e} \frac{\partial \theta}{\partial r}(r_1), \quad (2.14)$$

from which it is evident that

$$\tau_B = \frac{A_e}{\kappa} \left( \frac{\Delta L_B}{L_B} \right), \quad (2.15a)$$

$$\tau_R = \frac{A_e}{\kappa} \left( \frac{\Delta L_R}{L_R} \right), \quad (2.15b)$$

$$\text{which then gives } \Delta_{BR} = \left( \frac{\Delta L_B}{\Delta L_R} \right) \left( \frac{L_R}{L_B} \right). \quad (2.16)$$

As seen in Figure 1.17, the gradient off the boundary is much steeper than the gradient from the gyre to the reservoir. However this is compensated for in (2.16) by the fact that most of the gyre borders the reservoir. Using the steady state distributions to estimate  $\Delta L_B$  and  $\Delta L_R$  (and the streamline pattern to compute  $L_B$  and  $L_R$ ) this results in an estimate for  $\Delta_{BR}$  of .8 in  $\kappa_1$  and 1.2 in  $\kappa_5$ .

Consideration of the functions  $S$  and  $P$  thus results in the following ordering of the diffusive time scales,

$$\tau_G \ll \tau_B \sim \tau_R. \quad (2.17)$$

To simplify the transfer model we set  $\Delta_{BR}$  equal to the constant value of one ( $\tau_B = \tau_R$ ) which in effect leaves us with a single non-dimensional parameter

$$\Delta \equiv \frac{\tau_G}{\tau_B}. \quad (2.18)$$

The expressions (2.9) and (2.10) simplify to

$$S(\Delta) = \frac{1}{1 + \Delta - \sqrt{\Delta^2 + 1}}, \quad (2.19a)$$

$$P = \frac{1}{2}. \quad (2.19b)$$

The parameter  $\Delta$  expresses the relative strengths of the two fundamental time scales of the system. We can now quantitatively explain how diffusion from the boundary controls the spin up. As depicted in Figure 2.8 when  $\Delta > 0$ ,  $\tau > \tau_B$  and the system spins up on the boundary time scale

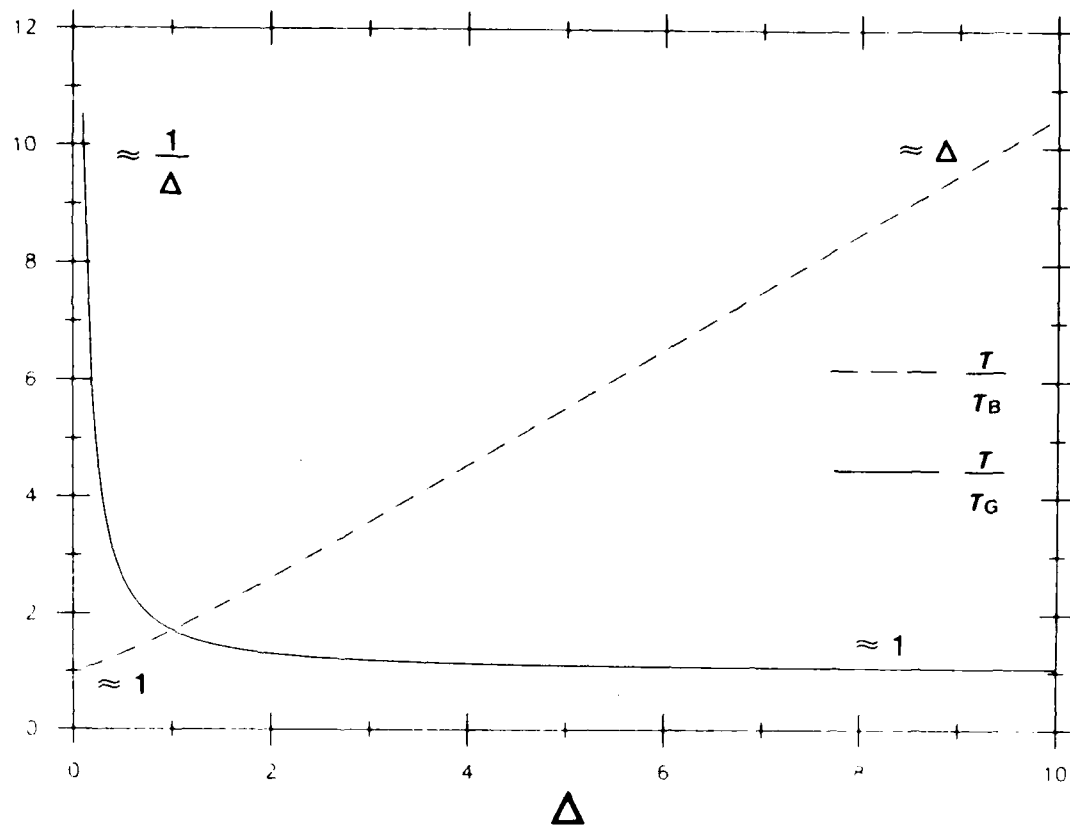


Figure 2.8: The relationship of the transfer model spin-up time to the boundary time scale and gyre time scale. The solid line is the function  $S$ , the dashed line  $\Delta \cdot S$ .

(once tracer diffuses from the boundary to the edge of the gyre it quickly spreads into the center). This is the case in the numerical model. On the other hand, when  $\Delta \gg \infty$ ,  $\tau > \tau_G$  which corresponds to the Rhines and Young example in which spin up occurs on the gyre time scale. In this case the edge of the gyre becomes equilibrated quickly, and tracer then proceeds to diffuse into the center. By matching (2.19a) to the numerical simulations using the gyre diffusive times estimated earlier for the  $\kappa_1$  and  $\kappa_5$  examples, we determine  $\Delta_1$  and  $\Delta_5$  such that the value of  $S(\Delta) \tau_G$  matches the associated  $\tau$ . (The magnitude of  $\Delta$  is determined in this fashion rather than from the definition (2.18) because it is uncertain what value of  $A_e$  to use in (2.15a).) With this information then we can use the diffusive transfer model to predict the amount of tracer at the center of the gyre in the numerical model as a function of time.

It was discussed above that both  $\phi_c$  and  $\phi_e$  are sums of a steady term and two transient modes. It is the case that in the small  $\Delta$  limit which applies here the faster transient decays so quickly relative to the slower one that it can be ignored. Consider the function  $R1(\Delta)$ , defined as the ratio of the time scales of the two transient modes in (2.8),

$$R1(\Delta) \equiv \left| \frac{\tau_2}{\tau_1} \right| = \frac{\Delta + 1 + \sqrt{\Delta^2 + 1}}{\Delta + 1 - \sqrt{\Delta^2 + 1}}.$$

This measures the relative importance of the two modes. The graph of  $R1$  versus  $\Delta$  is plotted in Figure 2.9 and for  $\Delta > 0$ ,  $R1 > \infty$  ( $R1 \approx \frac{2}{\Delta}$ ). Note also that when  $\Delta \gg \infty$  the same mode still dominates ( $R1 \approx 2\Delta$ ). The smallest amount of discrepancy between the decay time of the two modes occurs when  $\Delta \sim 1$  and  $\tau_2 \sim 5 \tau_1$ .

This means that in the  $\Delta \ll 1$  limit the time dependent part of  $\phi_c$  (and  $\phi_e$ ) is approximately a single exponential, and suggests that we redraw Figure 2.5 and normalize the time axis by the appropriate spin up times of the two examples. This is done in Figure 2.10. Also shown in the figure are the corresponding  $\phi_c$  curves from the diffusive transfer model, normalized in a similar fashion. Note that the  $\kappa_1$  and  $\kappa_5$  examples collapse to a single case. They agree reasonably well with the predictions. (Keep in mind



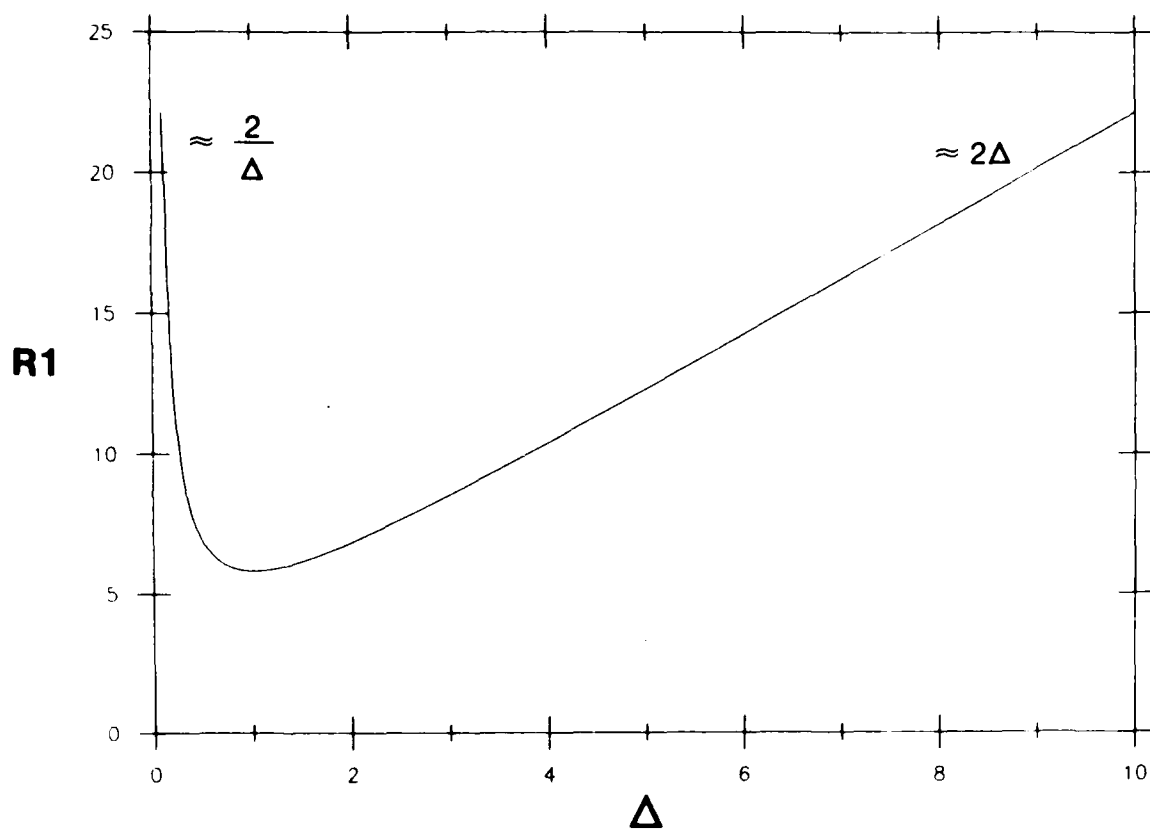


Figure 2.9: The relative decay of the two transient modes of the transfer model solutions. The faster mode can be ignored for both large and small values of  $\Delta$ .

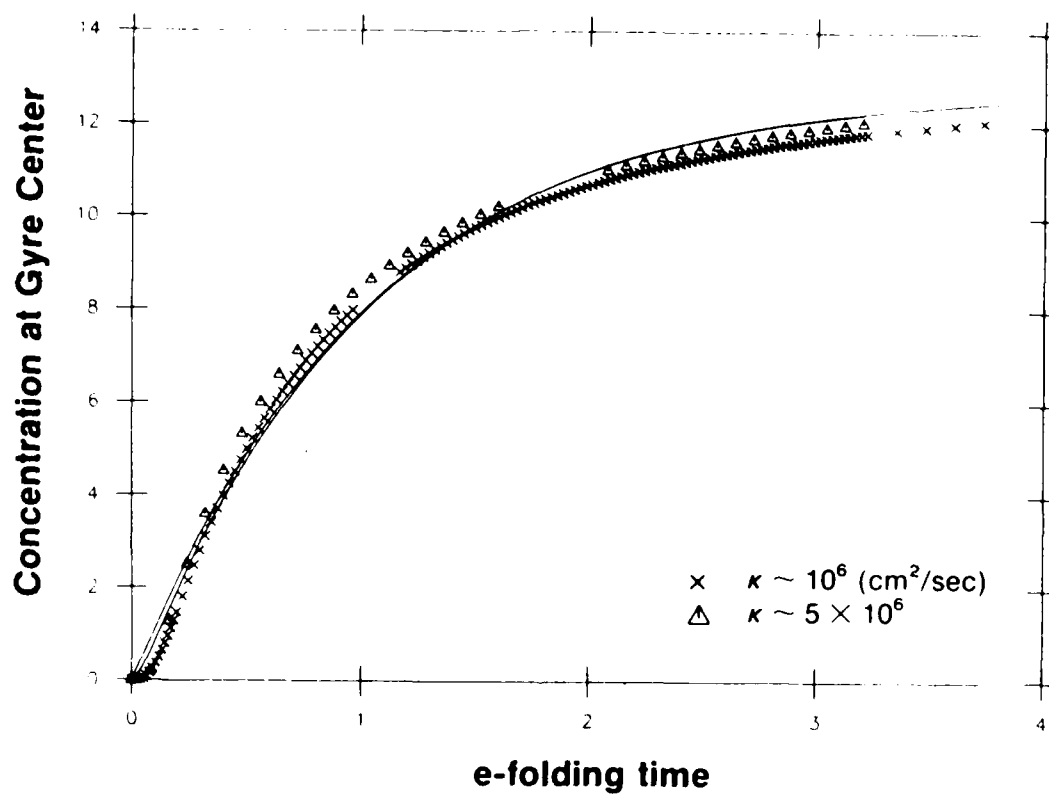


Figure 2.10: The accumulation curves of Figure 2.5 only the time axis has been normalized for each curve by the associated spin-up time. The solid lines are the predictions for the gyre center of the transfer model.

that the transfer model is a crude simplification, meant only to reveal some of the prominent diffusive processes at work.) Not shown in the figure are the associated  $\phi_e$  curves which closely resemble those for the gyre center. This is consistent with the numerical result that the level of tracer throughout the whole gyre rises at nearly the same rate (as  $t \rightarrow \infty$ ,  $\phi_e \rightarrow \phi_c$  and complete homogenization is achieved).

#### B) With Vertical Flux

We now consider the presence of vertical mixing and explore how this modifies the various results that have been obtained thus far. This corresponds to the oxygen case, and in the numerical model we now include the radioactive decay term in (2.2). The boundary conditions are identical to those in the salt case as we take  $\theta_u = \theta_L = 0$  (i.e. the vertical anomaly is just equal to the concentration in the center of the layer). Two different simulations were done, one with  $\nu = 1 \text{ cm}^2/\text{sec}$ ,  $H = 1000 \text{ m}$  and the other with  $\nu = 2 \text{ cm}^2/\text{sec}$ ,  $H = 750 \text{ m}$ . These will be referred to as  $\nu_1$  and  $\nu_2$  respectively (in both cases  $\kappa = 10^6 \text{ cm}^2/\text{sec}$ ).

Figure 2.11 shows a snapshot of the spin up of  $\nu_1$ . The first thing to notice is that it would be very difficult to distinguish between this distribution and a similar snapshot from the salt case (i.e. from the spin up of  $\kappa_1$ ). The plume of tracer extends from the boundary and spirals into the gyre in the same manner. A marked difference between the salt and oxygen cases occurs only in the context of steady state. The steady state distribution of the  $\nu_2$  experiment appears in Figure 2.12a, this is to be compared with Figure 1.17a for which the vertical flux is zero. The most striking thing in regards to such a comparison is that the level of tracer in the gyre in the non-zero vertical flux case is substantially smaller. This difference is highlighted in Figure 2.12b showing the accumulation of tracer in the gyre for the two cases. The reason for this discrepancy is straightforward in that for oxygen there is an additional mechanism present for removing tracer from the domain (this is also the cause for the decrease in time required for spin up).

Let us contrast the spin up of  $\nu_2$  to that of  $\kappa_1$ . The concentration of tracer in the boundary current is nearly identical to that when there is

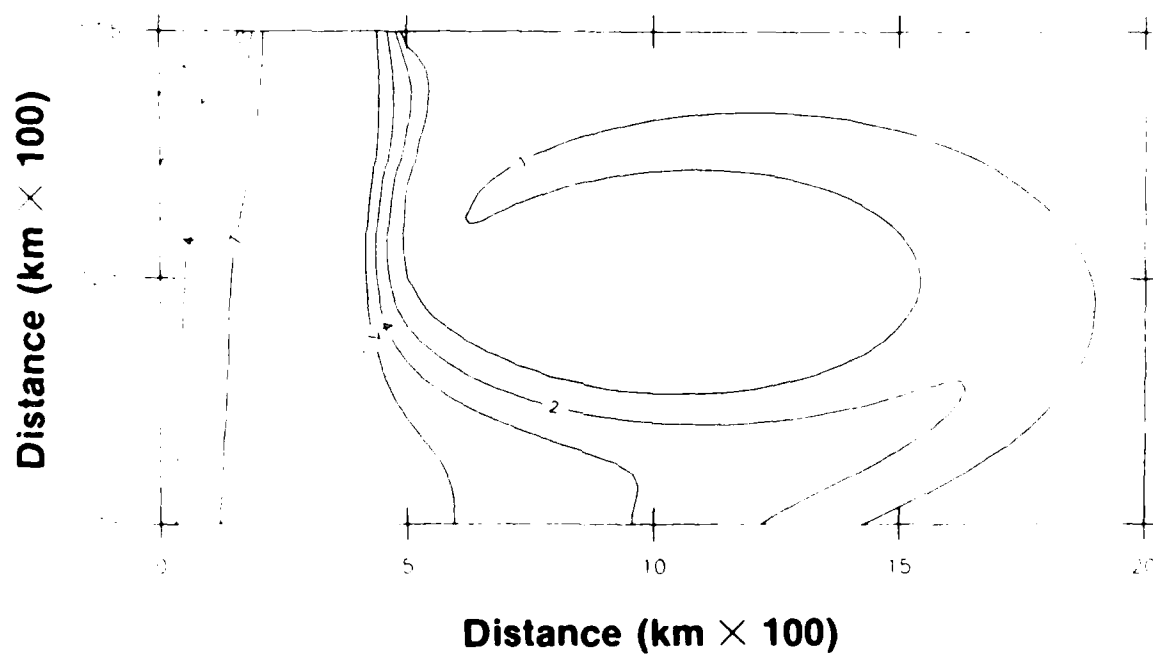


Figure 2.11: Instantaneous distribution of tracer during spin-up, for experiment  $v_1$  which includes vertical mixing.

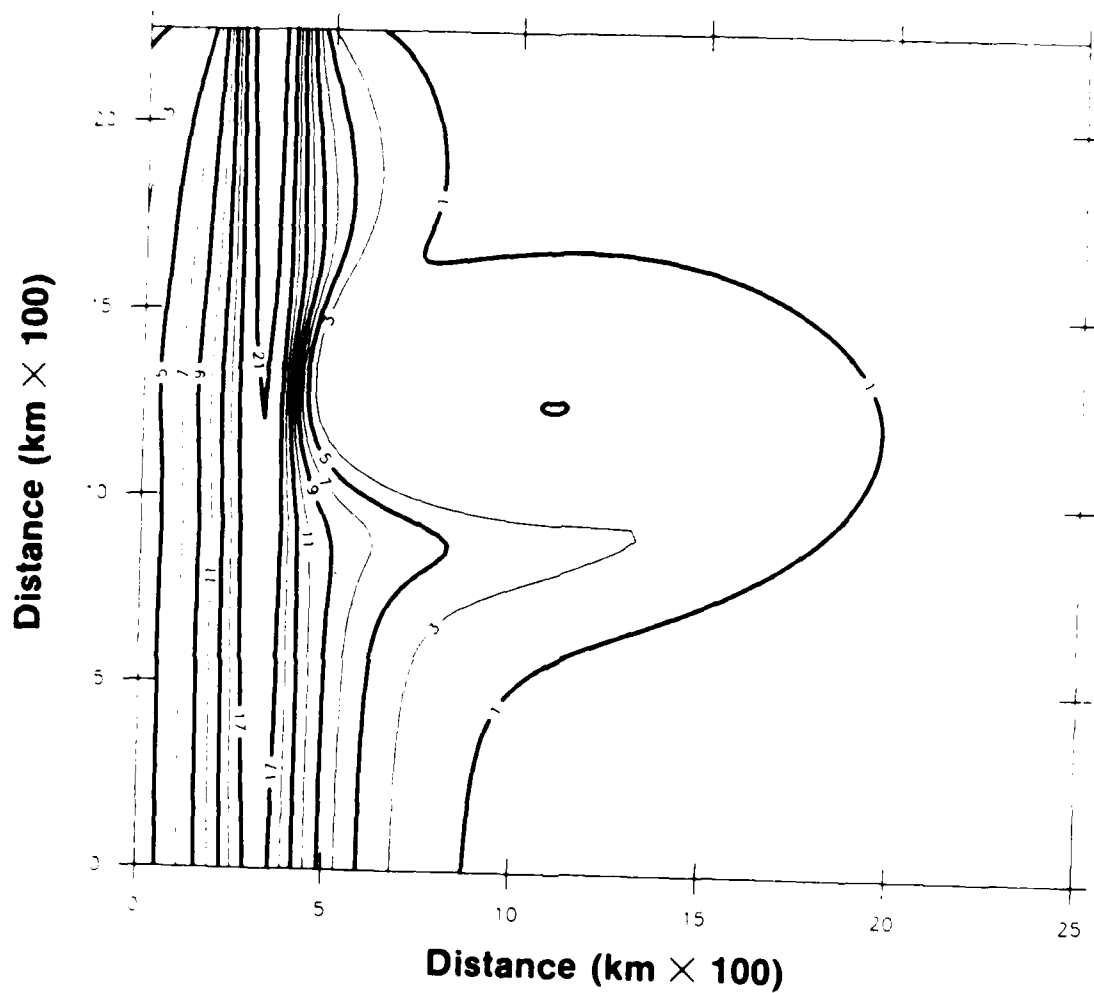
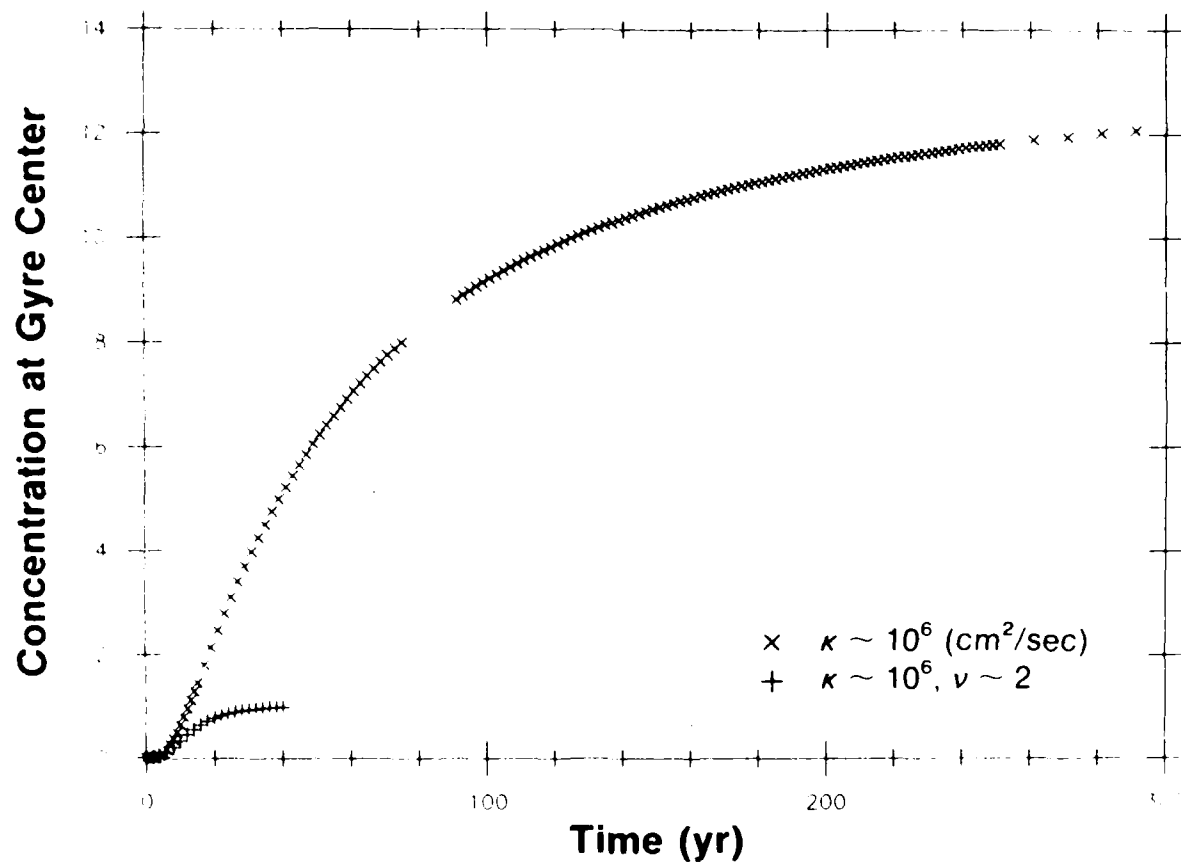


Figure 2.12: (a) Steady state distribution of tracer for  $\kappa \sim 10^6 \text{ cm}^2/\text{sec}$  with the addition of vertical mixing in which  $\nu \sim 2 \text{ cm}^2/\text{sec}$ .



(b) Time history of tracer accumulating at the center of the gyre for  $10^6 \text{ cm}^2\text{/sec}$  comparing the case with no vertical mixing to that with  $2 \text{ cm}^2\text{/sec}$ .

AD-A182 341

THE ENTRAINMENT AND HOMOGENIZATION OF TRACERS WITHIN  
THE CYCLONIC GULF ST. (U) WOODS HOLE OCEANOGRAPHIC  
INSTITUTION MA R 5 PICKART MAY 87 WHOI-87-9

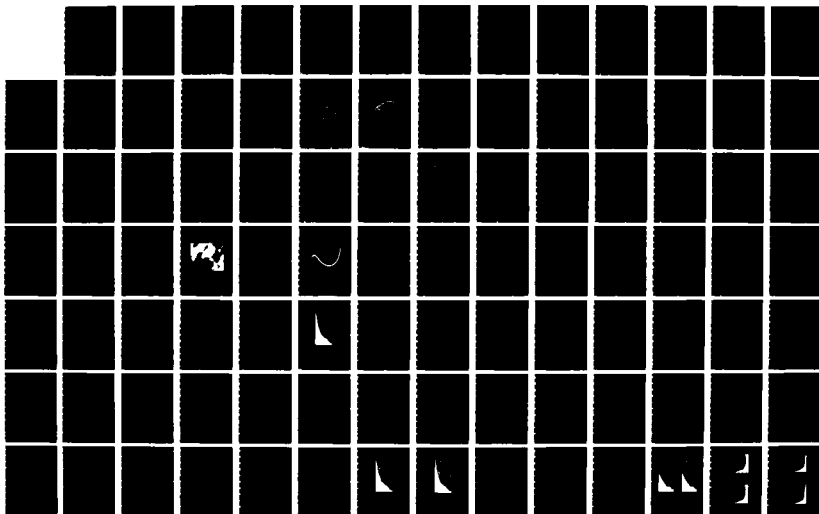
2/3

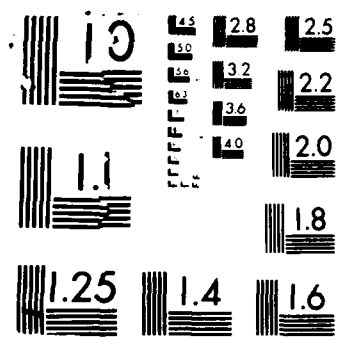
UNCLASSIFIED

N88014-76-C-0197

F/G 8/3

NL







no vertical flux. This is because the strong flow of the current does not allow the fluid to spend enough time in this region to be significantly influenced by vertical mixing. It is while the tracer diffuses laterally from the boundary that vertical exchange becomes prominent, acting as a sink. The small amount of tracer that does penetrate into the gyre does so in the same fashion as in  $\kappa_1$ . As steady state is approached though, whereas in  $\kappa_1$  the plume extending from the boundary becomes much less pronounced, here it remains prominent. Along with this, the slight bowl shaped tracer distribution in the gyre gives way to homogenization in  $\kappa_1$  but remains a permanent feature in  $v_2$  (Figure 2.13).

At steady state there can be no net flux of tracer into the region bounded by a streamline of the gyre. In  $\kappa_1$  this is accomplished in the center part of the gyre through homogenization. In the outer part, the remnant of the spiral weakly pumps tracer inward in the southern and eastern regions, and outward to the north and west. In the oxygen case there is a persistent vertical flux out of the region bounded by a streamline (true for every streamline) which must be balanced by an inward lateral flux. One way to view why the plume of salt is less pronounced than that for oxygen at steady state is to recall that each successive plume leaving the boundary current does so from further downstream. This tends to smear the intrusion as time progresses. For oxygen though spin up occurs more quickly so that this effect is not at work for as long.

It is interesting that in  $v_2$ , which contains a rather large vertical diffusion parameter  $\frac{8v}{H^2}$ , the penetration of tracer into the gyre so closely resembles that which occurs in  $\kappa_1$  (which has no vertical flux). This is due to the fact that so little tracer enters the gyre that the vertical anomaly is small, hence weak flux. Consider the steady state balance of terms in (2.2) that applies in the northward flow of the outer part of the gyre in  $v_2$ ,

$$v \frac{\partial \theta}{\partial y} \sim \kappa \frac{\partial^2 \theta}{\partial x^2} - \frac{8v}{H^2} \theta, \quad (2.20)$$

where it is assumed that alongstream diffusion is negligible with respect to cross-stream diffusion. In this region the spiral is significant (recall

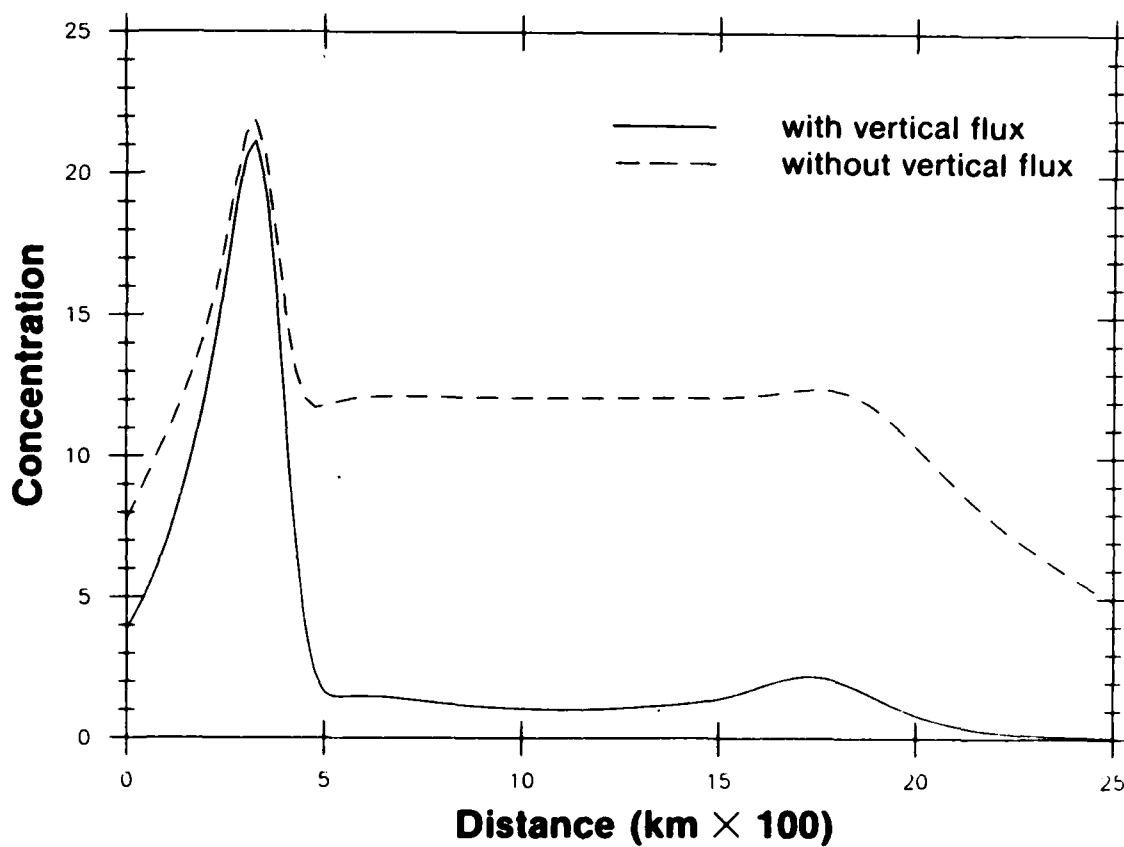


Figure 2.13: Zonal section of tracer through the boundary current and center of the gyre for the steady state distributions of Figure 1.17a ( $\kappa \sim 10^6 \text{ cm}^2/\text{sec}$ ) and 2.12a ( $\kappa \sim 10^6 \text{ cm}^2/\text{sec}$ ,  $\nu \sim 2 \text{ cm}^2/\text{sec}$ ) illustrating the effects of vertical mixing.

that in the example analyzed in chapter one  $\kappa \sim 10^6 \text{ cm}^2/\text{sec}$  as it is in  $v_2$ ) so that the cross-stream length scale is  $\sim L_{cm}$ . The size of the terms in (2.20) are then estimated as follows,

$$\frac{V}{L_{cm}} \sim \frac{\kappa}{L_a^2} - \frac{8v}{H^2} , \quad (2.21)$$

where  $V$  = representative velocity

$L_a$  = alongstream length scale.

Plugging in values for the scales from  $v_2$  it is found that the first two terms of (2.21) balance each other to within 5 percent, which is the same balance that characterized the spiral in the salt case.

This result has an interesting consequence. It says that a point balance in this region is one of advection versus lateral diffusion. From knowledge of the various scales then we can produce an estimate of the lateral diffusivity,

$$\kappa \sim \frac{VL_a^2}{L_{cm}} . \quad (2.22)$$

However, we know that in terms of an integrated balance within a streamline that the lateral flux of tracer inward balances the vertical flux outward (the contribution from advection identically vanishes). In particular, integrating the steady form of (2.2) within a streamline and applying the divergence theorem gives,

$$\frac{8v}{H^2} \iint_A \phi dA = \kappa \oint_S \frac{\partial \phi}{\partial n} ds , \quad (2.23)$$

where  $A$  = area enclosed within the streamline  $S$ ,

$n$  = normal to the streamline.

Having estimated  $\kappa$  then from (2.22), we can in turn use this value in (2.23) to determine  $v$ ,

$$v = \frac{\kappa \oint_S \frac{\partial \theta}{\partial n} ds}{\frac{8}{H^2} \iint_A \theta dA} \quad (2.24)$$

This procedure was applied to the  $v_2$  experiment to try and recover the values of lateral and vertical diffusivity from knowledge of the steady state tracer field and the velocity field. The values so obtained were  $\kappa \sim 1.6 \times 10^6 \text{ cm}^2/\text{sec}$ ,  $v \sim 2.3 \text{ cm}^2/\text{sec}$  (actual values in  $v_2$  were  $1.0 \times 10^6 \text{ cm}^2/\text{sec}$  and  $2.0 \text{ cm}^2/\text{sec}$ , respectively).

#### Transfer Model with Vertical Flux

The diffusive transfer model can also be modified to include the effects of vertical diffusion. The areas directly above and below the deep layer (represented by  $\theta_u$  and  $\theta_l$  in the numerical model) can be thought of as together forming another subregion of the domain, consistent with the premise of the model that this region be in contact diffusively with adjacent regions. The reasons for considering this additional case are the same as before, to help more fully understand the numerical model results by gaining insight into how the various diffusive processes interact, which in turn will be useful when considering the actual oceanic case. For instance, we saw that the addition of vertical flux influenced spin up times, as well as the amount and distribution of tracer in the gyre. It is desirable to quantify these effects.

The specifics of the expanded transfer model are as follows. The additional region is in contact with only two of the previous ones, those comprising the gyre (i.e. the edge and center). The reason why it is not in contact with the boundary current region is that we assume the tracer flushes through this region too quickly to be altered by vertical diffusion. It is not in contact with the background reservoir for the trivial reason that the reservoir is void of tracer. Because the new region represents a vast area as well, it too is assumed to be a reservoir whose value cannot be changed and is thus set equal to zero. From here on we must differentiate between the lateral background reservoir and the vertical background reservoir.

As such, although we are including another region it is not an active one, and consequently we are not faced with a third governing equation. We do however need to introduce another time scale,  $\tau_v \equiv \frac{H^2}{8\nu}$ , which is the time it takes tracer to decay into the vertical reservoir. The appropriate set of equations is,

$$\begin{aligned} \frac{d\phi_e}{dt} &= \frac{(\phi - \phi_e)}{\tau_B} + \frac{(\phi_c - \phi_e)}{\tau_G} + \frac{(0 - \phi_e)}{\tau_B} + \frac{(0 - \phi_e)}{\tau_v} \\ \frac{d\phi_c}{dt} &= \frac{(\phi_e - \phi_c)}{\tau_G} + \frac{(0 - \phi_c)}{\tau_v} . \end{aligned} \quad (2.25)$$

Note that we have set  $\tau_R = \tau_B$  as before. (The relation (2.17) must still apply.) The initial conditions are the same as before,  $\phi_c(0) = \phi_e(0) = 0$ . When  $\tau_v \rightarrow \infty$  (no vertical reservoir) the set (2.25) collapses to (2.7).

As before, it is convenient to discuss results in terms of nondimensional parameters. With the addition of  $\tau_v$  we introduce another such parameter,  $\epsilon \equiv \frac{\tau_G}{\tau_v}$ , in addition to  $\Delta (= \frac{\tau_G}{\tau_B})$  defined earlier. Since both of the numerical runs with vertical diffusion had  $\kappa \sim 10^6 \text{ cm}^2/\text{sec}$  (the value in  $\kappa_1$ ) we set  $\Delta = \Delta_1$ . This way we isolate the effect of vertical flux within the context of the numerical results previously analyzed. Solutions of (2.25) are thus presented in terms of the single parameter  $\epsilon$ , which measures the relative strength of lateral diffusion into the gyre versus vertical diffusion out of the gyre.

#### 1. Spin up time.

Because the expanded transfer model does not require a third governing equation, the solutions for  $\phi_c$  and  $\phi_e$  are still of the form (2.8), with two transient modes. The spin up time is defined as before (the time scale of the slower mode),

$$\tau = S_1(\epsilon) \tau_0(\Delta_1) = S_2(\epsilon) \tau_v ,$$

$$S_1(\epsilon) = \frac{1}{1 + \frac{\epsilon}{1 + \Delta_1 - \sqrt{\Delta_1^2 + 1}}},$$

$$S_2(\epsilon) = \frac{\epsilon}{\Delta_1 + 1 + \epsilon - \sqrt{\Delta_1^2 + 1}},$$

where  $\tau_0(\Delta_1)$  = spin up time of the system when there is no vertical flux, evaluated at  $\Delta = \Delta_1$ . We saw earlier that  $\tau_0(\Delta_1) \approx \tau_B$ , so the function  $S_1 (\leq 1)$  measures how much more quickly the system spins up relative to the boundary diffusive time. The function  $S_2 (\leq 1)$  measures how much smaller the spin up time is relative to the other fundamental time scale, the vertical diffusive time. In the limit  $\epsilon \rightarrow 0$ , which characterizes weak vertical mixing,  $\tau \rightarrow \tau_B$ . In the opposite limit  $\epsilon \rightarrow \infty$  (strong vertical mixing),  $\tau \rightarrow \tau_V$ . The graph of  $S_1$  versus  $\epsilon$  appears in Figure 2.14.

As was the case with no vertical flux, under certain conditions the solutions for  $\phi_c$  and  $\phi_e$  can be approximated by the slower transient mode (in addition to the steady term). Consider the function which measures the relative decay of the two transient modes according to the strength of vertical mixing (the analog of  $R1$ ),

$$R2(\epsilon) = \frac{\Delta_1 + 1 + \epsilon + \sqrt{\Delta_1^2 + 1}}{\Delta_1 + 1 + \epsilon - \sqrt{\Delta_1^2 + 1}}. \quad (2.26)$$

When the vertical mixing is weak ( $\epsilon \rightarrow 0$ ) the faster decaying mode can be ignored (in this case  $R2$  collapses to  $R1$  evaluated at  $\Delta = \Delta_1 \ll 1$ , and recall that for small  $\Delta$  the single mode approximation is a good one). However, as seen in Figure 2.15, as the vertical mixing increases the single mode approximation steadily worsens, and in the limit where vertical mixing dominates, the approximation is invalid.

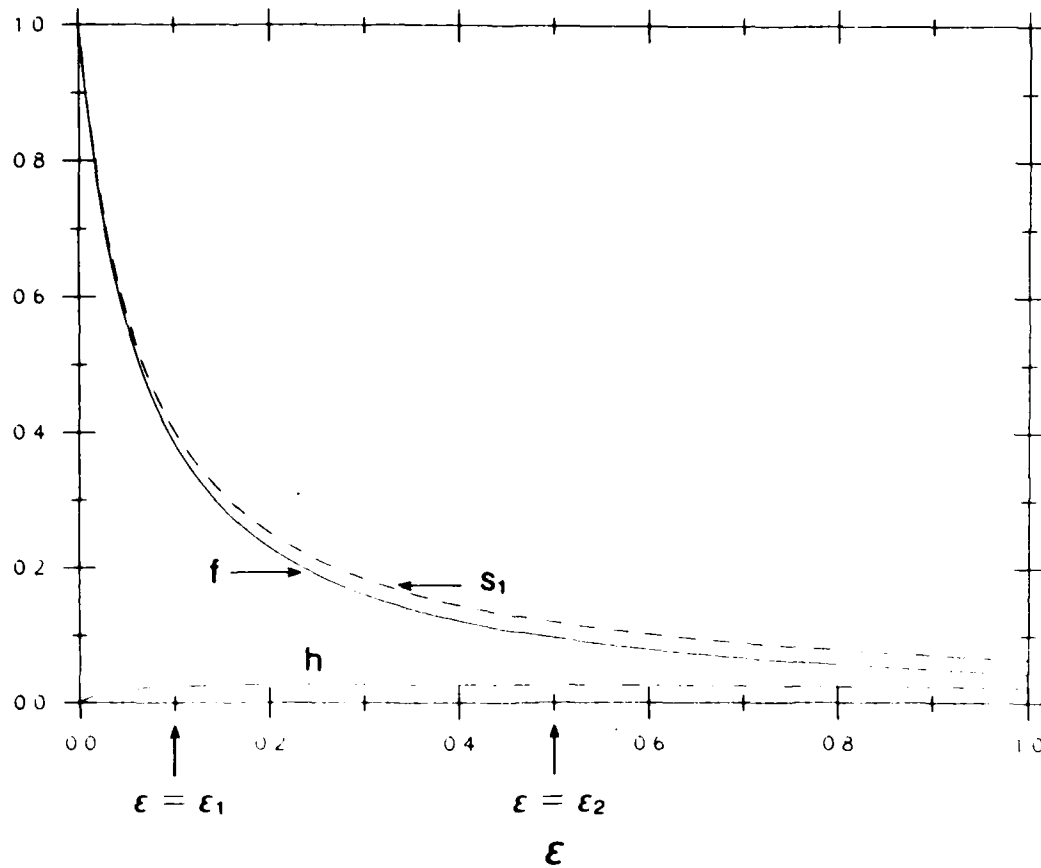


Figure 2.14: Comparison of the extent to which the transfer model spin-up time, final gyre level, and homogenization are affected by the presence of vertical mixing. The strength of the mixing is measured by the size of the parameter  $\epsilon$ . The value of  $\epsilon$  associated with experiment  $v_1$  and that with experiment  $v_2$  are indicated by  $\epsilon_1$  and  $\epsilon_2$  respectively.

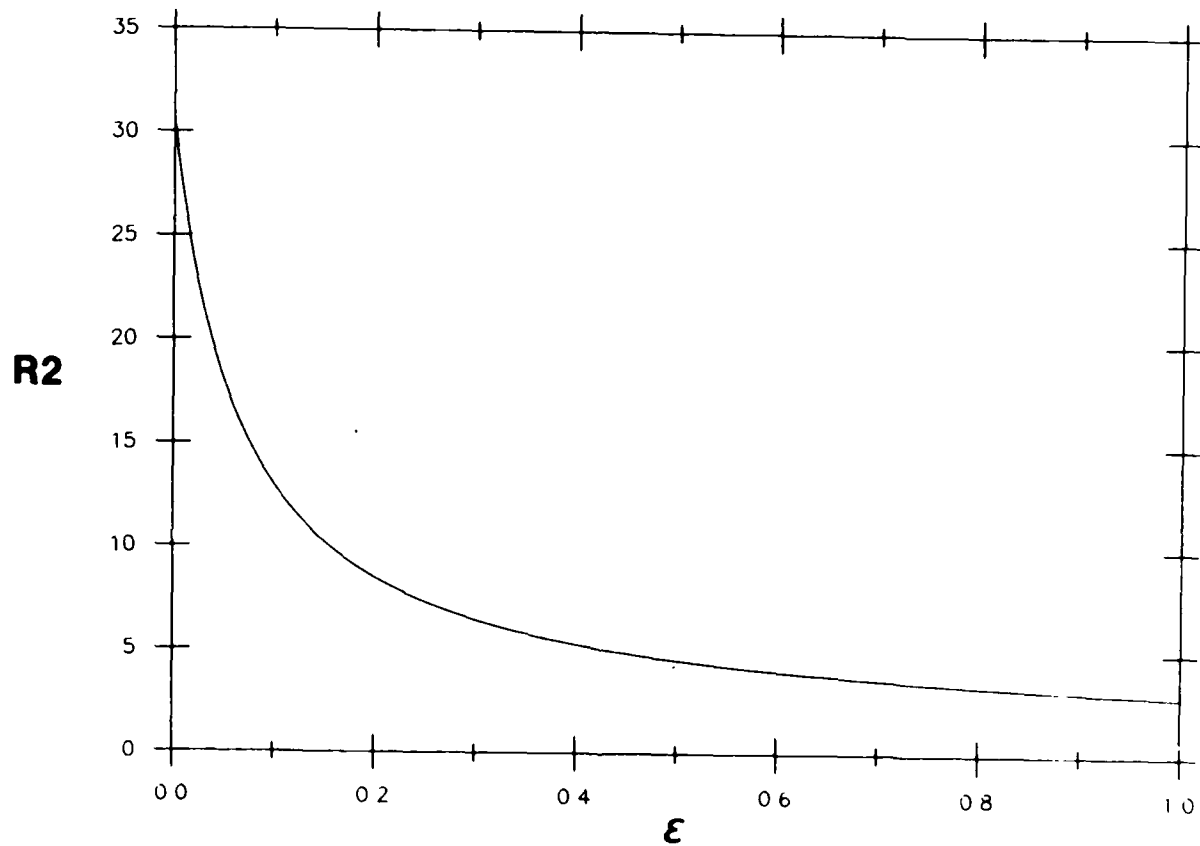


Figure 2.15: The relative decay of the two transient modes of the transfer model solutions when there is vertical mixing. For large values of  $\epsilon$  both modes must be considered.



## 2. Level in gyre.

The other major difference for the case of non-zero vertical flux, in addition to the shortened spin up time, is the reduced level of tracer in the gyre at steady state. Recall that when vertical flux is absent the final level is independent of the time scales (or in terms of the numerical model, the lateral diffusivity). It happens, however, that when vertical flux is made different from zero (i.e.  $\tau_v$  becomes finite) not only is this level dependent on the strength of that flux, it becomes dependent on the strength of the lateral fluxes as well. In the steady state, the expression for  $\phi_c$  is,

$$\phi_c(t \rightarrow \infty) \sim f(\epsilon) \frac{\phi}{2}, \quad (2.27)$$

$$f(\epsilon) = \frac{\Delta_1}{\Delta_1 + \Delta_1 \epsilon + \epsilon + \frac{\epsilon^2}{2}}.$$

The function  $f (\leq 1)$  measures the fraction of tracer in the gyre relative to how much would be there if the vertical flux were identically zero. The function is plotted versus  $\epsilon$  in Figure 2.14.

## 3. Homogenization

In the discussion of the previous transfer model it was mentioned that the evolution of  $\phi_e$  was nearly identical to that of  $\phi_c$ , and that in the large time limit  $\phi_e > \phi_c$  (i.e. complete homogenization occurs). In light of the numerical model results with vertical mixing, it is not surprising that this no longer is the case here. In the final state of  $v_2$  the distribution of tracer within the gyre is characterized by a slight minimum at the gyre center. The equivalent to this in the transfer model is the fact that  $\phi_c(t \rightarrow \infty) < \phi_e(t \rightarrow \infty)$ . As a measure of how significant this feature is in the transfer model we define the function  $h$ , which compares the gradient of tracer off of the boundary to the gradient across the gyre,

$$h(\epsilon) \equiv \frac{\phi_e(t \rightarrow \infty) - \phi_c(t \rightarrow \infty)}{\phi - \phi_e(t \rightarrow \infty)} = \frac{\Delta_1 \epsilon}{\Delta_1 + \Delta_1 \epsilon + 2\epsilon + \epsilon^2}.$$

The plot of  $h$  versus  $\epsilon$  appears in Figure 2.14.

It is interesting to note in Figure 2.14 that whereas the spin up time and level of tracer in the gyre are extremely sensitive to the strength of vertical mixing, the extent of homogenization, as measured by  $h$ , remains basically the same, i.e. the gyre is nearly homogenized regardless of the size of  $\frac{8\nu}{H^2}$ . Closer inspection of  $h$  shows that the point at which the gyre is least homogenized occurs for a finite value of  $\epsilon$  (Figure 2.16). The reason for this is straightforward. At very small values of the diffusion parameter  $\frac{8\nu}{H^2}$ , the vertical flux is so weak that the system behaves as in the salt case and homogenization occurs. At very large values of  $\frac{8\nu}{H^2}$ , the strong flux causes the vertical reservoir to draw away nearly all the tracer that reaches the edge of the gyre (having diffused from the boundary). Thus, very little tracer ends up in the edge of the gyre and even less in the center, so homogenization again occurs (in the sense that the gyre is uniformly void of tracer). The point at which the gyre is least homogenized then occurs between these limits.

Having reviewed these effects of vertical flux in terms of the parameter  $\epsilon$ , let us see where in this domain the two experiments  $\nu_1$  and  $\nu_2$  fall. Using the previously computed estimate of  $\tau_G$  and the appropriate values of  $\nu$  and  $H$ , we find that  $\nu_1$  corresponds to moderate vertical mixing and  $\nu_2$  corresponds to strong vertical mixing (the values of  $\epsilon$  so computed,  $\epsilon_1$  and  $\epsilon_2$ , are marked in Figure 2.14). As was done earlier, we can use this knowledge concerning the time scales to predict the spin up of the gyre in the numerical experiments. Such a prediction for the  $\nu_2$  example appears in Figure 2.17, where the concentration of the gyre center is compared with  $\phi_c$  when  $\Delta = \Delta_1$ ,  $\epsilon = \epsilon_2$ . Also shown are the similar comparisons for  $\kappa_1$  and  $\kappa_5$ . It is seen that for this case as well the transfer model provides a reasonable fit to the numerical data.

There are other interesting differences when vertical flux is added to the system in addition to those discussed above. Some of these are

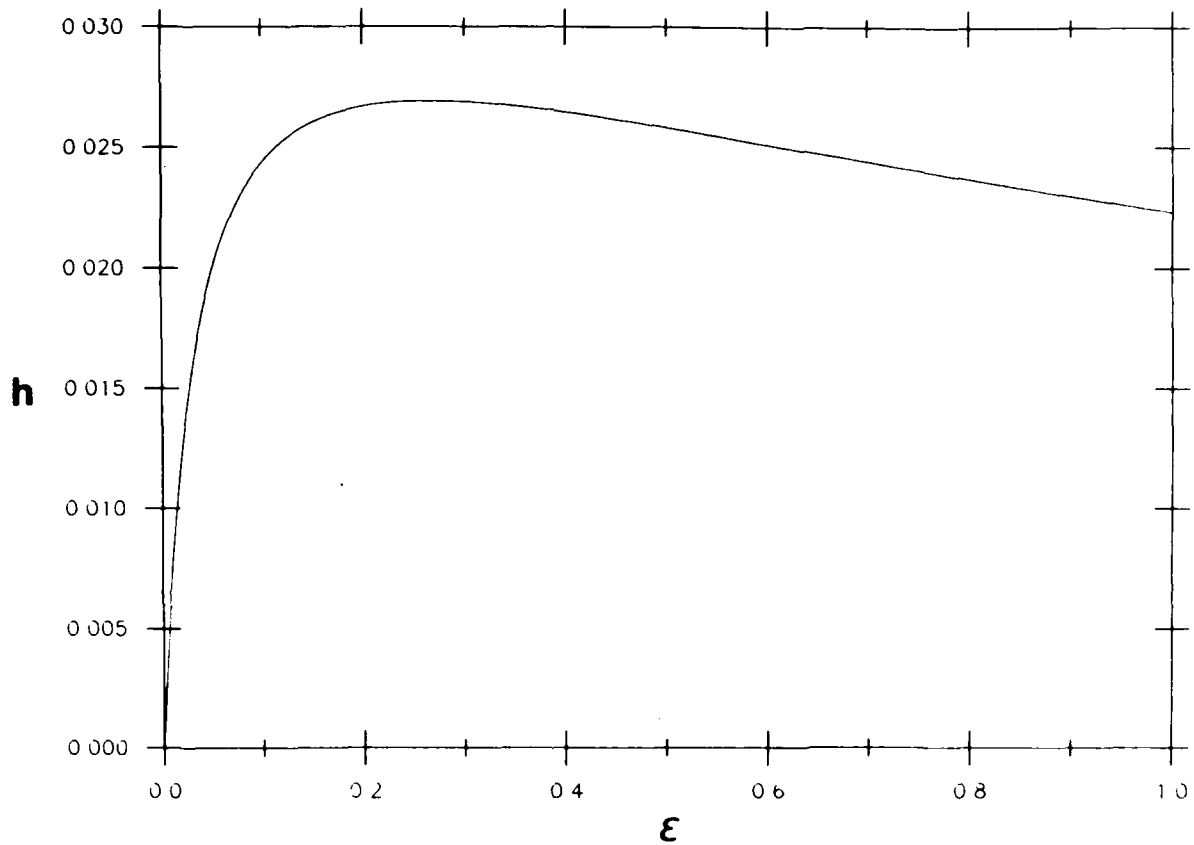


Figure 2.16: Enlargement of the graph of  $h$  in Figure 2.14 showing the degree of homogenization versus the strength of the vertical mixing. The gyre is least homogenized for  $\epsilon \sim .23$ .

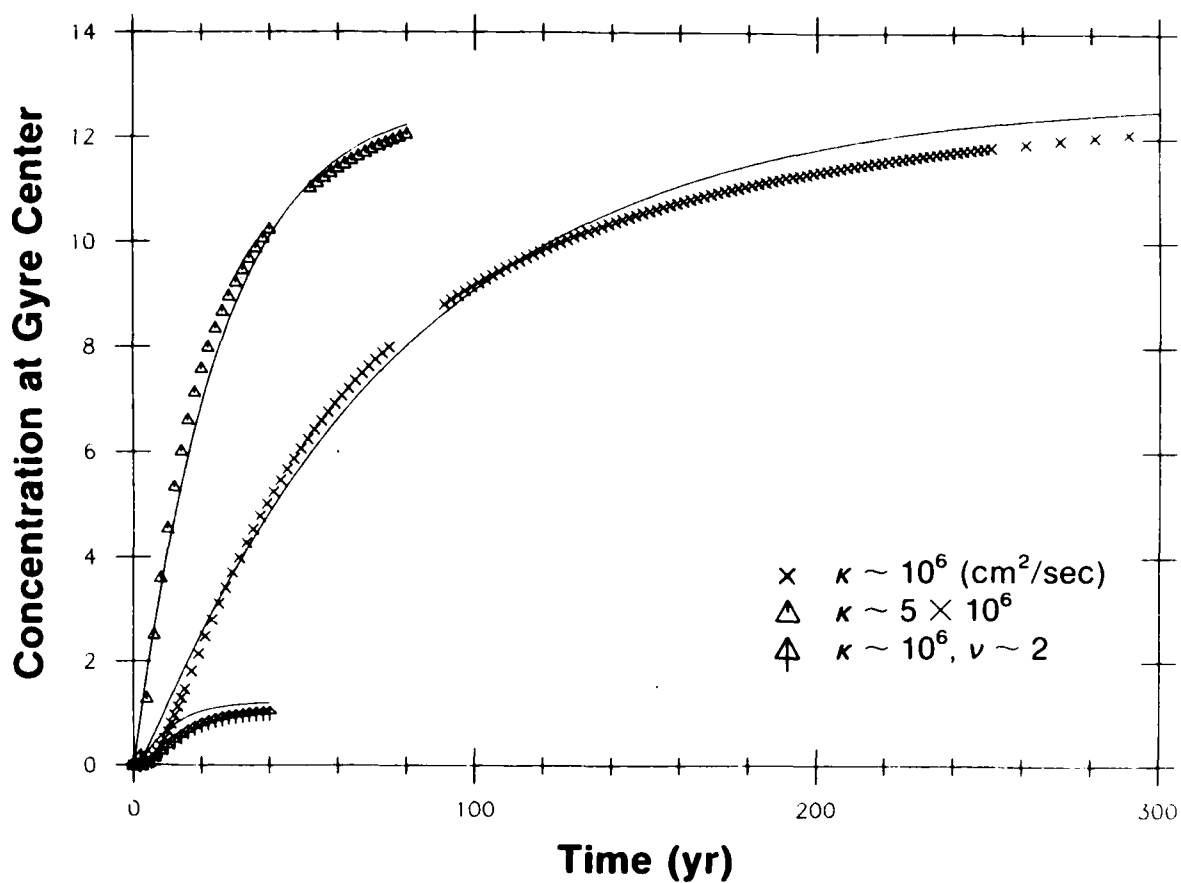


Figure 2.17: Comparison of the accumulation of tracer at the center of the gyre for the different values of lateral and vertical diffusivity. The solid lines are the corresponding predictions from the transfer model.

illustrated in Figure 2.18, within the context of the transfer model. When there is no vertical reservoir the steady state path of tracer is from the boundary to the lateral background via the edge of the gyre. This path becomes more complex when vertical flux is introduced. For instance, tracer is then fluxed into and out of the gyre center, although the strength of this flux is less than that through the edge of the gyre (which becomes stronger with increased vertical mixing). Also illustrated is the manner in which the flux away from the edge of the gyre is partitioned. In particular, when vertical mixing is weak the flux is nearly all to the lateral reservoir, but when vertical mixing is strong the flux is equally partitioned between the vertical reservoir and the center of the gyre. Note then that with a stronger vertical flux more tracer diffuses laterally from the boundary, but less makes it into the interior.

### C) Conclusions

Two types of tracers have been studied in some detail using a simple numerical model that was designed to represent the NRG/DWBC system. The first type, of which salinity is an example, is governed by lateral processes only whereas the second type, such as oxygen, is influenced by vertical mixing as well. The model produced various interesting results, among which is the fact that when vertical mixing is absent the final level of tracer in the gyre seems to be independent of the strength of the lateral mixing (provided it is weak). It also provided a method for recovering the values of the eddy diffusivities. Interpretation of the results though became clearer when an analogous diffusive transfer model was applied to the numerical model.

The transfer model was able to explain quantitatively what factors determine how much tracer diffuses into the gyre from the boundary current. In particular, it led to an expression for the gyre level which includes the core concentration of the boundary current and the lateral and vertical diffusivities. When the vertical mixing is identically zero, all dependence of the level on the strength of the lateral diffusion drops out as well, provided the nondimensional parameter  $\Delta_{BR} = \tau_B/\tau_R$  remains constant. It is not immediately obvious why this happens in the numerical model, and, as such, the transfer model does not offer an explanation as to why the level is independent of  $\kappa$  but rather explains what factors are involved.

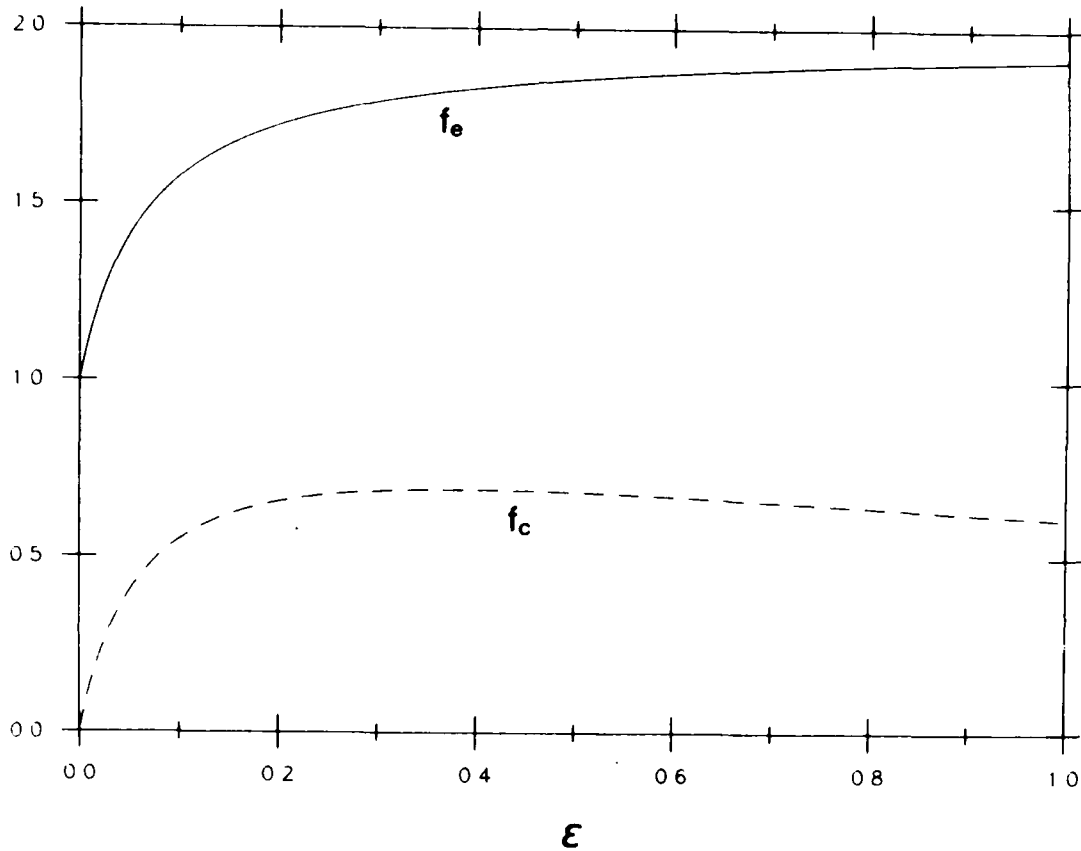
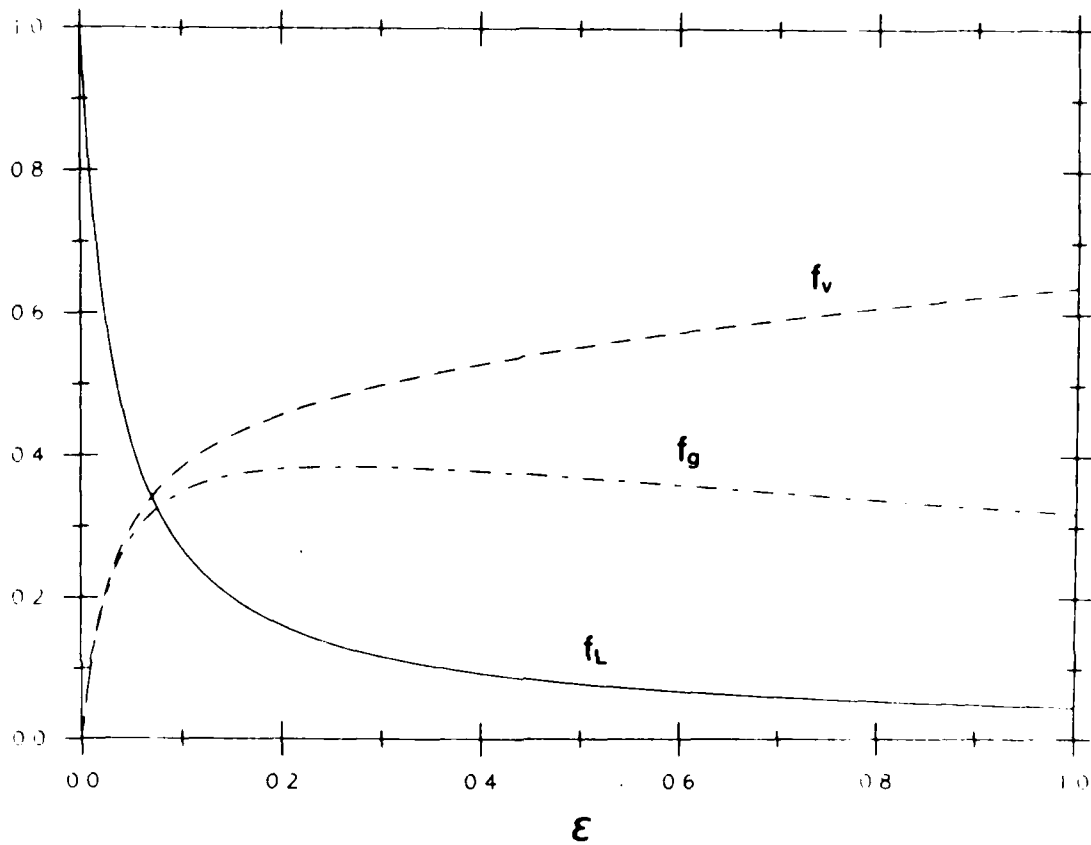


Figure 2.18: The effect of vertical mixing on the steady state flux of tracer between the regions of the transfer model.

(a) Comparison of the flux into and out of the edge of the gyre versus the center of the gyre. The non-dimensional functions  $f_e$  and  $f_c$  measure these quantities respectively, relative to the value for the edge when vertical mixing is absent.



(b) Comparison showing how the diffusion of tracer from the edge of the gyre is divided. Tracer is fluxed from the edge into the lateral background, the vertical background, and the gyre center. The strength of these fluxes, relative to the total flux out of the edge, is measured by the non-dimensional functions  $f_L$ ,  $f_v$ , and  $f_c$  respectively. Note that the sum of these functions is always equal to one.

The transfer model does, however, nicely explain various other features of the numerical results. The presence of homogenization within the gyre is a rigorous feature of the system. A nearly flat plateau develops regardless of the strength of the vertical diffusivity (provided the lateral diffusivity is small enough). The spin up of the system is slower than might be suggested by the size of the homogenized region in the different examples. This is because the spin up is dictated by the slow diffusion of tracer from the boundary current to the edge of the gyre (modified by diffusion vertically out of the domain). In addition to illuminating some of the results, as seen below the transfer model is also necessary in order to apply them to the data.

### Data Comparison

A major objective of the numerical model study (including the transfer model) was to use the acquired results to address the idea that this type of advective-diffusive situation exists in the ocean. Specifically, does tracer data from the region support the existence of the northern recirculation gyre? In this section we examine the data from this perspective. From the model we have learned what things to be looking for in the data, how to interpret various features, and how to extract specific information from these features. We now consider in some detail the tracer distributions from the data set described in Hogg et al. (1986).

The first thing to do is review general characteristics and see if they are consistent with what is believed to be the flow field. This was done in Hogg et al. (1986). The distinguishing feature of closed circulation, a region of homogenization, was present in all of the various tracer fields. Here we comment further on that analysis. The main thrust of this section, however, is a more detailed look at some of the specific features of the data.

In the model study we needed to specify boundary conditions and certain parameters (i.e. the diffusivities). In order to apply some of the results so obtained, we need then to identify the analogous boundary conditions in the data. It is results of this type which are examined (for instance, determining how much of a given tracer has diffused from the boundary current into the gyre). As a consequence, we acquire knowledge regarding the oceanic values of the diffusive parameters.



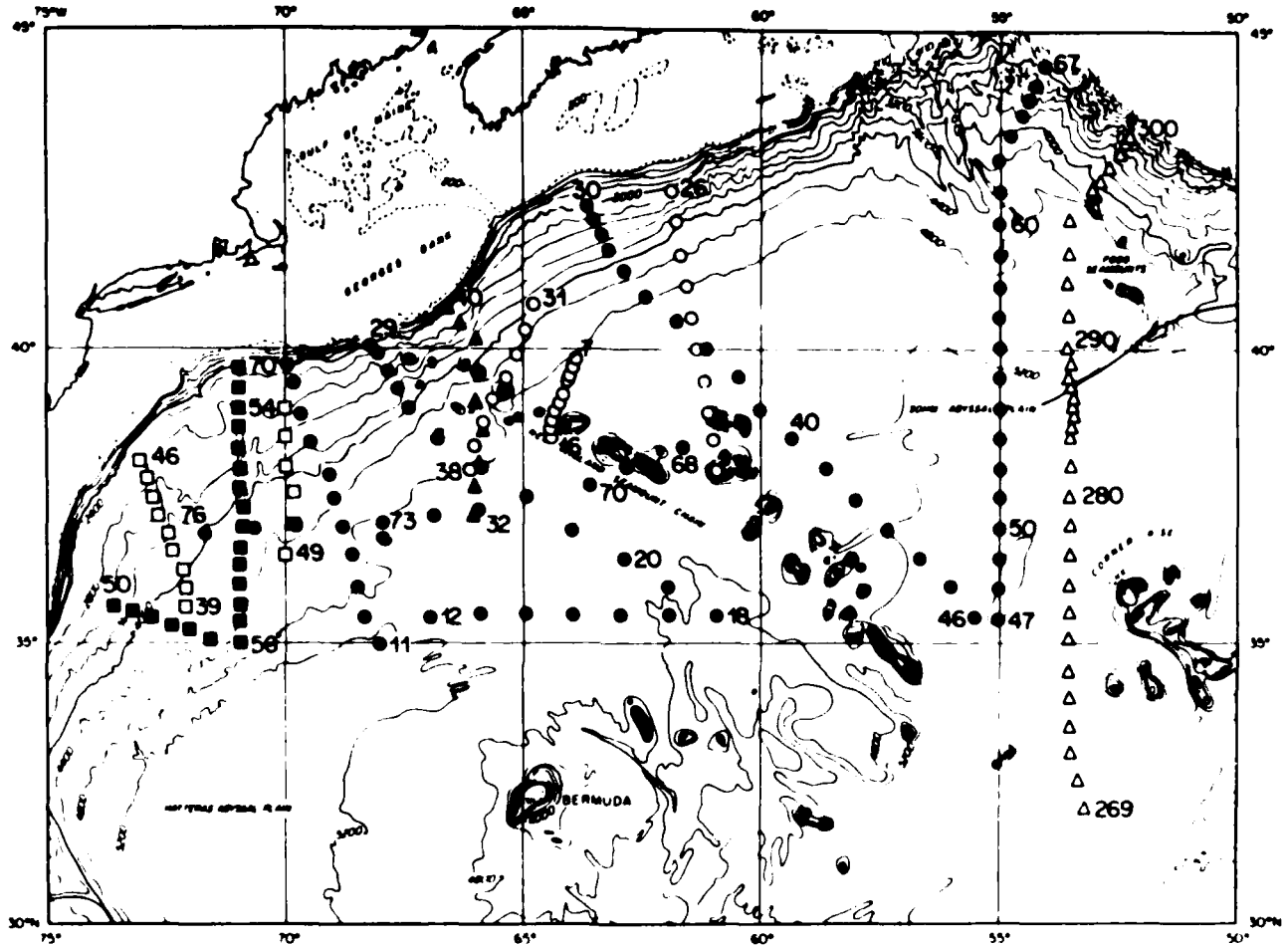
A detailed description of the data set appears in Hogg et al. (1986). The data includes tracer measurements from various cruises in the region north of  $35^{\circ}\text{N}$ , west of  $55^{\circ}\text{W}$ , and south of the 2000 m isobath of the continental slope (there are numerous crossings through the DWBC, Figure 2.19). Most of the data comes from a single cruise, OCEANUS 134, which was part of the Abyssal Circulation Experiment (1983-84) designed to study the NRG. The analysis centers on the distribution of oxygen, which is assumed to be in a nearly steady state. For this reason the results from the model regarding spin up are not directly applicable. We will discuss in turn some of the other important features.

## A) Results

### 1. Homogenization

We consider this feature first, as this was already addressed in Hogg et al. (1986). To detect homogenization requires only information about relative magnitudes of tracer concentrations; thus we need not concern ourselves with boundary conditions as yet. In order to reduce the noise level in the data, Hogg et al. employed a vertical averaging scheme. For each station in Figure 2.19 what is desired is the value of tracer at the density level corresponding to the core of the DWBC (consistent with the notion of isopycnal spreading). Rather than use this, Hogg et al. used the average concentration between two bounding density levels of the core (specifically, an anomaly averaged over the deep layer, defined here as  $\theta_{av}$ ). They presented lateral maps of  $\theta_{av}$  for various tracers.

The maps for oxygen appears in Figure 2.20. It is characterized by a strong gradient off the boundary that merges into a broad region which is nearly uniform. Further to the south the level once again drops off. Note the plume of high oxygen that extends off of the boundary and well into the interior. From this map, and a similar one for salinity, Hogg et al. computed a corresponding average section across the gyre through the boundary current. These are shown in Figure 2.21. Hogg et al. discussed the fact that although both tracers exhibit homogenization, the oxygen distribution has a slight minimum within this region, suggestive of vertical mixing.



OC 133  $\Delta$  MAY '83, OC 134  $\bullet$  JUNE '83, EN 74  $\Delta$  AUGUST '81, EN '83  $\square$  APRIL '82, EN '88  $\square$  AUGUST '82, EN 90  $\circ$  MAY '83

Figure 2.19: Station positions of the tracer measurements, from six different cruises, used in the data analysis (from Hogg et al., 1986).

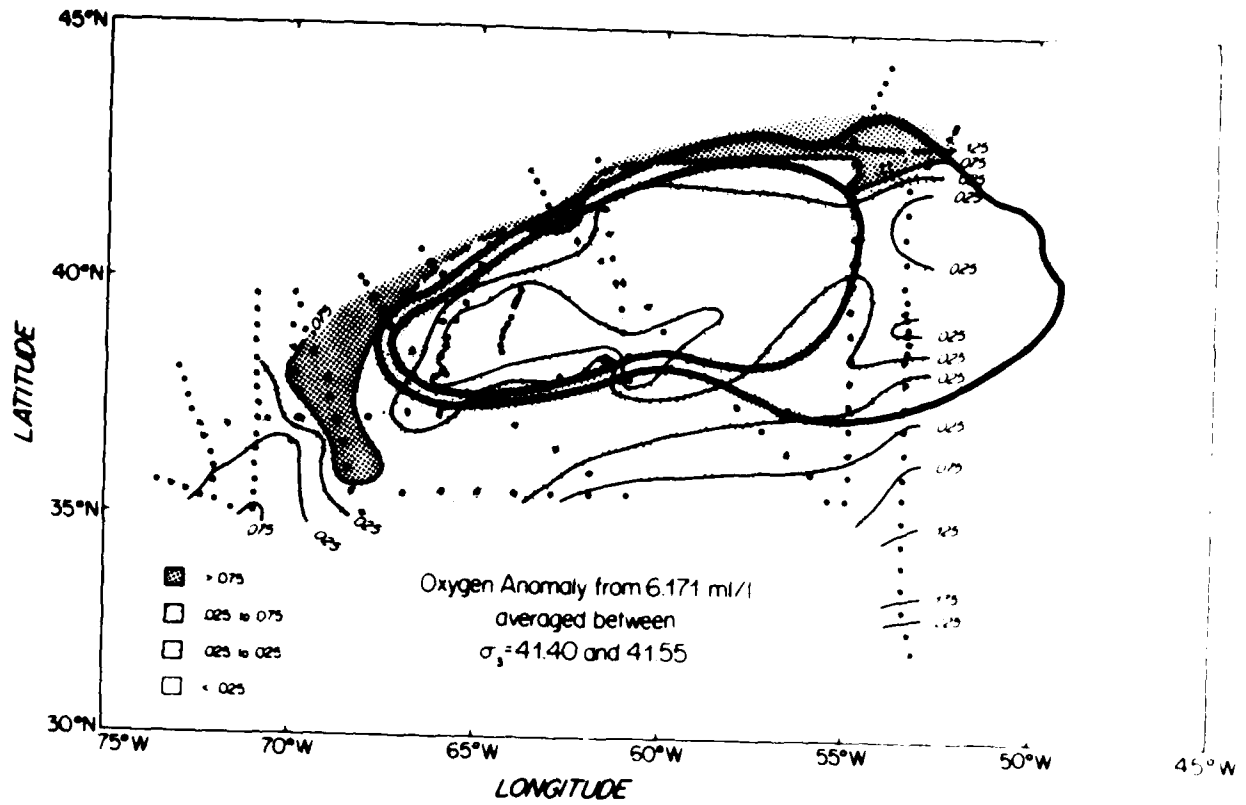


Figure 2.20: Lateral map of  $e_{av}$  for oxygen, from Hogg et al., 1986.

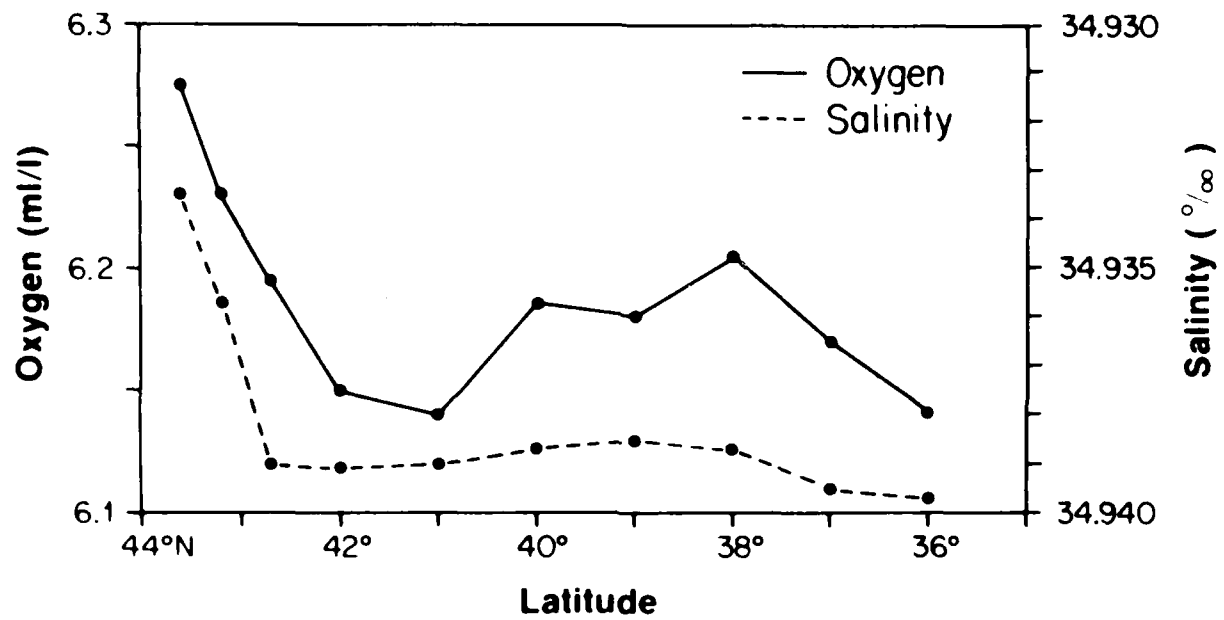


Figure 2.21: Average sections of oxygen and salinity through the DWBC and NRG (from Hogg et al., 1986). The graph plots the average of  $\theta_{av}$  in strips parallel to the DWBC versus the latitude of the strip at 55°W.

Superimposed on the lateral map of oxygen are two "streamlines." The outer one was constructed using the closed deep layer isopach in this region (from Hogg and Stommel, 1985) as a guide. The inner one was constructed to fit entirely within the region covered by the tracer data. Note that the oxygen plume emanates from the boundary beyond the region where the streamlines turn offshore. This is entirely consistent with the numerical model results and further supports the claim for a tight recirculation. The ridge of high oxygen then proceeds to penetrate into the gyre in a manner similar to the model. Note that the fact that this ridge is very slight does not imply that vertical mixing is weak, the transfer model shows that any vertical mixing, weak or strong, exhibits a subtle feature such as this.

## 2. Flux Balances

We saw earlier that the point balance of terms in (2.20) in the region of the spiral led to an estimate of the lateral diffusivity. In the oxygen distribution of Figure 2.20 we see evidence of such a spiral in the data. However, it should be noted that the distribution is a synoptic one, and, this being an area characterized by strong time-dependent fluctuations, such a distribution is sure to differ somewhat from the average pattern. For this reason, applying a point balance calculation involves a large amount of uncertainty, and therefore we do not make use of (2.22).

The other flux balance that was discussed was an integrated balance within a streamline of the gyre. The lateral flux of tracer into the gyre matches the vertical flux into the upper and lower layers. This equality led to an estimate of the vertical diffusivity,

$$v = \frac{\oint_S \frac{\partial \theta}{\partial n} ds}{\frac{H}{H^2} \iint_A \theta dA} \quad (2.28)$$

Since (2.28) involves spatial integrals, this removes some of the noise due to transients so the balance can be applied to the oxygen distribution with some confidence. In (2.28) recall that the value of  $\theta$  is actually the

vertical anomaly,  $\theta = \theta_M - \frac{\theta_u + \theta_L}{2}$  ( $\theta_u$  and  $\theta_L$  are the respective values at the top and bottom of the deep layer,  $\theta_M$  is the value in the center of the layer). In the model study we set  $\theta_u = \theta_L = 0$ , but in the ocean this is certainly not the case.

Consider again the oxygen profile versus depth in Figure 2.1 for a station in the center portion of the gyre. The profile is asymmetric in that the value near the top of the deep signal is smaller than that below the deep signal. This is true of most of the stations in the domain. As a result, the flux out of the top of the deep layer is greater than the flux out of the bottom, and in fact this downward flux can be ignored. In terms of (2.2), when there is upward flux only the value of the vertical mixing parameter decreases by a factor of two, and the anomaly simplifies to  $\theta = \theta_M - \theta_u$  (the expression (2.28) is altered accordingly). For reasons that will be explained later, the layer thickness was chosen to be  $H = 2500$  m. For each station,  $\theta_M$  was identified with the deep relative maximum in the oxygen profile, and  $\theta_u$  the value 1250 meters above this ( $\theta_M$  so defined conforms approximately to an isopycnal surface). With this definition of the anomaly, the denominator in (2.28) was estimated for the region within the inner streamline of Figure 2.20.

To compute the value of the line integral in (2.28) we broke the streamline into two parts, a northern half and a southern half, and used a single representative value of  $\frac{\partial \theta}{\partial n}$  for each part, estimated from the average section in Figure 2.21 (although the section plots values of  $\theta_{av}$ , the lateral gradients of  $\theta_{av}$  closely resemble those of  $\theta$ ). Thus we obtain an estimate for the term in brackets in (2.28) (for the case of upward flux only). Since there exists the uncertainty in an estimate for  $\kappa$ , it is best to keep it as a variable and think in terms of  $(\kappa, \nu)$  pairs, i.e. for a given value of  $\kappa$  the integrated flux balance implies an associated value of  $\nu$ . As such, (2.28) predicts the following pairs,

$\kappa$ (cm <sup>2</sup> /sec)	$\nu$ (cm <sup>2</sup> /sec)	(2.29)
$0(10^5)$	$0(1)$	
$0(10^6)$	$0(10)$	
$0(10^7)$	$0(100)$	

### 3. Gyre Level

We now address the question of how much oxygen is contained within the NRG with regard to the DWBC source. A functional relationship between the concentration of the gyre center and the boundary input was derived from the diffusive transfer model. It includes the values of the various time scales but also relies implicitly on the fact that the lateral and vertical background reservoirs are void of tracer. As this is not the case in the data, the expression (2.27) must be revised accordingly.

We will assume the following scenario for what happens in the ocean. Initially, when input from the DWBC begins to penetrate the interior, there exists a non-zero, uniform background oxygen concentration everywhere below the thermocline resulting from remote sources and sinks (e.g. diffusion from the surface water). Strong lateral diffusion from the boundary then influences the concentration in the deep layer, but vertical diffusion into the layers directly above and below is not substantial enough to significantly raise the level in these regions. Thus the upper and lower layers remain at the concentration of the initial state. This scenario is extremely oversimplified, but such a representation of events is necessary in order to analyze the data within the context of the transfer model.

To incorporate a non-zero background into the transfer model, the set (2.25) must be altered as follows. We define  $\phi$  as the value of both background reservoirs as well as the initial concentrations of  $\phi_c$  and  $\phi_e$ , and write the equations in terms of the  $\phi$ -anomaly,  $\phi_c' \equiv \phi_c - \phi$ ,  $\phi_e' \equiv \phi_e - \phi$ ,  $\phi' \equiv \phi - \phi$ . When written as such the equations for the primed variables have the same form as (2.25), thus we use those solutions derived earlier with the appropriate substitutions. In particular, the expression for the amount of tracer at the gyre center (2.27) becomes,

$$\phi_c(t \rightarrow \infty) \sim f \frac{\phi}{2} + (1 - \frac{f}{2}) \phi. \quad (2.30)$$

The second term on the right hand side represents the correction due to non-zero background.

It is of interest to contrast (2.30) with the analogous expression when vertical mixing is absent. In that case the amount of tracer in the gyre is

$$\phi_c(t \rightarrow \infty) \sim \frac{\phi}{2} + \frac{\phi}{2}. \quad (2.31)$$

Note that the background correction for the two cases is different. Consider then the analog to the function  $f$  when there is non-zero background (recall that  $f$  measures how much tracer accumulates in the gyre relative to the amount present if vertical mixing were absent). This quantity is the ratio of the expressions (2.30) and (2.31). When written in terms of the parameter  $\tilde{\phi} \equiv \frac{\phi}{\phi}$ , which measures the strength of the anomaly supplied by the DWBC, it takes the form

$$\tilde{f} \equiv \frac{(\tilde{\phi} - 1)f + 2}{\tilde{\phi} + 1}. \quad (2.32)$$

Figure 2.22, which plots  $\tilde{f}$  versus  $\tilde{\phi}$ , shows that for  $\tilde{\phi} \gg 1$  (small anomaly)  $\tilde{f} \gg 1$ , and for  $\tilde{\phi} \gg \infty$  (large anomaly)  $\tilde{f} \gg f$ . This quantifies the intuitive result that when there is non-zero background the effect of vertical mixing is lessened (for the same concentration of tracer in the DWBC).

In the data we can readily measure the equivalent of  $\phi_c(t \rightarrow \infty)$ , the concentration at the center of the gyre. However, in order to apply the result (2.30) we have to identify what the equivalent boundary conditions are in the data, i.e. the analogs to  $\phi$  and  $\phi$ . Consider first the boundary input value  $\phi$ . We saw from applying the results of the transfer model to the numerical model that in terms of the boundary current, the appropriate source concentration that dictates the level in the gyre is the value of tracer at the core of the current. It is a matter then of choosing the appropriate location along the DWBC for which this relation holds in the data.

If this location is chosen so far upstream of the gyre that some of the tracer diffuses directly from the boundary current into the lateral background (without having first been advected around the gyre) then the assumptions that accompany the transfer model are violated and the relation will be inaccurate. On the other hand if the location is not far enough upstream then some of the tracer that enters the gyre, having diffused from further upstream, will not be accounted for and again the relation will not hold.



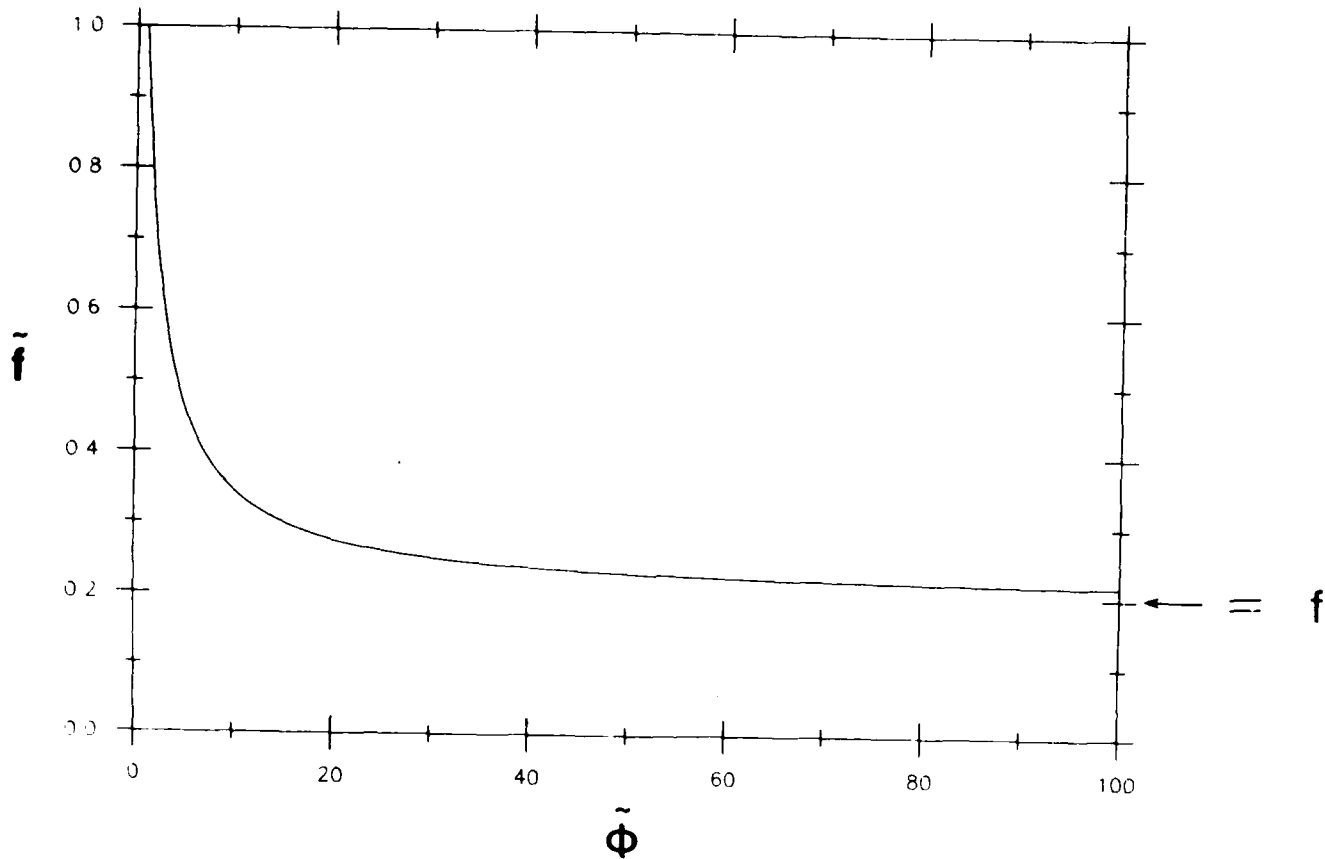


Figure 2.22: The effect of a non-zero background on the steady state gyre level of the transfer model. The level of the gyre, normalized by its value when vertical mixing is absent, is shown in relation to the strength of the input anomaly.

The correct location then lies just in between these limits, and in light of Figure 1.1 is near  $50^{\circ}\text{W}$ . Immediately upstream from there the current twists around the Grand Banks and most certainly communicates directly with the lateral background. (Note that in the numerical model the northern boundary could be anywhere south of this critical location and the relation would still hold.)

In regard to the background reservoir value  $\phi$ , it is not straightforward to identify such a quantity in the data. This being the case we turn the calculation around and treat  $\phi$  as the unknown (i.e. solve (2.30) for  $\phi$ ). This quantity is similar to a quantity such as the diffusivity in that we are unable to directly measure it, but can comment on whether an estimate is reasonable or not. As a guide for such an estimate we consider the following averaged layer value.

Recall that in the description of the numerical model governing equation (2.2) the upper and lower reservoir values,  $\theta_U$  and  $\theta_L$ , were independent of  $x$  and  $y$ . In order that the model behave in a manner similar to the ocean (in regard to vertical mixing) both the assumption of a reservoir and that of no spatial dependence must hold to some extent in the data. In view of the oxygen profile in Figure 2.1 the reservoir assumption for the upper layer seems valid (keep in mind that the shape of the oxygen profile is typical of the entire data set). However, the lower layer value never levels off, which may be related to the fact that this value is consistently higher than its upper layer counterpart. The idea is that the bottom boundary limits the size of the lower layer, and as a consequence the layer begins to fill up with oxygen that has diffused from above.

In order to address the question of spatial dependence, the concentration of the  $\text{O}_2$  maximum was compared to the concentration a given distance above and below for all the stations within the inner streamline. It was found that with increased separation the correlation between  $\theta_M$  and the upper value decreased substantially, whereas the correlation between  $\theta_M$  and the lower value did not. This is consistent with the reservoir discrepancy mentioned above, and suggests that when modelling the effect of vertical mixing we should in fact include two terms in the governing equation. One

should be a decay term like the one that was considered, but only as a representation of mixing with water above the deep layer. Mixing with the bottom layer is characterized more appropriately by a constant flux (independent of the concentration of the deep layer) which has the form of a consumption term. Recall, however, that the near bottom gradients are very weak and the consumption term can be ignored with respect to the radioactive decay term.

As a value then with which to compare estimates for  $\phi$ , the average of  $\theta_u$  at a distance well above the  $O_2$  maximum was computed over all the stations enclosed by the inner streamline. The distance that was chosen was  $H/2 = 1250$  m, as a distance greater than this does not cause the correlation to decrease significantly. The values of  $\theta_M$  and  $\theta_u$  for the group of stations appears in Figure 2.23 (also shown is  $\bar{\theta}_u$ ). The two quantities exhibit similar trends, although the standard deviation of  $\bar{\theta}_u$  is substantially smaller than that for  $\bar{\theta}_M$ . It should be noted that in the integrated flux balance calculation above, the result would be the same if we had used the value of  $(\theta_M - \bar{\theta}_u)$  at each station rather than  $(\theta_M - \theta_u)$ .

The value of  $\phi$  depends on the value of  $f$ , and recall that the function  $f$  depends on the parameters  $\Delta$  and  $\epsilon$  (where the expression for  $\epsilon$  now reflects the fact that there is flux through one layer only). Estimating the area of homogenization from the data set and using a value of  $H = 2500$  m, we can use the numerical model to compute an associated value of  $\epsilon$  and  $\Delta$  for each pair of diffusivities in (2.29). This in turn gives the corresponding magnitude of  $f$ . It is the case, however, that the values of  $\phi(f)$  so predicted from (2.30) are significantly larger than  $\bar{\theta}_u$ . In other words the transfer model says that there should be less oxygen than that which has diffused into the NRG according to the data. This discrepancy is reconciled below by considering variations in the numerical model streamfunction.

#### Western Intensification

Admittedly there is some question as to the validity of using  $\bar{\theta}_u$  as a measure of the "background" oxygen concentration in the deep layer. This being so, an inconsistency concerning the level of oxygen in the NRG should not in itself be cause to completely restructure the model that has been used.

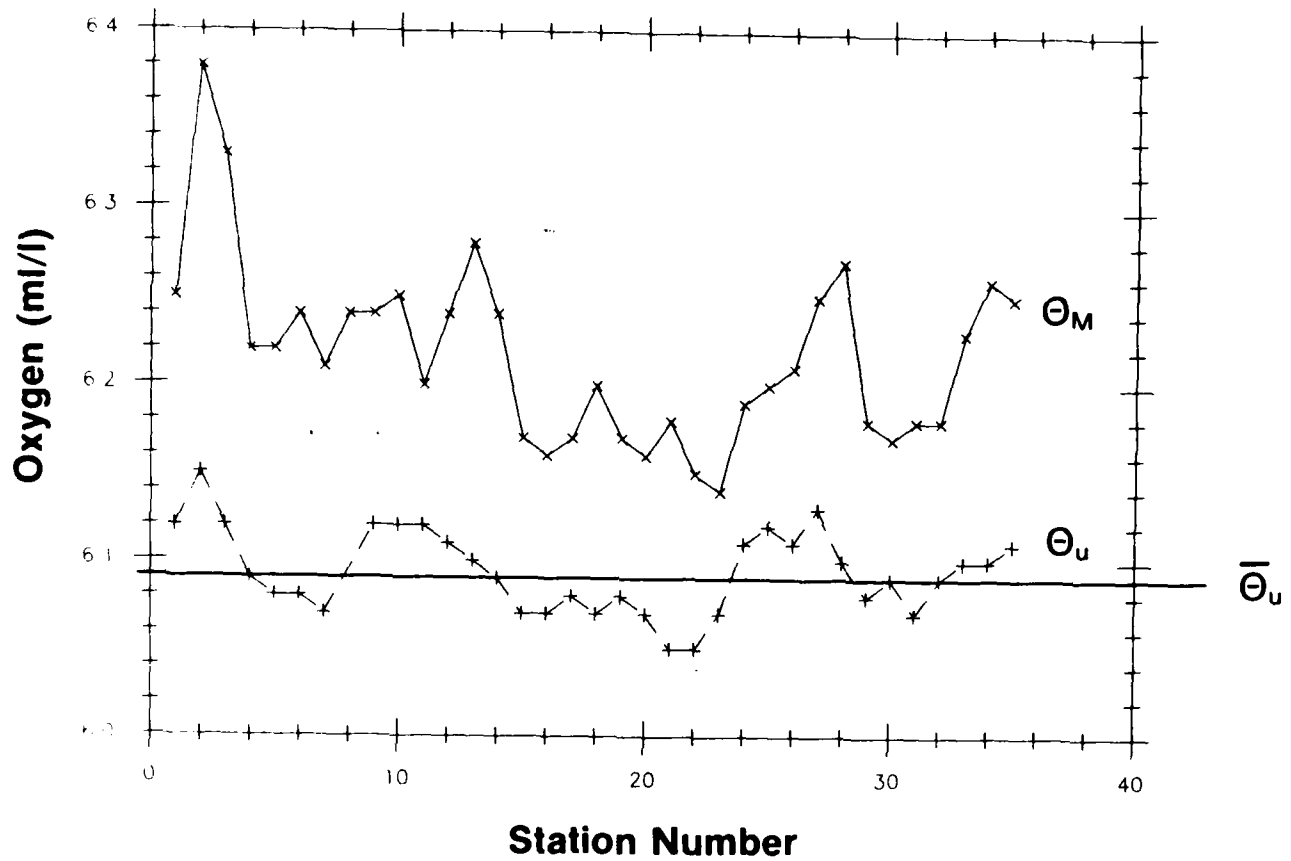


Figure 2.23: The value of the oxygen maximum in the deep layer, and the value 1250 m above this for each of the stations within the inner streamline of Figure 2.20.

In addition, there is uncertainty in the integrated flux balance calculation, and it is possible that (2.29) does not express the true relationship between the two diffusivities. Nonetheless it is desirable to try and fit all the pieces of the calculation together in a consistent fashion and offer the result as one possible interpretation of the data.

The velocity field of the numerical model was chosen as a simplified representation of the DWBC/NRG system, and, functioning as a tool to reveal processes, this flow field in conjunction with the remainder of the model proved useful. It is, however, certainly not the only streamfunction that could have been used, although it is hoped that employing a similar flow pattern would not alter the major results of the model but rather have only a mild effect on specific features. In light of the inconsistency above, one such feature that we concern ourselves with now is the strength of the flux of tracer into the gyre.

The reason why we choose to alter the velocity field is twofold. First, the strength of this flux is indeed sensitive to the specifics of the streamfunction. Second, the current meter data that was used to define the NRG is somewhat sparse, thus allowing for some leeway in specifying a corresponding simulated flow field, i.e. the specific details are really an unknown in the model that we are free to vary. This process of altering the streamfunction can be thought of as fine tuning.

There are several ways that the velocity structure can be changed to cause tracer to fill the gyre at a faster rate. Four such variations appear in Figure 2.24. In the first example the gyre is moved closer to the boundary current and the two flows partially merge. Tracer now diffuses into stronger flow and is advected more quickly into the interior. In the second example the gyre is again moved towards the boundary current but the two do not merge, rather the boundary flow converges. This strengthens the zonal gradient of tracer there causing a stronger offshore flux. In the third example the gyre is turned on its side so that there is a greater region of contact between the flows, which also serves to enhance the ventilation of the gyre. In the final example the gyre is no longer symmetric but western intensified. This causes it to fill up more rapidly for the same reason as in the first example.

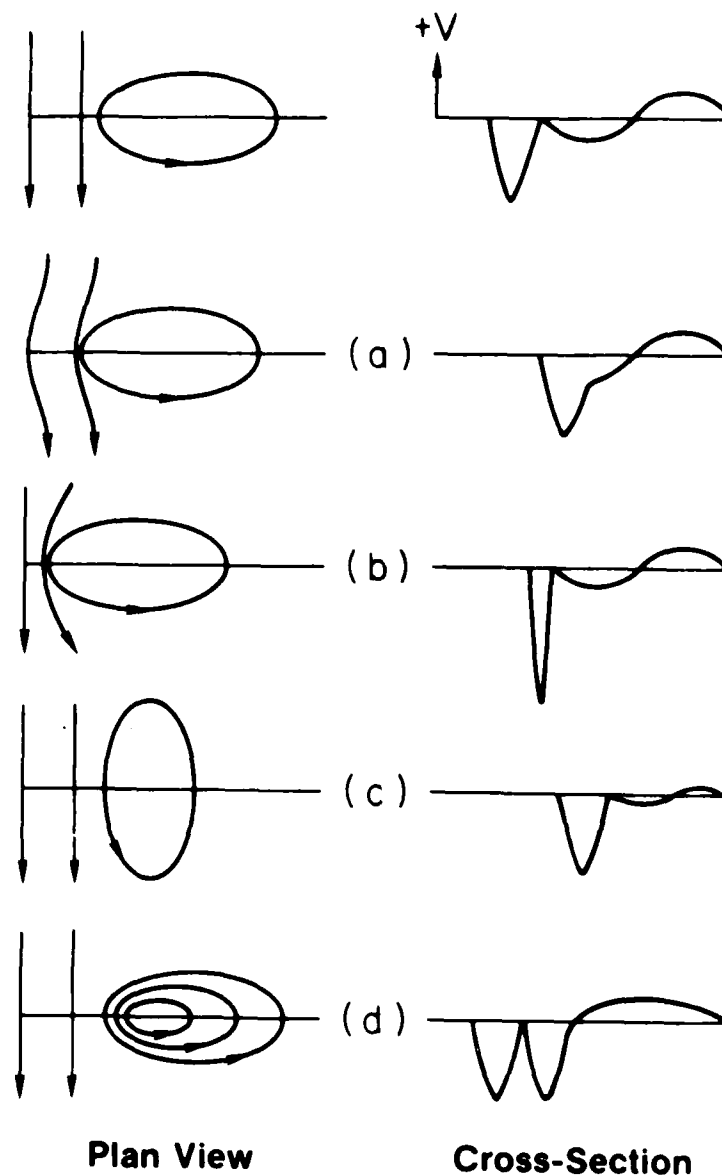


Figure 2.24: Schematic showing four examples in which the streamline pattern of Figure 1.2 is altered in a way that causes the gyre to accumulate tracer more rapidly. The bounding streamlines of the boundary current and gyre are shown alongside a zonal velocity section through the current and center of the gyre. The unaltered streamline pattern appears at the top. (a) The gyre is shifted towards the boundary current and partially merges with it. (b) The gyre is shifted towards the boundary current and causes the boundary current streamlines to converge. (c) The gyre is rotated by 90°. (d) The gyre is made western intensified.

It is possible that to one extent or another all of these effects are present in the ocean and have not been accounted for in the model. Certainly the NRG and DWBC are adjacent over a greater distance than is portrayed in the model. We have chosen here to consider the effect of western intensification, as the data implies that there is very little separation between the two flows when they are side by side. The streamfunction that was used is shown in Figure 2.25 compared to the previous streamfunction. The boundary current is identical in both cases, and the only major difference between the gyres is that now the maximum southward flow of the gyre is comparable in magnitude to the core speed of the boundary current and is closer in proximity to the boundary current.

A single experiment (abbreviated  $W_1$ ) was done in which  $\kappa = 1 \times 10^6 \text{ cm}^2/\text{sec}$  (lateral diffusion only). The resulting tracer field is shown in Figure 2.26 and should be compared to that of the  $\kappa_1$  experiment (Figure 1.17a). As a result of the increased speed with which tracer is transported into the interior, the center of the gyre is filled at a faster rate than in  $\kappa_1$ . However, this does not mean that more tracer ultimately diffuses into the gyre, for in Figure 2.27 it is seen that the level asymptotes to the same level as it did in  $\kappa_1$  (and  $\kappa_5$ ) which means only that the spin up time is shorter. Since we need more tracer in the gyre in order to reconcile the discrepancy with the data it seems then that altering the streamfunction in this way does not prove useful. Keep in mind, however, that for oxygen there is vertical flux present. This causes the system to spin up rapidly which in turn preserves any differences in the transient states of the two cases, in particular the fact that early on there is more tracer in the western intensified gyre.

In order to apply this result to the data it is first necessary to couple the transfer model to  $W_1$  (note that we do not have to alter the set up of the transfer model to reflect the change in the numerical model, because the specifics of the advective processes are not included within the realm of the transfer model). This coupling was done by matching (2.19a) to the spin up of  $W_1$  and determining  $\Delta$ . It is the case that the value of  $\Delta$  is again small as it was in the  $\kappa_1$  and  $\kappa_5$  experiments. This tells us immediately then that  $W_1$  is in the same limit, namely that the spin up is

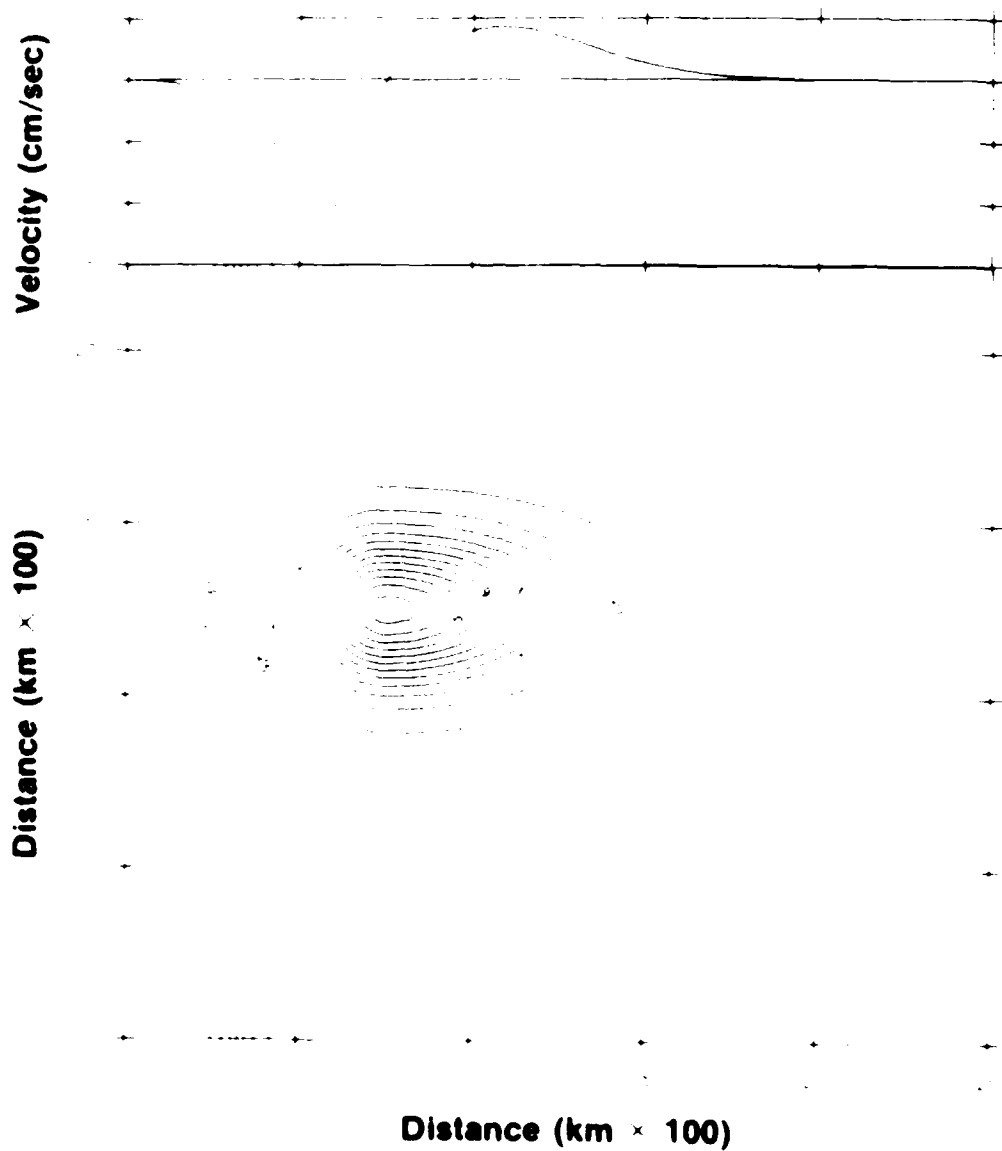
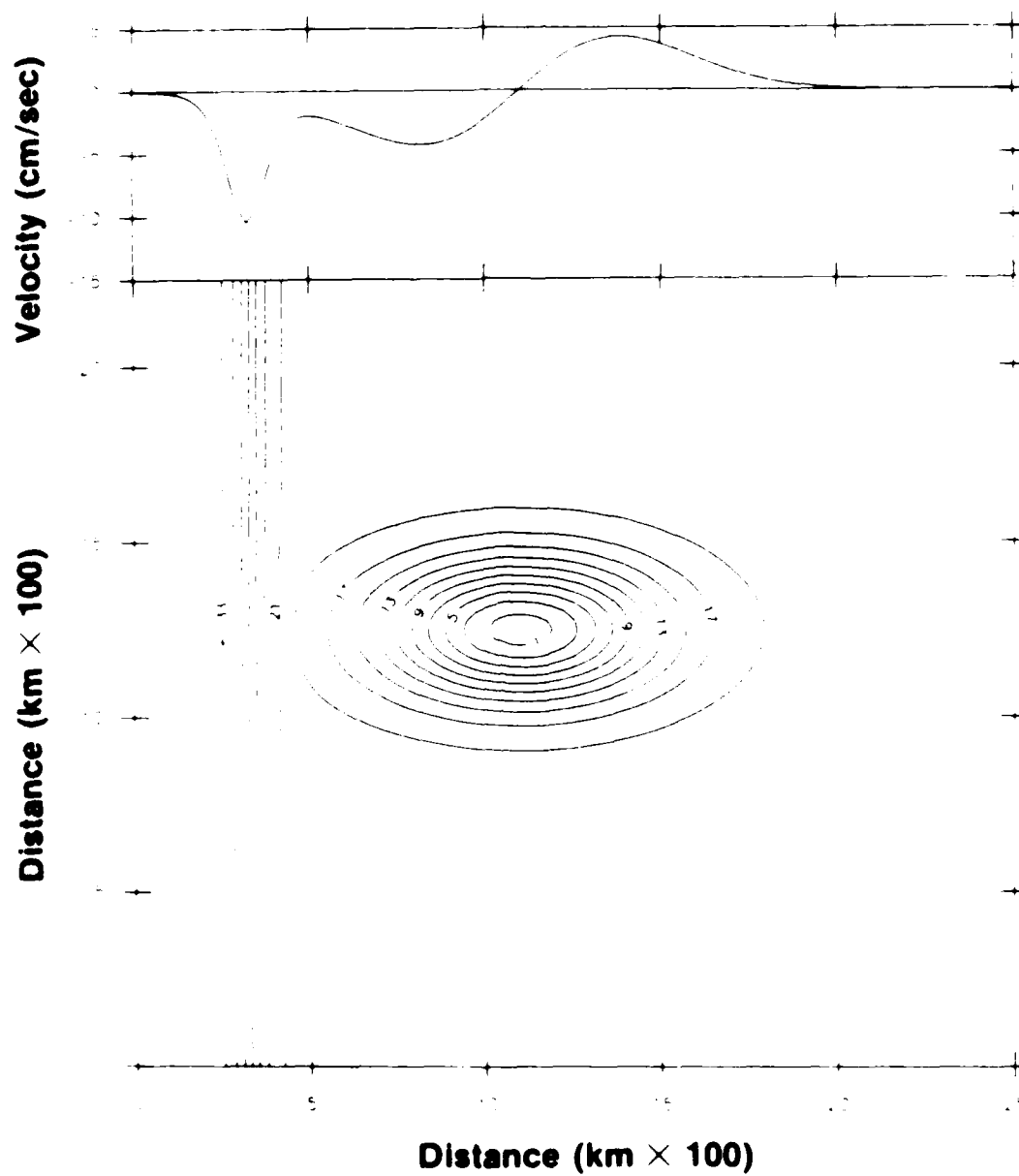


Figure 2.25: Streamlines of the boundary current and gyre, with a zonal velocity section through the current and center of the gyre shown above.

(a) The western intensified gyre used in experiment  $w_1$ .





(b) The zonally symmetric gyre of Figure 1.2 used in the previous experiments.

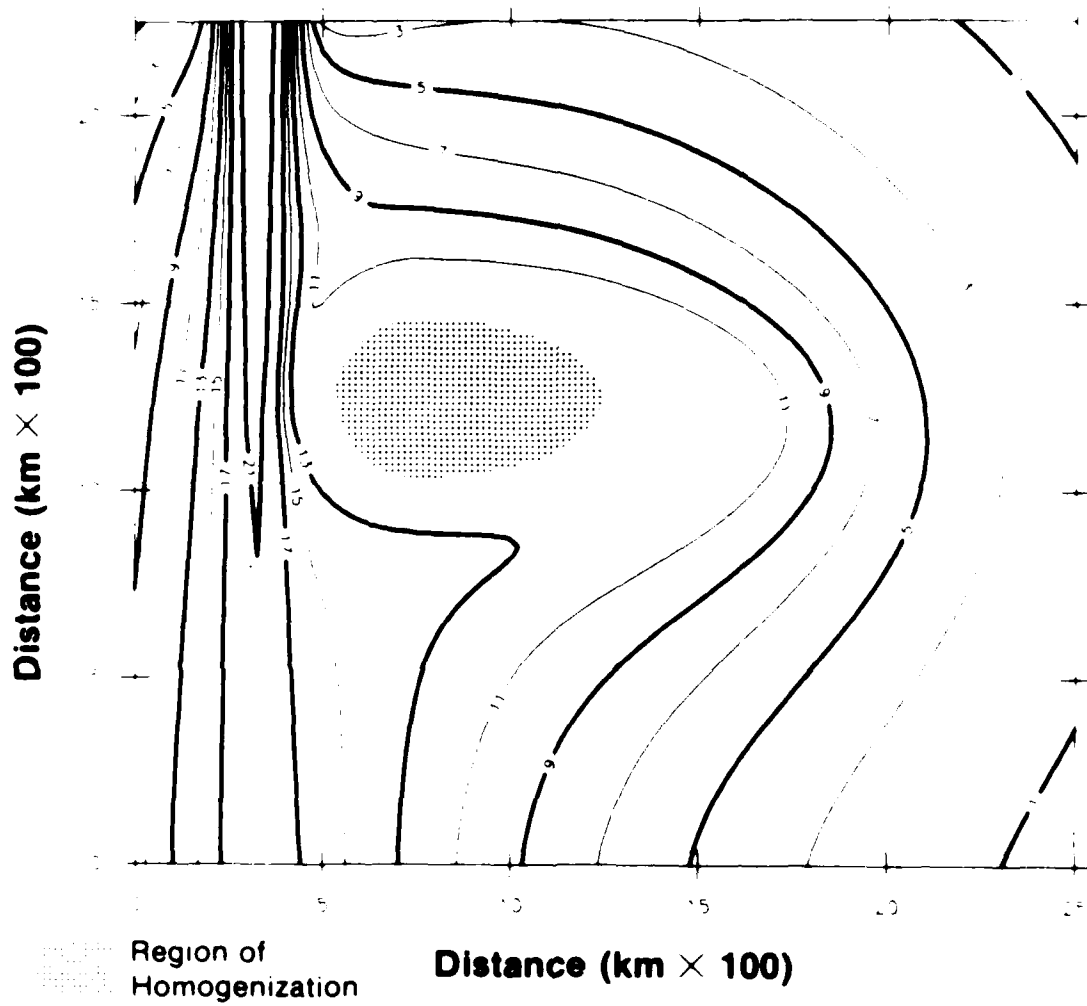


Figure 2.26: Steady state distribution of tracer for  $\kappa \sim 10^6 \text{ cm}^2/\text{sec}$  with the western intensified gyre of Figure 2.25.

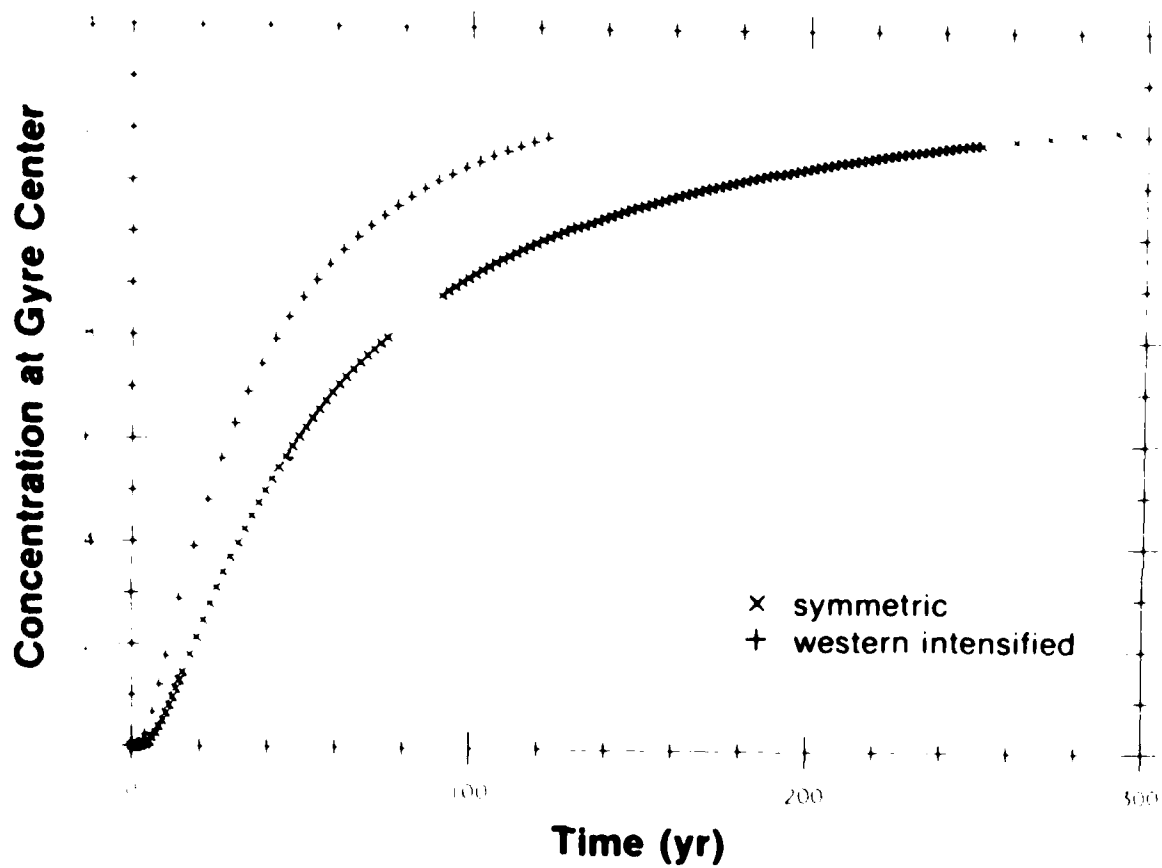


Figure 2.27: Time history of tracer accumulating in the western intensified gyre ( $\kappa \sim 10^6 \text{cm}^2/\text{sec}$ , no vertical mixing) compared with the same curve for the symmetric gyre.

controlled by diffusion from the boundary and behaves as a single exponential. Figure 2.28 shows that all the experiments with just lateral diffusion collapse to a single case.

To account for the effect of vertical flux on the gyre level within the context of western intensification, a corresponding value of  $\epsilon$  must accompany  $\Delta$ . Values of both parameters were computed for the diffusivities and length scales relevant to the data. Recall that  $\Delta = \frac{\tau_G}{\tau_B}$  and  $\epsilon = \frac{\tau_G}{\tau_V}$ . We need the numerical model to compute  $\tau_B$ , the spin up time of the system ( $\tau \sim \tau_B$ ), as this quantity can not be deduced from the data. It is here that the distinction appears between the western intensification case and the symmetric gyre case. The time scale  $\tau_B$  is the only one of the three time scales that is different for the two cases (with regard to the data) so while the values of  $\epsilon$  that accompany (2.29) will be the same here as before, the values of  $\Delta$  will be somewhat larger. This in turn alters the associated values of the function  $f$  used in (2.30).

As seen in Figure 2.29 we can now get good agreement between  $\bar{\theta}_U$  and one of the predicted values of  $\phi(f)$ . The pair of diffusivities that give this agreement are  $\kappa \sim 10^6 \text{ cm}^2/\text{sec}$  and  $\nu \sim 10 \text{ cm}^2/\text{sec}$ . (In order to get a prediction for  $\kappa \sim 5 \times 10^6 \text{ cm}^2/\text{sec}$  we assumed that a corresponding western intensification numerical run would be related to  $\kappa_5$  in the same manner that  $W_1$  was related to  $\kappa_1$ ). Also shown in the figure are the resulting predictions if we disregard the flux balance constraint and arbitrarily set  $\nu = 1$ . In that case the vertical flux is extremely weak which results in a comparatively small background. When the gyre of Figure 2.27a is rotated  $90^\circ$  to the left (which combines the effect of increased contact with western intensification) a spin up test shows that tracer fills the gyre a bit more quickly yet. This would cause even closer agreement in Figure 2.29.

A value of  $\sim 10 \text{ cm}^2/\text{sec}$  for  $\nu$  is substantially larger than some earlier estimates of the vertical diffusivity at thermocline depths (for instance Rooth and Östlund, 1972). However, values as large as  $3\text{--}4 \text{ cm}^2/\text{sec}$  have been calculated for the Antarctic bottom water flowing northward along the western boundary of the South Atlantic (Hogg et al., 1982; Whitehead and Worthington, 1982). The calculated value of  $\kappa \sim 10^6 \text{ cm}^2/\text{sec}$  on the other

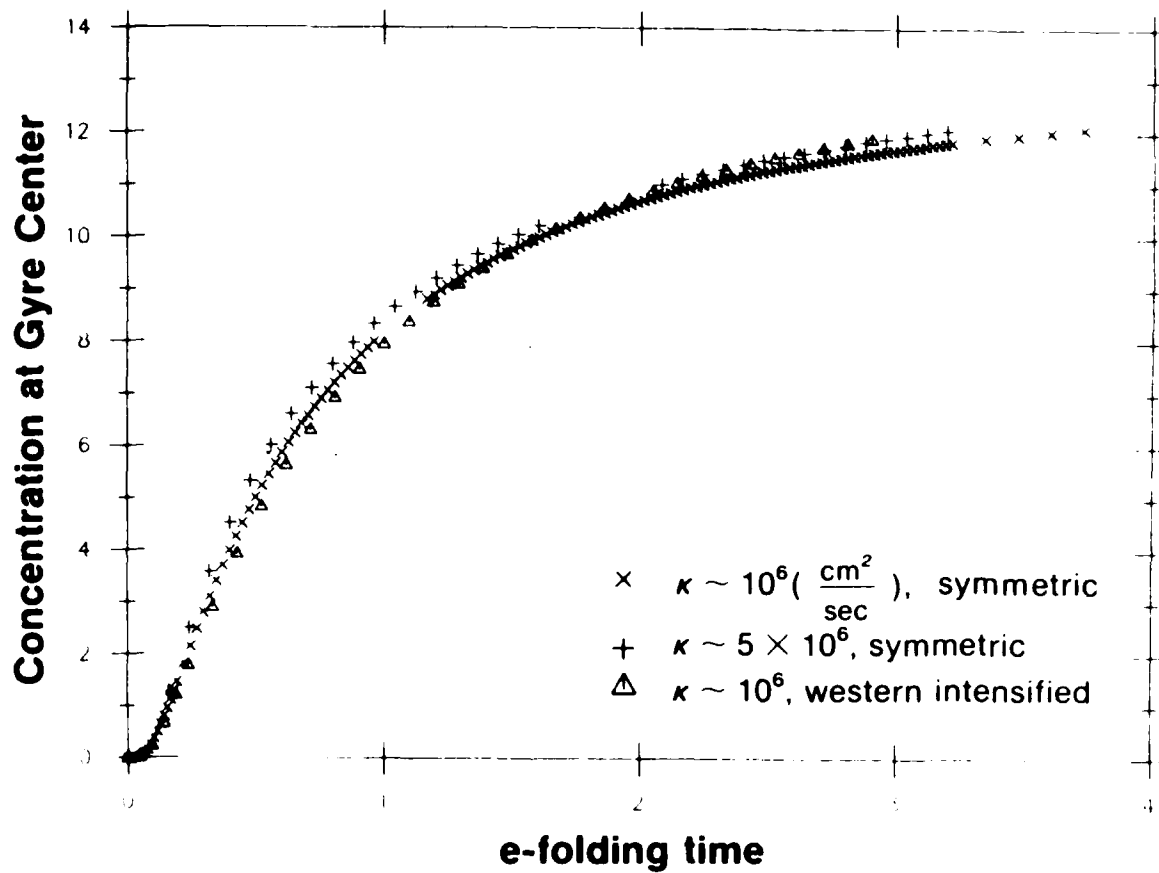


Figure 2.28: The accumulation curves for each of the three experiments without vertical mixing (Figures 2.5 and 2.27) where the time axis has been normalized by the associated spin-up time.

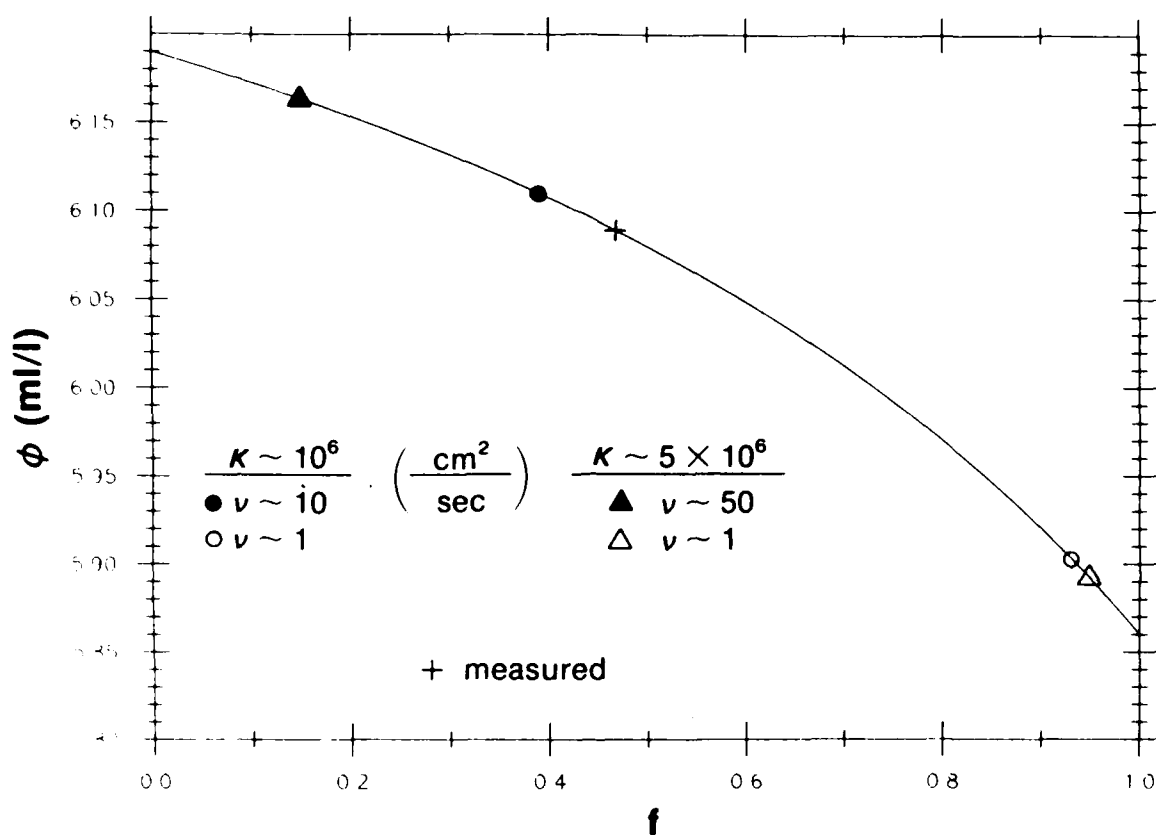


Figure 2.29: The value of the oxygen background concentration as predicted by the transfer model. The particular values for the examples discussed are shown in comparison to the measured quantity  $\bar{\theta}_u$ .

hand is smaller than most of the estimates found in the literature. For example, direct estimates of  $\kappa$  can be made using SOFAR float data, and Freeland et al. (1975) calculated a value of  $7 \times 10^6 \text{ cm}^2/\text{sec}$  using data collected for the MODE area ( $28^\circ\text{N}$ ,  $69^\circ\text{W}$ ). Using the same technique Price (personal communication) computed values in the range of  $1.5\text{--}8.2 \times 10^7 \text{ cm}^2/\text{sec}$  for the LDE region ( $31^\circ\text{N}$ ,  $70^\circ\text{W}$ ). It should be noted though that these estimates are for the thermocline, and Price detects a decrease in the size of  $\kappa$  with depth. Still, the eddy coefficients calculated here are for the area near the Gulf Stream which is an area of increased eddy activity.

### B) Conclusions

The review of the data in Hogg et al. (1986) showed that in the deep layer there is a broad region characterized by very weak property gradients to the south of the DWBC centered at roughly  $60^\circ\text{W}$ . Such homogenization is suggestive of closed circulation, i.e. the Northern Recirculation Gyre. In addition, it implies that the Peclet number of the flow is large in the sense discussed in chapter one. Closer inspection of the data, within the context of the present model study, yields a consistent picture in regards to this feature and other features which are less revealing.

The plume of oxygen which extends from the DWBC into the interior delimits the southern extent of the gyre flow that has turned offshore. This serves as additional evidence for the argument of tight recirculation of the NRG. In contrast to the salinity, the distribution of oxygen has a slight relative minimum in the center of the gyre which may be a trademark of vertical mixing. The inward flux of oxygen associated with this, along with the value of the minimum gives rise to oceanic mixing coefficients of  $\kappa \sim 10^6 \text{ cm}^2/\text{sec}$ ,  $\nu \sim 10 \text{ cm}^2/\text{sec}$  for this region.

The value of the vertical diffusivity seems somewhat large, but when viewed in terms of the model the system is characterized by only moderate vertical mixing. The model implies that the amount of tracer which enters the gyre is related to the amplitude of an appropriate section across the DWBC, most likely near  $50^\circ\text{W}$ . When applied to the data this says that the gyre contains approximately 40 percent of the oxygen that is available to it

(that is to say 40 percent of the level that would exist if there were no vertical mixing at all). In light of how sensitive the gyre level is to vertical mixing (Figure 2.14) it is the case then that this effect is mild.

This should in turn be contrasted to the case of the symmetric model gyre. When applying that case to the data it turns out that only 10 percent of the available oxygen makes it into the gyre (recall that this resulted in an inconsistency) which is approaching the limit of strong vertical mixing. We see then that it is a very important consequence that the gyre flow come in such close contact with the boundary current. It greatly increases the efficiency with which tracer is transported into the interior and enables the lateral flux to overcome the large vertical flux in supplying the NRG with a significant amount of oxygen. This effect has no bearing on the salinity distribution however. The results of the numerical model imply that without vertical flux certain characteristics of the flow field have no effect on the level of the gyre.



## CHAPTER THREE: TIME DEPENDENT INPUT

Preliminaries

In the previous two chapters a simple model was presented of the advection and diffusion of a passive tracer from the Deep Western Boundary Current into the Northern Recirculation Gyre of the deep Gulf Stream. In chapter two when the results were applied to the data, only the distributions of salt and oxygen were considered. It is assumed that these tracers are in quasi-steady state, that is to say the source of tracer provided by the DWBC is not changing substantially in time. In this chapter we consider what happens when this source grows in time, as is the case with freon.

The DWBC fluxes various tracers into the North Atlantic, among which are substances called chlorofluoromethanes. The two which are most readily measured are commonly referred to as freon-11 (F-11) and freon-12 (F-12). Freon is man-made (for instance it is used in refrigerants) and substantial amounts began to accumulate in the atmosphere around 1950. Since that time production has increased rapidly. As is the case with oxygen, the surface waters of the Norwegian-Greenland (N-G) Sea that sink to form the DWBC, having been in contact with the atmosphere, are high in freon content. In stark contrast to oxygen though, and what makes freon so interesting to study, is the fact that they have been present for only a short time.

By keeping track of the production of freon by industry versus natural depletion, the atmospheric source function from 1950 to the present is known with some certainty (Smethie, personal communication). This presents a very good opportunity to study the invasion of a passive tracer into the world oceans as related to its input. This is not the only appealing aspect of studying freon though. Unlike its counterpart tritium, with the advent of recent technology freon is relatively easy to measure and can be done so aboard ship. In addition, measurements tend to be characterized by a high signal to noise ratio (Hogg et al., 1986).

Within the realm of the present study it is of interest to consider freon in addition to the steady tracers already analyzed. (For instance we know how long freon has been injected at high northern latitudes: has this

been long enough for a substantial amount to accumulate in the NRG?) It is however not trivial to incorporate such time dependency into the machinery that has been developed. This is because there is much involved in the history of a water parcel as it passes from the surface water in the N-G Sea via the DWBC to  $50^{\circ}\text{W}$ , at which point it enters our domain of study. For the cases of salinity and oxygen we could ignore this previous history, it was assumed that a property section across the DWBC remains stationary in time. For freon this is obviously not true.

In the numerical runs of the previous chapters the input of tracer into the domain was specified as a Gaussian distribution across the upstream edge of the boundary current (a step function in time). In light of all the factors involved in the overflow process as well as the shear structure of the DWBC, it would be extremely difficult to estimate how this input would behave as a function of space and time for the freon case. As such, a numerical model with a regional domain is not useful here. However, recall that the input to the diffusive transfer model corresponds to just the core value of the distribution across the boundary current. Therefore to make use of the transfer model we need only know how the freon core value evolves in time at  $50^{\circ}\text{W}$  -- a problem which is much more tractable.

It is the case then that before we make use of the transfer model for the DWBC/NRG system, we must first model in a consistent fashion how the atmospheric input of freon is modified during the processes which eventually lead it around the Grand Banks in the core of the DWBC. This has been done in two stages: the deep water formation stage which simulates the overflow process, and the subsequent boundary current stage where the water travels away from the overflow region while mixing with surrounding water. Both of these representations are greatly simplified, but this is in the spirit of the transfer model. The end result of these processes is finally coupled to the transfer model and contrasted to the salt and oxygen cases.

In the literature there have been at least two cases in which the age of the water comprising a current has been estimated using its F-11:F-12 ratio values (Smethie and Trumbore, 1984; Weiss et al., 1985). The method assumes that the flow mixes with surrounding water which is mostly void of freon, and also that the ratio of the source waters is not altered during the

formation process. When the method is applied to the DWBC with the ABCE data set, the age of the water so calculated suggests an unreasonably slow core speed. Two separate boundary current models are presented here, each based on the premise that as time progresses the mixing that occurs is no longer with freon-free water. When considered along with the overflow process, this leads to substantially larger values of the core speed.

#### Overflow Basin Model

There are two areas at high latitude where convective overturning occurs supplying deep water into the northern North Atlantic: the Norwegian-Greenland Sea and the Labrador Sea. The water which is formed in the N-G Sea is more dense than its Labrador counterpart, and it is this water which upon entrainment forms the DWBC (Worthington, 1970). There are three sills over which the newly formed water in the N-G Sea flows into the Atlantic. These areas are the Denmark Straits, the Iceland-Faeroe Ridge, and the Faeroe Bank Channel (Figure 3.1). The latter two are so close to each other that they are usually considered as a single overflow region called the Iceland-Scotland Ridge.

At present it is uncertain as to what extent each of these overflows contributes to the water which comprises the DWBC downstream from this area. It is documented that the Iceland-Scotland overflow, having traveled down the slope from the sill, travels westward through the Gibbs fracture zone. According to Worthington (1970) this flow then joins the Denmark Straits overflow and the combined flow eventually makes its way southward as the DWBC. Swift (1984) argues that the density of the overflow water at the two locations is comparable, but the Iceland-Scotland flow undergoes more intense mixing as it progresses from the sill so that the water which passes through the Gibbs fracture zone is less dense than the Denmark Straits contribution. As a result the two flows don't really combine but rather influence one another. More in line with this, Smethie and Trumbore (1984) present a water property analysis that suggests the classical DWBC found south of the Grand Banks is comprised mainly of Iceland-Scotland overflow, and that in this area the flow which originated from the Denmark Straits occurs as weaker, more dense filament-type flows.

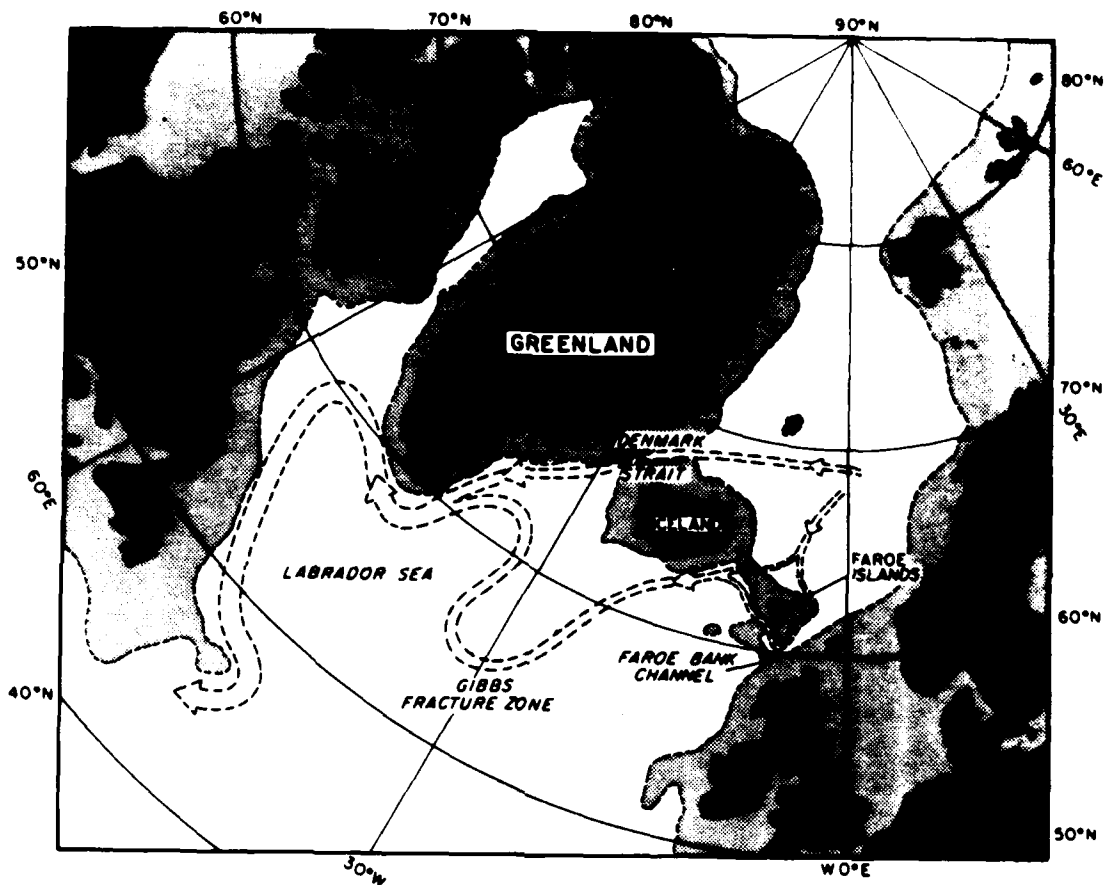


Figure 3.1: Map showing the three overflows of the Norwegian-Greenland Sea (from Warren, 1981) which eventually combine to form the DWBC as described by Worthington, 1970.

For this work it has been assumed that the DWBC is composed solely of water of Iceland-Scotland origin. It is clear though that there are other influences at work with regard to the freon signal of the current, and it would be beneficial to study this point in greater detail. It is an accepted idea now that the fluid which overflows the Iceland-Scotland Ridge (as well as that which overflows the Denmark Straits sill) originates not from abyssal depths, but from intermediate depths in the basin (Bullister, 1984). It is consistent then that the water at these depths is replenished convectively [due to surface cooling (Worthington, 1970)] and that there is only diffusive interaction with the deepest water.

This suggests the following overflow basin model to compute the flux of freon over the sill. An influx of water into the basin occurs in the surface layer, the water acquiring a freon concentration according to the atmospheric level at the time. As a result of heat loss to the atmosphere the fluid then sinks, ventilates the intermediate layer, and resides in the basin for a while before eventually overflowing. While below the surface the fluid can mix diffusively with both the water within the layer and with the abyssal water. Based on equilibration times for freon it is reasonable to assume that the surface layer is in equilibrium with the atmosphere at all times (Smethie, personal communication). Using estimates of solubility then, the freon concentration of the surface water becomes a known function of time. This information is the starting point of the model, it is from this function that the overflow concentration is computed and ultimately the DWBC core concentration at  $50^{\circ}\text{W}$ .

The details of the model are outlined in Figure 3.2 which shows the simplified scenario of the overflow process. In the ocean the convective process is believed to happen as localized events. Because such events are free to occur anywhere throughout the basin we envision a spatially uniform flux from surface layer to intermediate layer, which is represented by a specified volume transport of freon concentration  $\theta_i(t)$ . Lateral mixing also occurs uniformly throughout the basin stirring up tracer in the intermediate layer. It is therefore assumed that the amount of freon convected from above in a given time increment is "instantaneously" diluted to a uniform concentration throughout the intermediate layer. This representative

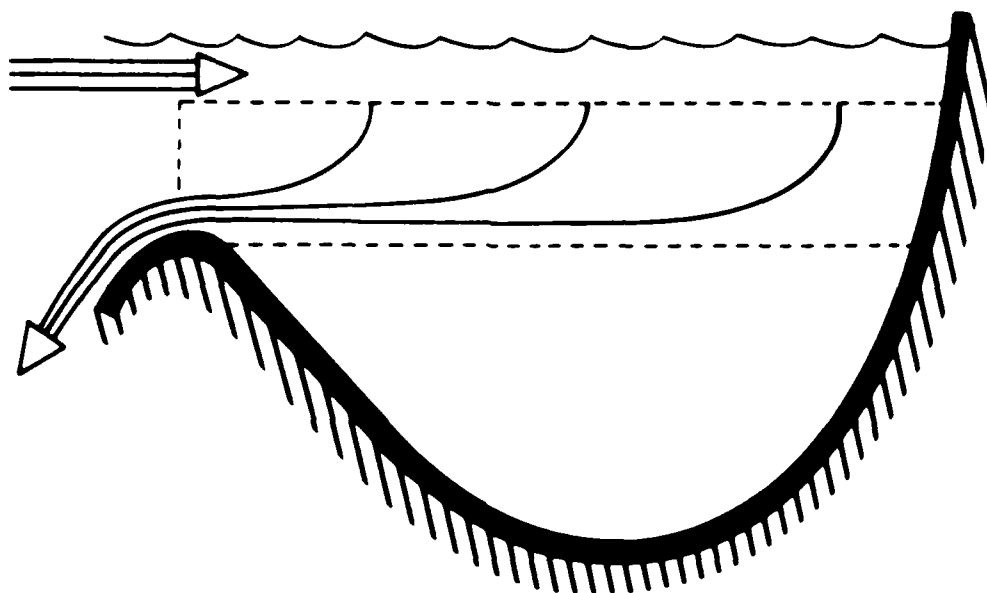


Figure 3.2: Schematic outlining the overflow process. The dashed region is the intermediate layer from where the overflow originates.

concentration  $\theta_0(t)$  is then also the concentration of the overflow, whose transport matches the convective transport. To keep the situation as simple as possible we have chosen to ignore any diffusion between the intermediate layer and the abyssal layer, arguing that the effect of such diffusion is of secondary importance relative to the convection.

The freon budget for the intermediate layer that results from this convective source and overflow sink is represented as follows,

$$\frac{dF}{dt} = Q(\theta_i(t) - \theta_0(t))$$

where  $F$  = total amount of freon in the intermediate layer,  
 $Q$  = transport into/out of the intermediate layer,  
 $\theta_i(t)$  = surface layer concentration,  
 and  $\theta_0(t)$  = intermediate layer concentration (overflow concentration).  
 The quantity of freon  $F$  is equal to  $V\theta_0(t)$  where  $V$  = volume of the intermediate layer, and constraining  $V$  to remain constant the above expression can be written

$$T_R \frac{d\theta_0(t)}{dt} + \theta_0(t) = \theta_i(t) \quad (3.1)$$

where  $T_R$  = residence time of the intermediate layer.

Assuming that the intermediate layer is initially freon-free, the solution to (3.1) is

$$\theta_0(t) = \frac{1}{T_R} \int_0^t e^{-\frac{t-t'}{T_R}} \theta_i(t') dt' \quad (3.2)$$

The two limits of (3.2) are as follows. If the residence time of the layer is much smaller than the time scale over which the input changes, then the overflow concentration mimics the surface water concentration, or in terms of (3.2),

$$\theta_0(t) \sim \theta_i(t) \quad (3.3)$$

In the opposite extreme when the input time scale is substantially shorter than the residence time, (3.2) gives

$$\theta_0(t) \sim \frac{1}{T_R} \int_0^t \theta_i(t') dt', \quad (3.4)$$

which says that successive input concentrations are continuously being mixed in the intermediate layer. In the former limit note then that there is no need for the overflow basin model in so far as determining the core concentration required at 50°W.

Figure 3.3 shows the surface layer F-12 concentration versus time from 1950 to 1983 using solubility values for 0°C, 35‰ (1983 is the year the freon data was collected in the region of the NRG). The sill depth of the Faeroe-Bank Channel is ~850 m. We assume that the surface layer is approximately 300 m thick, and that the intermediate layer extends from there to ~1000 m. Estimates for the overflow of the Iceland-Scotland System put the transport at roughly 1-2 Sverdrups (for example, Worthington, 1970). Approximating the lateral extent of the region which supplies water to this overflow then gives an estimate of the residence time of the intermediate layer  $T_R \sim 10$  years. This value is in between the limits (3.3) and (3.4), and the resulting F-12 overflow concentration versus time is shown in Figure 3.3 compared with the surface water concentration.

There has been only one cruise which has sampled freon near the Faeroe-Bank Channel. This was the HUDSON 82-001 expedition conducted in 1982. Bullister (1984) graphs the values of freon versus density for the two stations nearest the sill. Using the estimate of the overflow density there from Swift (1984) this gives a F-12 overflow concentration of ~1 p-mole/kg in 1982, which is reasonably close to the basin model value from Figure 3.3. (Note that the agreement could be made perfect by adding a small amount of mixing with the abyssal layer.)

#### The F-11:F-12 Ratio

One aspect of freon that has a useful application is the fact that the amount of F-11 in the atmosphere (and surface water) has been increasing at



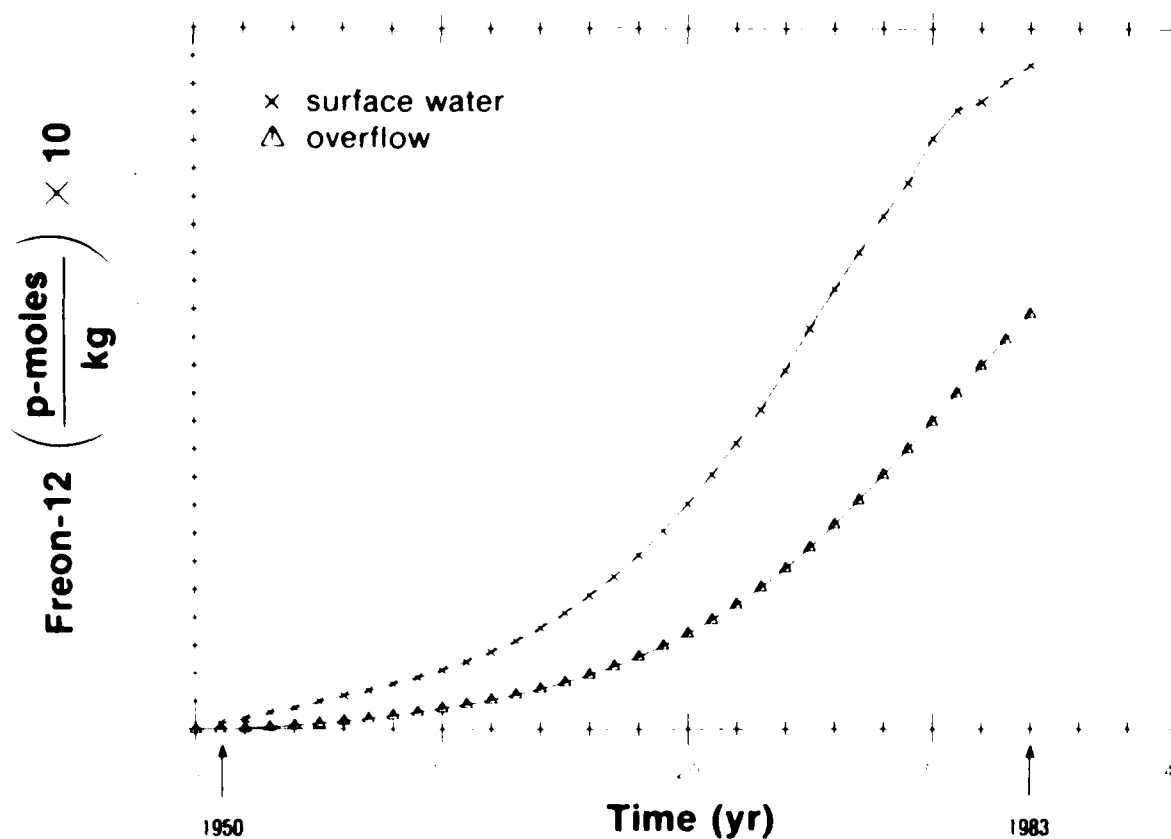


Figure 3.3: Concentrations of F-12 in the surface water and overflow water, assuming a residence time of 10 years for the intermediate layer of the overflow basin. The first measurement (year one) corresponds to 1950, and 1983 is the year the ABCE freon data was collected.

a quicker rate than that of F-12 over much of the time that the two have been present. Figure 3.4 plots the ratio of the concentration of F-11 to that of F-12 in the surface water versus time. Suppose the water which forms a current exhibits this trend and as it progresses downstream mixes entirely with fluid that is freon-free. This means that while the F-11 and F-12 content of the water decreases, the relative amount remains the same as it was when the water left its source, i.e. the value of the ratio remains constant. Since the ratio at the source is constantly increasing, this means the water downstream can be matched to the time when it was isolated from the source, so indicating the age of the water and the speed of the current.

This technique has been used by Weiss et al. (1985) to determine the age of high freon intermediate water along the western boundary of the South Atlantic, and by Smethie and Trumbore (1984) applied to the DWBC. In both instances input functions were derived from the atmospheric concentration data using solubilities appropriate to the source waters (the Labrador Sea and Norwegian-Greenland Sea respectively). The corresponding ratio curves were then used to determine the age. Note that this corresponds precisely to using  $\theta_i(t)$  as the input for the DWBC, i.e. ignoring the effect of the formation process. In Figure 3.4 it is seen that F-11:F-12 ratio of  $\theta_i(t)$  flattens out as of 1978. The above ratio curves exhibit this feature accordingly, which means that a measured value of the ratio near that level can at best determine the age within a range of possible values. This difficulty arose in both studies.

In the overflow basin model we can easily see how the F-11:F-12 ratio is affected by the overflow process. In the small residence time limit the ratio of the overflowing water is identical to that of the surface water (as are the concentrations themselves). In the large residence time limit, (3.4) gives

$$R_0(t) = \frac{\int_0^t \theta_{i1}(t') dt'}{\int_0^t \theta_{i2}(t') dt'} , \quad (3.5)$$

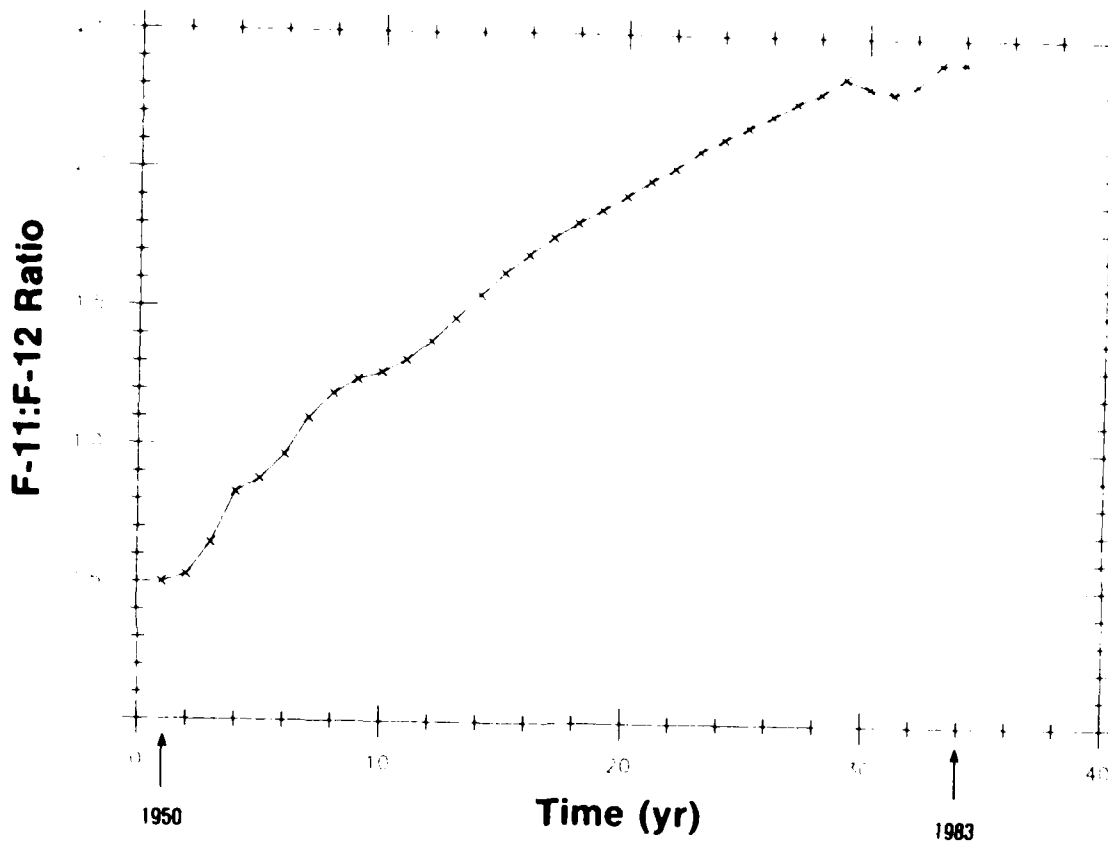


Figure 3.4: Value of the F-11:F-12 ratio in the surface water of the overflow basin.

where  $R_o(t)$  = ratio of overflow water,  
 $\theta_{i1}$  = surface water concentration of F-11,  
 $\theta_{i2}$  = surface water concentration of F-12.

Note that in both limits the ratio is independent of the residence time  $T_R$ . In one case it is the ratio of the concentrations, and in the other it is the ratio of their integrals. These two curves are plotted in Figure 3.5. The difference between them represents the maximum extent by which the F-11:F-12 ratio can be altered in the overflow basin.

In between these limits the ratio curve does depend on  $T_R$ . The case for  $T_R = 10$  yr is also plotted in Figure 3.5. Note that because of the averaging process that occurs in the basin the 10 year overflow curve monotonically increases in time in contrast to that for the surface water. This means then not only are the ratios lowered, but the ambiguity in determining the age no longer exists. These results suggest that it is important to consider the overflow process when applying the freon dating technique.

#### Boundary Current Models

In the ocean as newly formed water flows over a sill it proceeds downslope and entrains water, forming a current of increased strength. Throughout the length of the current it is constantly mixing with surrounding fluid. The fluid with which it mixes contains varying amounts of the properties which are being advected by the flow, and for the case of freon it is usually assumed that the level in the neighboring fluid is negligible compared with that in the current. We are presently considering only the core of the flow and within this context can devise a simulation of the mixing process that enables us to quantitatively discuss the ratio dating process and the freon-free mixing assumption that goes with it.

We assume that the current, which has no "thickness" and is represented by a speed  $U$ , flows adjacent to a reservoir which is characterized by a given (constant) concentration of freon  $\theta_B$ . The mixing that occurs is represented by a diffusive time scale (as in chapter two). The governing equation for the evolution of freon in the current is

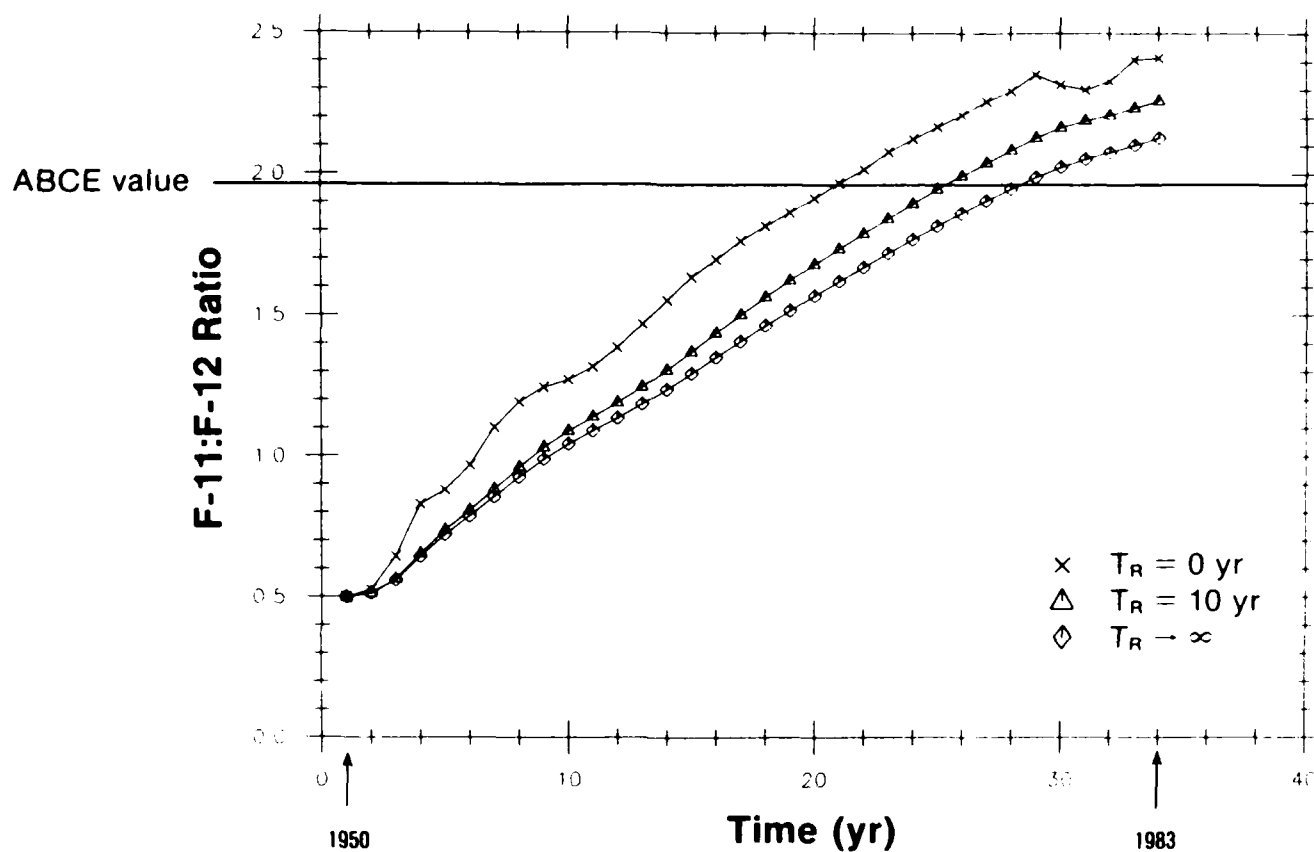


Figure 3.5: Value of the F-11:F-12 ratio in the overflow water compared to that in the surface water of the basin. The two overflow curves are those for a 10 year residence time and an infinitely long residence time. The solid line marks the ratio value of 1.97, that value at 50°W in the core of the DWBC as extrapolated upstream using the ABCE data from 1983. It is seen that the  $T_R = 10$  year curve reaches this value ~8.5 years prior to 1983, while the surface water curve reaches it ~13 years before.

$$\frac{\partial \theta}{\partial t} = -U \frac{\partial \theta}{\partial x} - \frac{(\theta - \theta_B)}{\tau}, \quad (3.6)$$

where  $\theta(x,t)$  = freon concentration in the current  
and  $\tau$  = diffusive decay time.

A simple scale analysis (using the diffusivities estimated in chapter two and typical lengths scales of the DWBC freon signal) suggests that vertical mixing in the current is as important as cross-stream lateral mixing, and that alongstream lateral mixing is negligible with respect to these. In line with this, in (3.6) we have ignored the latter and have represented the other two by a single decay term. The quantity  $\theta_B$  should be thought of as a basin-wide average concentration of the surrounding fluid. The upstream input of freon to (3.6) is the overflow concentration versus time that was computed from the overflow basin model, and the initial condition is that the level of tracer in the current (and overflow) is the same as that in the reservoir. The solution to (3.6) is

$$\theta(x,t) = \begin{cases} \theta_B & , \quad x > Ut \\ \theta_0 \left( \frac{Ut - x}{U} \right) e^{-\frac{x}{U\tau}} + (1 - e^{-\frac{x}{U\tau}}) \theta_B & , \quad x \leq Ut. \end{cases} \quad (3.7)$$

The data set that was described in chapter two contains freon measurements at the station locations of the OCEANUS 134 cruise in 1983 (Figure 2.19). This provides a value of the core concentration at 50°W with which to compare  $\theta(x = 5500 \text{ km}, t = 34 \text{ yr})$ , where  $x = 5500 \text{ km}$  is the estimated distance along the DWBC from the Iceland-Scotland overflow to 50°W, and  $t = 34 \text{ yr}$  corresponds to 1983. A value of  $\theta_B$  to use is the freon equivalent of the oxygen background that was used in chapter two (Figure 2.27). With these we use (3.7) to determine a value of  $\tau = 1.06 \text{ yr}$  and obtain how the core concentration of freon changes in time at 50°W, which is the information required for the NRG transfer model.

Consider the expression for the F-11:F-12 ratio at 50°W as computed from (3.7),

$$R(t) = \begin{cases} \frac{\theta_{B1}}{\theta_{B2}} & , \quad x > Ut \\ R_0 \left( \frac{Ut - L}{U} \right) \left[ \frac{1 + \frac{\alpha(p)\theta_{B1}}{\theta_{O1} \left( \frac{Ut - L}{U} \right)}}{1 + \frac{\alpha(p)\theta_{B2}}{\theta_{O2} \left( \frac{Ut - L}{U} \right)}} \right] & , \quad x \leq Ut \end{cases} \quad (3.8)$$

where  $\theta_{O1}, \theta_{B1}$  = overflow, background concentrations of F-11

$\theta_{O2}, \theta_{B2}$  = overflow, background concentrations of F-12

$$\alpha(p) = \frac{(1 - e^{-\frac{1}{p}})}{e^{-\frac{1}{p}}}$$

$$p = \frac{U\tau}{L}$$

$L$  = distance from overflow to 50°W.

The term in square brackets in (3.8) represents the deviation of the ratio from that at the overflow (besides from the delay in time due to advection).

In order for the deviation to be small, the quantity  $\frac{\alpha(p)\theta_B}{\theta_O(t)}$  must be small for both F-11 and F-12. The parameter  $p$  is a Peclet number which measures the advective strength of the current versus the mixing that occurs, and for large values of  $p$  the function  $\alpha(p)$  is small. So there are three conditions which will cause the ratio of the water to remain unchanged through the course of progressing downstream: very strong input, very weak background, or very weak mixing between the flow and surrounding fluid.

This implies that the freon overflow concentrations have indeed become large enough by 1983 that the deviation due to non-zero background is negligible, i.e. the freon dating technique is applicable to the present data set. However, when the measured ratio is matched to the overflow ratio it gives an advective time of 8.5 yrs, which translates to a core speed of approximately

2 cm/sec. This value seems too small. Below we discuss two separate boundary current models that treat the mixing differently and result in larger estimated core speeds for the same overflow ratio curve of Figure 3.5.

Using the value of  $\tau$  and a value of  $U = 8$  cm/sec, the Peclet number is found to be  $O(1)$ . This means that the freon overflow concentrations have become large enough by 1983 that the deviation due to nonzero background is negligible, i.e. the freon-free mixing assumption appears valid in the present case. If we compute the age of the water as was done in the studies described above, this results in a DWBC core speed of  $\sim 1$  cm/sec (Figure 3.5). If we include the overflow process but still make the freon-free mixing assumption, this increases the prediction to  $\sim 2$  cm/sec. These values seem too small. For example, to get a transport of 10 Sverdrups (the value estimated by Worthington (1970) for the DWBC) for a current 200 km wide and 1000 m deep, the average flow speed must be 5 cm/sec. Below we discuss two separate boundary current models which contain different mixing schemes that result in larger estimated core speeds for the same overflow ratio curve of Figure 3.5.

#### A) Back-Mixing Model

Expression (3.8) tells us just how large the background concentration of freon would have to be in order to affect the ratio of the current at  $50^\circ\text{W}$ . When applied as above, this of course assumes that the background value computed from the OCEANUS 134 data set is valid at all times and at every location along the current, which is certainly not the case. Even so, the assumption of freon-free mixing results in an unrealistic core speed and suggests that we explore the possibility that this is not the case. Two scenarios are considered here, the first of which is based on the following simple idea. We assume that the first bit of water containing freon which overflows the sill does mix entirely with freon-free water. However, the amount of freon that it imparts along its path to the surrounding fluid is enough to significantly raise the freon level there. Thus the next bit of water that flows through mixes not with freon-free water, but with water that has a concentration reminiscent of the previous flow, i.e. some of boundary current water that diffuses into the neighboring fluid then proceeds to



back-mix with newer boundary current water. It is evident then why this effect can reduce the ratio in the current, for its water is constantly mixing with older, lower ratio water. The difference between this model and the process described by equation (3.6) is that here we keep track of the surrounding fluid as well as the fluid in the current.

Consider a short section of boundary current (and surrounding fluid) as depicted in Figure 3.6, extending from the overflow region. We identify three regions: the inner core which moves with constant speed  $U_c$  (i.e. the current), the adjacent shoulder water (which is still), and the "infinite" amount of fluid which surrounds this. It was mentioned earlier that vertical mixing and lateral cross-stream mixing are of comparable strength in the current (and that alongstream mixing can be ignored). We are now more precise about this. Consider the advective-diffusive equation

$$\theta_t + u\theta_x = \kappa\theta_{xx} + \kappa\theta_{yy} + v\theta_{zz} \quad (3.9)$$

where  $x$  = alongstream distance,  
 $y$  = cross-stream distance,  
 $z$  = vertical distance,  
 $\kappa, v$  = lateral, vertical diffusivity (assumed constant),  
 $u$  = flow speed,  
 and  $\theta$  = freon concentration.

We let  $H$ ,  $L_y$ , and  $L_x$  represent the vertical, cross-stream, and alongstream length scales of the tracer distribution. Inspection of the ABCE data shows that in the boundary current  $H \ll L_y \ll L_x$ . If (3.9) is scaled accordingly it is seen that the ratio of the alongstream diffusive term to the cross-stream diffusive term is  $O(L_y/L_x)^2 \ll 1$ , and so to lowest order the balance is

$$\theta_t + u\theta_x = \kappa\theta_{yy} + v\theta_{zz} \quad (3.10)$$

We now introduce a stretched coordinate in the vertical direction. In particular, we define

$$z' = \left(\frac{L_y}{H}\right)z,$$

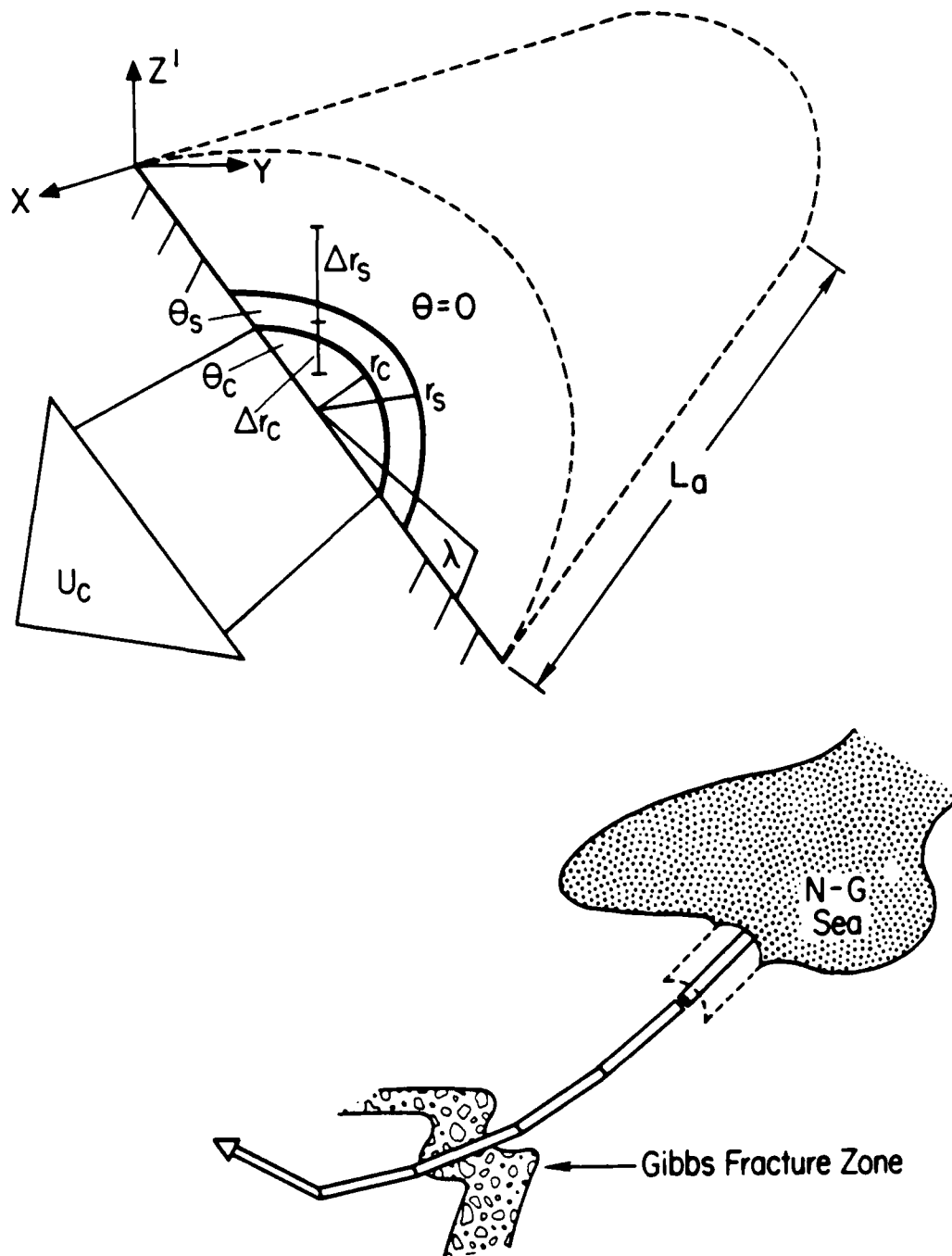


Figure 3.6: Schematic depicting the DWBC as being composed of many short sections of length  $L_a$ . An enlargement is shown of the first such section originating from the overflow basin. The flow is confined to the innermost region.

in terms of which (3.10) becomes

$$\theta_t + u\theta_x = \kappa\theta_{yy} + \left(\frac{L_y^2}{H^2}\right)\nu\theta_{z'z'} \quad (3.11)$$

In chapter two we constrained the values of  $\kappa$  and  $\nu$  by the relation (2.28), which says that  $\kappa/\nu \sim 10^5$  (see (2.29)). Using  $H \sim 1000$  m,  $L_y \sim 300$  km (Figure 3.7) this results in  $L_y^2/H^2 \sim 10^5$  as well, which implies that both types of mixing are equally as important. We therefore set the ratio  $\kappa H^2/\nu L_y^2 = 1$ , and rewrite (3.11) as

$$\theta_t + u\theta_x = \kappa(\theta_{yy} + \theta_{z'z'}) \quad (3.12)$$

where

$$\kappa = \left(\frac{L_y^2}{H^2}\right)\nu.$$

The stretched coordinate then increases the vertical diffusive length to the size of the cross-stream diffusive length, so that diffusion acts isotropically in the  $y$ - $z'$  plane.

It is this coordinate frame in which the freon signal associated with the boundary current appears circular (Figure 3.7) and for which the schematic in Figure 3.6 applies. Accordingly, the section of boundary current is described using cylindrical coordinates  $(x, r, \lambda)$ . The  $x$  direction is taken alongstream, and  $r$  and  $\lambda$ , the radial and azimuthal coordinates, are defined by

$$\begin{aligned} y &= r \cos \lambda, \\ z' &= r \sin \lambda. \end{aligned}$$

Equation (3.12) is then written

$$\theta_t + u\theta_x = \frac{\kappa}{r} (r\theta_r)_r \quad (3.13)$$

It is assumed that the concentration of tracer is independent of  $\lambda$ . (In the outer reservoir the concentration is taken to be zero.) The alongstream and

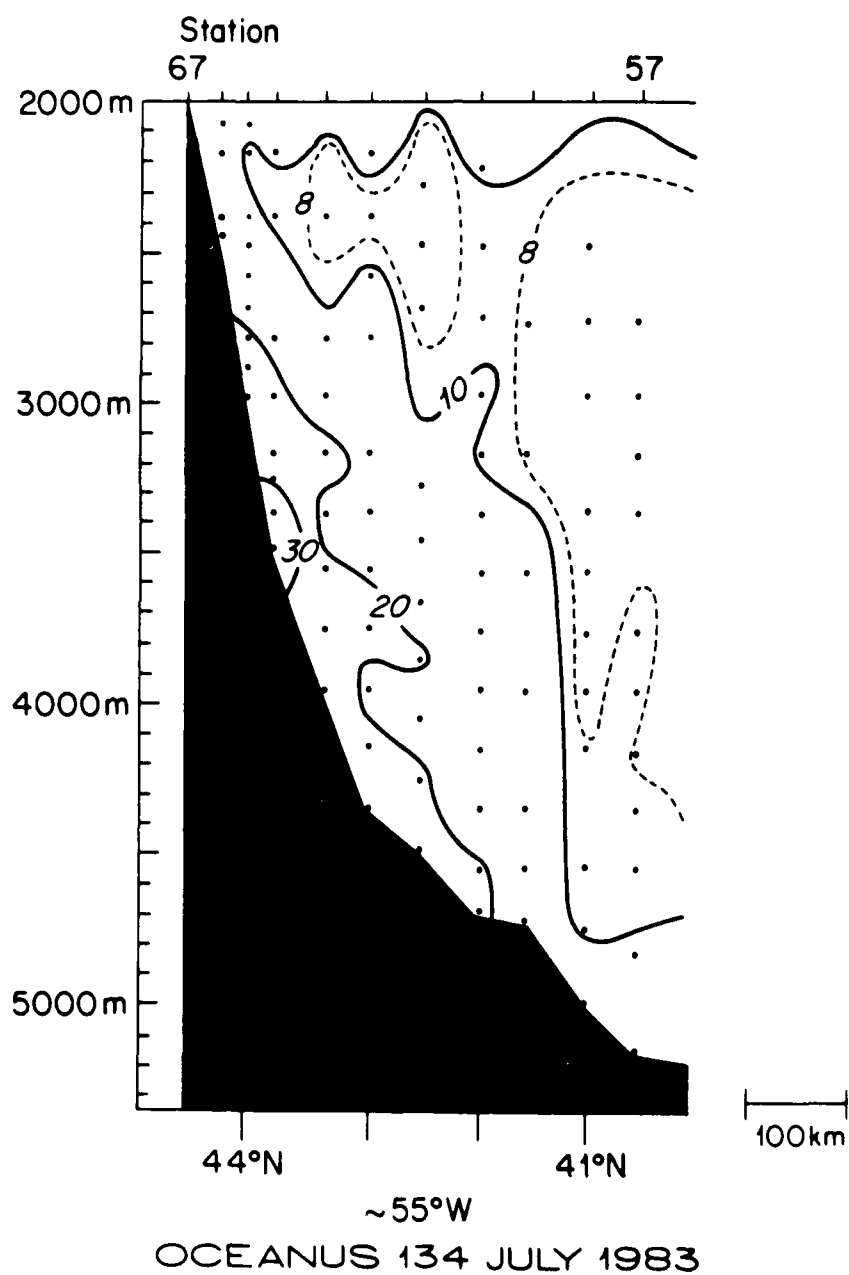


Figure 3.7: Vertical section of F-12 (p-moles/kg x 10) used to estimate the scales of the DWBC signal (present against the slope).

radial dependency is treated using a finite-difference representation so that the concentration in each region is characterized by a single value.

The length of the section  $L_a$  is taken small enough that fluid flushes through the core region very quickly. Correspondingly, it is assumed that the region adjusts instantly to changes in input, and so is governed by the steady state balance

$$U_c \theta_x = \frac{\kappa}{r} (r \theta_r)_r \quad \text{at all times.} \quad (3.14a)$$

The shoulder water acquires tracer by way of diffusion from the core, and loses tracer through mixing with the fluid in the outer reservoir. The shoulder water is governed by the equation

$$\theta_t = \frac{\kappa}{r} (r \theta_r)_r . \quad (3.14b)$$

Using upstream differencing in the alongstream direction, (3.14a) and (3.14b) become

$$U_c \left( \frac{\theta_j(r,t) - \theta_{j-1}(r,t)}{L_a} \right) = \frac{\kappa}{r} \frac{\partial}{\partial r} \left( r \frac{\partial}{\partial r} \theta_j(r,t) \right) \quad (3.15a)$$

$$\frac{\partial}{\partial t} \theta_j(r,t) = \frac{\kappa}{r} \frac{\partial}{\partial r} \left( r \frac{\partial}{\partial r} \theta_j(r,t) \right) , \quad (3.15b)$$

where the subscript  $j$  denotes the x-grid point index ( $L_a$  is the grid spacing). Integrating (3.15a) and (3.15b) over the cross-sectional area of the core and shoulder regions respectively gives

$$\frac{U_c}{L_a} \int_0^{r_c} \int_{\lambda_1}^{\lambda_2} dr d\lambda r (\theta_j(r,t) - \theta_{j-1}(r,t)) = \kappa \pi r_c \frac{\partial}{\partial r} \theta_j(r_c, t) \quad (3.16a)$$

$$\int_{r_c}^{r_s} \int_{\lambda_1}^{\lambda_2} dr d\lambda r \frac{\partial}{\partial t} \theta_j(r,t) = \kappa \pi \left( r_s \frac{\partial}{\partial r} \theta_j(r_s, t) - r_c \frac{\partial}{\partial r} \theta_j(r_c, t) \right) , \quad (3.16b)$$

where the limits of integration are depicted in Figure 3.6.

Using centered differencing in the radial direction, (3.16a) and (3.16b) become

$$\frac{A_c U_c}{L_a} (\theta_{c_j}(t) - \theta_{c_{j-1}}(t)) = \frac{\kappa \pi r_c}{\Delta r_c} (\theta_{s_j}(t) - \theta_{c_j}(t)) \quad (3.17a)$$

$$A_s \frac{d}{dt} \theta_{s_j}(t) = \frac{\kappa \pi r_s}{\Delta r_s} (0 - \theta_{s_j}(t)) - \frac{\kappa \pi r_c}{\Delta r_c} (\theta_{s_j}(t) - \theta_{c_j}(t)), \quad (3.17b)$$

where  $\Delta r_c$  and  $\Delta r_s$  are the grid spacings,  $A$  denotes cross-sectional area, and the subscripts  $c$  and  $s$  are the radial grid point indices referring to the core and shoulder regions respectively (Figure 3.6).

The input into the core region,  $\theta_{c_{j-1}}(t)$ , is set equal to the over-flow  $\theta_0(t)$ . Also, we do not want the shoulder region to be too vast (to allow it to readily accumulate tracer), so  $A_s$  is set equal to  $A_c$ . (This serves as a simplification as well.) Then with some rearrangement (3.17a) and (3.17b) become

$$\theta_{c_j}(t) = \theta_0(t) - \frac{T_r}{\tau_c} (\theta_{c_j}(t) - \theta_{s_j}(t)) \quad (3.18a)$$

$$\frac{d}{dt} \theta_{s_j}(t) = \frac{(\theta_{c_j}(t) - \gamma \theta_{s_j}(t))}{\tau_c}, \quad (3.18b)$$

where  $T_r = \frac{L_a}{U_c}$  = residence time of the fluid in the core region,

$\tau_c = \left(\frac{A_c \Delta r_c}{p_c}\right) \frac{1}{\kappa}$  = diffusive time between the core and shoulder,

$\tau_s = \left(\frac{A_s \Delta r_s}{p_s}\right) \frac{1}{\kappa}$  = diffusive decay time of the shoulder into the reservoir,

$$\gamma = 1 + \frac{\tau_c}{\tau_s},$$

and  $p_c, p_s$  = outer perimeter of core, shoulder region.

The parameter  $\gamma$  is called the reservoir parameter. The value of  $1/\gamma$  represents the fraction of the core concentration that the shoulder water would equilibrate to if given sufficient time. This parameter is the key to the model. When  $\tau_s \gg 0$  ( $\gamma \gg \infty$ ) the outer reservoir prohibits any tracer from accumulating in the shoulder region, so the core mixes with freon-free water. We are interested then in finite values of  $\gamma$ . When  $\tau_s \gg \infty$  ( $\gamma = 1$ ) this corresponds to the case when the shoulder water is most readily filled with tracer (the outer reservoir is "turned off"). Thus the larger the value of  $\gamma$ , the more the shoulder water acts as a reservoir sink for the core. When  $\gamma = 1$  this is referred to as the finite reservoir case, and when  $\gamma \gg \infty$  this is called the infinite reservoir case. In between these limits, the shoulder water can be thought of as a semi-infinite reservoir.

In the limit when the mixing between the core and shoulder goes to zero ( $\tau_c \gg \infty$ ) the concentration of freon leaving the core is the same as that which enters. In the limit of very strong mixing ( $\tau_c \gg 0$ ) the coupled set (3.18) gives

$$\theta_{c_j}(t) = \theta_{s_j}(t)$$

$$\theta_{c_j}(t) = \gamma \theta_{s_j}(t)$$

(remember that  $\theta_{c_j}(t)$  and  $\theta_{s_j}(t)$  vary on the time scale of the input). For  $\gamma > 1$  this implies that  $\theta_{c_j}(t) = \theta_{s_j}(t) = 0$ , which is consistent in that no freon can accumulate in either the core or shoulder. When  $\gamma = 1$  the shoulder will instantly equilibrate to the level in the core, and the governing equations tell us only that  $\theta_{c_t}(t) = \theta_{s_j}(t)$ . It is obvious that we do not wish to consider either of these cases, thus  $\tau_c$  is constrained to be  $\geq T_r$  (and finite).

Because the fluid spends only a short time inside the core and because the ratio of the shoulder continually increases as well, the amount by which the ratio of the boundary current is lowered is minimal. However if this process occurs along the entire length of the current the effect can be substantial. So we think of the boundary current (and shoulder water) then as

being made up of many of these sections, each one represented by a different value of the index  $j$ . The output from the core of a given section is in turn the input to that of the adjacent one. However we do not allow interaction between adjacent shoulder regions. (Note that this is consistent in that we are ignoring alongstream diffusion.) It is evident that the amount by which the core ratio decreases depends on the length of time the fluid spends in each section, which will enable us to track the ratio versus advective time and match the observed ratio in the data.

The solution to (3.18) is

$$\theta_{c_j}(t) = \frac{\theta_0(t)}{1+\delta} + \frac{\delta}{\tau_c(1+\delta)^2} e^{rt} \int_0^t \theta_0(t') e^{-rt'} dt' \quad (3.19a)$$

$$\theta_{s_j}(t) = e^{rt} \int_0^t \frac{\theta_0(t')}{\tau_c(1+\delta)} e^{-rt'} dt' , \quad (3.19b)$$

where  $r = -\frac{1}{\tau_c} \left( \gamma - \frac{\delta}{1+\delta} \right) ,$

and  $\delta = \frac{\tau_r}{\tau_c} .$

These represent the concentrations for the first section ( $j=1$ ), and (3.19a) should in turn be used as the input to the next core. Considering successive sections as such, however, results in an insurmountable amount of algebra, and a simplifying assumption must be made. What we do is approximate the overflow concentration curve of Figure 3.3 (for both F-11 and F-12) by an exponential.

When the expression  $\theta_0(t) = Ae^{t/T}$  is substituted into (3.19), this gives

$$\theta_{c_j}(t) = \frac{\theta_0(t)}{1+\delta} + \frac{\delta}{\tau_c(1+\delta)^2(-r + \frac{1}{T})} (\theta_0(t) - Ae^{rt}) \quad (3.20a)$$

$$\theta_{s_j}(t) = \frac{1}{\tau_c(1+\delta)(-r + \frac{1}{T})} (\theta_0(t) - Ae^{rt}) . \quad (3.20b)$$



The important thing here is that the terms proportional to  $e^{rt}$  decay very quickly relative to those proportional to  $\theta_0(t)$  (which grow in time). This means that to a good approximation,

$$\theta_{c_j}(t) \sim G_c(\tau_c, T_r, T, \gamma) \theta_0(t) \quad (3.21a)$$

$$\theta_{s_j}(t) \sim G_s(\tau_c, T_r, T, \gamma) \theta_0(t), \quad (3.21b)$$

where 
$$G_c = \frac{1}{1 + \delta} + \frac{\delta}{\tau_c (1 + \delta)^2 (-r + \frac{1}{T})},$$

and 
$$G_s = \frac{1}{\tau_c (1 + \delta) (-r + \frac{1}{T})}.$$

With this being the case it is straightforward to combine successive sections. After  $n$  sections (3.21) gives that the concentrations are

$$\theta_{c_{j=n}}(t) \sim (G_c)^n \theta_0(t) \quad (3.22a)$$

$$\theta_{s_{j=n}}(t) \sim (G_s)(G_c)^{n-1} \theta_0(t) \quad (3.22b)$$

The functions  $G_c$  and  $G_s$  are called decay factors (whose magnitudes are  $\leq 1$ ). For F-11 the overflow concentration growth scale  $T$  is  $\sim 5$  yr, and for F-12,  $T \sim 7$  yr. It is this slight difference which is the reason why the ratio proceeds to decrease as the fluid progresses downstream. The quantity  $\left[ \frac{G_c(T=5)}{G_c(T=7)} \right]^n$  measures this decrease, and in line with what was mentioned above, only for a large enough  $n$  is the difference substantial. Figure 3.8 plots the core concentration decay factor and ratio decay factor versus the strength of the mixing between core and shoulder for the three different types of reservoirs (there is no ratio decay for the infinite reservoir). As expected the concentration decays more with smaller  $\tau_c$ . Note the difference between the ratio decay of the finite reservoir case

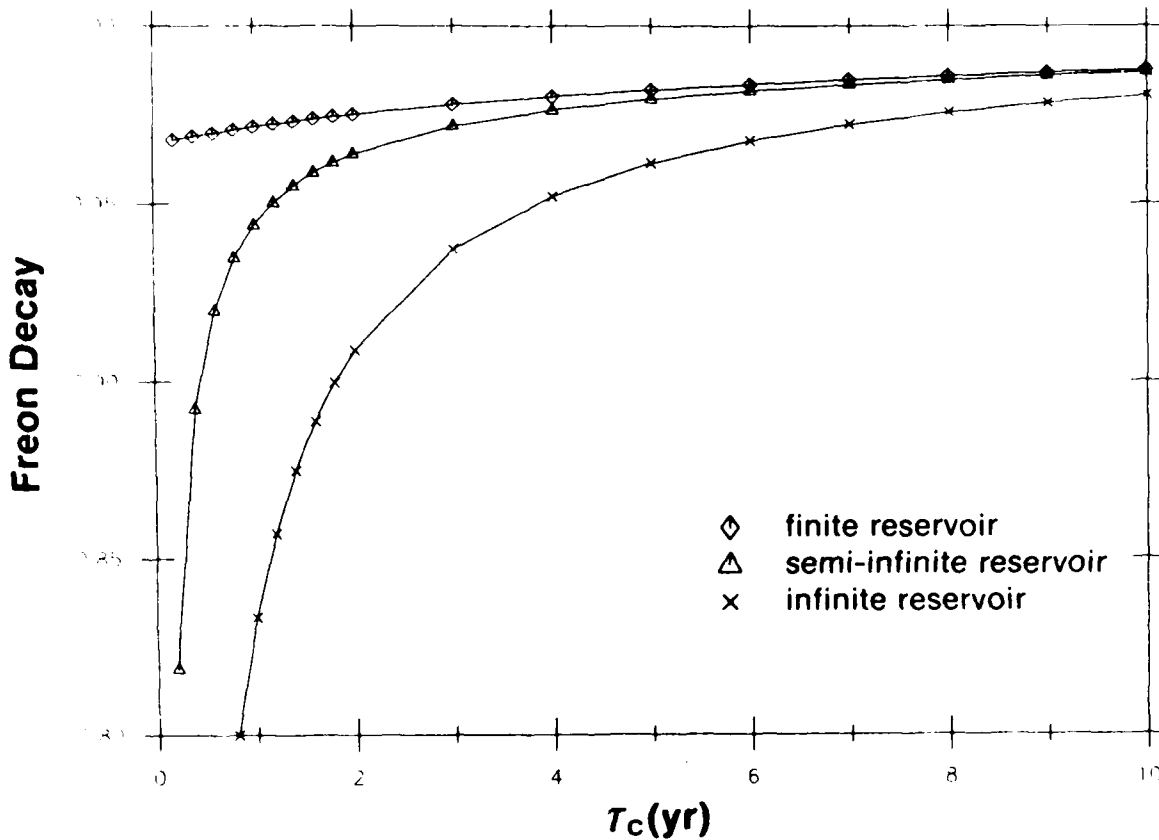
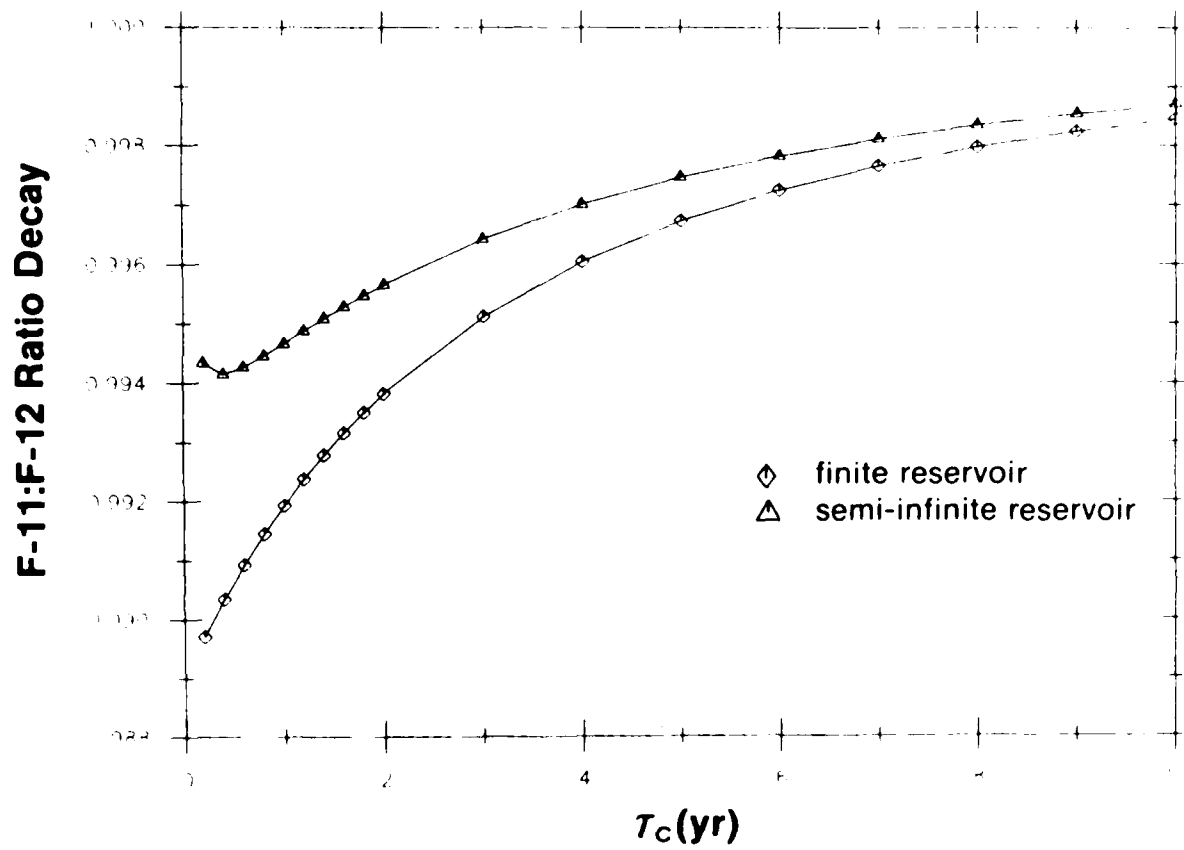


Figure 3.8: The dependence of the core decay factor on the strength of the mixing between the core and shoulder for three different values of the reservoir parameter  $\gamma$ :  $\gamma = 1$  (finite reservoir),  $\gamma = 1.25$  (semi-infinite reservoir),  $\gamma \rightarrow \infty$  (infinite reservoir). The value of the residence time of the sections is taken to be .2 years. (a) The freon concentration decay

factor  $\frac{G_c(T = 5 \text{ yr}) + G_c(T = 7 \text{ yr})}{2}$ .



(b) The freon ratio decay factor  $\frac{G_c(T = 5 \text{ yr})}{G_c(T = 7 \text{ yr})}$ .

versus the semi-infinite case. In the latter, not only is the decay less pronounced, but for small values of  $\tau_c$  the decay decreases with increased mixing. This is because for very strong mixing no tracer is able to accumulate within the shoulder water (in contrast to a finite reservoir where the shoulder level approaches that of the current).

As seen in Figure 3.9, for a given value of mixing, as the size of the reservoir parameter gets smaller the amount of ratio decay increases, whereas the amount of concentration decay decreases. So depending on the value of  $\gamma$  which is chosen, the model will predict a different core speed. Note also that within the context of this model the freon dating technique involves not only matching the ratio but the concentration as well. The technique is applied as follows.

First we choose the magnitude of the residence time that characterizes the component sections. The value that was used is  $T_r = .2$  yr (this is arbitrary, although the smaller the value of  $T_r$ , the higher the resolution). For a given value of  $\gamma$  then there are two unknowns, the strength of the mixing  $\tau_c$  and the value of  $n$ . It is then just a matter of determining these unknowns by forcing the core concentration of F-12 and the value of the ratio (or equivalently the two concentrations themselves) to match the data at  $50^\circ\text{W}$ . (The ABCE region extends only to  $55^\circ\text{W}$ ; an extrapolation was used to obtain a core value of  $3.34$  p-moles/kg  $\times 10$  for F-12 and  $1.97$  for the F-11:F12 ratio at  $50^\circ\text{W}$ .) It should be noted that even though we make use of (3.22), the actual  $\theta_0(t)$  curves are used in the calculation (rather than the exponential approximations).

For the case of a finite reservoir ( $\gamma = 1$ ) it is not possible to get a consistent solution. This is because when the ratio is matched to the value in the data there is too much tracer in the shoulder water to drive down the F-12 concentration. In the infinite reservoir case,  $G_c = \frac{1}{1+\delta}$  so the concentration decay amplitude after  $n$  sections is  $(\frac{1}{1+\delta})^n$ . From (3.7) we see that in the continuous case the equivalent quantity is  $e^{-\frac{L}{U\tau}}$  (there is no background so  $\theta_B = 0$ ). In the limit as  $n \rightarrow \infty$  the finite-difference solution approaches the continuous result. This can be seen by

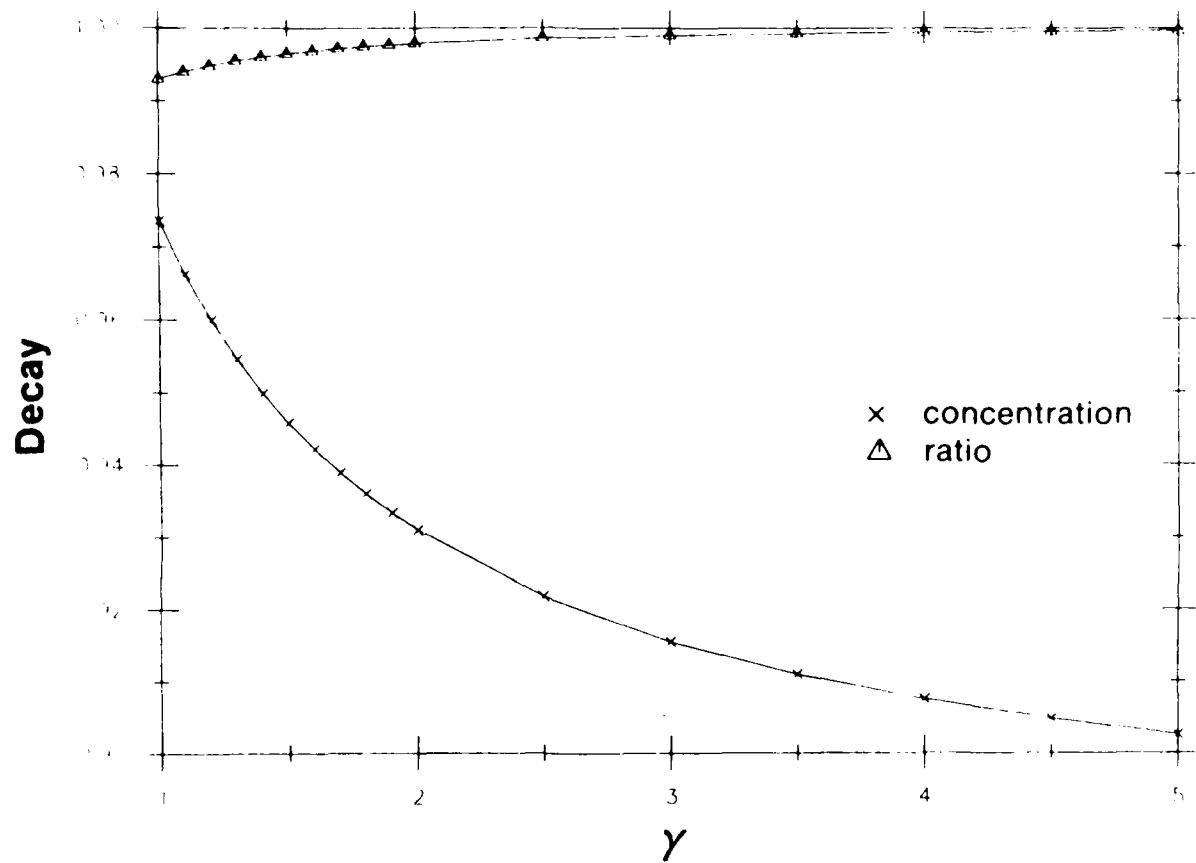


Figure 3.9: The dependence of the core concentration decay factor and core ratio decay factor on the size of the reservoir parameter  $\gamma$ . The strength of the mixing between the core and shoulder is held constant ( $\tau_c = 1.5$  yr) as is the residence time of the sections ( $T_r = .2$  yr).

noting that  $\delta = \frac{L_a}{u\tau_c} = \frac{L}{u\tau_c n}$ , and by definition  $\lim_{n \rightarrow \infty} \left[ \frac{1}{1 + \left(\frac{L}{u\tau_c}\right) \frac{1}{n}} \right]^n = e^{-\frac{L}{u\tau_c}}$  ( $\tau_c$  and  $\tau$  are equivalent in this case). Thus the scenario which accompanies the freon-free mixing assumption is contained as a special case within the present boundary current model.

In Figure 3.10 the resulting core speeds are plotted versus various values of  $\gamma$ . For  $\gamma$  nearly equal to one, the model gives a core speed as large as 6 cm/sec (remember this is an average over the length of current, from the overflow to 50°W). As a possible guide in determining which of these examples might be the most realistic in terms of the ocean, we can consider the corresponding values of  $\tau_c$  and  $\theta_{sj}(t)$  for each example. Smaller values of the reservoir parameter require stronger mixing (in each example  $\tau_c > T_r$ ) which accompany higher shoulder water concentrations (Figure 3.11).

An observation that has led to the freon-free mixing assumption is that successive locations along a current show little variation in the core value of the F-11:F-12 ratio (Smethie and Trumbore, 1984). Because the ratio is not a conserved quantity in this model (for finite  $\gamma$ ) it might seem then that the resulting downstream variation contradicts this observation. This is not the case however. In fact, even though the amount of decay varies with  $\gamma$ , the alongstream change in ratio is comparable in each case.

The OCEANUS 134 data set contains several crossings of the DWBC with which to compare the model predictions concerning this point. In the limit of freon-free mixing ( $\gamma \rightarrow \infty$ ) the core ratio varies slightly alongstream because the ratio at the source (overflow) is changing in time and the core speed is only 2 cm/sec. With such a small core speed the input at a given time cannot propagate very far downstream before another change in input occurs. The resulting downstream trend in ratio agrees well with what is observed in the data. In the opposite limit of  $\gamma \rightarrow 1$ , the ratio decays as the fluid proceeds downstream, but because it flows so quickly a signal will propagate a long way before the input changes appreciably. Thus the effect that caused the variation for the  $\gamma \rightarrow \infty$  case has little consequence here, and it turns out that the decay process results in an alongstream gradient of nearly identical magnitude. In between these limits the importance of the

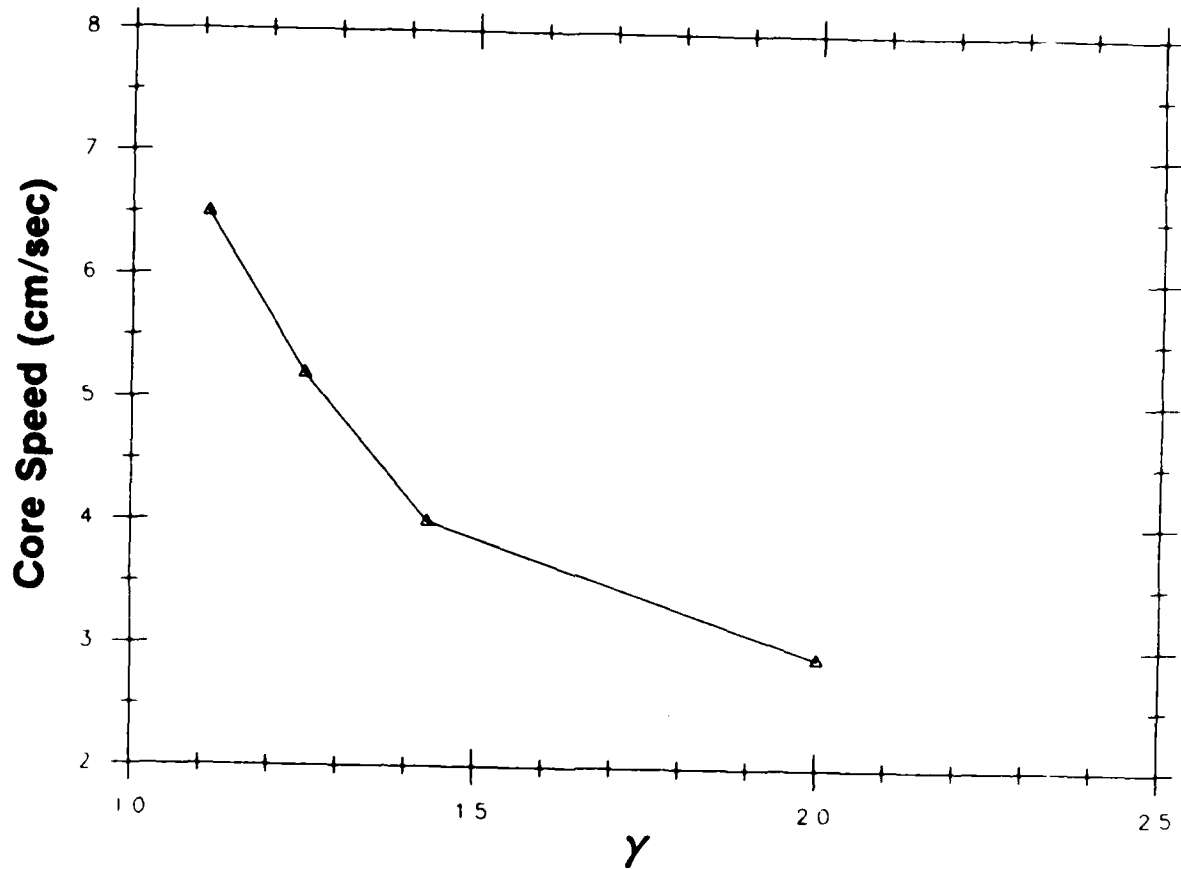


Figure 3.10: The boundary current core speed associated with the value of the reservoir parameter.

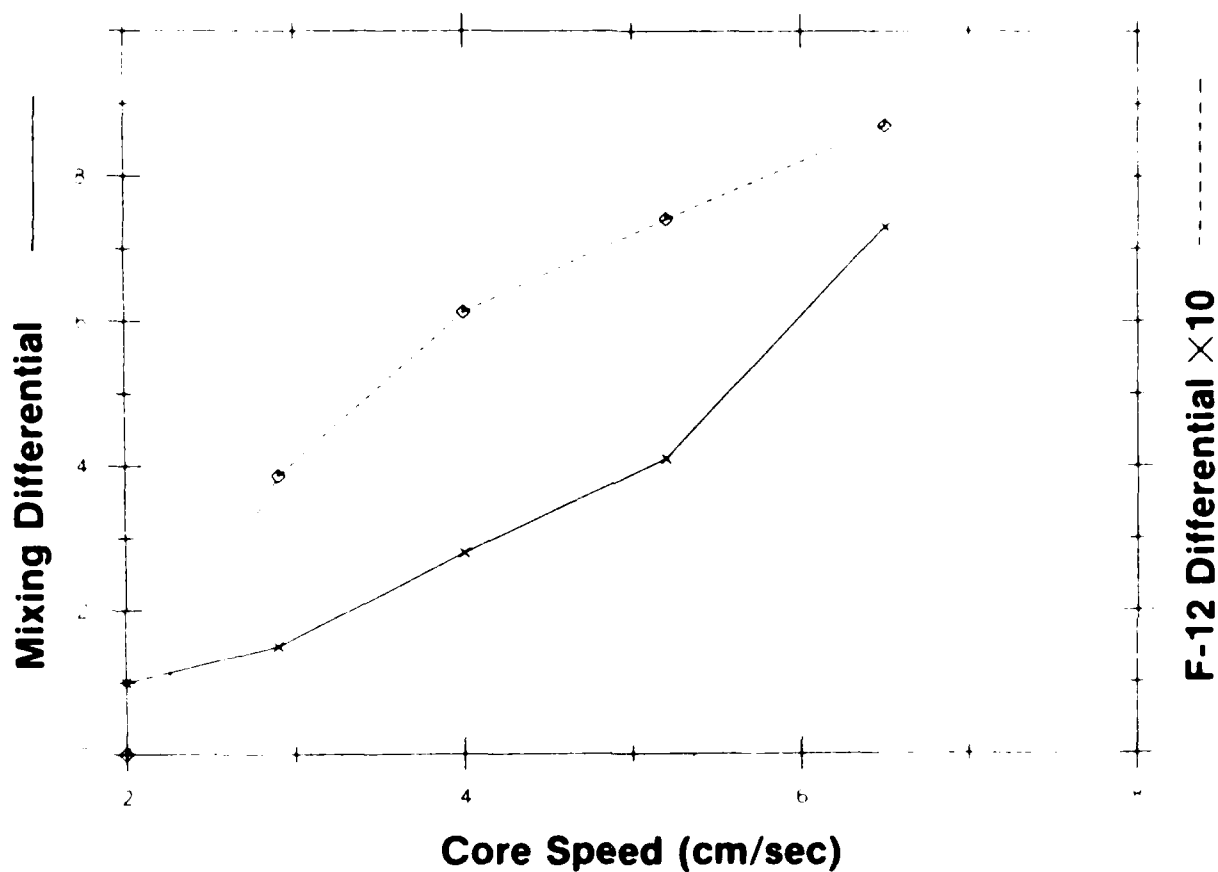


Figure 3.11: Graph showing the mixing that is required for the different core speeds and the resulting cross-stream variation in concentration for the back-mixing model. The solid line measures the strength of the mixing between the core and shoulder relative to what it would be if the core were mixing with a freon-free shoulder. The dashed line plots the concentration of the shoulder relative to that of the core ( $\times 10$ ).



two effects varies inversely making it hard to distinguish between any of the cases. The observed feature in the data can therefore be explained by any of the examples of the model (as can the variation in concentration, Figure 3.12).

#### B) Shear Model

In the above representation it was assumed that the boundary current had no structure to it, i.e. the flow was represented by a single core velocity. It was seen that the mixing between the core and shoulder water resulted in decay of the core ratio when the shoulder did not act as an infinite reservoir sink. It is easy to envision a different type of scenario which could also decrease the freon ratio of the core. We consider a boundary current that has cross-stream shear (so that the core refers to only the fastest part of the flow) and assume that the core mixes entirely with the outlying weaker flow. Because this slower travelling water is older and has a lower freon ratio, this will tend to drive down the core ratio. We structure the model the same way as the previous back-mixing model in that the boundary current is represented as a number of sections.

Consider the first such section, which receives its input from the overflow as depicted in Figure 3.13. As before it is comprised of the core, the shoulder, and the vast amount of surrounding fluid (which again is taken to be an infinite sink). The difference here though is that the shoulder water is moving as well -- the core is characterized by speed  $U_c$  and the shoulder by  $U_s (< U_c)$ . So whereas previously the current corresponded to just the core region, now it is made up of the core and shoulder together. We assume again that the concentrations are uniform in the azimuthal direction and apply the same finite-difference approximations radially and along-stream.

In the core region the governing equation is as before,

$$U_c \theta_x = \frac{\kappa}{r} (r \theta_r)_r . \quad (3.23)$$

Because of the advection in the shoulder, (3.23) is the governing equation there as well, with  $U_s$  replacing  $U_c$ . After integrating over the cross-section and finite-differencing, the two governing equations become

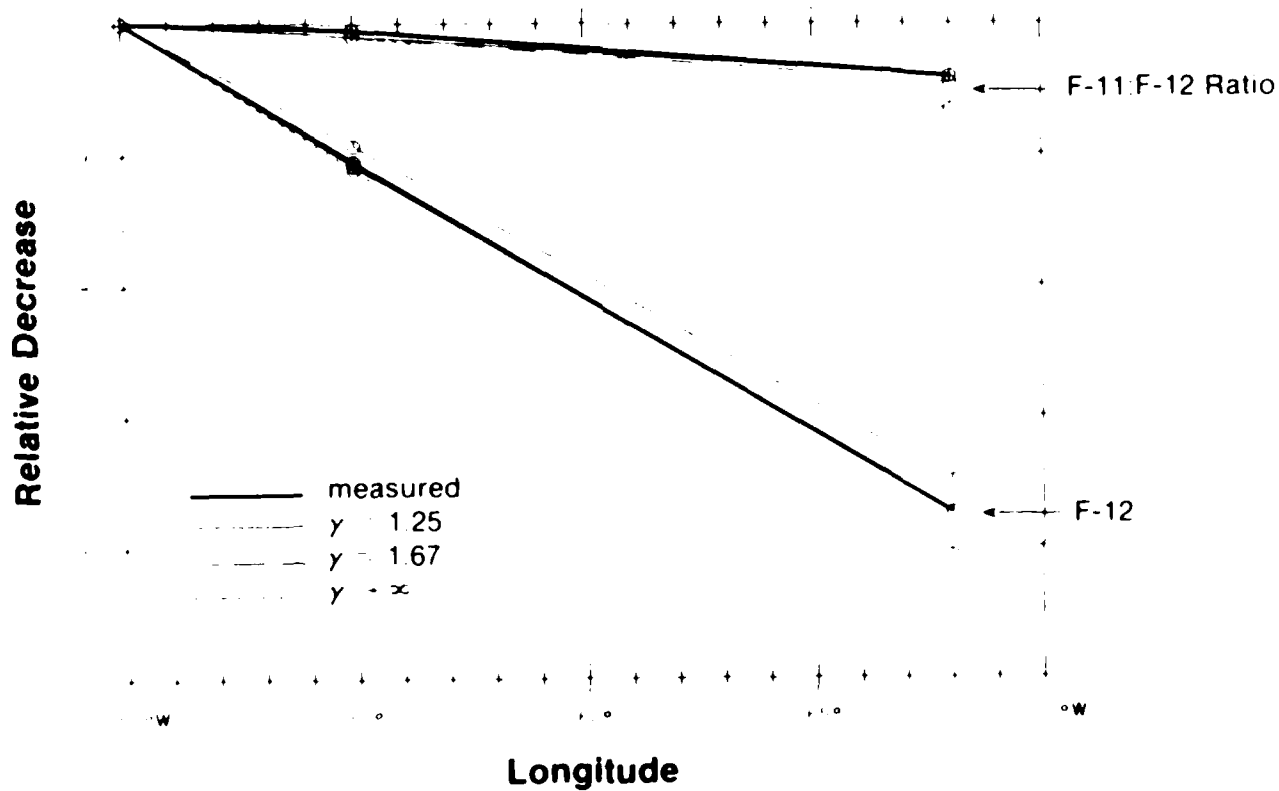


Figure 3.12: The alongstream variation in core concentration and ratio as predicted from the back-mixing model, compared with that observed in ABCE. Three different examples are shown. The curves are normalized by the values at 50°W.

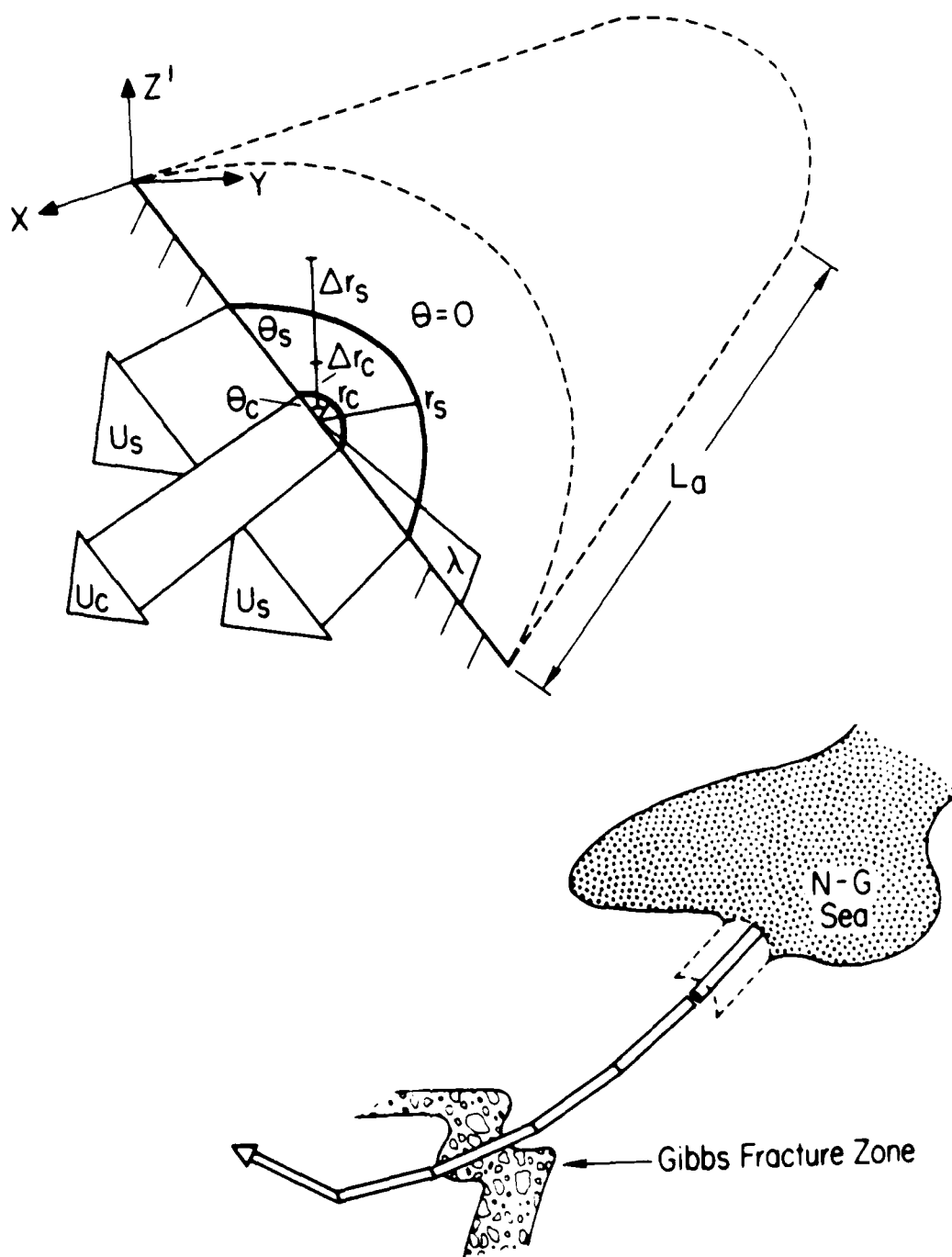


Figure 3.13: Schematic depicting the DWBC as being composed of many short sections, as in Figure 3.6. In the shear model flow occurs in both the core and shoulder regions.

$$A_c \frac{U_c}{L_a} (\theta_{c_j}(t) - \theta_{c_{j-1}}(t)) = \frac{\kappa \pi r_c}{\Delta r_c} (\theta_{s_j}(t) - \theta_{c_j}(t)) \quad (3.24a)$$

$$A_s \frac{U_s}{L_a} (\theta_{s_j}(t) - \theta_{s_{j-1}}(t)) = \frac{\kappa \pi r_s}{\Delta r_s} (0 - \theta_{s_j}(t)) - \frac{\kappa \pi r_c}{\Delta r_c} (\theta_{s_j}(t) - \theta_{c_j}(t)) \quad (3.24b)$$

which should be compared to (3.17a,b). [All labels here are the same as in (3.17a,b).]

Both  $\theta_{c_{j-1}}(t)$  and  $\theta_{s_{j-1}}(t)$  are set equal to the overflow  $\theta_0(t)$ .

Also, we take  $r_c \ll r_s$  so that the last term on the right hand side of (3.24b) can be ignored. (Note that as  $r_c \rightarrow 0$ ,  $\Delta r_c$  remains finite.) This says that the area of contact between the core and shoulder is so small that the diffusive flux into the shoulder across this surface is negligible compared with the flux across the outer surface of the shoulder. The set (3.24a,b) can then be written as

$$\theta_{c_j}(t) = \theta_0(t) - \frac{T_{r_c}}{\tau_c} (\theta_{c_j}(t) - \theta_{s_j}(t)) \quad (3.25a)$$

$$\theta_{s_j}(t) = \theta_0(t) - \frac{T_{r_s}}{\tau_s} \theta_{s_j}(t), \quad (3.25b)$$

where  $T_{r_c} = \frac{L_a}{U_c}$  = residence time of fluid in core region,

$T_{r_s} = \frac{L_a}{U_s}$  = residence time of fluid in shoulder region,

and  $\tau_c$  and  $\tau_s$  are defined as before. Note that whereas in the previous back-mixing model the amount of shoulder water is comparable to the amount of core water, in the present shear model the shoulder region is much larger than the core region. Also note that in the previous model the shoulder receives all of its tracer by way of diffusion from the core, whereas in this model the shoulder receives all of its tracer through advection from the overflow.

The solutions to (3.25) are determined straightforwardly,

$$\theta_{s_j}(t) = \frac{\theta_0(t)}{1 + \delta_s} \quad (3.26a)$$

$$\theta_{c_j}(t) = \frac{\theta_0(t)}{1 + \delta_c} + \frac{\delta_c}{1 + \delta_c} \left( \frac{\theta_0(t)}{1 + \delta_s} \right) \quad (3.26b)$$

where  $\delta_c = \frac{T_{rc}}{\tau_c}$  and  $\delta_s = \frac{T_{rs}}{\tau_s}$ .

However, we must account for the fact that once freon has filled the core, the fluid there mixes with freon-free water until that time later when freon also fills the shoulder. The time over which this freon-free mixing occurs is  $T_{rs} - T_{rc} \equiv \Delta T_r$ . The term in parenthesis in (3.26b) represents the shoulder concentration that mixes with the core. It should therefore be delayed in time by the increment  $\Delta T_r$ ,

$$\theta_{c_j}(t) = \frac{\theta_0(t)}{1 + \delta_c} + \frac{\delta_c}{1 + \delta_c} \left( \frac{\theta_0(t - \Delta T_r)}{1 + \delta_s} \right). \quad (3.27)$$

The degree to which the core speed and shoulder speed vary can be taken as a parameter in the model. Specifically let  $T_{rs} = \beta T_{rc}$  ( $\beta \geq 1$ ). Also, we define the ratio  $\frac{\tau_s}{\tau_c} \equiv \alpha$ , which measures the discrepancy in decay times between the core and shoulder. It follows that  $\delta_s = (\frac{\beta}{\alpha})\delta_c$ . Dropping the subscripts on the core variables, the expression (3.27) then becomes

$$\theta_{c_j}(t) = \frac{\theta_0(t)}{1 + \delta} + \frac{\delta}{1 + \delta} \left( \frac{\theta_0(t - (\beta - 1)T_r)}{1 + (\frac{\beta}{\alpha})\delta} \right). \quad (3.28)$$

This represents the core output after the first section ( $j=1$ ) and must in turn be used as the input into the next core. A similar coupling occurs with the shoulder, but note that the shoulder evolves independently of the

core. After  $n$  sections the shoulder concentration with which the core mixes is

$$\theta_{s_{j=n}}(t) = \frac{\theta_0(t - n(\beta - 1)T_r)}{(1 + (\frac{\beta}{\alpha})\delta)^n}$$

where  $n(\beta - 1)T_r$  is the discrepancy in advective time between the core and shoulder. It follows that the concentration of the core after  $n$  sections is

$$\theta_{c_{j=n}}(t) = \left(\frac{1}{1 + \delta}\right)^n \theta_0(t) + \delta \sum_{i=1}^n \left(\frac{1}{1 + \delta}\right)^{n-(i-1)} \frac{\theta_0(t - i(\beta - 1)T_r)}{(1 + (\frac{\beta}{\alpha})\delta)^i} \quad (3.29)$$

Note that expression (3.29) involves no simplifying assumption concerning the overflow concentration, as was necessary in the back-mixing model (the reason for this is the governing equations (3.25a,b) are algebraic, and the task of coupling sections together remains manageable).

As was the case in the back-mixing model, the core ratio in the shear model is only altered significantly when  $n$  is large (i.e. the process must occur throughout the length of the current). As the magnitude of  $\beta$  is made larger the discrepancy in ratio between the core and shoulder increases, and the mixing then causes a greater ratio decay in the core. However,  $\beta$  eventually becomes so large that for the majority of the time the core mixes with freon-free water. For this range of  $\beta$  then the ratio decay decreases with increasing  $\beta$ . The effect of making  $\alpha$  larger is to cause the shoulder concentration to decay more slowly relative to the core. This means simply that there is more freon with which to influence the core, so the ratio decay of the core will be more pronounced.

Figure 3.14 illustrates these effects on the ratio decay of the core. The figure plots the freon ratio as predicted from (3.29) at  $t = 34$  yr (i.e. the year the data was collected) versus the magnitude of  $\beta$ . Note that when  $\alpha$  is made greater than 1 not only is the ratio lowered, but the value of  $\beta$  corresponding to the maximum decay is shifted. As  $\beta \rightarrow \infty$  all the curves will converge to the input ratio. For the case when  $\beta = 1$  the curves also maintain the value of the input. In this case the core and

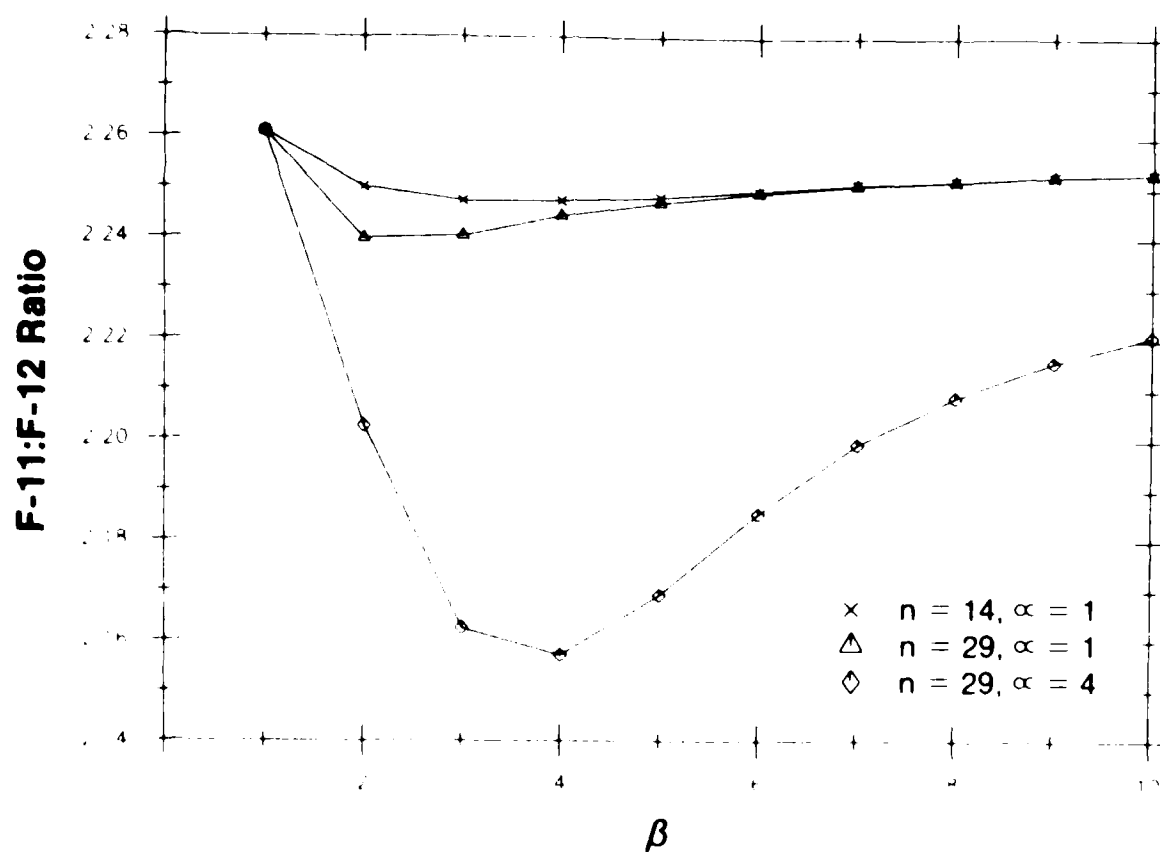


Figure 3.14: Three different examples showing the value of the core ratio after a number of sections, as a function of the discrepancy in speeds between the core and shoulder.

shoulder progress as one unit, surrounded by a freon-free reservoir (hence no ratio decay). Note that this is the same set up as the infinite reservoir case of the back-mixing model.

The manner in which the shear model is applied to the data to determine age is exactly the same as was done previously with the back-mixing model, only in this case there is an additional parameter. If  $\alpha$  is maintained at a fixed value, then for each  $\beta$  the matching process described earlier gives an estimate of the mixing coefficient  $\tau_c$  and the core speed. As expected, the core speed estimate will at first increase with increasing  $\beta$  but eventually fall back to the freon-free value of 2 cm/sec. Similar curves can be generated for different values of  $\alpha$ . Three such curves are shown in Figure 3.15 ( $T_r$  is set equal to .2 yr as before) and it is evident now successive curves with larger  $\alpha$  take longer to reach their peak. As seen, it is possible to obtain core speeds in the range of 6-8 cm/sec.

Figure 3.16 shows two examples of the cross-stream variation in F-12 (at 50°W) and the strength of the mixing as a function of core speed. It is the analog to Figure 3.11. In the present case the cross-stream variation increases with larger core speed: this is in contrast to the previous back-mixing case in which it decreases. Also recall that stronger mixing is required at larger core speeds in the previous case. Here the mixing remains nearly constant. (In each example the diffusive times are larger than the residence times as required.)

Although the core speed is sensitive to the value of  $\beta$ , the corresponding shoulder speed stays in the range of 1-2 cm/sec. This can be understood as follows. The shoulder water mixes with a freon-free reservoir, thus if it flows at 2 cm/sec then at 50°W its ratio will match that which is observed in the data for the core. However, the core has to decay by way of mixing with water of a lower ratio. This puts an upper bound on the shoulder of 2 cm/sec. Recall that in the back-mixing model the alongstream variation in core ratio was nearly independent of core speed. For the same reasons this is also true in the shear model.



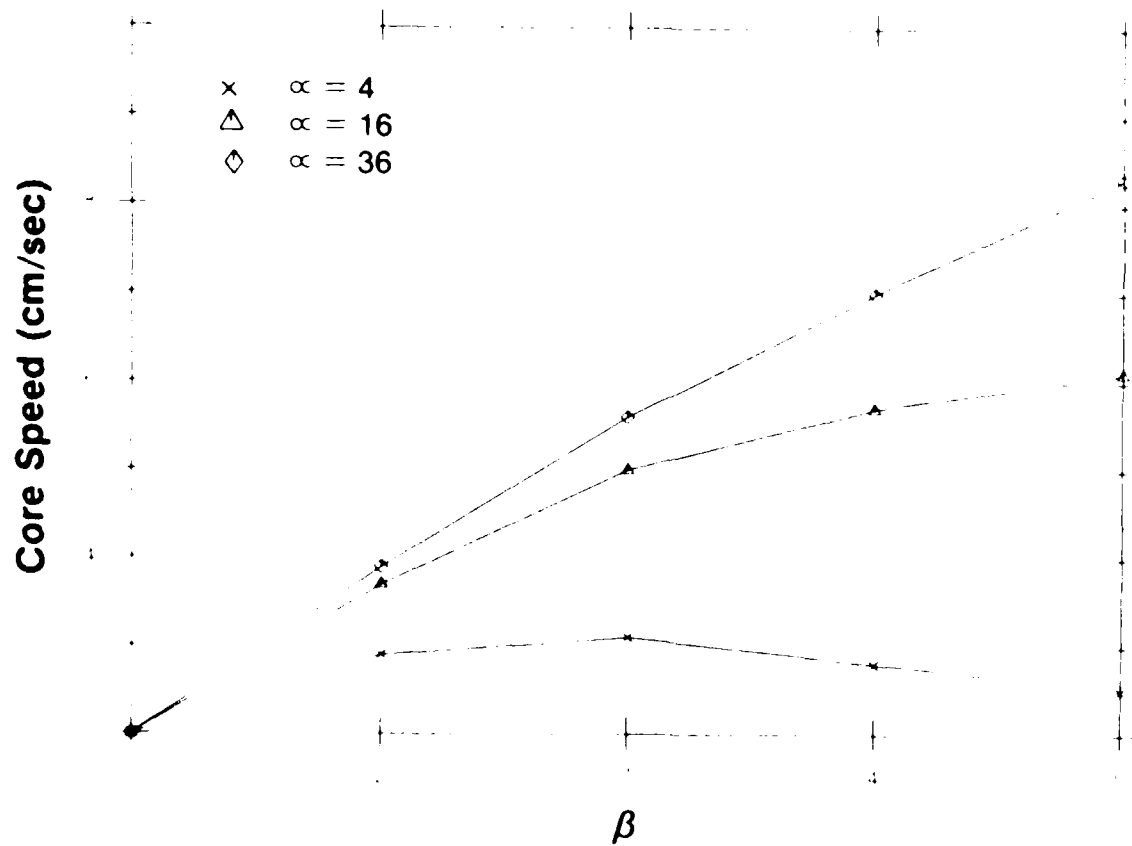


Figure 3.15: The boundary current core speed associated with the magnitude of  $\beta$ , for three chosen values of  $\alpha$ .

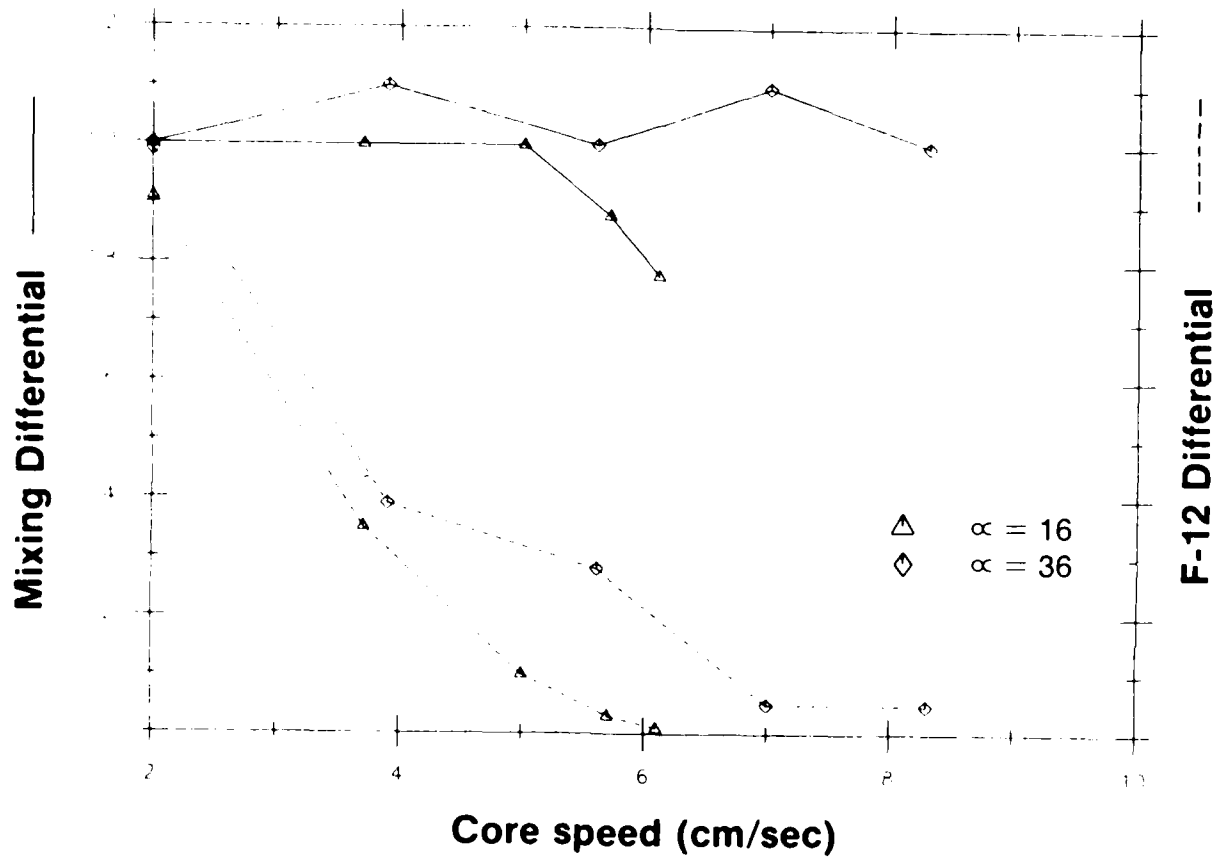


Figure 3.16: Graph showing the mixing and cross-stream variation in concentration corresponding to the different core speeds, as in Figure 3.11, for the shear model. Two examples with different values of  $\alpha$  are compared.

### A Comparison of the Back-mixing and Shear Models

For both of the above boundary current models there is a whole range of possible solutions, each one associated with a different value of the core speed and mixing coefficient  $\tau_c$ . It is informative to compare a solution from each model with regard to what is known about the DWBC and its associated freon signal. This can help us better understand the distinguishing aspects of the two models.

It is obvious that we do not wish to consider solutions with a small core speed, as such a value does not seem to be representative of the DWBC. (This was the point in developing the two models.) However we also cannot use the large core speed extremes in either of the cases, for a different reason. In the back-mixing model, in the limit of small  $\gamma$ , the concentration of the shoulder water approaches that of the core so that there is no cross-stream variation in freon, which is certainly not the case in the data (Figure 3.7). In the large  $\beta$  limit of the shear model the opposite happens, and the concentration of the shoulder water approaches zero. This is unacceptable as well. In fact, there is really only a very small range of core speed for which the solutions are reasonable physically.

The two examples which are compared are the 5 cm/sec solution from the back-mixing model and the 6 cm/sec ( $\alpha = 36$ ) solution from the shear model. Referring to Figure 3.6 of the back-mixing model, we are free to specify the value of  $r_s$ , i.e. the width of the freon signal ( $r_c$  is constrained by the fact that the core and shoulder cross-sectional areas are the same). The width is also freely specified in the shear model. (There  $r_c$  must satisfy the relation  $r_c \ll r_s$ , Figure 3.13). We consider a variety of widths and show how the two solutions vary accordingly.

Recall that each solution was determined by matching the value of the core concentration and core ratio to the data. This was accomplished by evaluating the core speed (the value of  $n$ ) and the mixing time scale  $\tau_c$ . When written entirely in terms of the radial distances, the mixing time scale takes the form  $\tau_c = \left(\frac{r_c r_s}{4}\right) \frac{1}{\kappa}$ . It is therefore evident that in specifying the width  $r_s$  (and  $r_c$ ), this determines both the transport of the current and the value of the diffusivity  $\kappa$ . Figure 3.17 plots the transport

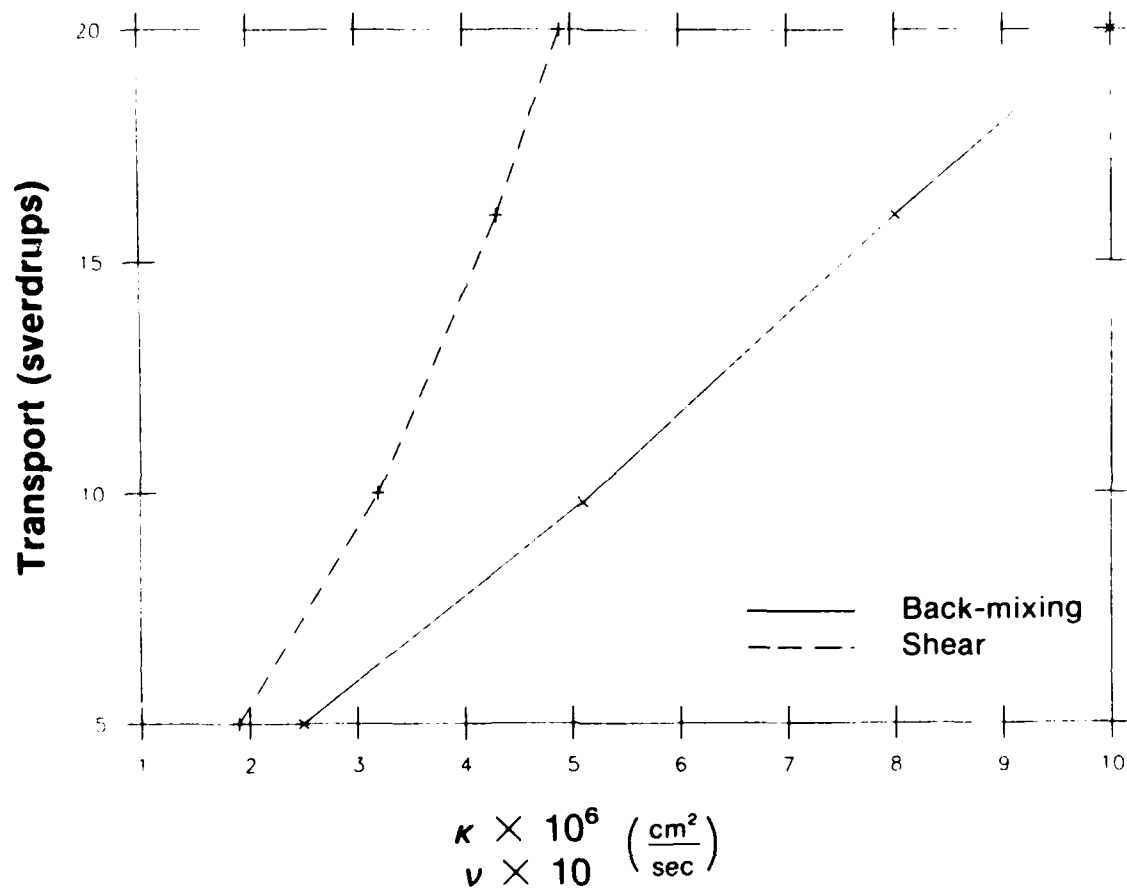


Figure 3.17: Transport of the DWBC associated with the value of diffusivity as predicted by the two boundary current models.

versus  $\kappa$  for different choices of the width. (Recall that the vertical diffusivity  $\nu$  is related to  $\kappa$  by (2.28).) Table 3.1 shows the corresponding values of the radial distances  $r_c$ ,  $r_s$  and grid spacings  $\Delta r_c$ ,  $\Delta r_s$ . It is seen that both models produce comparable transports, however we can use another consistency check with the data to pin down which values are most realistic for each model.

Consider again the trends in the cross-stream variation of freon for the two models (Figures 3.11 and 3.16). For the two examples here, the back-mixing model predicts the shoulder concentration to be ~70 percent that of the core; the shear model predicts 20 percent. For the freon section of Figure 3.7, as with any such section across the DWBC, a Gaussian-type distribution is associated with a radial cut extending from the core. For purposes of comparison, a Gaussian was fit to the horizontal cut for the section in the figure. We take the average value of the cut from  $r = 0$  to  $r = r_c$  as a measure of the core concentration, and the average from  $r = r_c$  to  $r = r_s$  as the shoulder concentration. Figure 3.18 shows the comparison of these concentrations to the corresponding model predictions for a range of transports (i.e. range of widths). It shows that the back-mixing model gives better agreement for smaller transports (~5 Sv), whereas the shear model does so for larger transports (~15 Sv). (A smaller width clearly means a larger percent concentration for the shoulder, as this means the shoulder region is closer in proximity to the peak of the Gaussian.)

We can now more fully appreciate how the scenarios of the two boundary current models differ. The current in the back-mixing model is characterized by thin, uniform flow with a small transport. High concentrations of tracer are found in the water directly surrounding the flow. In the shear model the boundary current is much more broad with more intense flow at the core, and has a large transport. Only a small amount of tracer accumulates in the water just outside of the current. These differences are depicted in Figure 3.19. In the former, the freon ratio of the core decays because of a diffusive mechanism; in the latter it decays because of an advective mechanism (although diffusion is still important).

At the present time there is some uncertainty as to what constitutes a representative value of the core speed of the DWBC, as well as a

TABLE 3.1: Magnitudes of the radial distances and grid spacings (Figures 3.6 and 3.13) associated with the different values of transport in Figure 3.17, for the two boundary current models.

Transport (Sverdrups)	$r_s$ (width) (km)	$r_c$ (km)	$\Delta r_c$ (km)	$\Delta r_s$ (km)
<u>Back-mixing model</u>				
5.0	195	136	98	485
9.8	275	192	138	685
16.0	350	245	175	875
20.0	390	275	195	982
<u>Shear model</u>				
5.0	200	50	100	900
10.0	300	50	150	900
16.0	400	50	200	900
20.0	450	50	225	900

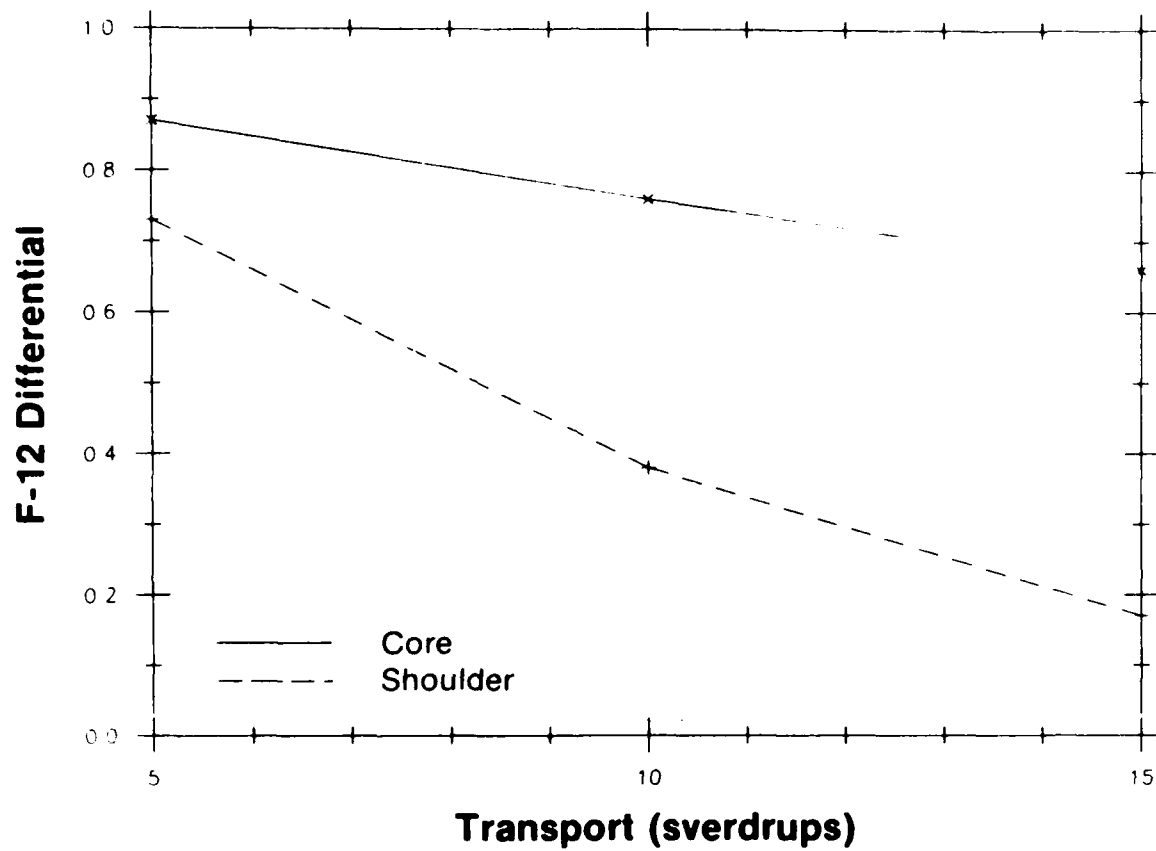
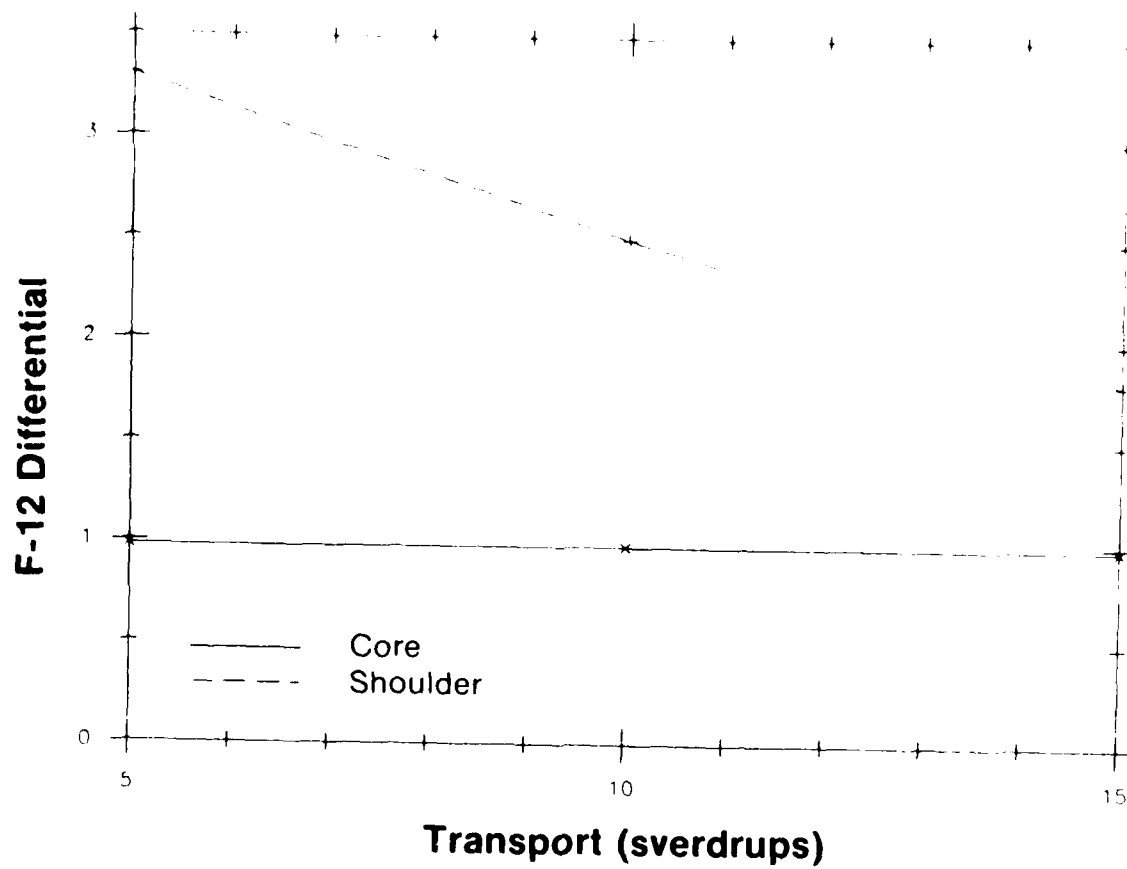


Figure 3.18: Predicted concentrations relative to those measured from Figure 3.7 for the core and shoulder regions, for different values of the DWBC transport. (a) Back-mixing model.



(b) Shear model.



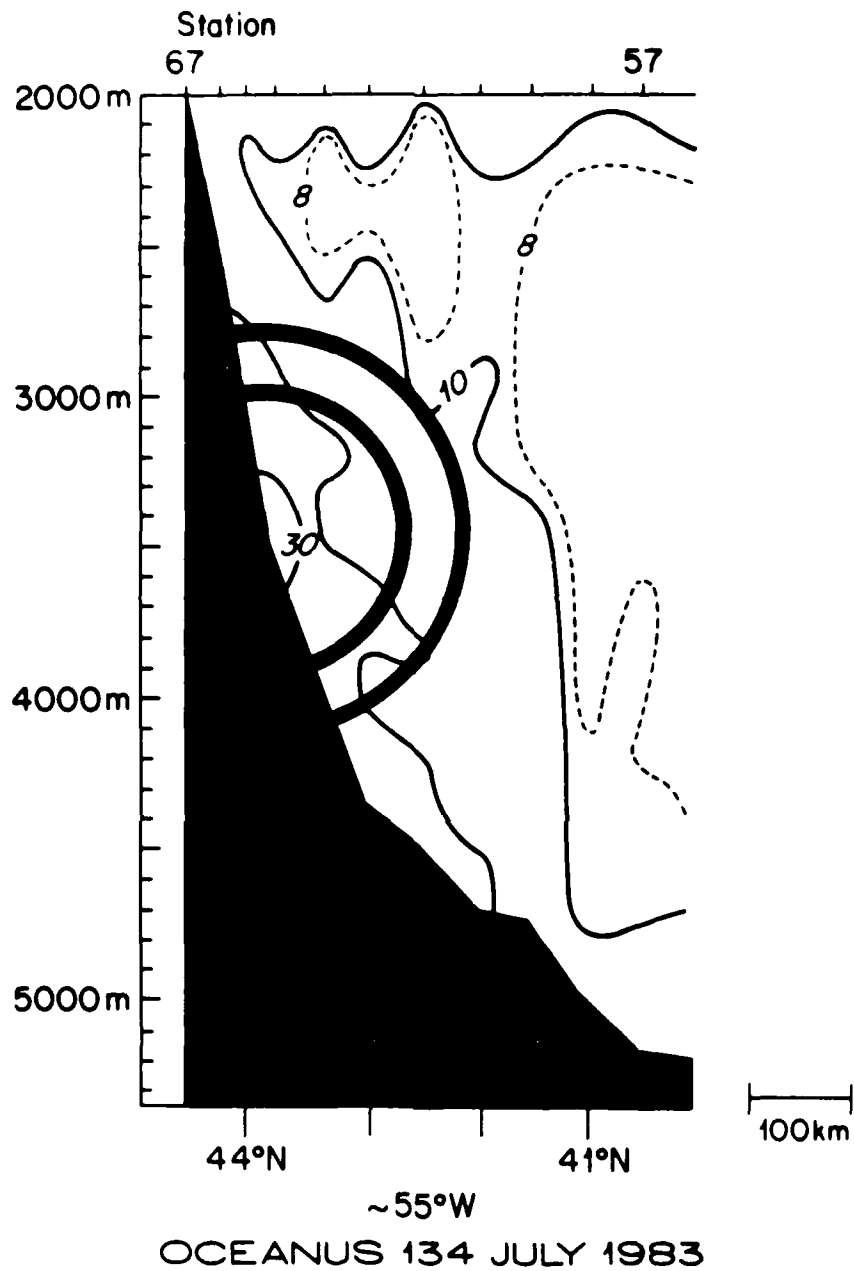
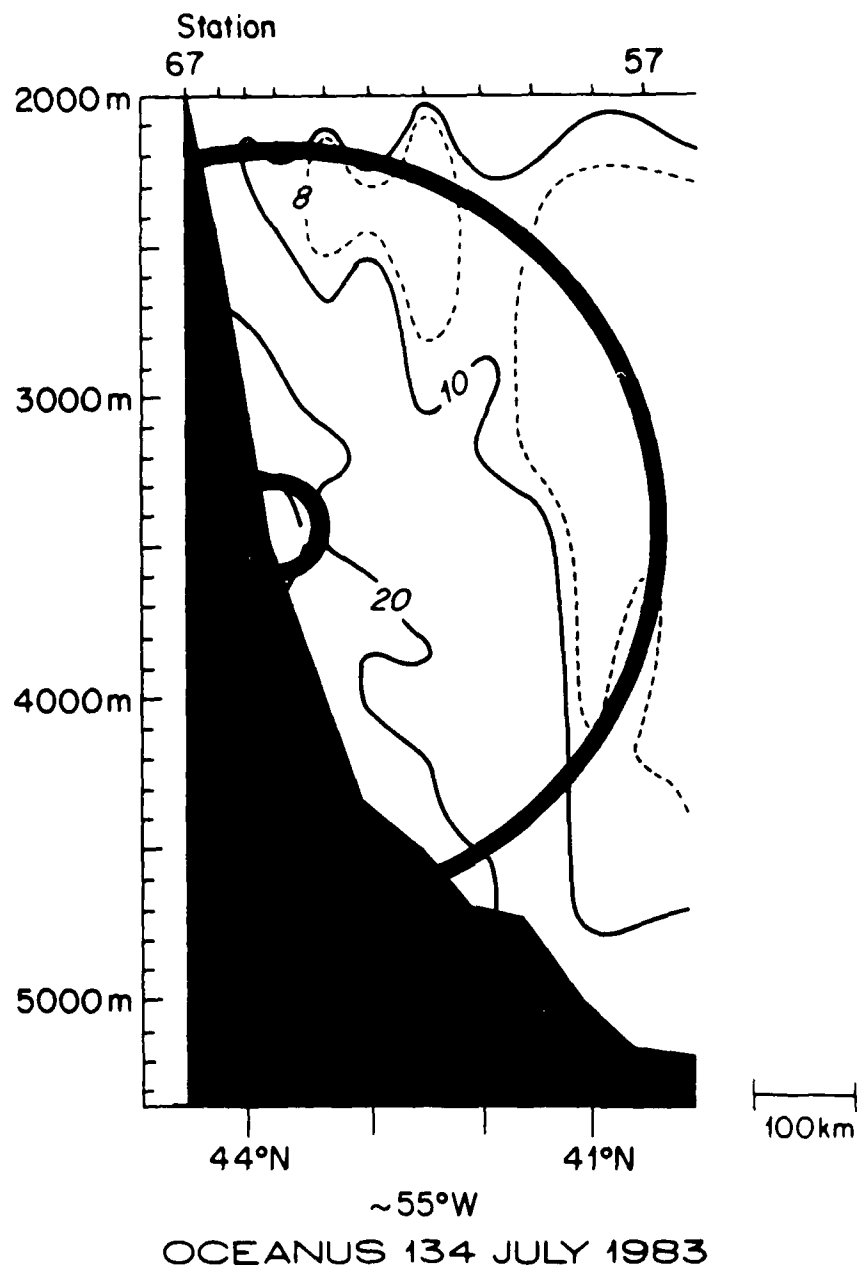


Figure 3.19: The core and shoulder regions (denoted by thick lines) for an example from each of the two boundary current models superimposed on the F-12 section of Figure 3.7. (a) Back-mixing model case in which the DWBC transport is 5 Sverdrups.



(b) Shear model case in which the DWBC transport is 15 Sverdrups.

representative value of the transport. The DWBC is known to pulsate in time (for example Richardson, 1977) as well as meander up and down the slope (Luyten, 1977) which complicates the determination of these quantities. Estimates of the transport vary from values as small as 4 Sverdrups (Pierce, 1986) to those as large as 24 Sverdrups (Richardson, 1977), although the former is a synoptic estimate and the latter includes slope water as shallow as 200 m. More of the estimates are in the range of 8-12 Sverdrups (for example Joyce et al., 1986; Hogg, 1983; Richardson and Knauss, 1971).

In regard to the core speed, numerous direct measurements have been made. Instantaneous values have been recorded as large as 50 cm/sec (Richardson, 1977), although mean speeds appear to be more in the range of 5-8 cm/sec (Luyten, 1977; Richardson, 1977). Jenkins and Rhines (1980) found a mean DWBC core speed of 21 cm/sec near the Blake-Bahama outer ridge, but this region is characterized by strong convergence of the isobaths which should accelerate the flow.

Both of the boundary current solutions mentioned here fall within this range of transports and core speeds. Although neither of the models is entirely satisfactory by itself, they do suggest that to one extent or another both of the freon ratio decay mechanisms may be present in the DWBC. For a transport of 5 Sverdrups in the back-mixing model and 15 Sverdrups in the shear model, the diffusivities so predicted are in the range of  $2-4 \times 10^6 \text{ cm}^2/\text{sec}$  for  $\kappa$  ( $20-40 \text{ cm}^2/\text{sec}$  for  $\nu$ ), which is in reasonable agreement with the estimate from the flux balance calculation of chapter two.

#### Time Dependent Transfer Model

In the previous sections we have investigated various advection/diffusion schemes which influence the signal of freon being carried by the core of the DWBC. The boundary current represents the primary source of freon into the deep layer in this part of the ocean, and it is of interest to study the process by which the freon eventually fills the entire layer (throughout the various basins). Of the components of mean circulation in the interior abyssal western North Atlantic are regions of closed circulation, and here we comment on the penetration of freon into the cyclonic recirculation gyre of

the Gulf Stream, or the Northern Recirculation Gyre (NRG) as it has come to be called.

OCEANUS cruise 134 (part of the Abyssal Circulation Experiment in 1983-84) collected water sample data in the region of the NRG, and it included several crossings of the DWBC which nicely show the signal of F-12 associated with the current. The entire cruise track is shown in Figure 3.20. The vertical sections of F-12 and potential temperature, for lines 1-4, are presented in Figure 3.21. Note in each section that there are two distinct regions in which the freon is higher near the inshore edge than on the same temperature surfaces further in the interior. A strong upper signal appears in the potential temperature range  $4^{\circ}$ - $6^{\circ}$ C, which is interesting in its own right. A water property analysis suggests that this water is of Labrador Sea origin, yet it is not in the temperature range of classical Labrador Sea Water (which is  $\sim 3.5^{\circ}$ C, Talley and McCartney, 1982). This feature warrants further investigation, although it is not addressed in this study.

Deeper in the water column, against the slope, is a somewhat weaker signal associated with the DWBC. As explained in chapter two it is believed that the eastward flow of the NRG pulls a plume of tracer from this DWBC signal. If this is indeed the case then the offshore signal from the gyre should become more distinct from the DWBC signature as one progresses from section 1 to 4. Evidence for such a separation is clear in Figure 3.21.

The difference between tracers such as salt and oxygen (whose characteristics within the NRG were discussed in chapter two) and freon is that the source of freon has only just been "turned on," so we are presently in the midst of the spin up process. This presents an ideal situation in the ocean to monitor the accumulation of a passive tracer into a closed circulation, knowing that initially there was no freon present. In this section we make use of the machinery that was developed in chapter two regarding the flux of tracer into the NRG, and incorporate a time-dependent source. The data to which these ideas are applied is a single synoptic view of the region. It would be beneficial to add to both its spatial and temporal resolution, thus allowing for a more extensive investigation into the accumulation process.

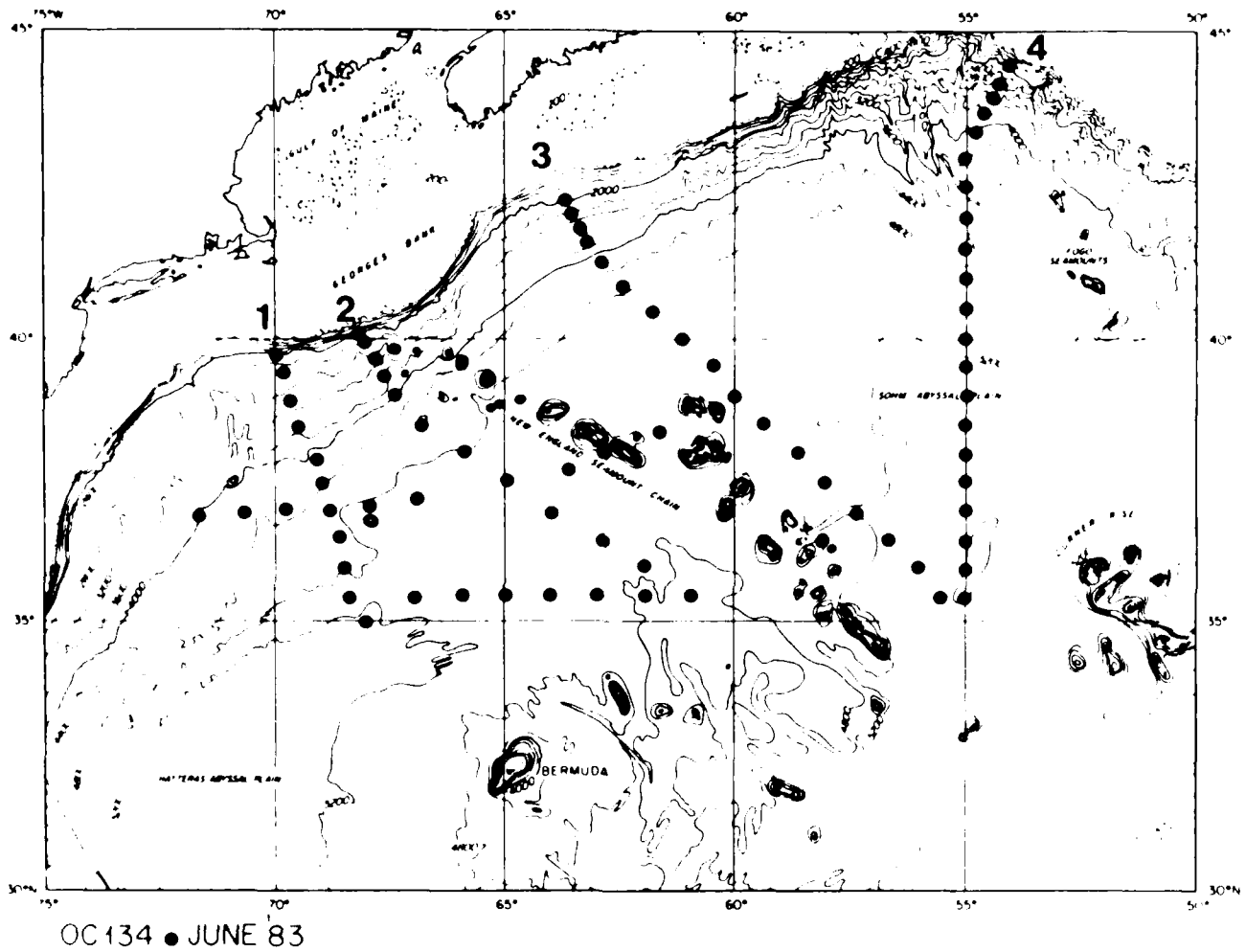


Figure 3.20: Station positions of OC134, June/July 1983. Sections 1 through 4 are marked.

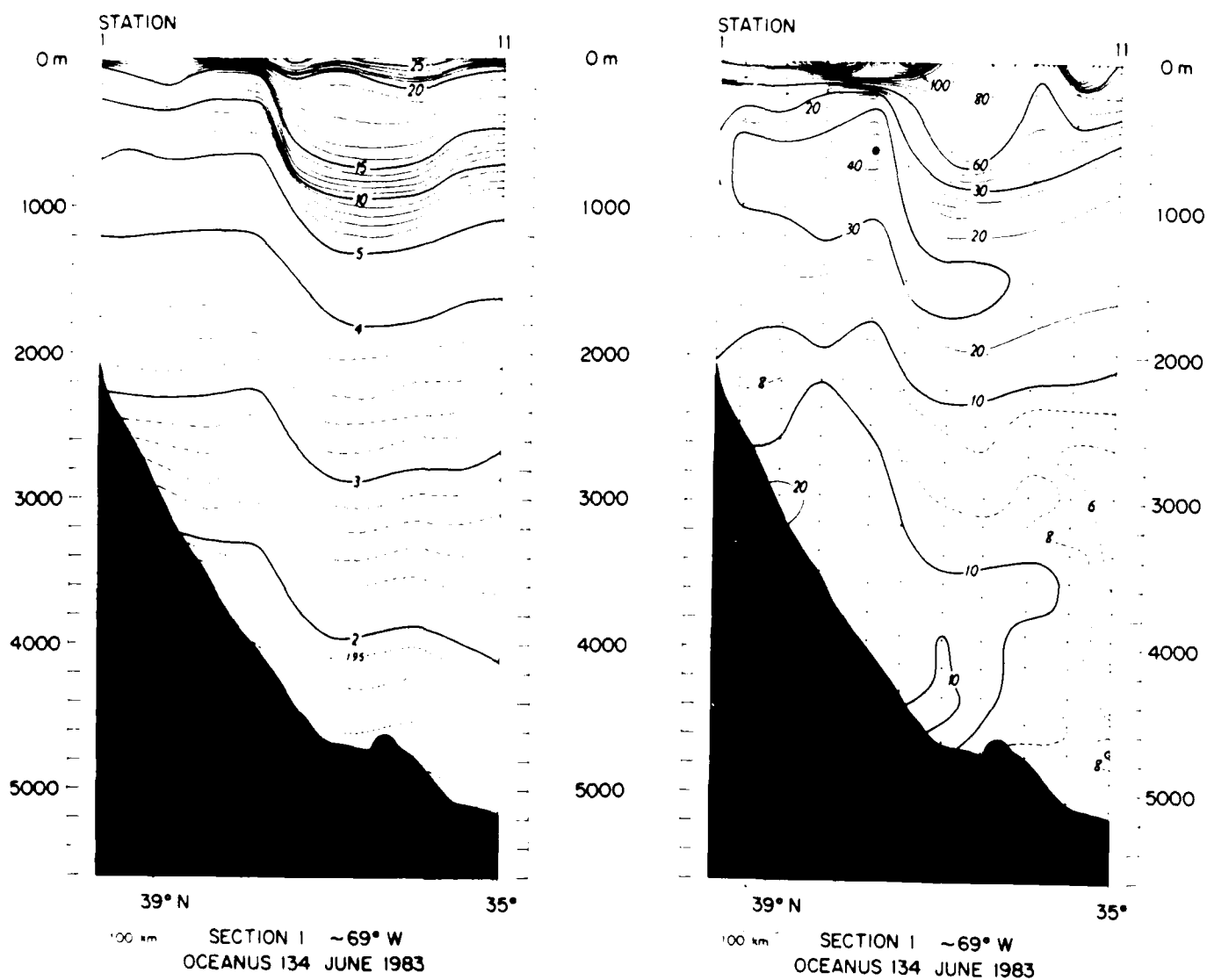
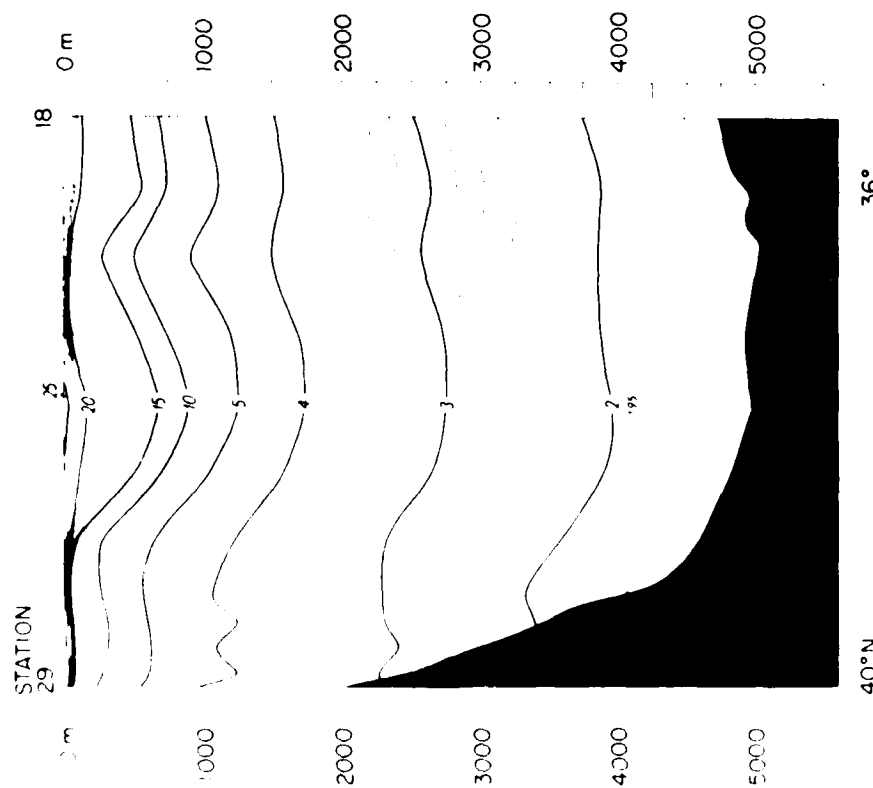
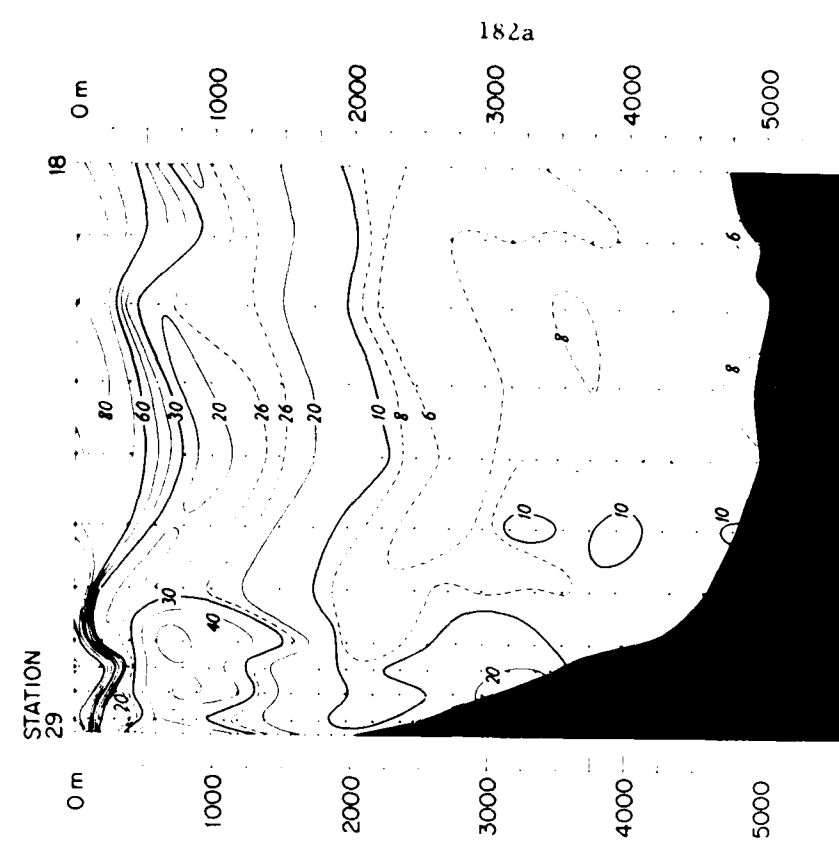


Figure 3.21: Vertical sections of F-12 (p-moles/kg x 10) and potential temperature (°C) corresponding to sections 1-4 of Figure 3.20.

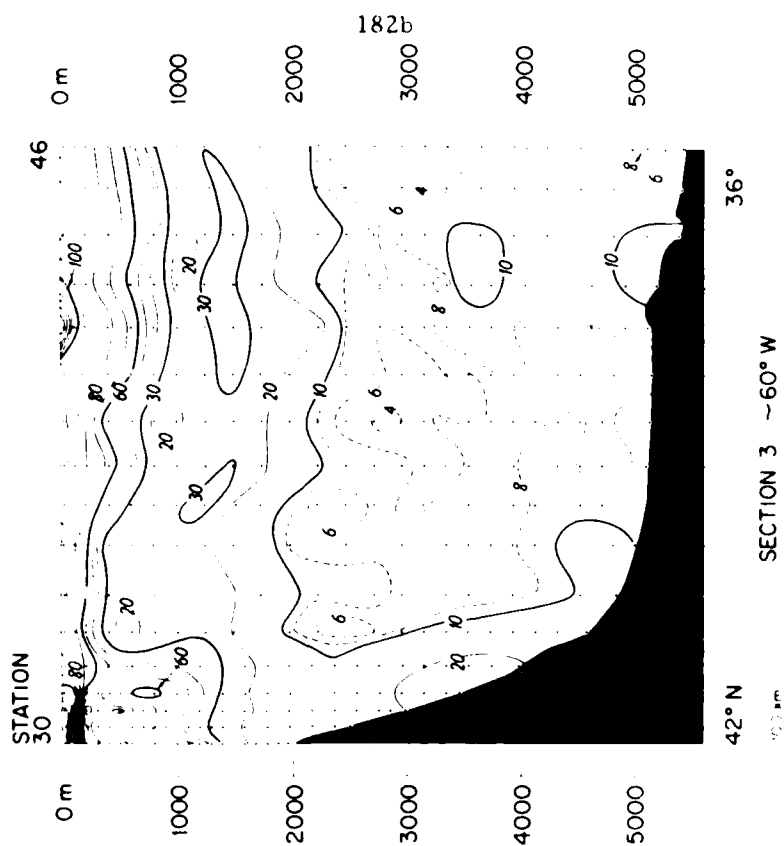
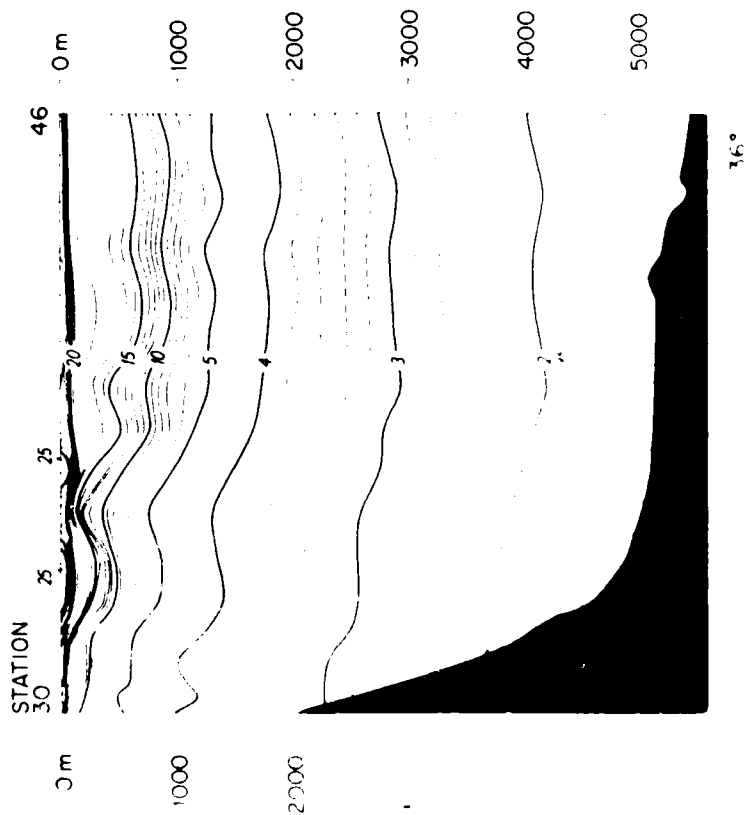


SECTION 2 ~65° W  
OCEANUS 134 JUNE 1983



SECTION 2 ~65° W  
OCEANUS 134 JUNE 1983

182a





AD-A182 341

THE ENTRAINMENT AND HOMOGENIZATION OF TRACERS WITHIN  
THE CYCLONIC GULF ST (U) WOODS HOLE OCEANOGRAPHIC  
INSTITUTION MA R S PICKART MAY 87 WHOI-87-9

3/3

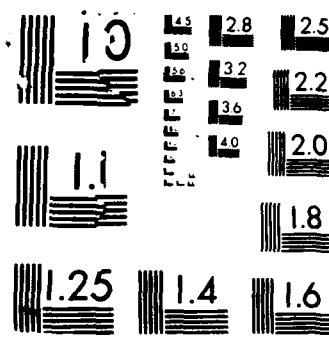
UNCLASSIFIED

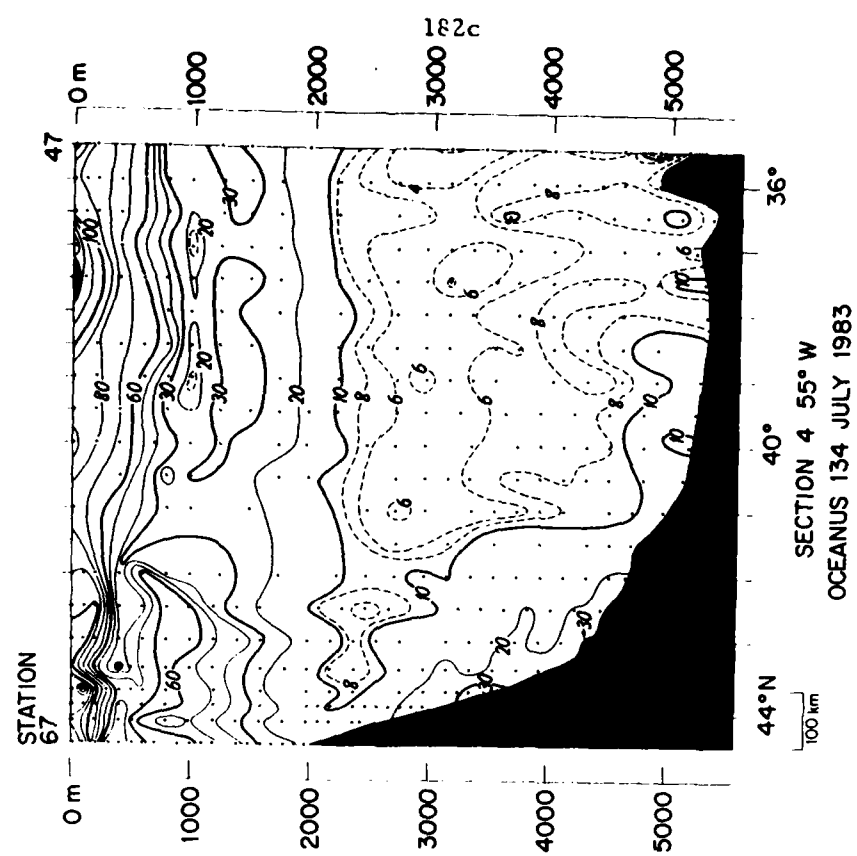
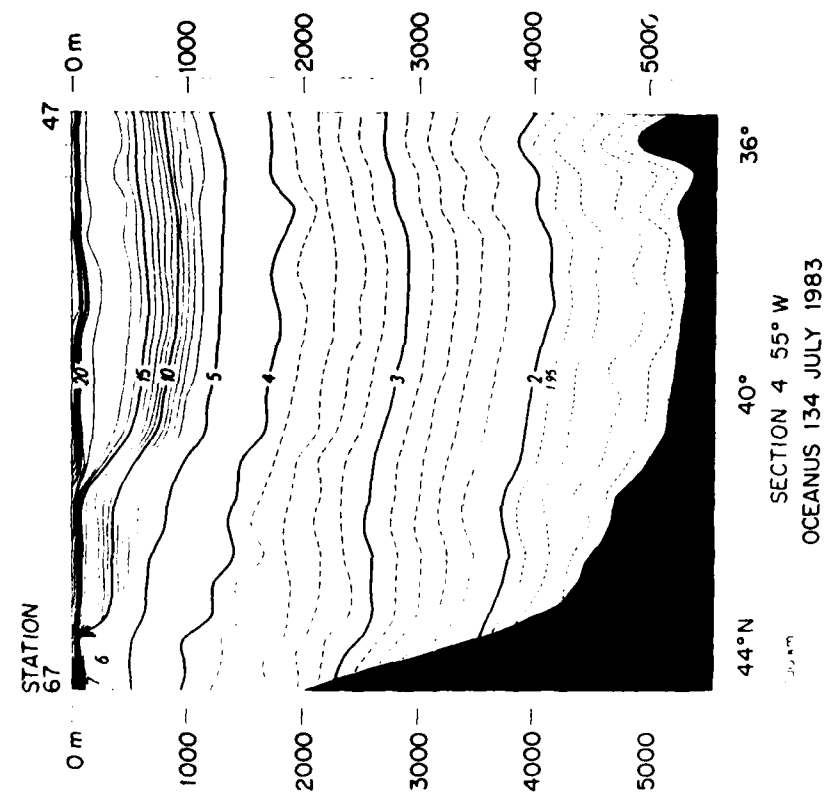
N00014-76-C-0197

F/G 8/3

NL

END  
8-77  
J.T.C.





### A) Boundary Input of Freon

As is the case with oxygen, the deep layer in this region is characterized by higher concentrations of freon than those found in the layers above and below. This means that we must consider the effects of vertical mixing. In particular, we will apply the diffusive transfer model developed earlier to the distribution of F-12. Recall that the input to the transfer model corresponds to the value at the core of the DWBC near 50°W. The time history of the F-12 core is provided by the boundary current models discussed above (although it is seen that there is more than one possible input curve). Before making use of this information we first examine the case of an arbitrary source in the context of the transfer model.

The only change that must be made in the model is to allow the input value to vary in time. Thus the appropriate equations are (2.25) where  $\phi(t)$  replaces  $\phi$ . The solutions can still be obtained easily, and are of the form

$$\phi(t) = \phi_1(t)e^{-\frac{t}{\tau_1}} + \phi_2(t)e^{-\frac{t}{\tau_2}} \quad (3.30)$$

Note the similarity of (3.30) to (2.8). Recall that in the constant input case the transient mode proportional to  $e^{-\frac{t}{\tau_1}}$  was negligible. In the present case the two amplitudes  $\phi_1(t)$  and  $\phi_2(t)$  grow in time, yet it is still true (over the time period being considered) that the term proportional to  $e^{-\frac{t}{\tau_1}}$  can be ignored. Accounting for the fact that there is a slight non-zero background, the expression for the level of freon in the gyre center is then given approximately by

$$\phi_c(t) \sim c e^{-\frac{t}{\tau}} \int_0^t \phi(t') e^{\frac{t'}{\tau}} dt' + (1 - c\tau)\phi \quad (3.31)$$

where

$$c = \frac{1}{2\sqrt{1 + \frac{\tau}{\Delta}}} \frac{1}{\tau G}$$

$$\tau = \left( \frac{1}{\Delta + 1 + \epsilon - \sqrt{\Delta^2 + 1}} \right) \tau_G$$

$\phi$  = (constant) background concentration.

It is of interest to consider how the F-11:F-12 ratio varies in the center of the gyre. Using (3.31), the expression for the ratio is

$$R_c(t) = R_\phi(t) \left[ \frac{1 + \frac{(1 - c\tau)\phi_1}{ce^{-\frac{t}{\tau}} \int_0^t \phi_1(t') e^{\frac{t'}{\tau}} dt'}}{1 + \frac{(1 - c\tau)\phi_2}{ce^{-\frac{t}{\tau}} \int_0^t \phi_2(t') e^{\frac{t'}{\tau}} dt'}} \right] \quad (3.32)$$

where

$$R_\phi(t) = \frac{\int_0^t \phi_1(t') e^{\frac{t'}{\tau}} dt'}{\int_0^t \phi_2(t') e^{\frac{t'}{\tau}} dt'}$$

$\phi_1(t), \phi_2(t)$  = input concentrations of F-11, F-12

$\phi_1, \phi_2$  = background concentrations of F-11, F-12.

Note the similarity between (3.32) and (3.8), as the bracketed term in both expressions measures the effect of non-zero background on the ratio. In the present case the quotient

$$\frac{(1 - c\tau)\phi}{ce^{-\frac{t}{\tau}} \int_0^t \phi(t') e^{\frac{t'}{\tau}} dt'} \quad (3.33)$$

must be small for both freons in order to ignore the background.

The quantity  $\tau$  measures how quickly the system would spin up if the input were to become steady (i.e. it is just the spin up time for the oxygen case). When  $\tau$  is large (3.33) is approximated by

$$\left[ \frac{1 - c\tau}{c} \right] \frac{\phi}{\int_0^t \phi(t') dt'} . \quad (3.34)$$

This limit applies when either  $\tau_B$  or  $\tau_G$  is large ( $\tau_V$  must be large in either case). It happens that regardless of which one is specified as such the term in brackets  $\rightarrow \infty$ . This means that even for a large input and small background the ratio is altered by the background concentration (because it takes so long for tracer to accumulate in the gyre).

In the opposite case when  $\tau$  is small (3.33) reduces to

$$\left[ \frac{1 - c\tau}{c\tau} \right] \frac{\phi}{\phi(t)} . \quad (3.35)$$

In order for this to be true either  $\tau_V$  must be small or both  $\tau_G$  and  $\tau_B$  have to be small. When the former is true the term in brackets  $\rightarrow \infty$ , but when the latter applies the quotient approaches a finite value. Thus in the first instance the background contribution is substantial, but in the second instance it will become negligible if in time the input concentration becomes significantly larger than that of the background. (This makes sense in that when  $\tau_V > 0$  all the tracer diffusing off the boundary immediately gets fluxed vertically out of the deep layer, but when  $\tau_B$  and  $\tau_G > 0$  tracer rapidly accumulates in the gyre.)

If it is such that the background concentration can be ignored then  $R_C(t) \sim R_\phi(t)$ . Note that  $R_\phi(t)$  has the exact same form as the expression for the freon ratio in the overflow basin (i.e. the ratio formed from (3.2)). Even though diffusion into the gyre is a different process than that which occurs in the overflow basin, because in both instances the mixing is assumed to occur instantaneously throughout the region it turns out that the two processes are described by the same type of equation. This means that the same limits concerning the freon ratio that were discussed in the context of the

overflow apply here (only with the diffusive time  $\tau$  replacing the residence time). In particular, if the input time scale varies more slowly than  $\tau$ , then

$$R_{\phi}(t) \sim \frac{\phi_1(t)}{\phi_2(t)}, \quad (3.36)$$

whereas in the opposite case when the input time scale varies more quickly than  $\tau$ ,

$$R_{\phi}(t) \sim \frac{\int_0^t \phi_1(t') dt'}{\int_0^t \phi_2(t') dt'}. \quad (3.37)$$

#### B) F-12 Level in the NRG

In chapter two when the numerical model and transfer model were applied to the distribution of oxygen it was determined that roughly 40 percent of the available oxygen from the DWBC had accumulated in the NRG. We are now in a position to obtain the analogous information concerning F-12 (or F-11). It is just a matter of applying (3.31) to determine the level in 1983 using the values for the unknowns suggested by the data. In regard to the DWBC input value we consider only the back-mixing case, i.e. (3.22a).

As was done with oxygen, a western intensified gyre is considered, and the value of the background is taken to be the average concentration at 1250 m above the deep freon maximum. In light of the discussion of the previous section it seems that we should use for the input a boundary current solution that has a core speed near 5 cm/sec. As it turns out however we can use any of the solutions, for they all result in nearly identical predictions for the F-12 level in the gyre versus time. The reason for this is that the F-12 level (at 50°W) in the boundary current is itself nearly the same for each case. When the core speed is small the level in the current is zero over a large extent of time, but when the core speed is large the increased mixing that is required keeps the level near zero for almost the same amount

of time (and keep in mind that all the curves are constrained to reach the same value in 1983). Although this result may seem surprising remember that for small levels a small change in concentration can mean a significant change in ratio. It is the case that after 1983 the curves will begin to separate, so that subsequent freon measurements in this region of the DWBC would help indicate if the 5 cm/sec solution is in fact the correct one.

The level of F-12 that is predicted for the gyre agrees closely with that measured in the data. However, this level is hardly distinguishable from the small amount of background present. The model predicts that the amount of F-12 in the gyre is only ~7 percent of that which is available from the boundary as of 1983 (the available amount is one-half the concentration of the core). The data says that the level is ~9 percent. Figure 3.22 compares the gyre level for oxygen and freon. That the F-12 level is only around 10 percent (versus 40 percent for  $O_2$ ) is consistent with the fact that the spin up time  $\tau$  is in fact longer than the freon input time scale (i.e. the gyre cannot respond quickly enough to changes in the input). Note that this also means the limit (3.37) would apply for the gyre ratio. However the level is so close to the background that the quotient (3.33) is large and thus causes  $R_c(t)$  to deviate significantly from  $R_\phi(t)$ . In time, although the level may remain near 10 percent of the available amount, it will nonetheless increase substantially above the background concentration.

### Conclusions

The process by which freon accumulates in the Northern Recirculation Gyre, the freon having originally come from the surface water in the Norwegian-Greenland Sea, is quite complicated. It has been described here very crudely as being composed of three stages. In the first stage the surface water in the N-G Sea sinks to mid-depths where it undergoes continual mixing for roughly 10 years before overflowing a sill and forming a boundary current. It has been assumed that the major contributor to the DWBC is the Iceland-Scotland overflow, but this point remains unclear. The second stage corresponds to the time during which the freon travels in the boundary current, making its way around the Grand Banks to the region near the NRG.



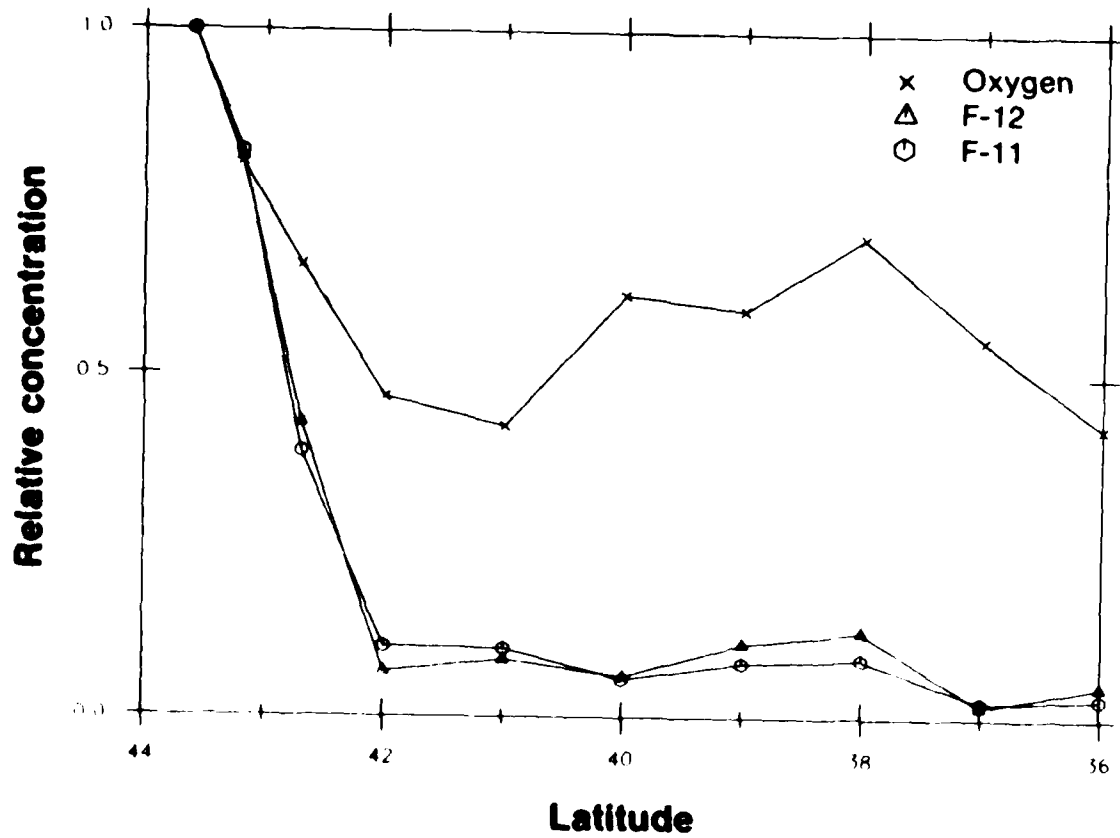


Figure 3.22: Average sections of freon and oxygen through the DWBC and NRG as in Figure 2.21. The concentration of the deep anomaly is plotted, normalized by its value at the boundary.

Finally, in the last stage, the freon diffuses from the DWBC and becomes entrained into the gyre.

For the case of oxygen which was discussed in chapter two it was only necessary to consider the last stage, but unlike oxygen the level of freon in the ocean is increasing at a rapid rate. It is assumed that the surface water concentration of freon versus time in the N-G Sea is known with some certainty. This information represents the boundary condition for the three coupled components. Because there is a discrepancy in the increase of F-11 versus F-12 this means that the F-11:F-12 ratio in the surface water, and consequently the water which overflows the sill, changes (increases) continually in time.

In the description of the second stage two different schemes were presented in which the core of the current mixes with surrounding water of a lower F-11:F-12 ratio. Extreme cases in both models predict that the ratio of the core remains unchanged, and this is in line with previous ideas in which the boundary current core speed is estimated using the value of the ratio. However there are many other solutions in the two models which alter this prediction by varying amounts. At present each of these solutions produces an accurate estimate of the F-12 level in the NRG, as the level is barely above that of the background.

### Summary

The diffusive transfer of properties from the Deep Western Boundary Current (DWBC) into the Northern Recirculation Gyre of the Gulf Stream was investigated in some detail. An advective-diffusive numerical model was implemented to aid in the study. The model consisted of a specified gyre circulation located alongside a boundary current, both flows being steady. Tracer was injected continuously into the boundary current upstream of the gyre, and the manner in which the tracer eventually fills the domain was monitored.

The entrainment of tracer into the elliptical model gyre from the boundary current is characterized by a plume encircling the gyre, while spiralling in towards its center. The extent of the spiral can be related to the characteristics of the gyre velocity field. In particular, where the flow is strong and the cross-stream shear is large the spiral is hardly noticeable, whereas in the weak flow where the cross-stream shear is small the spiral is more pronounced. The inward progression of the spiral eventually halts as the plume penetrates the interior, faster flowing portion of the gyre. It is this region which becomes homogenized in the steady state, provided the lateral diffusivity is small enough. As the diffusivity is increased, the manner of entrainment is altered and the pool of homogenized tracer shrinks in size.

A simple box-model representation of the processes occurring in the numerical model was solved analytically, which led to a more quantitative understanding of some of the numerical results. Two different types of tracers were studied, one of which was subject to lateral diffusion only, the other subject to lateral and vertical diffusion. It was found that the presence of vertical mixing has little effect on the homogenization that occurs in the gyre, but has a profound effect on the amount of tracer which gets entrained and how quickly the steady state is reached. With no vertical mixing, the level of the homogenized pool in the gyre is independent of the strength of the lateral mixing and is equal to one-half the core concentration of the boundary current at the upstream boundary. When vertical mixing is added the gyre level decreases and also becomes dependent on the size of the lateral diffusivity. The equilibration time of the gyre decreases as well.

Various results from the numerical and box-model study were applied to the ABCE tracer data set. The presence of vertical mixing appears to be the reason for a discrepancy between the deep lateral distributions of salt and oxygen, the latter being characterized by a slight minimum in the region of the NRG. The values of diffusivity which give the best agreement between data and model concerning the level of oxygen in the NRG and the associated diffusive fluxes are  $\kappa \sim 10^6 \text{ cm}^2/\text{sec}$  (lateral) and  $\nu \sim 10 \text{ cm}^2/\text{sec}$  (vertical). Although seemingly large, such a value for  $\nu$  results in only a moderate effect on the oxygen level for an NRG which is western-intensified.

The evolution of freon within the NRG was studied as well, but only in the context of the box-model. Because of the time dependency of freon a broader perspective had to be taken which addresses what happens to the freon prior to when it diffuses from the DWBC into the NRG. A simple representation of the overflow process in the Norwegian-Greenland Sea predicts that both the freon concentration and freon ratio are altered by this process. Two different boundary current models show how the ratio may be further altered by way of mixing in the DWBC. These mixing schemes suggest a DWBC core speed of 5-6 cm/sec. When the prior history of the freon is viewed together with the regional box-model, it implies that freon is only now beginning to accumulate in the NRG.

Acknowledgements

I would like to thank my committee members Dale Haidvogel, Bill Young, Harry Bryden, and Mike McCartney for their guidance with this work. Bill and Dale, by way of numerous discussions, gave me very useful ideas and suggestions. Bill Smethie kindly allowed me to use unpublished freon data and provided much insight concerning its application. I would also like to thank Fred Grosse, whose enthusiasm for teaching increased my enthusiasm for learning. My parents, Stan and Louise, have always given me support and confidence. My wife Anne has been patient and giving. I thank Mary Ann Lucas very much for preparing the manuscript.

Lastly, I would like to thank my advisor, Nelson Hogg, who constantly shared his time, his ideas, and his experience with me. I have learned very much from him.

This work was supported by the office of Naval Research through contracts N00014-76-C-0197 and N00014-84-C-0134, NR 083-400; and N00014-82-C-0019 and N00014-85-C-0001, NR 083-004, and the National Science Foundation through grant OCE82-14925.

## References

- Bullister, J. L., 1984. Atmospheric chlorofluoromethanes as tracers of ocean circulation and mixing: measurement and calibration techniques and studies in the Greenland and Norwegian Seas. Ph.D. Thesis, University of California, San Diego.
- Freeland, H. J., P. B. Rhines, and T. Rossby, 1975. Statistical observations of the trajectories of neutrally buoyant floats in the North Atlantic. Journal of Marine Research, 33, 383-404.
- Harrison, D. E., 1982. On deep mean flow generation mechanisms and the abyssal circulation of numerical model gyres. Dynamics of Atmospheres and Oceans, 3, 289-325.
- Hogg, N. G., 1983. A note on the deep circulation of the western North Atlantic: its nature and causes. Deep-Sea Research, 30, 945-961.
- Hogg, N. G., P. Biscaye, W. Gardner, and W. J. Schmitz, Jr., 1982. On the transport and modification of Antarctic Bottom Water in the Vema Channel. Journal of Marine Research, Supplement to 40, 231-263.
- Hogg, N. G., and H. Stommel, 1985. On the relationship between the deep circulation and the Gulf Stream. Deep-Sea Research, 32, 1181-1193.
- Hogg, N. G., R. S. Pickart, R. M. Hendry, and W. J. Smethie, 1986. The northern recirculation gyre of the Gulf Stream. Deep-Sea Research, 33, 1139-1165.
- Holland, W. R., 1978. The role of mesoscale eddies in the general circulation of the ocean -- numerical experiments using a wind-driven quasi-geostrophic model. Journal of Physical Oceanography, 8, 363-392.
- Holland, W. R., and L. B. Lin, 1975. On the generation of mesoscale eddies and their contribution to the oceanic general circulation. Parts I and II. Journal of Physical Oceanography, 5, 642-669.
- Holland, W. R., and P. B. Rhines, 1980. An example of eddy-induced ocean circulation. Journal of Physical Oceanography, 10, 1010-1031.
- Jenkins, W. J., and P. B. Rhines, 1980. Tritium in the deep North Atlantic Ocean. Nature, 286, 877-880.
- Joyce, T. M., C. Wunsch, and S. D. Pierce, 1986. Synoptic Gulf Stream velocity profiles through simultaneous inversion of hydrographic and acoustic Doppler data. Journal of Geophysical Research, 91, 7573-7585.

- Luyten, J. R., 1977. Scales of motion in the Deep Gulf Stream and across the continental rise. Journal of Marine Research, 35, 49-74.
- McCartney, M. S., L. V. Worthington, and M. E. Raymer, 1980. Anomalous water mass distributions at 55°W in the North Atlantic in 1977. Journal of Marine Research, 38, 147-172.
- McDowell, S., P. Rhines, and T. Keffer, 1982. North Atlantic potential vorticity and its relation to the general circulation. Journal of Physical Oceanography, 12, 1417-1436.
- Musgrave, D. L., 1985. A numerical study of the roles of subgyre-scale mixing and the western boundary current on homogenization of a passive tracer. Journal of Geophysical Research, 90, 7037-7043.
- Niiler, P. P., 1982. The general circulation of the oceans. Proceedings of the 50th Anniversary Symposium, Woods hole Oceanographic Institution.
- Pierce, S. D., 1986. Gulf Stream velocity structure through combined inversion of hydrographic and acoustic doppler data. M. S. Thesis, Massachusetts Institute of Technology, 65 pp.
- Rhines, P. B., 1983. Lectures in geophysical fluid dynamics. In: Fluid Dynamics in Astrophysics and Geophysics, Norman R. Lebovitz, editor; Lectures in Applied Mathematics, 20, American Mathematical Society, Providence, Rhode Island; pp. 3-58.
- Rhines, P. B., and W. R. Young, 1982a. Homogenization of potential vorticity in planetary gyres. Journal of Fluid Mechanics, 122, 347-367.
- Rhines, P. B., and W. R. Young, 1982b. A theory of the wind-driven circulation. I. Mid-ocean gyres. Journal of Marine Research, Supplement to 40, 559-596.
- Rhines P. B., and W. R. Young, 1983. How rapidly is a passive scalar mixed within closed streamlines? Journal of Fluid Mechanics, 133, 133-145.
- Richardson, P. L., 1977. On the crossover between the Gulf Stream and the western boundary undercurrent. Deep-Sea Research, 24, 139-159.
- Richardson, P. L., 1985. Average velocity and transport of the Gulf Stream near 55°W. Journal of Marine Research, 43, 83-111.
- Richardson, P. L., and J. A. Knauss, 1971. Gulf Stream and western boundary undercurrent observations at Cape Hatteras. Deep-Sea Research, 18, 1089-1109.

- Roache, P. J., 1972. Computational Fluid Dynamics. Hermose, 434 pp.
- Rooth, C. G., and H. G. Östlund, 1972. Penetration of tritium into the Atlantic thermocline. Deep-Sea Research, 19, 481-492.
- Smethie, W. M., and S. Trumbore, 1984. Chlorofluoromethanes (F-11 and F-12) in the western North Atlantic Ocean and the deep western boundary undercurrent. Eos, Transactions, American Geophysical Union, 64, p. 1089.
- Smith, R., 1982. Dispersion of tracers in the deep ocean. Journal of Fluid Mechanics, 123, 131-142.
- Smolarkiewicz, P. K., 1983. A simple positive definite advection scheme with small implicit diffusion. Monthly Weather Review, 111, 479-486.
- Swift, J. H., 1984. The circulation of the Denmark Strait and Iceland-Scotland overflow waters in the North Atlantic. Deep-Sea Research, 31, 1339-1355.
- Talley, L. D., and M. S. McCartney, 1982. Distribution and circulation of Labrador Sea Water. Journal of Physical Oceanography, 12, 1189-1205.
- Warren, B. A., 1981. Deep circulation of the world ocean. In: Evolution of Physical Oceanography, Scientific Surveys in Honor of Henry Stommel, B. A. Warren and C. Wunsch, editors; The MIT Press, Cambridge, Massachusetts; pp. 6-41.
- Weiss, R. F., J. L. Bullister, R. H. Gammon, and M. J. Warner, 1985. Atmospheric chlorofluoromethanes in the deep equatorial Atlantic. Nature, 314, 608-610.
- Whitehead, J. A., Jr., and L. V. Worthington, 1982. The flux and mixing rates of Antarctic Bottom Water within the North Atlantic. Journal of Geophysical Research, 87, 7903-7924.
- Worthington, L. V., 1970. The Norwegian Sea as a Mediterranean basin. Deep-Sea Research, 17, 77-84.
- Worthington, L. V., 1976. On the North Atlantic circulation. The Johns Hopkins Oceanographic Studies, 6, 110 pp.
- Wunsch, C., and B. Grant, 1982. Towards the general circulation of the North Atlantic ocean. Progress in Oceanography, 11, 1-59.
- Zill, D. G., 1979. Differential Equations. Prindle, Webster, and Schmidt, 486 pp.



## APPENDIX A

## Abbreviations and symbols:

$\Delta X, \Delta Y$	zonal, meridional grid spacing
$\Delta t$	temporal grid spacing
ADE	approximate difference equation
FT	forward in time
US	upstream in space
CT	centered in time
CS	centered in space

Interior Scheme

The governing equation is,

$$\frac{\partial}{\partial t} \theta(x, y, t) + \underline{u}(x, y) \cdot \underline{\nabla} \theta(x, y, t) = \underline{\nabla} \cdot \kappa \underline{\nabla} \theta(x, y, t) \quad (\text{A.1})$$

Several finite-difference schemes were tested.

## 1. CTCS advection/FTCS diffusion

The diffusive test produced accurate results. However, it is a property of the CTCS scheme that advective phase error occurs. Briefly, this means that the phase speed of a wave depends on its wave number, so rather than a disturbance propagating as a unit at the advective speed (the analytical result) it disperses into its component as shorter waves lag longer ones. Figure A.1a shows the result of a zonal advective test. There are two ways to reduce phase error. One is to choose the parameters  $\Delta x$  and  $\Delta t$  such that the courant number,  $C_x = u \Delta t / \Delta x$ , is close to one. ( $C_x \equiv 1$  eliminates phase error altogether.) The other is to increase the spatial resolution. The effect of these adjustments is illustrated in Figures A.1b and A.1c.

Many numerical schemes include a stipulation on the parameters of the ADE in order to avoid numerical instability (an artifact of the ADE that gives rise to an unstable solution). Some schemes are unconditionally

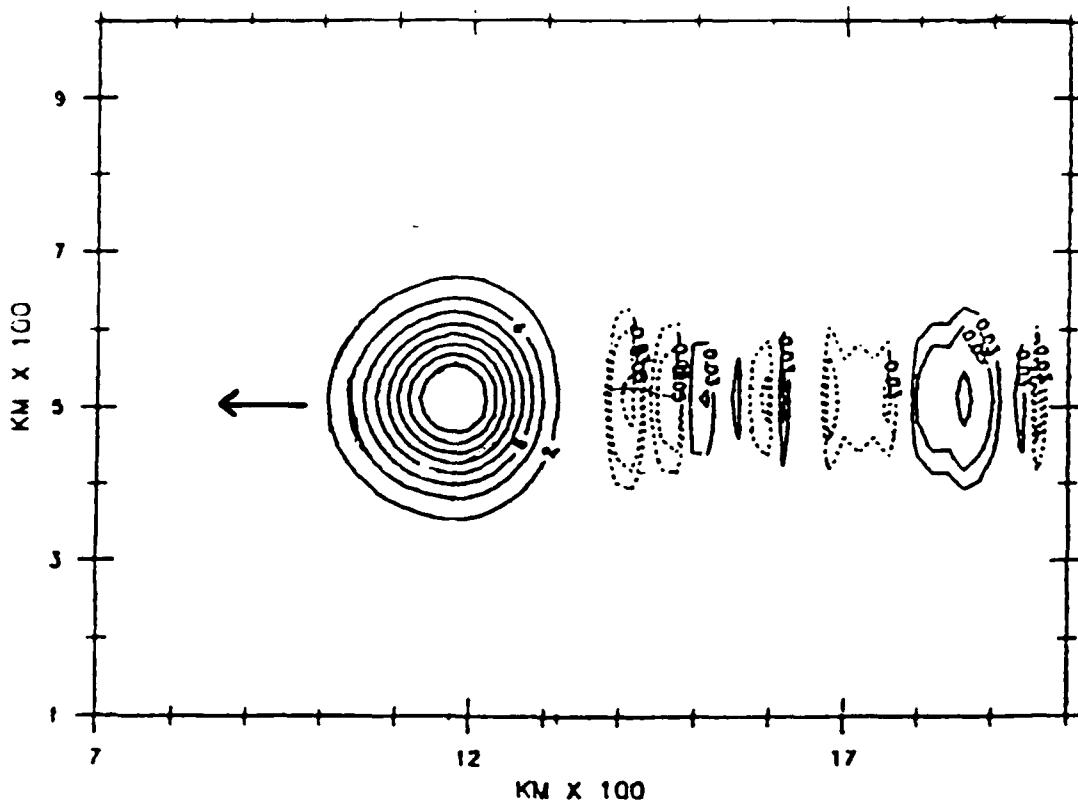
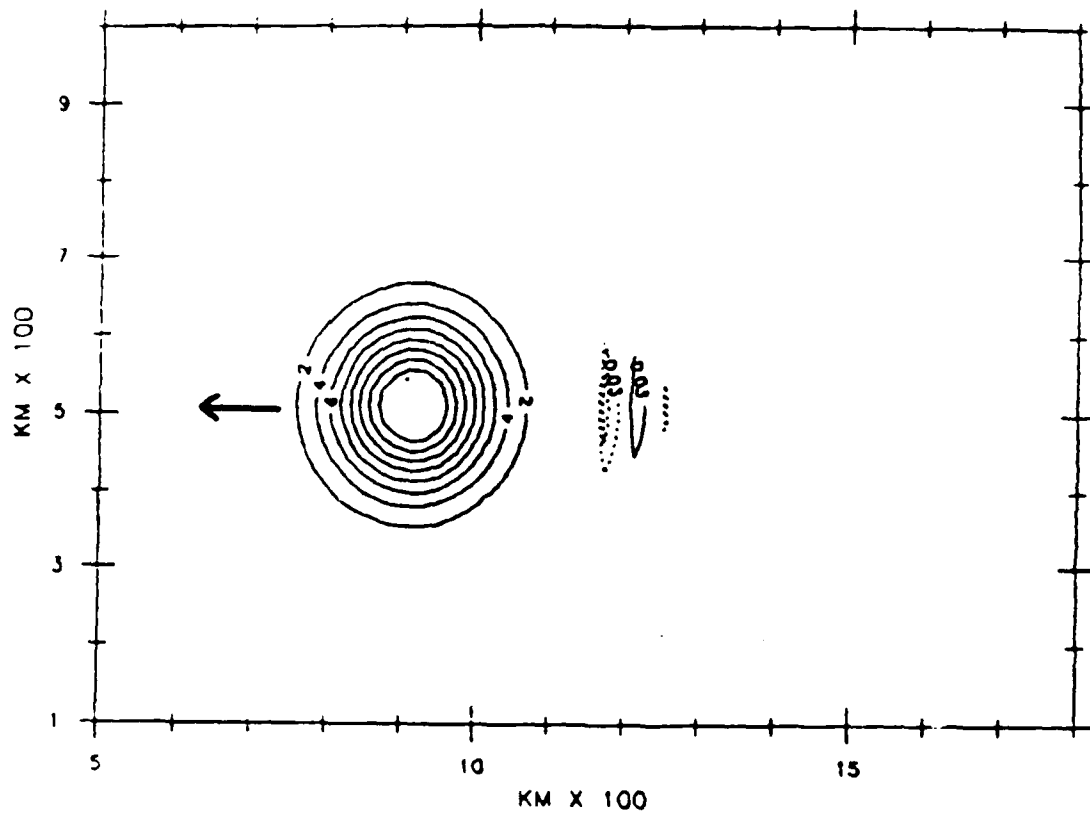
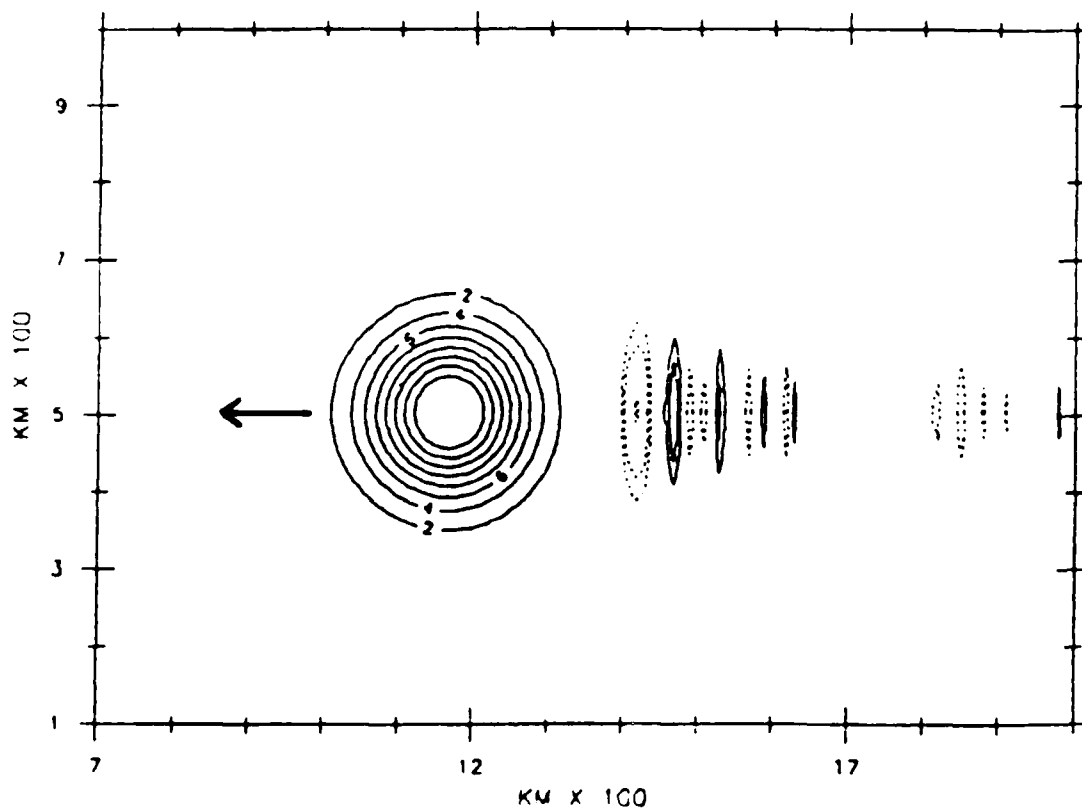


Figure A.1: (a) The effect of phase error on a Gaussian distribution of tracer being advected by a uniform flow. The amplitude of the strongest trailing wave is  $\sim 2$  percent that of the Gaussian. Note that in addition to the dispersion, phase error manifests itself through distortion of the (initially symmetric) distribution.



(b) The same distribution and flow field as in (a) only the courant number  $u\Delta t/\Delta x$  has been made close to one.



(c) Same conditions as in (a) but with twice the spatial resolution.

unstable as such. (An example is CTCS for diffusion, which is why FTCS was chosen even though it is a less accurate approximation.) For CTCS advection, stability places an upper bound on the size of the courant number. For this application of the scheme,  $\Delta x$  and  $\Delta y$  cannot be made small enough to keep the phase error at an acceptable level while still satisfying the stability criterion. As for the other adjustment to minimize phase error, the velocity field is too complex (among other reasons) to keep the courant number close to one everywhere in the domain.

## 2. FTUS advection/FTCS diffusion

Although phase error is absent in the lower order scheme, another phenomenon, implicit diffusion, is present. This error source causes a distribution of tracer to spread as if it were being acted upon by explicit diffusion (Figure A.2). As with the higher order scheme, increased spatial resolution reduces the error. However, it is impossible to keep the implicit diffusion less than the explicit diffusion without causing numerical instability, within the realm of desired parameters.

It is a property of higher order advective schemes to exhibit phase error and those of lower order to exhibit implicit diffusion (Smolarkiewicz, 1983). The approximation that was applied to (A.1) makes use of a lower order advective scheme developed by Smolarkiewicz (1983) that includes a separate step to counteract the implicit diffusion. The procedure is based on the fact that the form of the implicit diffusivity can be determined. (It depends on the parameters in the problem.) Therefore a process that acts as the reverse of diffusion can be adjusted to offset the implicit diffusion. The anti-diffusion procedure is cast into the form of advection (with an effective velocity).

The composite scheme that was used then consists of three steps:

- 1) FTUS advection
- 2) FTUS advection with effective velocity (i.e. anti-diffusion)
- 3) FTCS diffusion

The accompanying stability criterion is (Roache, 1972)

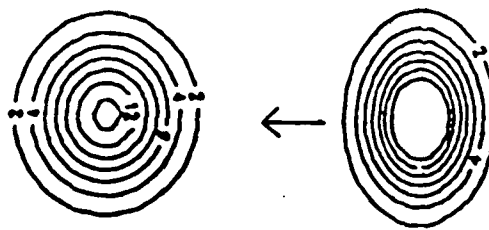


Figure A.2: The effect of implicit diffusion on a Gaussian distribution in a uniform flow.

$$\Delta t \leq \frac{1}{2\kappa\left(\frac{1}{\Delta x^2} + \frac{1}{\Delta y^2}\right) + \left(\frac{|u| + |v|}{\Delta x \Delta y}\right)}$$

Although the problem of implicit diffusion is addressed, this scheme is not without errors. For example, artificial diffusion occurs during the second advective step (Smolarkiewicz, 1983). Another drawback of FTUS for advection is the presence of a directionally dependent distortion. This error reveals itself only when both  $u$  and  $v$  are non-zero and is most prevalent when  $|u|$  and  $|v|$  are equal (see Figure A.3 for a discussion).

### Boundary Conditions

The edges of the domain do not correspond to solid boundaries but rather open ocean. There are three flow regimes that exist along different portions of the boundary.

#### A) Inflow

Where the boundary current flows into the domain the concentration of tracer is specified.

#### B) Outflow

Where the boundary current flows out of the domain diffusion normal to the boundary is omitted, as is anti-diffusion. Advection and cross-stream diffusion are carried out as in the interior. (Figure A.4 shows results from an experiment testing the outflow boundary condition.)

#### C) No Flow

The inflow and outflow boundary conditions are applied where the boundary current velocity is significantly greater than zero (which was chosen to be greater than .2 cm/sec). Along the remaining part of the boundary velocities are smaller than this and are set equal to zero, so that only the diffusion step requires a boundary condition. However, CS diffusion requires that the concentration be known at neighboring grid points, which is not possible at the boundary. An extrapolation boundary condition was developed which attempts to simulate open boundary diffusion. It is based on the fact that the normal gradient of tracer along the no-flow segments will be everywhere inward, i.e. there will be an outward diffusive flux.

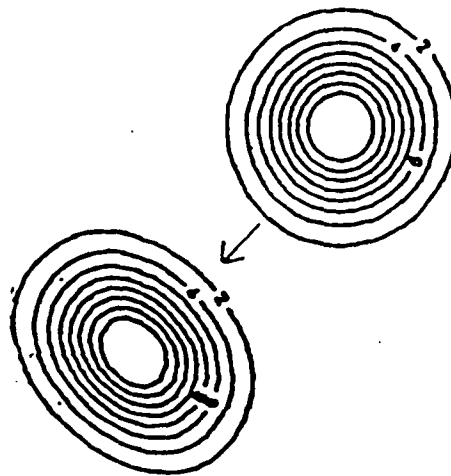
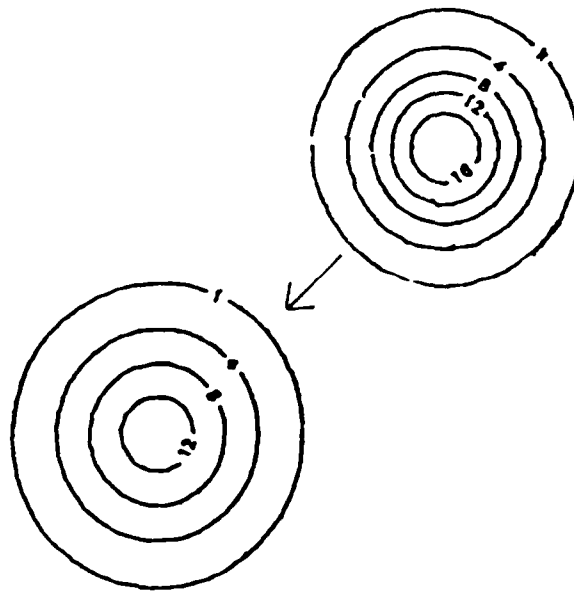


Figure A.3: (a) Gaussian in a uniform flow in which  $|u| = |v|$  demonstrating another type of error associated with the FTUS scheme. (There is negligible implicit diffusion because the corrective step has been employed.)





(b) Same conditions as in (a) only the advection is performed in two steps -- each dimension separately. This eliminates the distortion. (Implicit diffusion is present because the corrective step was omitted.) This technique is not feasible, however, because it must be accompanied by two anti-diffusive steps, and the resulting computational expenses would be too high.

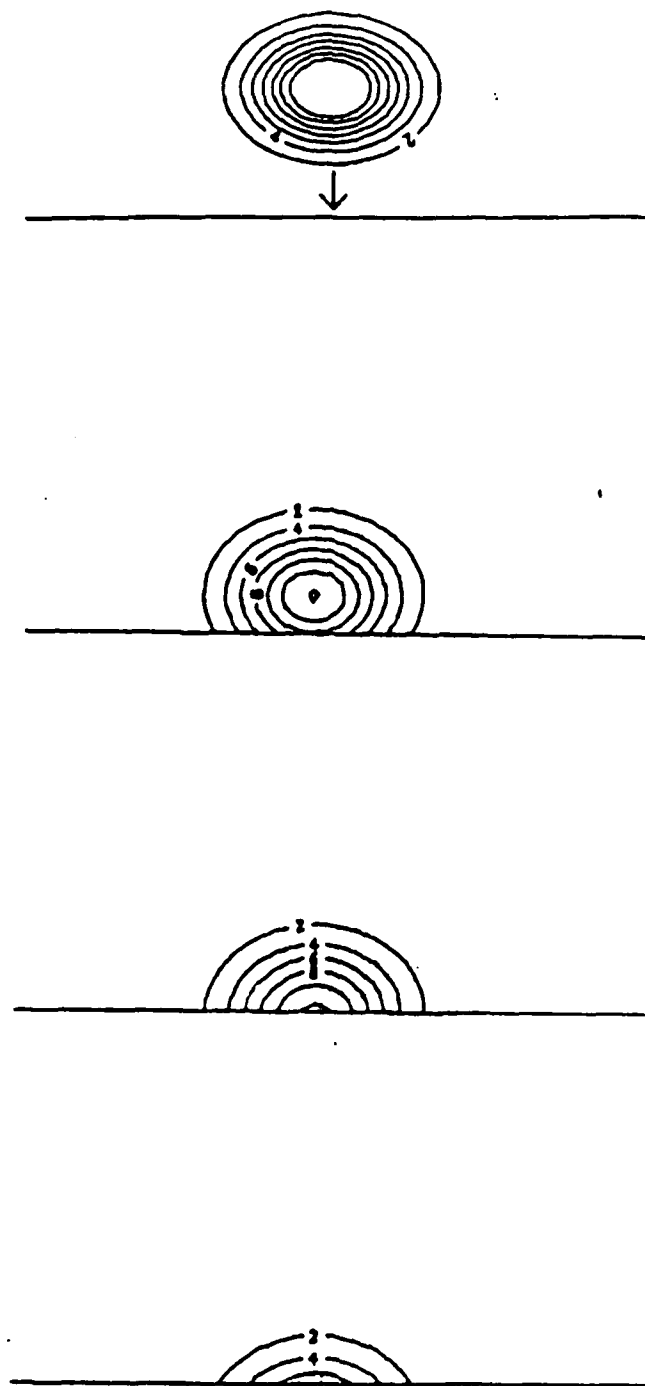


Figure A.4: Test of the outflow boundary condition. Gaussian distribution, uniform current.

The simplest approximation to an open boundary consists of specifying a constant flux at the boundary (a passive flux). This means that the concentration there would evolve in time (an active concentration). Allowing the flux to change in time according to a specified criterion (an active flux) forms an improved estimate. A natural way to come up with such a criterion would be to make use of what is known about the flux just inside of the boundary; in particular, compute the trend of outward flux approaching the boundary along lines perpendicular to it, and extrapolate to compute the flux at the boundary -- from which the concentration is then determined. In line with this, consider the following procedure to be performed at each time step after the interior solution has been determined.

- i) The value of the flux at a point is defined in an upwind sense

$$F_i = \kappa \left( \frac{\theta_i - \theta_{i+1}}{\Delta s} \right),$$

where  $\theta_{i+1}$  is the concentration adjacent to  $\theta_i$  in the direction of the inward normal, and  $\Delta s$  is the grid spacing (equal to  $\Delta x$  or  $\Delta y$ ). The value of  $F_i$  near the boundary must always be  $\leq 0$ .  $F_i$  is computed at the three points prior to the boundary along the normal ( $i = 1$  corresponds to the point closest to the boundary).

- ii) Let  $F_0$  denote the value of  $F_i$  at the boundary. If  $F_1 = 0$ ,  $F_0$  is set  $= 0$ .
- iii) If  $F_1$  is non-zero,  $F_0$  is predicted using a three-point extrapolation:  $F_0 = 3F_1 - 3F_2 + F_3$ .
- iv) If the predicted  $F_0$  is  $> 0$ ,  $F_0$  is reset  $= 0$ .
- v) The concentration of tracer at the boundary is then determined from the value of  $F_0$ . (If the calculated concentration is  $< 0$ , then it is reset  $= 0$ .)

This procedure was applied in a test-run which consisted of having a Gaussian spot of tracer diffuse near a boundary. Results of the test are shown in Figure A.5. Note that as time progresses the contours right next to the boundary become artificially squished, indicating that the gradients

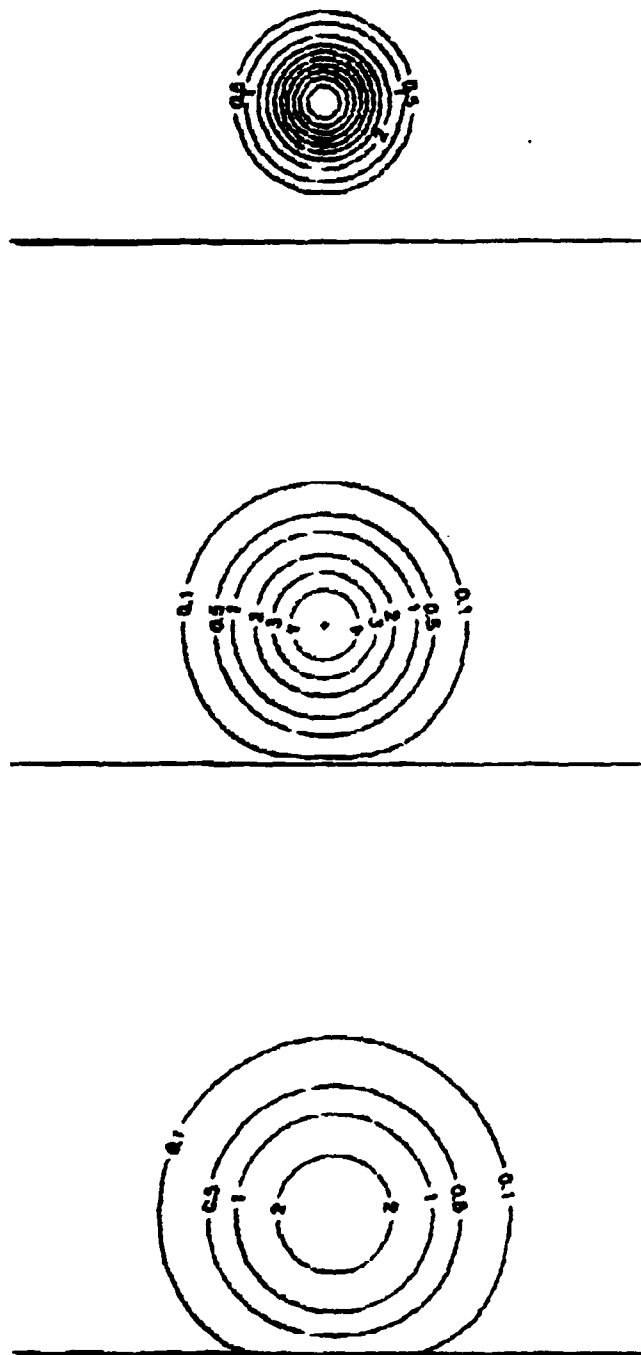


Figure A.5: Test of the flux-extrapolation (active flux) boundary condition. Gaussian distribution.

there are too large. This problem can be corrected by extrapolating a different quantity other than the flux.

Consider the parameter  $R_i = \left( \frac{\theta_i}{\theta_{i+1} + \epsilon} \right)$ , which is the ratio of adjacent concentrations in the direction of the inward normal ( $\epsilon$  is a small number to prevent division by zero). In the region near the boundary  $R_i$  will always fall between zero and one (the former means tracer is just beginning to penetrate the area, the latter corresponds to no flux). If  $R_i$  is extrapolated in the manner described above in order to calculate the boundary concentration, this results in weaker gradients than the with flux extrapolation. The reason for this is that this procedure involves percents rather than differences. For example, if there were a linear decrease in concentration towards the boundary, the flux prediction for  $\theta$  at the boundary would continue this trend, whereas the ratio prediction would cause the trend to flatten out, which is more realistic of diffusion.

The active flux condition that was used in the model then is outlined as follows.

- i) The value of  $R_i$  is computed at the three points prior to the boundary along the normal ( $i = 1$  corresponds to the point closest to the boundary).
- ii) Let  $R_0$  denote the value of  $R_i$  at the boundary. If  $R_1 = 0$ ,  $R_0$  is set = 0.
- iii) If  $R_1$  is non-zero,  $R_0$  is predicted using a three-point extrapolation:  $R_0 = 3R_1 - 3R_2 + R_3$ .
- iv) If the predicted  $R_0 > 1$ ,  $R_0$  is reset = 1.
- v) If the predicted  $R_0 < 0$ ,  $R_0$  is reset = 0.
- vi) The concentration of tracer at the boundary is then determined from the value of  $R_0$ .

Results from the same test-run applied above, using this scheme, are shown in Figure A.6. It is seen that the isolines near the boundary no longer appear to get distorted.

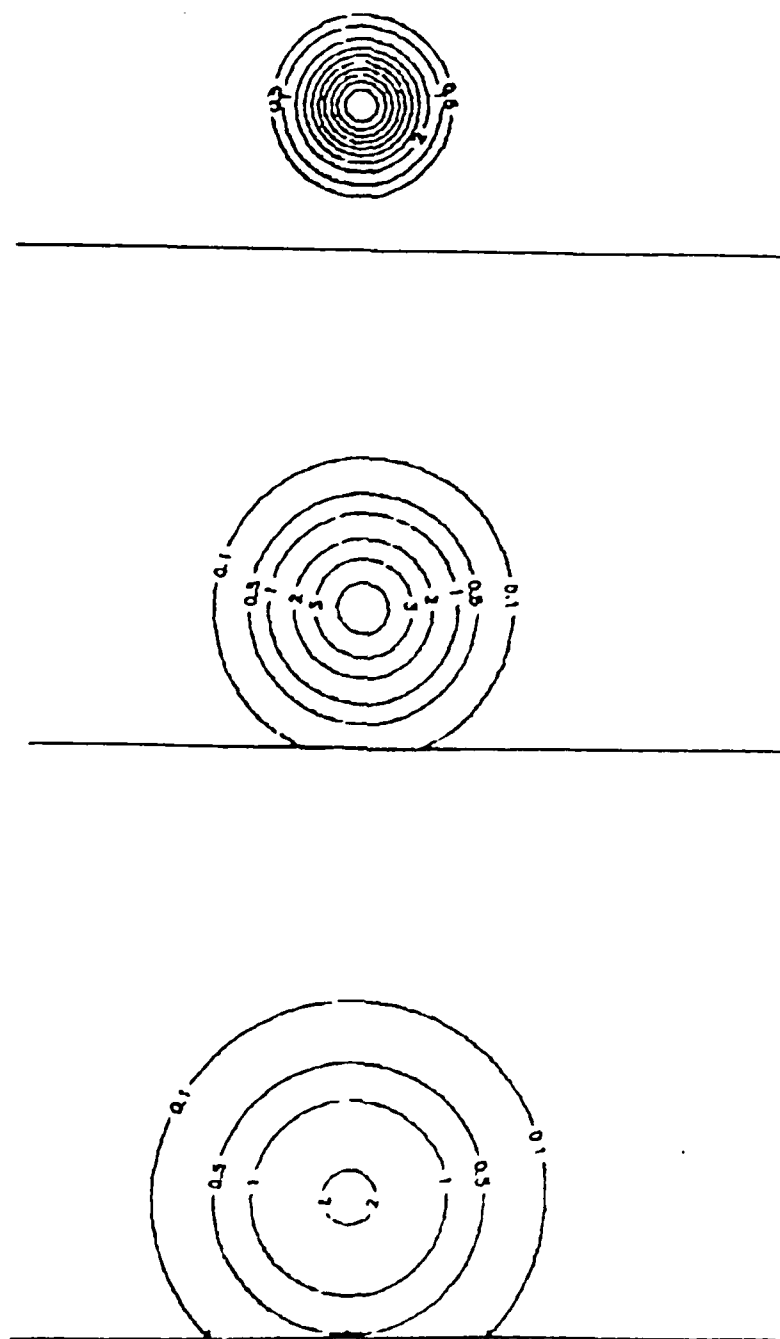


Figure A.6: Test of the ratio-extrapolation (active flux) boundary condition. Gaussian distribution.

### Corners

The four corners of the domain lie in the no-flow region; the active flux condition is applied at each, with the extrapolation performed along the diagonal.

Table A.1 contains a summary of the boundary conditions.

TABLE A.1  
BOUNDARY CONDITIONS

I. First Step: Advection

- |                |                       |
|----------------|-----------------------|
| (i) inflow,    | specify concentration |
| (ii) outflow,  | _____                 |
| (iii) no-flow, | _____                 |

II. Second Step: Anti-diffusion

- |                |                       |
|----------------|-----------------------|
| (i) inflow,    | specify concentration |
| (ii) outflow,  | omit normal flux      |
| (iii) no-flow, | _____                 |

III. Third Step: Diffusion

- |                |                       |
|----------------|-----------------------|
| (i) inflow,    | specify concentration |
| (ii) outflow,  | omit normal flux      |
| (iii) no-flow, | active flux           |



## DOCUMENT LIBRARY

November 21, 1986

### *Distribution List for Technical Report Exchange*

Institute of Marine Sciences Library  
University of Alaska  
O'Neill Building  
905 Koyukuk Ave., North  
Fairbanks, AK

Attn: Stella Sanchez-Wade  
Documents Section  
Scripps Institution of Oceanography  
Library, Mail Code C-075C  
La Jolla, CA 92093

Hancock Library of Biology & Oceanography  
Alan Hancock Laboratory  
University of Southern California  
University Park  
Los Angeles, CA 90089-0371

Gifts & Exchanges  
Library  
Bedford Institute of Oceanography  
P.O. Box 1006  
Dartmouth, NS, B2Y 4A2, CANADA

Office of the International  
Ice Patrol  
c/o Coast Guard R & D Center  
Avery Point  
Groton, CT 06340

Library  
Physical Oceanographic Laboratory  
Nova University  
8000 N. Ocean Drive  
Dania, FL 33304

NOAA/EDIS Miami Library Center  
4301 Rickenbacker Causeway  
Miami, FL 33149

Library  
Skidaway Institute of Oceanography  
P.O. Box 13687  
Savannah, GA 31416

Institute of Geophysics  
University of Hawaii  
Library Room 252  
2525 Correa Road  
Honolulu, HI 96822

Library  
Chesapeake Bay Institute  
4800 Atwell Road  
Shady Side, MD 20876

MIT Libraries  
Serial Journal Room 14E-210  
Cambridge, MA 02139

Director, Ralph M. Parsons Laboratory  
Room 48-311  
MIT  
Cambridge, MA 02139

Marine Resources Information Center  
Bldg. E38-320  
MIT  
Cambridge, MA 02139

Library  
Lamont-Doherty Geological Observatory  
Columbia University  
Palisades, NY 10964

Library  
Serials Department  
Oregon State University  
Corvallis, OR 97331

Pell Marine Science Library  
University of Rhode Island  
Narragansett Bay Campus  
Narragansett, RI 02882

Working Collection  
Texas A&M University  
Dept. of Oceanography  
College Station, TX 77843

Library  
Virginia Institute of Marine Science  
Gloucester Point, VA 23062

Fisheries-Oceanography Library  
151 Oceanography Teaching Bldg  
University of Washington  
Seattle, WA 98195

Library  
R S M A S  
University of Miami  
4600 Rickenbacker Causeway  
Miami, FL 33149

Maury Oceanographic Library  
Naval Oceanographic Office  
Bay St. Louis  
NSTL MS 39322-0001  
ATTN: Code 4601

<b>REPORT DOCUMENTATION PAGE</b>	<b>1. REPORT NO.</b> WHOI-87-9	<b>2.</b>	<b>3. Recipient's Accession No.</b>
<b>4. Title and Subtitle</b> The Entrainment and Homogenization of Tracers within the Cyclonic Gulf Stream Recirculation Gyre		<b>5. Report Date</b> May 1987	
<b>7. Author(s)</b> Robert S. Pickart		<b>8. Performing Organization Rept. No.</b> WHOI-87-9	
<b>9. Performing Organization Name and Address</b> Woods Hole Oceanographic Institution Woods Hole, Massachusetts 02543 and Massachusetts Institute of Technology Cambridge, Massachusetts		<b>10. Project/Task/Work Unit No.</b>  <b>11. Contract(C) or Grant(G) No.</b> N0014-76-C-0197, N00014-84-C-0184, NR 083-004; N00014-82-C-0019, N00014-85-C-0001, NR 083-400; and OCE 82-14925	
<b>12. Sponsoring Organization Name and Address</b> The Office of Naval Research and The National Science Foundation		<b>13. Type of Report &amp; Period Covered</b>  Ph.D. Thesis	
<b>15. Supplementary Notes</b> This thesis should be cited as: Robert S. Pickart, 1987. The Entrainment and Homogenization of Tracers within the Cyclonic Gulf Stream Recirculation Gyre. Ph.D. Thesis. MIT/WHOI, WHOI-87-9.			
<b>16. Abstract (Limit 200 words)</b>  The distributions of tracer associated with the Northern Recirculation Gyre of the Gulf Stream NRG are studied to try to obtain information about the flow. An advective-diffusive numerical model is used whose streamlines consist of a gyre situated alongside a boundary current which inputs tracer into the domain. This is meant to simulate the lateral transfer of properties from the Deep Western Boundary Current (DWBC) to the NRG. Tracer is entrained into the model gyre as a plume which spirals across the streamlines, the characteristics of which depend on the flow parameters. Homogenization occurs at steady state, consistent with recently collected tracer data. The presence of vertical mixing is considered in an attempt to explain a difference between salinity and oxygen observed in the data. Comparison of the model results to the oxygen data is favorable, and leads to an estimate of the lateral and vertical diffusivity. The time dependent nature of freon is addressed using a coupled model of the deep water overflow process, advection mixing in the DWBC, and subsequent entrainment into the NRG. Comparison with the data shows that very little freon has accumulated in the NRG, and that these processes affect the freon 11/freon 12 ratio as well.			
<b>17. Document Analysis &amp; Descriptors</b> a. Homogenization of tracers b. Gulf Stream recirculation c. Deep Western Boundary Current  b. Identifiers: Open Ended Terms  c. COSATI Field Group			
<b>18. Availability Statement</b>  Approved for publication; distribution unlimited.		<b>19. Security Class (This Report)</b> UNCLASSIFIED <b>20. Security Class (This Page)</b>  <b>21. No. of Pages</b> 210 <b>22. Price</b>	

END

8-87

DTIC